Single photons from single ions: quantum interference and distant ion interaction

Dissertation

zur Erlangung des Grades
des Doktors der Naturwissenschaften
der Naturwissenschaftlich-Technischen Fakultät II
– Physik und Mechatronik –
der Universität des Saarlandes
von

Michael Schug

Saarbrücken

2015

Tag des Kolloquiums:	11.09.2015
Dekan:	Prof. Dr. Georg Frey
Mitglieder des Prüfungsausschusses:	Prof. Dr. Jürgen Eschner
	Prof. Dr. Klaus Blaum
	Prof. Dr. Christian Wagner
	Dr. Béatrice Hallouet

Abstract

One possible physical implementation of a quantum network consists of single trapped ions which serve as quantum processors and single photons for the transmission of quantum information between the processors.

Toward this, the present work contains fundamental studies on the interaction of single photons with single trapped ions. For this purpose the controlled emission of single Raman-scattered photons from a single $^{40}Ca^{+}$ ion is explored for two different emission wavelengths.

The generated photons from one ion are used to perform photonic interaction measurements between two single ions in two distant traps. For continuous emission of photons from the sender ion, absorption events at the receiver ion are detected with a quantum-jump technique. Moreover, the interaction is demonstrated in triggered photon-generation mode by coincidental events in a correlation measurement.

Finally, the thesis presents experiments which investigate the coherence character of the Raman process. In two level configurations, Λ and V, it is shown that the quantum-mechanical phase is reflected as quantum beats in the wave packet of the generated Raman photons. The experimental data and the theoretical description reveal two different origins of the quantum beats, namely, the quantum interference in either the absorption or the emission process.

Zusammenfassung

Eine mögliche physikalische Implementierung eines Quantennetzwerks besteht aus einzelnen Ionen, die als Quantenprozessoren dienen, und einzelnen Photonen für die Übertragung von Quanteninformation zwischen den Prozessoren.

Die vorliegende Arbeit beinhaltet dahingehende, grundlegende Untersuchungen zur Wechselwirkung von einzelnen Photonen mit einzelnen gefangen Ionen. Dazu wird zunächst die kontrollierte Emission einzeln gestreuter Raman-Photonen für zwei verschiedene Emissionswellenlängen aus einem $^{40}Ca^{+}$ Ion untersucht.

Die erzeugten Photonen aus einem Ion werden genutzt, um die photonische Wechselwirkung zwischen zwei einzelnen Ionen in zwei getrennten Fallen durchzuführen. In kontinuierlicher Photonenemission am Sender-Ion werden Absorptionsereignisse am Empfänger-Ion mit einem Nachweis von Quantensprüngen detektiert. Darüber hinaus zeigt sich die Wechselwirkung in sequenzieller Photonenerzeugung durch koinzidente Ereignisse in einer Korrelationsmessung.

Abschließend werden in der Arbeit Experimente präsentiert, die den Kohärenzcharakter des Ramanprozesses untersuchen. In zwei verschiedenen Niveaustruktur-Anordnungen, Λ und V, wird gezeigt, dass die quantenmechanische Phase sich als Quantenschwebung im Wellenpaket der Ramanphotonen wiederfindet. Die experimentellen Daten und die theoretische Beschreibung lassen die verschiedenen Ursprünge der Quantenschwebungen erkennen, nämlich, die Quanteninterferenz im Absorptions- oder Emissionsprozess.

Contents

Introduction

One of the important inventions of the 20th century was the one of the computer. In his 1936 paper [1], Alan Turing introduced a description for a machine, known as the Turing machine which can be seen as a prototype for a programmable computer. Nowadays, computers have become an integral part of everyday life, particularly through the evolution of the internet, which accelerated the global exchange of information.

Based on the historical development of the computer, the trend was to increase the computing power. Upon this trend, Gordon Moore formulated his law in 1965 [2] that the complexity of integrated circuits doubles for constant cost about every year. Besides, the simultaneous miniaturization of the components used for computation has evolved in the last decades. Both developments led to a reduction of the number of atoms that are needed to realize or store a bit of information with the consequence that today's industry of information technology starts to enter a new regime where quantum effects play a more and more pronounced role [3].

With this trend, it began the inclusion of a new type of physics for computation and information processing, namely *quantum mechanics*. With the latter, it turns out that *quantum computers* offer an essential speed advantage for certain mathematical problems over classical computers through their *efficient* computation. Efficient means that the computation needs time that increases polynomial with the size of the problem instead of computation with superpolynomial (typically exponential) time consumption [4].

One of the first to address the idea of a quantum computer was Richard Feynman [5, 6] around 1980. He suggested that a computer can be built of quantum-mechanical elements, which allows one to simulate quantum physics more easily with a universal quantum computer (or *quantum simulator*) instead of a classical computer. In 1985, David Deutsch transferred the idea of Feynman to the first description of a universal quantum computer by a general, fully quantum model for computation [7] which can efficiently simulate physical systems, in contrast to classical computers. One of the most prominent algorithms for quantum computing was discovered in 1994 by Peter Shor. He discussed that the problem of finding the prime factors of an integer can be solved efficiently on a quantum computer, in contrast to the classical Turing machine [8]. Besides Shor, it was Lov Grover [9] who further emphasized the performance of a quantum computer by another algorithm. He tackled a search problem, i.e. finding an item in an unsorted database with a quantum algorithm which turned out to be polynomially faster than any classical algorithm. Up to now, more and more algorithms appeared, although it is still challenging to come up with problems which are solved with higher efficiency by a quantum computer than by a classical one.

Quantum information processing

In classical computation and information processing, the elementary unit for calculation is the binary digit (bit). In quantum computation and quantum information, it is replaced by the *quantum bit*, also called the *qubit*. In contrast to the classical bit, which can be either in state 0 or 1, the qubit is represented by a superposition of these two states. This novelty builds the basis for *quantum parallelism* where a function is evaluated for two input values simultaneously with one quantum circuit. Including quantum interference in the computation, quantum parallelism allows for the evaluation of a function to be balanced or constant in exponentially reduced time than a classical deterministic computer [7, 10]. Besides the single- and multi-qubit states, we have to emphasize *entangled* states. Their measurement outcomes contribute to the core of quantum information processing which cannot be explained classically.

In analogy to the classical computer, the quantum computer uses gates to process quantum information. There is a finite set of quantum gates that are called universal, such that an arbitrary quantum computation on any number of qubits can be generated [4]. Single qubit gates (e.g. NOT gate, Hadamard gate, phase gate) are distinguished from multi-qubit gates (e.g. AND, NOR, CNOT). Both can build universal sets of gates. One example is given by the CNOT and single qubit gates which can compose any multi-qubit logic gate.

The experimental implementation of quantum information-processing units is nowadays widely spread to various fields. Naming only a few out of the various types of experimental implementations, we can categorize them into quantum-optical systems like photons [11], single atoms [12], solid state systems (e.g. spin states of single-electron quantum dots [13]), molecular systems using nuclear magnetic-resonance techniques [14] and superconducting qubits in circuit quantum electrodynamics [15]. The viability of these systems to fulfill the requirements for the implementation of quantum computation is characterized by the five criteria of David DiVincenzo [16]. The experimental realization needs

1. a physical system which is scalable with well-characterized qubits,
2. the initialization of the qubit state to a simple fiducial state,
3. long coherence times which are much longer than the gate operation time,
4. a universal set of quantum gates,
5. and a qubit-specific measurement capacity.

The physical system with which these criteria can be optimally met must therefore itself be well studied and characterized. The early development of traps for charged particles in the 1950s led to the well-studied system of trapped ions which represent the qubits. Thus single ions confined in Paul traps offer one of the most promising experimental platform for quantum information processing tasks due to their high degree of isolation from environmental disturbances and the ability to investigate the properties of the ion with laser

light. The starting signal for using single trapped ions to realize a quantum computer was given by Cirac and Zoller [17]. In their seminal proposal, they indicate that quantum gates can be realized by coupling ion strings through the collective quantized motion. Based on the well-established technique of laser cooling the motion of a single ion [18], people started to control the motional states in ion strings [19]. The control allowed to perform the first gates, like the geometric phase gate [20], the CNOT gate [21] or the powerful Mølmer-Sørensen gate [22]. The latter is used to generate genuine multiparticle entangled states which has already been shown with 14 qubits [23]. Recent progress have been shown by the use of trapped ions as a quantum information processor [24] for quantum simulations [25] and for quantum error correction [26].

Besides the advantages of using linear Paul traps for confining ion strings, the scalability to many ions remains a demanding task. Trapping many ions increases the complexity of the motional mode spectrum which reduces the speed of gate operations [27]. To address this problem, new the traps have been designed, e.g. microfabricated surface-electrode ion traps [28] or ion traps in a semiconductor chip [29] to use them in a new architecture. It interconnects processing and memory zones where the ion qubits are selectively shuttled between these zones [30]. This type of system allows for scaling up the number of qubits.

Quantum networks

An alternative approach to ion shuttling lies in the implementation of a network of small-scale quantum information-processing units. This aspect has also been taken into account by DiVincenzo who added two more criteria to his five points necessary for computation alone, which are

6. the ability to interconvert stationary and flying qubits,

7. the ability to faithfully transmit flying qubits between specified locations.

The stationary nodes in the quantum network are the quantum processors, where quantum information is stored and manipulated [31]. The nodes are represented by single trapped ions interconnected by quantum channels with flying qubits, provided by single photons. The photons carry quantum information, e.g. in their polarization degree of freedom, which is transmitted between the nodes enabling fast *quantum communication*. One drawback for communication with noisy channels over long distances between distant nodes is the scaling of the error probability with the length of the channel [32]. For transmission channels like optical fibers, the probability for absorption or depolarization of the transmitted photons increases exponentially with the length of the fiber. To solve this problem, Briegel et al. presented the model of a *quantum repeater*, which uses entangled nodes over short distances to create entanglement of network nodes over arbitrarily large distances [32]. Once the nodes are entangled, quantum information can be transferred between the nodes by quantum teleportation [33, 34, 35]. Thus a basic requirement

for long-range quantum communication is the entanglement of nodes in the network. We can categorize three different approaches to realize distant entanglement.

One approach is the *direct quantum state transfer* between spatially distant atoms in cavities [36]. The quantum state of the sender atom is entangled with the emitted photon which is transmitted to the receiver atom where the quantum information is absorbed, resulting in entanglement of the two nodes. For single ^{87}Rb atoms in distant cavities separated by 21 meters, the protocol has been impressively realized [37], although the scheme has still a probabilistic nature. With respect to single trapped ions, the first realization of direct photonic interaction between two distant single ions is presented in this thesis and published in [38].

A second approach is the creation of *heralded entanglement* of distant nodes based on the emission process of photons from distant nodes. In contrast to the direct photonic interaction, the entangled state of two single emitters is not generated by an effective interaction between the two nodes, but by an interference effect and state-projective measurement which heralds the entanglement. For interference and detection of a single photon from two distant ions, the protocol of Cabrillo et al. [39] was experimentally shown with two single $^{138}Ba^{+}$ ions confined in the same trap [40]. Using two-photon interference, a scheme proposed by Simon et al. describes the entanglement of distant ions by the joint detection of two photons [41]. For that the two photons ideally have to be Fourier-transform limited and indistinguishable in all degrees of freedom [42]. The implementation has been performed with two distant single ^{87}Rb atoms trapped independently 20 meters apart [43], with two distant single $^{171}Yb^{+}$ ions separated by one meter distance [44] and with two NV center spin qubits separated by three meters [45].

The third approach toward entangling distant nodes is pursued in our group and employs *entanglement transfer* from entangled photon pairs, as from a spontaneous parametric down-conversion source (SPDC), to two single distant-trapped ions [46]. The successful absorption event is heralded locally by the detection of a single Raman-scattered photon which does not destroy or reveal the mapped photonic quantum state. The main advantage against schemes without a heralding signal is that the herald leads to a high state-transfer fidelity also for the case that the photon absorption probability is low.

The scheme based on heralded entanglement showed that *quantum interference*, as a pure quantum optical phenomenon, is a pivotal element [47] in the field of quantum-information theory [48]. For the two other schemes quantum interference becomes important for photonic information exchange at the atom-photon interface which is ideally performed in a *coherent* way to faithfully transfer the quantum information.

Ion-photon interface

Besides the coherent conversion of quantum information from photons to ions and vice versa, entangling different nodes requires a high efficiency to ideally reach deterministic control. Thus it is imperative to improve the coupling between the ion and the photons at the interface. Different strategies are used to improve the coupling, i.e. to increase the solid

angle covered by the collection optics surrounding the ion for efficient photon absorption and for high fiber-coupling efficiency of emitted photons. Strong coupling is achievable by using a cavity around the atoms or ions [49, 50, 51] which enables in principle deterministic generation of entangled states. It competes with the use of high-numerical-aperture objectives [52, 53, 54, 55] covering only a fraction of the solid angle. Current improvements toward covering the full solid angle are achieved with a deep parabolic mirror reaching a level of 81% of the solid angle [56]. Another strategy which circumvents the huge technical effort for increasing the coupling strength with cavities but using objectives is the implementation of an entanglement scheme which intrinsically incorporates a heralding signal. With the herald, deterministic post processing of quantum information becomes feasible, even for low coupling efficiencies.

In order to successfully perform quantum-networking operations at the quantum interface, it is a main prerequisite to control the absorption and emission of single photons at the nodes. Controlled single-photon emission is realized in various systems [57] such as cavity-assisted systems with single atoms [58, 59], trapped ions [60, 61] or solid state systems [62]. Without a cavity, tailoring the properties of the emitted single photons was shown with trapped ions [63] in our group. In order to treat the nodes as fully bidirectional quantum interfaces, the absorption of single photons by a single atom has to be controlled. We have demonstrated the heralded absorption of resonant single photons from an entangled-photon source by a single ion [64, 65] for entanglement distribution in a quantum network.

This thesis

The present work contains fundamental studies on the interaction of single photons with single trapped ions. This concerns both the photonic interaction between two ions confined in two distant traps and the ion-photon interface at a single ion.

For this purpose, we first present the controlled emission of single Raman-scattered photons from a single $^{40}Ca^{+}$ ion which is confined in a linear Paul trap. For the 393 nm emission wavelength, we show that Fourier-limited photons are emitted in a pure quantum state. In addition, the controlled emission of single photons at 854 nm is presented. At both wavelengths, we are able to control the temporal shape of the photons by the intensity of the exciting lasers.

In a further step, the generated photons from one ion are used to establish photonic interaction between two single ions in two distant traps, separated by a distance of one meter. For continuous emission of photons from the sender ion, we detect absorption events at the receiver ion with a quantum-jump technique for both wavelengths, 393 nm and 854 nm. Moreover, we demonstrate for 854 nm wavelength the interaction in triggered photon-generation mode by coincidental events in a correlation measurement.

Besides we present experiments which investigate the coherence character of the Raman process for the generation of 393 nm photons. In two level configurations, Λ and V, we show that an oscillating atomic phase is reflected as quantum beats in the wave packet of

the generated Raman photons. With the atomic and photonic control phase, we change the phase of the quantum beat in order to highlight the two different origins of the quantum beats for the two level configurations: In the Λ scheme, the quantum interference occurs in the absorption process and causes suppression and enhancement of the emission process, while in the V scheme, quantum interference in the emission process leads to a rotation of the emission profile. The work shows an example how quantum optical phenomena become tools in the context of quantum information technologies.

The last section treats related work with a femtosecond frequency comb. Experimental techniques that were presented in the previous chapters are applied to show the generation of 393 nm photons with pulses at 854 nm from the frequency comb. Thereto we show the phase lock of the comb repetition rate to the atomic clock. The lock is also necessary to perform 866 nm spectroscopy with two diode lasers that are locked to the comb.

1. Experimental setup

The first chapter of this thesis is devoted to the description of the experimental setup with which the measurements reported here were obtained. An unusual opportunity to get a deep insight into technical aspects and contexts of the experimental setup was the move of the complete apparatus from Barcelona to Saarbrücken at the end of the first year during my Ph.D. time. The dismounting and the rebuilding of the whole experiment lasted about one year.

The content of the following two sections describes the components that constitute the essential elements in a laboratory where quantum optics experiments with single ions are performed. It starts with a description of the linear Paul traps in a double-trap configuration including the theory for single-ion trapping and the main experimental tools setting the framework for scientific investigations. Then follows the description of the laser systems and their current frequency stabilization principle.

1.1. Double-trap apparatus

With his idea in the 1950s to use time-dependent electric quadrupole potentials as a radiofrequency quadrupole mass filter [66], W. Paul paved the way for further technical developments of the mass filter. One important step was the extension of the filter to three dimensions [67] by the implementation of static and time-dependent potentials to trap charged particles [68] which is known nowadays as the Paul trap. Since then ion traps like the Paul trap were widely used for many experiments in mass spectrometry and atomic physics due to the possibility to trap and perform laser cooling with a single ion [69]. An overview of the many applications of ion traps in physics is found in [70].

In the field of quantum information processing, linear Paul traps are the main workhorse in most of the experiments with single ions [71, 24] due to the high degree of isolation of trapped ions from the environment. They also allow investigations in quantum optics [72] and they are utilized for precision measurements such as ion-trap-based frequency standards [73, 74].

1.1.1. Trapping theory

In a linear Paul trap, the basic trapping principle for charged particles is based on a combination of a time-varying potential together with a static potential. The need for the combination originates from Earnshaw's theorem, which states that it is impossible to obtain

an confinement of a charge in all three dimensions only with a static potential. The linear Paul traps we operate have two diagonally opposed pairs of electrodes (Fig.1.1(a) and (b)), where one pair is connected to ground and the other pair is connected to a voltage U_{RF} which oscillates with the radio-frequency (RF) Ω_{RF}. The static potential is generated by two end tips which are connected to a DC voltage U_{Et}. The overall trapping potential is thus described as

$$\Phi = \Phi_{RF} + \Phi_{Et} = \frac{U_{RF}}{2r_0^2}(x^2 - y^2)\cos(\Omega_{RF}t) + \frac{\alpha' U_{Et}}{2l^2}(2z^2 - x^2 - y^2), \tag{1.1}$$

with the distances r_0, l from the trap center to the RF-electrodes and to the end tips, respectively. The numerical factor α' depends on the trap geometry and takes shielding effects of the axial trapping potential into account. The equation of motion of a particle with charge e is generally described by $\vec{F} = -e\,\nabla\Phi$, and with the substitution of the following parameters

$$a_x = a_y = -\frac{1}{2}a_z = -\frac{4e\alpha' U_{Et}}{ml^2\Omega_{RF}^2}, \quad q_y = -q_x = \frac{2eU_{RF}}{mr_0^2\Omega_{RF}^2}, \quad q_z = 0, \tag{1.2}$$

it is formulated by the Mathieu equation

$$\frac{d^2r_i}{dt^2} + (a_i - 2q_i\cos(\Omega_{RF}t))\,\frac{\Omega_{RF}^2}{4}r_i = 0. \tag{1.3}$$

The parameters a and q are used to identify stable trapping regions by plotting a over q in the Mathieu stability diagram. One stable solution is found in the limit $|a|, q^2 \ll 1$ for which we obtain the approximate solution of the Mathieu equation

$$r_i(t) = r_{0,i}\cos(\omega_i t)\left(1 - \frac{q_i}{2}\cos(\Omega_{RF}t)\right), \tag{1.4}$$

which describes the motion of the ion in the x-y plane as a *secular motion* superimposed by a driven motion at Ω_{RF}, the *micromotion*. Further assumptions in the *pseudopotential* approximation [70] lead to a neglection of the micromotion which allows the description of the particle motion by a harmonic potential in the trap center with the two radial frequencies

$$\omega_x = \frac{\Omega_{RF}}{2}\sqrt{a_x + \frac{q_x^2}{2}}, \quad \omega_y = \frac{\Omega_{RF}}{2}\sqrt{a_y + \frac{q_y^2}{2}}. \tag{1.5}$$

Along the end tip axis, which is the z-direction, the motion is independent from the radial one and oscillates with the frequency

$$\omega_z = \frac{\Omega_{RF}}{2}\sqrt{a_z} = \sqrt{\frac{2e\alpha' U_{Et}}{ml^2}}. \tag{1.6}$$

However, the axial trapping frequency influences the radial frequency ω_r by

$$\omega_r = \sqrt{\omega_0^2 - \frac{1}{2}\omega_z^2}, \tag{1.7}$$

where the pure radial trap frequency is

$$\omega_0 = \frac{\Omega_{\mathrm{RF}} q}{2\sqrt{2}}. \tag{1.8}$$

1.1.2. Paul traps

In Fig.1.1(a) and (b) the linear Paul trap is shown with two pairs of blades for radial confinement and two end-tip electrodes for axial trapping. The trap was designed in the group of Prof. R. Blatt at the University of Innsbruck where also the parts of the two traps were machined. To indicate the real size of the trap, the distance of 5 mm between the end-tip electrodes is shown. The distance from the trap axis to each of the blades is 0.8 mm. Further extensive information about the traps, their setup and specifications is found in [27, 75]. The trap is surrounded by two High numerical Aperture Laser Objectives (HALOs) (see Fig. 1.1(c)) which can be moved by xyz translation stages. The HALOs are described in more detail in Sec. 1.1.3.

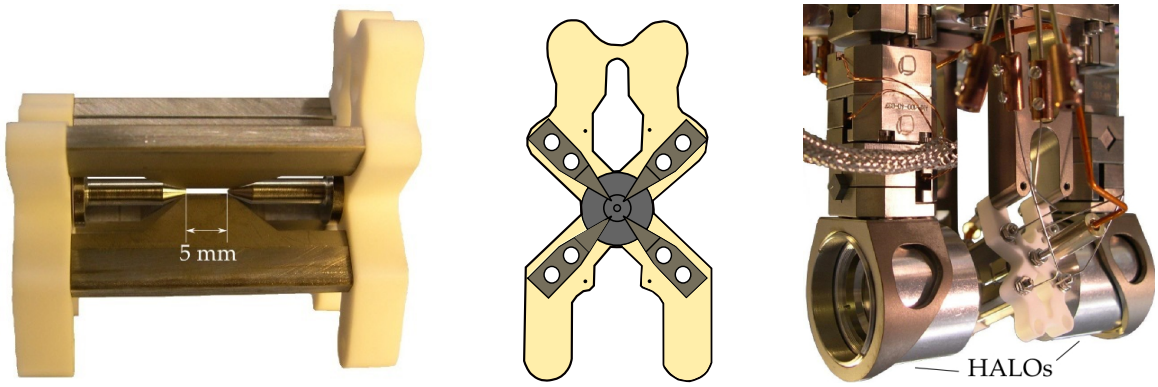

(a) (b) (c)

Figure 1.1.: (a) Picture of the linear Paul trap with four diagonally opposed blade electrodes and two end tips separated by 5 mm. (b) Drawing of the trap cross section. (c) Picture of the trap between the two High numerical Aperture Laser Objectives (HALOs) mounted on xyz translation stages which are suspended from above.

The photonic interaction experiments between two distant single ions described in this thesis are realized with two Paul traps separated by one meter distance, which are shown in Fig. 1.2. The picture shows the two vacuum vessels with the traps and HALOs inside. Most of the experiments presented in this thesis are performed with the *"bright trap"*[1] on the right-hand side in Fig. 1.2 since this trap allows a higher level of sophisticated laser sequences. For the sake of clarity, a typical optical path of photons coming out of the

[1] The names of both traps come from the different colors of the surrounding vacuum chambers after the first bake-out procedure.

bright trap and being send to the *"dark trap"* is drawn in the picture as an orange beam. Typical trapping parameters are presented for the bright trap, but they can be taken as almost similar for the dark trap. In axial direction, we typically apply an end-tip voltage of 400 V, leading to an axial trapping frequency of $\omega_z = 2\pi \cdot 1.197\,\mathrm{MHz}$ and to a shielding parameter $\alpha' = 0.183$. The applied frequency for the radial trapping potential of $\Omega_{\mathrm{RF}} = 2\pi \cdot 26.133\,\mathrm{MHz}$ generates radial sidebands of $\omega_r = 2\pi \cdot 3.647\,\mathrm{MHz}$ for a power of 8.8 W. This allows one to calculate with Eq. (1.2) and (1.8) the trapping parameters as $a_x = 0.004$, $q_y = 0.405$ and the applied voltage as $U_{\mathrm{RF}} = 1449\,\mathrm{V}$.

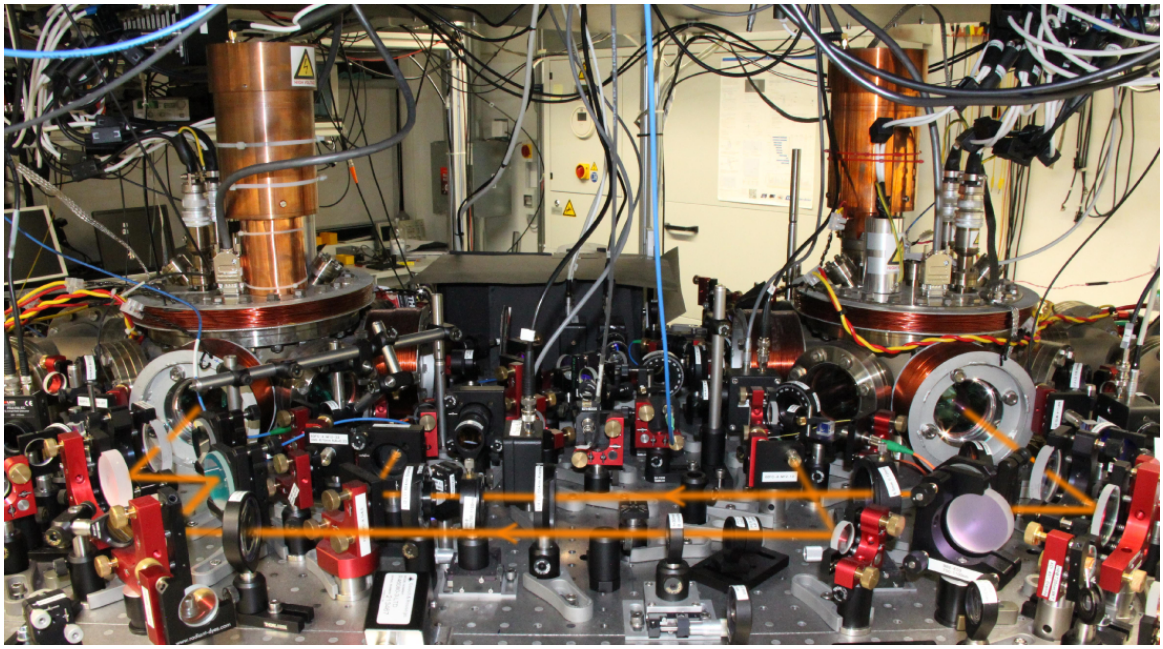

Figure 1.2.: Picture of the double-trap apparatus consisting of the dark trap on the left-hand side which is separated by one meter distance from the bright trap on the right-hand side for single-ion–single-photon interaction experiments. One example of an optical path of the photons for interaction measurements between the two traps is drawn in orange.

1.1.3. Experimental tools

HALOs

In each of the two vacuum chambers in Fig. 1.2 there are two HALOs. Fig. 1.1(c) shows their mounting on xyz translation stages[2] which allow one to position the HALOs for optimal centering with sub-micrometer precision and for optimal focusing a specific wavelength. Designed to be diffraction limited over a wavelength range from 400 nm to 870 nm,

[2] Attocube, ANPx100

the focal spot size of diameter ranges from 1.2 µm ($\lambda = 397$ nm) to 2.6 µm ($\lambda = 866$ nm). Beside the focusing of laser light to the ion, the HALOs are used to efficiently collect photons emitted by the ion. A single HALO covers 4.18 % of solid angle with a numerical aperture (NA) of 0.4. The addressing of individual ions necessary for future quantum logical operations in a string becomes feasible since the diffraction limited spot size is smaller than typical distances between two neighboring ions ($\sim 5 - 10$ µm). The HALOs are fully characterized in [27] and [54].

Photoionization

The loading of $^{40}Ca^{+}$ ions into the Paul trap requires the ionization of ^{40}Ca atoms emitted from an oven. The ionization is realized in a two-photon resonance-enhanced photoionization process, described in detail in [27]. We use a diode laser[3] at 846 nm which is frequency doubled in a second harmonic generation process to 423 nm. The laser has an output power of 120 mW and a free running linewidth of < 1 MHz. This light is needed to excite resonantly the $4s^2\,{}^1S_0 \rightarrow 4s4p\,{}^1P_1$ transition in a thermal beam of calcium atoms that traverses the trap. In a second step the atom is excited from the $^1P_1$ state to high-lying Rydberg states from which it is ionized by the strong electric fields of the Paul trap. It requires light at 390 nm coming from LED[4] with an emission spectrum centered around 380 nm and a full-width at half maximum (FWHM) of 30 nm. Both beams are coupled into a multi-mode fiber and are imaged to the trap center with a spot size of ~ 250 µm. This efficient setup allows us to ionize atoms and thus trap ions within a typical loading time of 3 to 7 minutes.

Magnetic field

Each trap is equipped with three independent pairs of coils to set a static magnetic field in three orthogonal directions. Out of the three, there is one which is supplied by a current up to 3 A, that defines the quantization axis at the ion position. Depending on the pair of coils we reach with this current a magnetic-field strength of $\sim 2.8 - 6$ G. If the current is applied to the pair of coils which creates the magnetic-field direction perpendicular to the HALO axis and parallel to the optical table, it creates a magnetic field strength of ~ 2.8 G. The other two coils serve for magnetic field compensation of offset fields like the earth magnetic field and surrounding stray magnetic fields. The coils are directly connected to current supplies[5] with an instability below 100 µA at 3 A over one measurement day of 8 hours. This means for a magnetic field of 2.8 G that the long term drift of the magnetic field due to a current drift from the current supplies is expected to be below 0.1 mG.

[3] Toptica, DL pro
[4] Nichia, NCCU001-LED
[5] TTI, QL355

Detection devices

The daily procedure for trapping a single $^{40}Ca^{+}$ demands the monitoring of fluorescence light from the ion on an EMCCD camera[6]. With an overall ion-image magnification of 20 we are able to resolve the individual positions of two or more ions on the CCD camera. In this case that we trap more than one ion we switch off the RF drive of the trap for a short time and start the trapping procedure again.

For single-photon detection we use two photomultiplier tubes (PMT)[7] collecting photons at 393 nm and 397 nm with the HALOs via multi-mode fibers. The quantum efficiency of the PMTs for these wavelengths is 28 %. The time resolution is determined by the electron transit time spread, which is specified with 300 ps. The detection of single photons at 854 nm wavelength requires an avalanche photodiode (APD)[8] since this wavelength lies outside the spectral response of the PMTs. The APD has a very low dark count rate ($\leqslant 10\,\frac{c}{s}$) and a detection efficiency of 24(5) % determined with a calibrated light source at 854 nm within our group [76].

Experimental control unit

The realization of experimental protocols in quantum information processing requires controlled manipulation of internal states of the ion by applying sequences of laser pulses with a high degree of reliability over many timescales. This includes the short-term stability (from ns to µs) between successive pulses within one sequence period. Since the sequences are repeated many times the long-term stability should reach several hours of total measurement time.

For this purpose, M. Almendros developed within his Ph.D. thesis our pulse sequencer, called *HYDRA* [77]. The main processing unit is a digital signal processor (DSP) which is connected via a backplane to digital input / output cards and RF generator cards. On each RF generator card a field programmable gate array (FPGA) controls the interface between the backplane and the direct digital synthesizers (DDS) and digital to analog converters (DAC). Both are used to generate RF-pulses tailored in frequency, phase, amplitude and length which are sent to acousto-optic modulators (AOM) for defined laser pulses. Additionally the DDS is used to stabilize the laser intensity via the AOM. The DSP has a clock rate of 1 GHz which is synchronized to a reference rubidium clock[9]. This allows us to execute phase-stable pulse sequences with a maximum frequency of 80 MHz which means pulses with a minimum length of 12.5 ns. The interface between the user and HYDRA is the *HYDRAPC*-software written in C++, which is installed on a PC connected with HYDRA. The two basic modes of operations are *real time* and *sequence*. In *real time* the user is able to control any of the outputs or to read inputs, e.g. PMT counting signals read

[6] Andor, DV887DCS-BV
[7] Hamamatsu, H7422P-40 SEL
[8] Laser Components, Count-10C-FC
[9] Stanford Research Systems, FS725

by General Purpose Counters. In *sequence* mode, any predefined sequence of pulses can be launched into the DSP and thus be executed by HYDRA. Future experiments will include the next generation of the sequencer from the spin-off company[10] by M. Almendros. It allows for ultra-fast real-time parallel execution and processing up to 800 Mbps corresponding to pulses as short as 1.25 ns. The input channels for single photon counting have a time-stamping resolution of 320 ps. Faster timing resolutions are achieved with a time-correlated single-photon counting system[11]. It has a maximum time resolution of 4 ps and is mainly used for correlation measurements presented in this work.

1.2. Laser system

A major advantage to use alkaline earth ions like Ca for quantum optics experiments is the fact, that commercially available and reliable diode laser systems often can deliver the optical frequencies that match the individual transition frequencies in the atomic level scheme. The level scheme of $^{40}Ca^{+}$ in Fig 1.3 has two short-lived excited states $4^2P_{1/2}$ and $4^2P_{3/2}$ with natural decay rates $\Gamma_{P_{1/2}} = 2\pi \cdot 22.4\,\text{MHz}$ [78] and $\Gamma_{P_{3/2}} = 2\pi \cdot 22.99\,\text{MHz}$ [79], respectively. Beside the $4^2S_{1/2}$ ground state there are also two long-lived metastable states $3^2D_{3/2}$ and $3^2D_{5/2}$ with natural decay rates $\Gamma_{D_{3/2}} = 2\pi \cdot 0.135\,\text{Hz}$ [80] and $\Gamma_{D_{5/2}} = 2\pi \cdot 0.136\,\text{Hz}$ [81]. The different decay rates over eight orders of magnitude between the short and long-lived states impose different stability requirements to the laser frequencies at the transition frequencies. They are separated into four optical dipole transitions at 397 nm, 850 nm, 854 nm and 866 nm and one optical quadrupole transition at 729 nm which all are addressed by the lasers used in the experiment.

1.2.1. Laser sources

The following list gives an overview of the laser systems[12] which are in use for ion excitation in the experiment.

- **397 nm**
  The fundamental laser light at 794 nm of this system is generated with a grating-stabilized diode laser which is frequency doubled in a second-harmonic generation process to 397 nm. The free running linewidth (for a integration time of 5 µs) is specified to $\sim$ 300 kHz. The output power at 397 nm of 30 mW is distributed to the two traps for Doppler cooling and fluorescence-based state detection. In the bright trap it is also used for optical pumping (397 nm pump).

- **729 nm**
  The 729 nm diode laser has up to 500 mW output power together with a free running

[10] Signadyne
[11] PicoQuant, PicoHarp 300
[12] All laser are from Toptica. The models are different depending on the wavelengths: 397 nm, 854 nm: TA/DL-SHG pro; 850 nm, 866 nm: TA, DL pro; 729 nm: TA pro

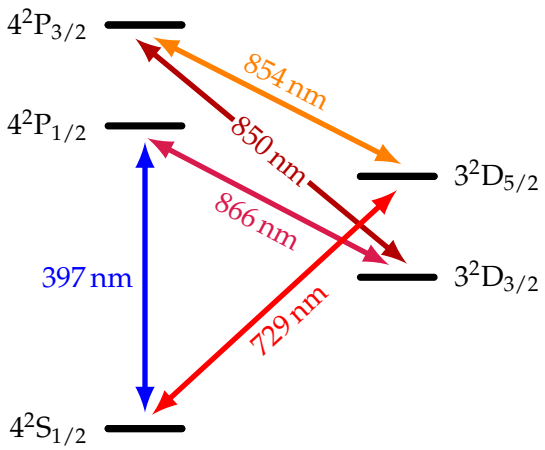

Figure 1.3.: Level scheme of $^{40}Ca^+$ including the transitions that are excited by laser radiation in the experimental setup of this thesis.

linewidth of 150 kHz. Due to the small decay rate of the $D_{5/2}$ state, the coherence time of the laser should be long, corresponding to a narrow spectral linewidth, to address the optical quadrupole transition for coherent manipulations. This is achieved by a stabilization of the laser frequency to an ultra-stable high-finesse cavity made of ultra-low expansion glass. The cavity has a linewidth of 4 kHz, and together with the Pound-Drever-Hall locking technique (see Sec. 1.2.2) and a high-speed control amplifier[13], the linewidth of the laser can be reduced below 32 Hz. Many more details about the laser setup and its characterization are found in [82].

- **850 nm**
  The laser for the excitation on the $D_{3/2} - P_{3/2}$ transition is used in combination with the 397 nm and 866 nm laser to transfer the population from $S_{1/2}$ to $P_{3/2}$ in a three-photon resonance and thus allows the generation of photons on the $P_{3/2} - D_{5/2}$ transition at 854 nm wavelength.

- **854 nm**
  The laser for the excitation from $D_{5/2}$ to $P_{3/2}$ serves for optical pumping (854 nm pump) and as master laser for the production of entangled-photon pairs at 854 nm in a spontaneous parametric down-conversion process. The most important application within this work is the use for generation of photons on the $P_{3/2} - S_{1/2}$ transition at 393 nm wavelength.

- **866 nm**
  The laser serves for repumping the population from the $D_{3/2}$ state to the $P_{1/2}$ state

[13] Toptica, FALC 110

while Doppler cooling. It is also used for a three-photon excitation from the $S_{1/2}$ to $P_{3/2}$ level and has a 30 mW output power with a free running linewidth of 150 kHz.

All laser beams are sent through AOMs to be controlled in frequency, phase and amplitude by the pulse sequencer HYDRA. For monitoring the wavelength a small part of their power is sent to a wavemeter[14]. Using fiber couplers[15] the light is guided in polarization maintaining single-mode fibers to the double trap apparatus. There the light is first collimated to a beam diameter (at $\frac{1}{e^2}$) of 2.15 mm. For adressing the ion with different lasers we use different windows of the vacuum chamber. Due to the different distances of the windows to the position of the ion, plano-convex lenses with different focal lengths f focus the light to the ion resulting in different focal spot-size diameters d (at $\frac{1}{e^2}$). In Tab. 1.1 we list the lasers that excite the dipole transitions and which are used in the experiments with the different focusing. We give the maximum power values that are measured in front of the windows resulting in the calculated intensities I. We see that we can tune the power to values that result in much higher intensities compared to the saturation intensities I_{sat} of the corresponding transitions from i to k. The saturation intensities for a two-level system are calculated as

$$I_{\text{sat}} = \frac{2\pi\, h\, c\, A_{k-i}}{\lambda^3}, \tag{1.9}$$

with the Einstein coefficient A_{k-i}, representing the oscillator strength of the corresponding transition (see Sec. 2.1) and the laser wavelength λ.

Transition $i-k$	Laser	f (mm)	d (µm)	P	I ($\frac{\text{mW}}{\text{cm}^2}$)	I_{sat} ($\frac{\text{mW}}{\text{cm}^2}$)
$S_{1/2} - P_{1/2}$	397 nm	250	60	300 µW	$2.2 \cdot 10^4$	43.9
$S_{1/2} - P_{1/2}$	397 nm	500	120	300 µW	$5.5 \cdot 10^3$	43.9
$S_{1/2} - P_{1/2}$	397 nm pump	250	60	4 µW	$3 \cdot 10^2$	43.9
$D_{3/2} - P_{1/2}$	866 nm	500	250	3 mW	$2 \cdot 10^7$	0.29
$D_{3/2} - P_{3/2}$	850 nm	250	125	300 µW	$4.8 \cdot 10^3$	0.032
$D_{5/2} - P_{3/2}$	854 nm pump	250	125	20 µW	$3.2 \cdot 10^2$	0.28
$D_{5/2} - P_{3/2}$	854 nm	500	250	3 mW	$1.2 \cdot 10^4$	0.28

Table 1.1.: Different lasers are used to excite the dipole transitions from i to k. The light is focused by plano-convex lenses with focal lengths f to spot-size diameters d at the position of the ion. For a maximum laser power P, the maximum intensity I is calculated for comparing to the calculated saturation intensities I_{sat} of the transitions.

[14] High Finesse, WS7

[15] Schäfter+Kichhoff, 60FC-4-M12

1.2.2. Frequency-locking scheme

Transfer lock

The laser frequency stabilization system in our laboratory consists of a complex chain of transfer locks that are described in detail in [75] and [83]. It was developed to have low laser linewidths ($\sim 100 - 200\,\mathrm{kHz}$) and low drifts of the frequency on a daily time basis. The stabilization chain starts with an 852 nm laser[16] which is referenced via a Fabry-Perot transfer cavity to the D2 line of cesium in a vapor cell. The locking scheme is a combination of the Pound-Drever-Hall technique with Doppler-free absorption spectroscopy. The acquired stability of this laser frequency is then transferred first to Fabry-Perot cavities by stabilizing them to this laser with self-made electronics called *cavity locker* [77]. Then all the lasers (except 729 nm and 846 nm) are locked to their transfer cavities with a feedback controlyzer[17]. This finally results in a transfer of the stability from the Cs-lock via the 852 nm laser and the transfer cavities to the individual lasers. Once the lasers are locked to the cavities, the remaining frequency detuning to the atomic transition frequency is compensated by the acousto-optic modulators.

Pound-Drever Hall technique

The invention of the Pound-Drever-Hall technique goes back to frequency stabilization of microwave oscillators by Pound [84] and was taken over to stabilize a laser to a cavity by Drever and Hall [85]. The Pound-Drever-Hall laser frequency stabilization is a well established technique to stabilize a laser frequency to a Fabry-Perot cavity. The measurement of the frequency is fed back to the laser to suppress frequency fluctuations. The main idea behind this technique is to measure the derivative of the reflected intensity from the cavity with respect to the modulation frequency. The reflected beam contains the information whether the frequency of the laser is above or below the cavity resonance through modulated sidebands which interfere with the reflected beam. In the sum one gets a beat at the modulation frequency which allows to measure the phase of this beat pattern. The phase of the incident electric field E_{inc} is modulated with the modulation frequency ω_{M}

$$E_{\mathrm{inc}} = E_0 e^{i(\omega_{\mathrm{c}} t + \beta \sin(\omega_{\mathrm{M}} t))} \tag{1.10}$$

with β as the modulation depth and ω_{c} as the unmodulated carrier frequency of the electric field. With a fast photodiode the power of the reflected beam is measured which contains the carrier frequency ω_{c}, and the two sidebands $\omega_{\mathrm{c}} \pm \omega_{\mathrm{M}}$. From this signal, an error signal is derived which is used in a feedback loop to reduce the linewidth of the laser below the linewidth of the cavity, since the light stored in the cavity is averaging the fluctuations over the storage time of the cavity. This reduces the laser linewidth to $\sim 130\,\mathrm{kHz}$ outgoing from the cavity linewidth of 1.9 MHz. However the cavity can only measure the frequency of

[16] Toptica, DL
[17] Toptica, Digilock 110

the laser and thus it is not possible to reach a high relative phase coherence between the lasers. In order to get the latter, we set up a new phase-locking technique based on an optical frequency comb as a stable phase reference which is discussed in Chapter 7.

2. Light-matter interaction

This chapter treats light-matter interaction to establish the basic understanding for the absorption and emission process of single photons by a single trapped ion. To this end, the fundamental properties of $^{40}Ca^{+}$ are introduced first, followed by the explanation of Doppler cooling of the motion of an atom in a harmonic trap potential.

In a semiclassical treatment of laser-ion interaction, we describe in a simplified three-level-system the dynamics of the interaction using the optical Bloch equations. Besides the Bloch equations, a three-level rate-equation model is developed with which it becomes straightforward to derive the process of spontaneous Raman scattering. The latter strongly depends on the transition matrix elements between the associated atomic states. The matrix elements are connected to the geometry of the absorbed and emitted light and the Clebsch-Gordan coefficients which both are discussed in the last part of this chapter.

2.1. The $^{40}Ca^{+}$ ion

Neutral calcium has an atomic number of 20 and mass of 40.078 u. Out of six stable isotopes, ^{40}Ca is the most abundant with 97 % natural occurrence. Singly charged ^{40}Ca has a nuclear spin $I = 0$ and a level structure, of which the five lowest levels with their Zeeman manifolds are shown in Fig. 2.1. The total angular momentum j of the valence electron defines for each level the number of Zeeman sublevels with the quantum number $m_j = -j..j$. Table 2.1 gives an overview of the level decay properties. It lists the natural lifetimes τ [78, 80, 81] which are related to the natural decay rates Γ_k as

$$\tau = \frac{1}{\Gamma_k} \tag{2.1}$$

and the transitions from $k = P_{3/2}$, $P_{1/2}$, $D_{3/2}$, $D_{5/2}$ to $i = S_{1/2}$, $D_{3/2}$, $D_{5/2}$ with their wavelengths[1] λ and the Einstein coefficients A_{k-i}. Given an excited level k, the relation of the Einstein coefficients to the total decay rate Γ_k is

$$\Gamma_k = \sum_i A_{k-i}. \tag{2.2}$$

The Einstein coefficients represent the oscillator strength of a transition whose magnitude is fixed by the branching fractions $\frac{A_{k-i}}{\Gamma_k}$ [79, 86] of the excited level. The branching fractions

[1] Note that the wavelengths for 393 nm and 732 nm are calculated from the remaining wavelengths that are measured with the wavemeter.

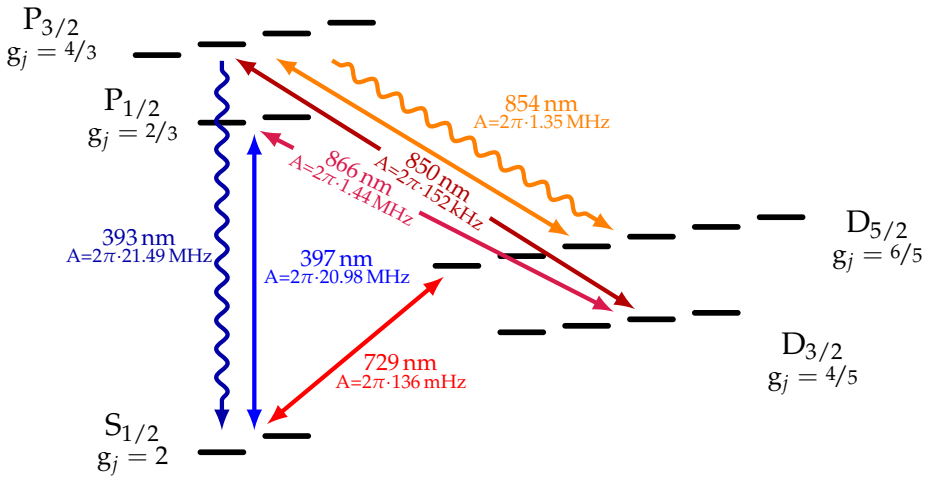

Figure 2.1.: Level scheme of $^{40}Ca^{+}$ with the Zeeman sublevels, laser-driven transitions (double arrows) and the level properties: the Einstein coefficients A and the Landé factors g_j. Within this work single photons are generated on the $P_{3/2}$ to $S_{1/2}$ transition (blue wavy arrow) at 393 nm wavelength and on the $P_{3/2}$ to $D_{5/2}$ transition (orange wavy arrow) at 854 nm wavelength.

describe the decay probability distribution of an excited state k via possible decay channels into the final states i. From the branching fractions, the branching ratio is calculated; for the decay of an excited level, e.g. $P_{3/2}$, Table 2.1 shows that compared to the decay probability into $D_{5/2}$, the decay probability into $S_{1/2}$ is enhanced by a factor of 15.92 and reduced by a factor of 0.11 for the decay into $D_{3/2}$.

The coefficients play a dominant part in the calculations of photon absorption probabilities and of emission probabilities of single photons, i.e. at 393 nm and 854 nm wavelength. In addition, they also contribute to the temporal (and thus spectral) properties of the generated photons, i.e. they define the time-bandwidth product which will become obvious in Sec. 3.1.4 and 3.2.4 where the spectral properties of spontaneously generated Raman photons are discussed.

2.2. Doppler cooling

Doppler cooling serves as one of the most important cooling techniques when working with single trapped ions. It is important to precool the ion into the Lamb-Dicke regime (motional excursions of the ion $\ll$ wavelength of light) [87] before continuing with sideband cooling to the motional ground state [88] to perform quantum-logic operations [89].

In our group the main goal related to Doppler cooling is the reduction in the amplitude of the secular motion of the ion to perform efficient electron shelving (see Sec. 5.2)

Level, τ	Transition $k-i$	λ (nm)	$A_{k-i}/2\pi$	A_{k-i}/Γ_k	Branching ratio
$P_{3/2}$, 6.924 ns	$P_{3/2} - S_{1/2}$	393.3660	21.49 MHz	93.47 %	15.92
	$P_{3/2} - D_{3/2}$	849.8015	152 kHz	0.66 %	0.11
	$P_{3/2} - D_{5/2}$	854.2087	1.35 MHz	5.87 %	1
$P_{1/2}$, 7.098 ns	$P_{1/2} - S_{1/2}$	396.8466	20.98 MHz	93.565 %	14.54
	$P_{1/2} - D_{3/2}$	866.2137	1.44 MHz	6.435 %	1
$D_{3/2}$, 1.176 s	$D_{3/2} - S_{1/2}$	732.3886	135 mHz	100 %	1
$D_{5/2}$, 1.168 s	$D_{5/2} - S_{1/2}$	729.1464	136 mHz	100 %	1

Table 2.1.: Level properties of $^{40}Ca^{+}$: natural lifetimes τ, transitions from k to i and their wavelengths (in air), Einstein coefficients A_{k-i}, branching fractions $\frac{A_{k-i}}{\Gamma_k}$ and branching ratios.

and coherent manipulations, both on the 729 nm quadrupole transition. Moreover, good cooling conditions also enable stable conditions to keep one ion trapped over one day. After Ca atoms are ionized in our trap, they can have a high energy corresponding to some hundreds of Kelvin. In order to cool them quickly to a low motional state, a dipole transition with a high scattering rate is favorable. In our case the 397 nm laser (together with the 866 nm laser for repumping from $D_{3/2}$) drives the $S_{1/2} - P_{1/2}$ transition which allows a high scattering rate set by the natural decay rate of $\Gamma_{P_{1/2}} = 2\pi \cdot 22.42\,\text{MHz}$. Since this value is higher than the axial and radial trapping frequencies ($\omega_r = 2\pi \cdot 3.647\,\text{MHz}$ and $\omega_z = 2\pi \cdot 1.197\,\text{MHz}$), the cooling process occurs in the unresolved sideband regime [72].

The following classical description from [72] for cooling a particle only concerns the axial motion in a linear trap and neglects the fact that we do not have two levels but a third one. The description includes the assumption that the scattering process happens on a short timescale compared to the ion velocity ($\Gamma \gg \omega_{\text{trap}}$) which means that the cooling of the trapped ion is essentially the same as for a free particle. The average radiation pressure force on the ion is

$$F_a = \hbar k \Gamma \rho_{ee} \tag{2.3}$$

with the probability to be in the excited state

$$\rho_{ee} = \frac{\Omega^2/4}{\delta^2 + \Omega^2/2 + \Gamma^2/4}. \tag{2.4}$$

Here $\delta = \omega_L - \omega_0 - \mathbf{k} \cdot \mathbf{v}$ is the effective Doppler shift including the detuning $\Delta = \omega_L - \omega_0$ of the laser frequency ω_L to the atomic resonance ω_0. For the case that Doppler broadening

is small compared to Γ, F_a is approximated by

$$F_a \approx F_0(1+\alpha v), \tag{2.5}$$

with

$$F_0 = \hbar k \Gamma \frac{\Omega^2/4}{\Delta^2 + \Omega^2/2 + \Gamma^2/4} \tag{2.6}$$

and

$$\alpha = \frac{2k\Delta}{\Delta^2 + \Omega^2/2 + \Gamma^2/4}. \tag{2.7}$$

The friction coefficient α is responsible for cooling in the case of a negative detuning Δ. The cooling rate for a trapped ion where $\langle v \rangle = 0$ is then described as

$$\dot{E}_\mathrm{c} = \langle F_a v \rangle = F_0 \left(\langle v \rangle + \alpha \langle v^2 \rangle \right) = F_0 \alpha \langle v^2 \rangle = 4\hbar k^2 \frac{s\Delta/\Gamma}{\left(1 + s + \frac{4\Delta^2}{\Gamma^2}\right)^2} \langle v^2 \rangle \tag{2.8}$$

with the saturation parameter $s = 2\frac{\Omega^2}{\Gamma^2} = \frac{I}{I_\mathrm{sat}}$. Heating occurs due to momentum kicks in random directions from spontaneously emitted photons and the random times in the absorption process of photons which both lead to a diffusion of $\langle \Delta p^2 \rangle \neq 0$ resulting in a heating rate of

$$\dot{E}_\mathrm{h} = \frac{1}{2m}\frac{d}{dt}\langle p^2 \rangle = \dot{E}_\mathrm{abs} + \dot{E}_\mathrm{em} \approx \frac{1}{2m}(\hbar k)^2 \Gamma \rho_{ee}(v=0)(1+\xi). \tag{2.9}$$

The anisotropy between the cooling and heating forces is represented by the parameter ξ. The minimum temperature is reached if the heating and cooling rates are equal ($\dot{E}_\mathrm{c} = \dot{E}_\mathrm{h}$) such that

$$T_\mathrm{min}(\Delta) = \frac{m\langle v^2 \rangle}{k_\mathrm{B}} = \frac{\hbar\Gamma}{8k_\mathrm{B}}(1+\xi)\left((1+s)\frac{\Gamma}{2\Delta} + \frac{2\Delta}{\Gamma}\right). \tag{2.10}$$

The Doppler-cooling limit in Eq. (2.10) is reached for the detuning $\Delta = \frac{\Gamma}{2}\sqrt{1+s}$. For low laser intensities far below the saturation intensity ($s \ll 1$), the detuning is half the natural linewidth, which is in our case $\sim 10\,\mathrm{MHz}$. For isotropic emission of spontaneously emitted photons ($\xi = \frac{1}{3}$) [90] the final temperature we could ideally reach in the limit of a two level system between $\mathrm{S}_{1/2}$ and $\mathrm{P}_{1/2}$ is

$$T_\mathrm{min} = \frac{\hbar\Gamma_{\mathrm{P}_{1/2}}}{3k_B} = 0.36\,\mathrm{mK}. \tag{2.11}$$

Experimental situation

The cooling laser at 397 nm wavelength has an angle of $\beta = 22.5^\circ$ to the trap axis along the end tips. This results in a projection of the wavevector $\vec{k}$ of the cooling light to the axial and radial oscillation modes whereby cooling is enabled in these directions. The minimum

temperature given in Eq. (2.11) is not reached in the experiment for several reasons. First the derivation given above was done for a two level system. In the experiment we use the 397 nm laser together with the 866 nm laser as a repumper which both couple an eight-level system (cf. Fig. 2.1). Using both lasers leads to the observation of dark resonances which strongly change the cooling dynamics for different laser parameters like detuning or intensity [82]. This means that for weak laser excitation the rule of $\Delta = \frac{\Gamma}{2}$ is not valid anymore. However, we measured that the mean vibrational number for the axial mode is $\langle n \rangle \sim 15$. Since the motional state of the ion has a thermal distribution, we calculate from $\langle n \rangle$ the corresponding minimum temperature to

$$T_{\text{axial}} = \frac{\hbar \omega_z}{k_{\text{B}} \ln\left(\frac{\langle n \rangle + 1}{\langle n \rangle}\right)} = 0.89\,\text{mK} \tag{2.12}$$

with the Boltzmann constant k_{B}.

2.3. Three-level system interacting with coherent light

The generation process of single photons from a single trapped $^{40}Ca^{+}$ needs the description of the interaction of coherent laser light with the atomic transition. The theoretical description starts with a simplified level scheme consisting of three levels, namely $S_{1/2}$, $P_{3/2}$ and $D_{5/2}$ (with degenerate Zeeman sublevels), assuming direct excitation from $S_{1/2}$ to $P_{3/2}$ with a laser at 393 nm. In the experiment described later, we need three lasers for excitation from $S_{1/2}$ to $P_{3/2}$ including 397 nm, 866 nm and 850 nm laser, which is investigated in Sec. 3.2.2. A further simplification in the 3-level model, arising from a very small branching fraction from $P_{3/2}$ to $D_{3/2}$ of 0.66 %, is that the decay on the 850 nm transition is neglected. This reduces the description to an effective three level system, following the model in [91].

The interaction of a three level atom with two coherent light fields is described by

$$\hat{H} = \hat{H}_{\text{atom}} + \hat{H}_{\text{field}} + \hat{H}_{\text{int}}. \tag{2.13}$$

The eigenvectors $|a\rangle$, $a \in \{\text{S}, \text{P}, \text{D}\}$ of the atomic Hamiltonian fulfill the equation

$$\hat{H}_{\text{atom}} |a\rangle = \hbar \omega_a |a\rangle \tag{2.14}$$

with the atomic frequencies ω_a. With the basis

$$a = \text{S}, \text{P}, \text{D} \rightarrow (1,0,0)^{\text{T}}, (0,1,0)^{\text{T}}, (0,0,1)^{\text{T}} \tag{2.15}$$

the matrix representation of $\hat{H}_{\text{atom}}$ reads

$$\hat{H}_{\text{atom}} = \hbar \begin{pmatrix} \omega_{\text{S}} & 0 & 0 \\ 0 & \omega_{\text{P}} & 0 \\ 0 & 0 & \omega_{\text{D}} \end{pmatrix}. \tag{2.16}$$

Setting the energy of $P_{3/2}$ to zero and defining $\omega_{SP} = \omega_S - \omega_P$ and $\omega_{DP} = \omega_D - \omega_P$ gives

$$\hat{H}_{atom} = \hbar \begin{pmatrix} \omega_{SP} & 0 & 0 \\ 0 & 0 & 0 \\ 0 & 0 & \omega_{DP} \end{pmatrix}. \tag{2.17}$$

For the treatment of the field operator $\hat{H}_{field}$, we introduce the description of a laser field where the number of photons is high such that the absorption of one photon by the ion changes the energy of the light field only by a negligible amount. This means that the interaction between laser field and ion does not affect the light field and the term $\hat{H}_{field}$ is neglected. Instead we follow the *semiclassical* treatment of the interaction term $\hat{H}_{int}$ through two oscillating electric fields [92]

$$\vec{E}_{393} = E_{0,393}\cos(\omega_{393}t)\vec{e}_{393}, \quad \vec{E}_{854} = E_{0,854}\cos(\omega_{854}t)\vec{e}_{854} \tag{2.18}$$

with the amplitude E_0, the laser wavelength ω and the polarization vector $\vec{e}$ for the two transitions at 393 nm and 854 nm. Each field couples to the electric dipole moment of the respective transitions. This is not the case for the quadrupole transition from $S_{1/2}$ to $D_{5/2}$, whereby the $D_{5/2}$ level is taken to be stable. A comparison of the $D_{5/2}$ lifetime (1 s) to the $P_{3/2}$ lifetime (7 ns) shows the validity of the assumption. The interaction in the dipole approximation[2] is thus described as

$$\hat{H}_{int} = -\hat{\vec{d}} \cdot \vec{E}, \tag{2.19}$$

with the atomic dipole operator $\hat{\vec{d}} = -e \cdot \hat{\vec{r}}$. In terms of the atomic energy eigenvectors it is expressed as

$$\hat{\vec{d}} = \vec{d}_{SP}\Big(|S\rangle\langle P| + |P\rangle\langle S|\Big) + \vec{d}_{DP}\Big(|P\rangle\langle D| + |D\rangle\langle P|\Big), \tag{2.20}$$

with $\vec{d}_{SP} = \langle S|\hat{\vec{d}}|P\rangle$, $\vec{d}_{DP} = \langle D|\hat{\vec{d}}|P\rangle$, and the interaction term is written

$$\hat{H}_{int} = \Big(\vec{d}_{SP}\left(|S\rangle\langle P| + |P\rangle\langle S|\right) + \vec{d}_{DP}\left(|P\rangle\langle D| + |D\rangle\langle P|\right)\Big)\Big(\vec{E}_{393} + \vec{E}_{854}\Big). \tag{2.21}$$

If the light fields interact only with their respective transitions and using the rotating-wave approximation Eq. (2.21) simplifies to

$$\hat{H}_{int} = \frac{\hbar\Omega_{SP}}{2}\left(|S\rangle\langle P|e^{i\omega_{393}t} + |P\rangle\langle S|e^{-i\omega_{393}t}\right) + \frac{\hbar\Omega_{DP}}{2}\left(|P\rangle\langle D|e^{-i\omega_{854}t} + |D\rangle\langle P|e^{i\omega_{854}t}\right), \tag{2.22}$$

using $\hbar\Omega = \vec{d} \cdot \vec{e}\, E_0$ with the Rabi frequency Ω. The total Hamiltonian in matrix representation is now

$$\hat{H} = \hbar \begin{pmatrix} \omega_{SP} & \frac{\Omega_{SP}}{2}e^{i\omega_{393}t} & 0 \\ \frac{\Omega_{SP}}{2}e^{-i\omega_{393}t} & 0 & \frac{\Omega_{DP}}{2}e^{-i\omega_{854}t} \\ 0 & \frac{\Omega_{DP}}{2}e^{i\omega_{854}t} & \omega_{DP} \end{pmatrix}. \tag{2.23}$$

[2]The dipole approximation is valid for a laser wavelength much greater than the size of the atomic wave packet.

With the transformation into the reference frame rotating with the laser frequencies one finally obtains

$$\hat{H}' = \hbar \begin{pmatrix} \Delta_{393} & \frac{\Omega_{\mathrm{SP}}}{2} & 0 \\ \frac{\Omega_{\mathrm{SP}}}{2} & 0 & \frac{\Omega_{\mathrm{DP}}}{2} \\ 0 & \frac{\Omega_{\mathrm{DP}}}{2} & \Delta_{854} \end{pmatrix} \tag{2.24}$$

with the detuning $\Delta_{393} = \omega_{393} - (\omega_{\mathrm{P}} - \omega_{\mathrm{S}})$, $\Delta_{854} = \omega_{854} - (\omega_{\mathrm{P}} - \omega_{\mathrm{D}})$ of the laser frequencies to their transition frequencies.

2.4. Optical Bloch equations

The full description of the atomic dynamics needs the inclusion of the spontaneous decay of excited levels which generally leaves the ion no longer in a pure state. The density-matrix formalism has to be used by writing the density operator $\hat{\rho}$ in terms of the eigenvectors

$$\hat{\rho} = \sum_{a,b=\mathrm{S,P,D}} \rho_{ab} |a\rangle\langle b|. \tag{2.25}$$

The probability to find the ion in one of these states is given by the expectation value, e.g. $\rho_{\mathrm{SS}} = \langle S|\hat{\rho}|S\rangle$, whereas $\langle a|\hat{\rho}|b\rangle$ represent the non-diagonal elements which are called coherences. With this description the trace of $\hat{\rho}$ is preserved

$$\mathrm{Tr}(\hat{\rho}) = \rho_{\mathrm{SS}} + \rho_{\mathrm{PP}} + \rho_{\mathrm{DD}} = 1. \tag{2.26}$$

The time evolution of the density operator is described by the master equation in Lindblad form with the Hamilton operator from Eq. (2.24) as

$$\frac{\mathrm{d}\hat{\rho}'}{\mathrm{d}t} = \hat{\mathcal{L}}(\hat{\rho}') = \frac{\mathrm{i}}{\hbar}\left[\hat{\rho}', \hat{H}'\right] + \hat{\mathcal{L}}_{\mathrm{damp}}(\hat{\rho}). \tag{2.27}$$

The density matrix $\hat{\rho}'$ is described in the rotating frame whereas the damping term $\hat{\mathcal{L}}_{\mathrm{damp}}$ is not affected by the transformation. The latter is formulated as

$$\hat{\mathcal{L}}_{\mathrm{damp}}(\hat{\rho}) = \frac{1}{2}\sum_k \left(2\hat{C}_k\hat{\rho}\hat{C}_k^\dagger - \hat{\rho}\hat{C}_k^\dagger\hat{C}_k - \hat{C}_k^\dagger\hat{C}_k\hat{\rho}\right), \tag{2.28}$$

with the operators $\hat{C}_k$ that describe the decay processes like from the P to the S level

$$\hat{C}_{\text{P-S}} = \sqrt{A_{393}}|\mathrm{S}\rangle\langle\mathrm{P}|, \tag{2.29}$$

with the Einstein coefficient $A_{393} = A_{\text{P-S}}$. The linear differential equation in Eq. (2.27) is solved in vector form

$$\frac{\mathrm{d}\vec{\rho}}{\mathrm{d}t} = \sum_j \hat{L}_{ij}\,\vec{\rho}_j \tag{2.30}$$

with the $N^2 \times N^2$ Liouville superoperator $\hat{L}$ and N being the number of levels. $\vec{\rho}$ is now written in a vector form of matrix elements

$$\vec{\rho} := (\rho_{SS}, \rho_{SP}, ...\rho_{DD}), \tag{2.31}$$

that finally leads to the solution for the initial condition $\vec{\rho}(0)$

$$\vec{\rho}(t) = e^{\hat{L}t}\,\vec{\rho}(0). \tag{2.32}$$

In order to fully simulate the atomic dynamics during light-atom interaction, P. Müller wrote within his Ph.D. time a program in Matlab presented in [93], which incorporates all 18 Zeeman sublevels (see Fig. 2.1) for the numerical solution of the optical Bloch equations. With this program, it is possible to investigate the temporal evolution of excitation- and decay processes between various quantum states, dependent on initial laser parameters like intensity, detuning, polarization or angle of incidence with respect to the quantization axis. Within the present thesis, the program is used as a tool wherever dynamical aspects of internal states, that are reflected in the temporal dynamics of arrival-time distributions of single photons, become important to compare with experimental results. Beside the simulation the program is also used for fitting the modulated arrival-time distributions of generated photons presented in Chapter 6.

2.5. Spontaneously Raman-scattered photons

After the introduction of the density-matrix formalism, we have now the tools to describe atomic rate equations for the three-level system. The equations are used to describe the atomic dynamics in a compact analytical form which is used to derive a simple model for the temporal evolution of the atomic population during photon generation. Since the atomic dynamics reflects the temporal shape, i.e. the wave packet, of the generated single photon, we use the simple model from the rate equations to obtain temporal properties of the emitted photons. We check the validity of the rate-equation model by comparing its numerical solution against the solution of the optical Bloch equations for two different excitation regimes. The experimental implementation of photon generation is presented and discussed in Chapter 3.

We consider the three-level scheme shown in Fig. 2.2 and the situation that all the population is initially in the metastable $D_{5/2}$ level. From there it is optically pumped to the $S_{1/2}$ level with the 854 nm laser which couples the $D_{5/2}$ and $P_{3/2}$ level. During this process the population in $P_{3/2}$ spontaneously decays to $S_{1/2}$, thereby releasing a single 393 nm photon. Since the initial energy level of $D_{5/2}$ is higher than the final state $S_{1/2}$, the energy of the emitted 393 nm photon is higher than the absorbed 854 nm laser photon. In contrast to the case of *Rayleigh scattering* in a two-level system, this is an inelastic scattering process which is termed *(Anti-Stokes) Raman scattering*. In reference to the 393 nm photon which is generated by a spontaneous decay from $P_{3/2}$ to $S_{1/2}$, the photon is called *spontaneously*

Raman-scattered photon. As we will see in Sec. 3.2 it is also possible to implement the inverse process, i.e. we optically pump the population from the $S_{1/2}$ level to the $D_{5/2}$ level, thereby generating 854 nm photons in a *(Stokes) Raman scattering* process.

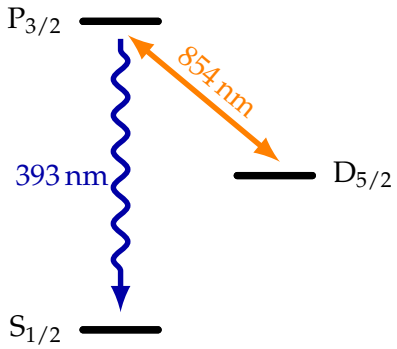

Figure 2.2.: Three-level system with laser excitation at 854 nm on the two-level subsystem between $D_{5/2}$ and $P_{3/2}$ and the scattered photon at 393 nm from the intermediate state $P_{3/2}$ to the ground state $S_{1/2}$.

2.5.1. Atomic rate equations for the three-level system

The dynamical evolution of the atomic population, necessary to formulate an analytical expression for temporal properties of the Anti-Stokes Raman scattered photons, is derived from the following simple rate-equation model for the three-level system [94], neglecting the spontaneous decay of the metastable $D_{5/2}$ level to $S_{1/2}$,

$$\dot{\rho}_{SS}(t) = A_{393}\,\rho_{PP}(t), \tag{2.33}$$

$$\dot{\rho}_{PP}(t) = -(A_{393} + A_{854})\,\rho_{PP}(t) + r_{854}\,\rho_{DD}(t) - r_{854}\,\rho_{PP}(t), \tag{2.34}$$

$$\dot{\rho}_{DD}(t) = -r_{854}\,\rho_{DD}(t) + A_{854}\,\rho_{PP}(t) + r_{854}\,\rho_{PP}(t), \tag{2.35}$$

where the Einstein coefficients are defined as $A_{P_{3/2}-S_{1/2}} = A_{393}$, $A_{P_{3/2}-D_{5/2}} = A_{854}$ and $\Gamma_{P_{3/2}} = A_{393} + A_{854}$ is the total decay rate. The population transfer rate induced by the 854 nm laser is defined by r_{854} which describes the population transfer in the two-level subsystem between $P_{3/2}$ and $D_{5/2}$ by absorption and stimulated emission processes.

Numerical solution

The equations (2.33)-(2.35) are solved numerically for the initial conditions $\rho_{SS}(0) = 0$, $\rho_{PP}(0) = 0$ and $\rho_{DD}(0) = 1$. We typically work with 854 nm laser parameters as the intensity such that the population transfer rate r_{854} is low compared to the total decay rate $\Gamma_{P_{3/2}} = 2\pi \cdot 22.99\,\text{MHz}$. Here we choose $r_{854} = 2\pi \cdot 1\,\text{MHz}$ and show the population dynamics in Fig. 2.3. There we observe that the population $\rho_{DD}(t)$ is optically pumped out

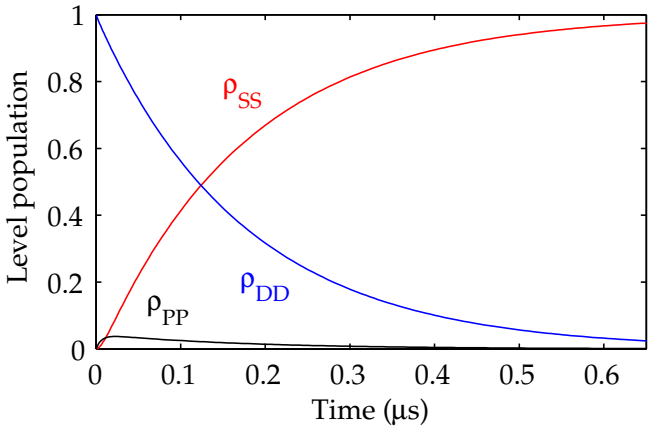

Figure 2.3.: Evolution of the populations ρ_{SS}, ρ_{PP} and ρ_{DD} corresponding to the $S_{1/2}$, $P_{3/2}$ and $D_{5/2}$ level populations for generation of 393 nm photons. The simulation is executed for $r_{854} = 2\pi \cdot 1\,\mathrm{MHz}$.

from the $D_{5/2}$ level with an exponential decay while $\rho_{SS}(t)$ is filled accordingly. From the dynamics we infer that $\dot{\rho}_{DD}(t) = -\dot{\rho}_{SS}(t)$. In between the $P_{3/2}$ level is weakly populated such that $\rho_{PP}(t) \ll 1$ persists during the whole process.

Analytical solution

The analytical solutions for the different levels are quite lengthy. However, we want to obtain an analytical expression of the $D_{5/2}$ population to see how the level is depopulated, which is useful for the deviation of a (simplified) analytical expression for the $P_{3/2}$ population. From the analytical solution we obtain with $\Gamma = A_{393} + A_{854}$

$$\begin{aligned}\rho_{DD}(t) = \frac{1}{2}\Bigg(& \frac{e^{-\frac{1}{2}(\Gamma+2r_{854}-\sqrt{\Gamma^2+4A_{854}r_{854}+4r_{854}^2})t}A_{393}}{\sqrt{\Gamma^2+4A_{854}r_{854}+4r_{854}^2}} - \frac{e^{-\frac{1}{2}(\Gamma+2r_{854}+\sqrt{\Gamma^2+4A_{854}r_{854}+4r_{854}^2})t}A_{393}}{\sqrt{\Gamma^2+4A_{854}r_{854}+4r_{854}^2}} \\ & + \frac{e^{-\frac{1}{2}(\Gamma+2r_{854}-\sqrt{\Gamma^2+4A_{854}r_{854}+4r_{854}^2})t}A_{854}}{\sqrt{\Gamma^2+4A_{854}r_{854}+4r_{854}^2}} - \frac{e^{-\frac{1}{2}(\Gamma+2r_{854}+\sqrt{\Gamma^2+4A_{854}r_{854}+4r_{854}^2})t}A_{854}}{\sqrt{\Gamma^2+4A_{854}r_{854}+4r_{854}^2}} \\ & + e^{-\frac{1}{2}(\Gamma+2r_{854}-\sqrt{\Gamma^2+4A_{854}r_{854}+4r_{854}^2})t} + e^{-\frac{1}{2}(\Gamma+2r_{854}+\sqrt{\Gamma^2+4A_{854}r_{854}+4r_{854}^2})t}\Bigg). \end{aligned} \tag{2.36}$$

In the limit of $r_{854} \ll \Gamma$ and including that $A_{854} < \Gamma$, the equation reduces to

$$\begin{aligned}\rho_{DD}(t) &= \frac{1}{2}\left(\frac{A_{393}+A_{854}}{\Gamma}e^{-r_{854}t} - \frac{A_{393}+A_{854}}{\Gamma}e^{-(\Gamma+r_{854})t} + e^{-r_{854}t} + e^{-(\Gamma+r_{854})t}\right) \\ &= e^{-r_{854}t}. \end{aligned} \tag{2.37}$$

Since the population is pumped from the $D_{5/2}$ to the $S_{1/2}$ level, we rename the rate $r_{854} = R_{D\to S}$ and formulate the time derivative

$$\dot{\rho}_{DD}(t) = -R_{D\to S}\, e^{-R_{D\to S}t} = -R_{D\to S}\,\rho_{DD}(t) = -\dot{\rho}_{SS}(t). \tag{2.38}$$

In order to understand the temporal evolution of the population in $P_{3/2}$ when switching on the 854 nm laser, we first have to point out the different timescales that occur during excitation on the $D_{5/2}$ to $P_{3/2}$ transition. For the subsystem between the $D_{5/2}$ and $P_{3/2}$ level we introduce a situation similar to a two-level system by a steady-state excitation probability. Since we work in a regime where the Rabi frequency Ω_{854} of the driving field is much lower than the natural decay rate of the upper state $\Gamma_{P_{3/2}}$, the overall population in $P_{3/2}$ is very low. The two states $D_{5/2}$ and $P_{3/2}$, however, reach their steady state with rate $\Gamma_{P_{3/2}}$, much faster than the rate with which population is transferred to $S_{1/2}$. Thus we formulate the steady-state population ratio in the two-level subsystem of $P_{3/2}$ and $D_{5/2}$,

$$\frac{\rho_{PP}(t)}{\rho_{DD}(t)} = \frac{\Omega_{854}^2}{4\Delta^2 + \Gamma_{P_{3/2}}^2 + 2\Omega_{854}^2}. \tag{2.39}$$

The detuning Δ between the atomic transition frequency and the laser frequency and Ω_{854} as the Rabi frequency

$$\Omega_{854} = \sqrt{\frac{1}{2} A_{854}^2 \frac{I_{854}}{I_{sat}}}, \tag{2.40}$$

with the laser intensity I_{854} and the saturation intensity

$$I_{sat} = \frac{\pi}{3} \frac{hc}{\lambda^3 \frac{1}{A_{854}}}, \tag{2.41}$$

result from the theory of the two-level Bloch equations [92]. For the population ratio given in Eq. (2.39) we insert Eq. (2.33) and Eq. (2.38) leading to

$$\frac{\rho_{PP}(t)}{\rho_{DD}(t)} = \frac{R_{D\to S}}{A_{393}}, \tag{2.42}$$

and we finally obtain, in terms of the steady-state population, the rate at which population is transferred from $D_{5/2}$ to $S_{1/2}$

$$R_{D\to S} = \frac{\Omega_{854}^2}{4\Delta^2 + \Gamma_{P_{3/2}}^2 + 2\Omega_{854}^2}\, A_{393}. \tag{2.43}$$

Eq. (2.43) constitutes the time independent rate of spontaneously Raman-scattered photons from which we already notice that we can control the rate of 393 nm photons by the laser detuning Δ and by the Rabi frequency Ω_{854} on the $D_{5/2}$ to $P_{3/2}$ transition. In the *weak* excitation regime $\Omega_{854} \ll \Gamma_{P_{3/2}}$, Eq. (2.43) simplifies to

$$R_{D\to S} = \frac{\Omega_{854}^2}{4\Delta^2 + \Gamma_{P_{3/2}}^2}\, A_{393}, \tag{2.44}$$

which has a linear dependence on the laser intensity I as shown in Eq. (2.40). For higher Rabi frequencies in the *strong* excitation regime $\Omega_{854} \gg \Gamma_{P_{3/2}}$ the description becomes more complex. In this regime damped Rabi oscillations on the $D_{5/2}$ to $P_{3/2}$ cause the rate $R_{D\to S}$ to become time dependent, as discussed below.

Now we are able to calculate the temporal dynamics of the population in $P_{3/2}$ by first inserting Eq. (2.34) into Eq. (2.35) which gives

$$\dot{\rho}_{DD}(t) = -\dot{\rho}_{PP}(t) - A_{393}\rho_{PP}(t). \tag{2.45}$$

Inserting Eq. (2.38) into Eq. (2.45) allows us to solve the differential equation and derive the population in $P_{3/2}$ which evolves like

$$\rho_{PP}(t) = \frac{R_{D\to S}(1 - e^{-t(R_{D\to S} - A_{393})})}{R_{D\to S} - A_{393}}\, e^{-A_{393}t}. \tag{2.46}$$

According to [95], the total average intensity at time t of the emitted light is $\langle I(t)\rangle \propto \rho_{PP}(t)$ which indicates that the temporal profile of the photonic wave packet is formed by the temporal evolution of the population in $P_{3/2}$[3]. In the experiment we want to record the envelope function of the photonic wave packet and deduce the exponential decay time. Instead of using the more complex Eq. (2.46) for fitting the photon, we further simplify Eq. (2.46) in the limit of $\frac{\rho_{PP}(t)}{\rho_{DD}(t)} \ll 1$ where we know that $R_{D\to S} \ll A_{393}$. Thus we obtain the approximation

$$\rho_{PP}(t) = \frac{\rho_{PP}(t)}{\rho_{DD}(t)}\, e^{-R_{D\to S}t}. \tag{2.47}$$

Comparison between the models

We show the temporal behavior of the population in $P_{3/2}$ for the three different models and check their validity for weak and strong excitation. In Fig. 2.4(a) we numerically calculate for a weak excitation with $\Omega_{854} = 2\pi \cdot 2\,\mathrm{MHz}$ the solution of the Bloch equations (solid green line), the solution of the rate equation model as given in Eq. (2.46) (solid blue line) and the approximated exponential decay function in Eq. (2.47) (dashed red line). The evolution of the solution from the Bloch equations and rate equations follows of a fast rising slope and a slow decay given by the inverse of $R_{D\to S}$ as the $\frac{1}{e}$ time

$$\tau_{ph} = \frac{1}{R_{D\to S}} \sim 1\,\mu\mathrm{s}. \tag{2.48}$$

We see that for the low Rabi frequency, corresponding to an intensity well below the saturation intensity, the pure exponential decay without the rising slope is a good approximation to the rate-equation model and both agree well with the full dynamics from the Bloch equations. That is why we use in the next chapters the simple exponential decay for fitting the

[3] A further description of spectro-temporal properties of photons is given in Chapter 3.

photonic wave packets. The temporal shape given in Fig. 2.4(a) reflects the temporal evolution of the photonic wave packet and Eq. (2.48) shows that we are able to tune the temporal length of the photonic wave packet by the rate $R_{D\to S}$. In Fig. 2.4(b) we present the strong

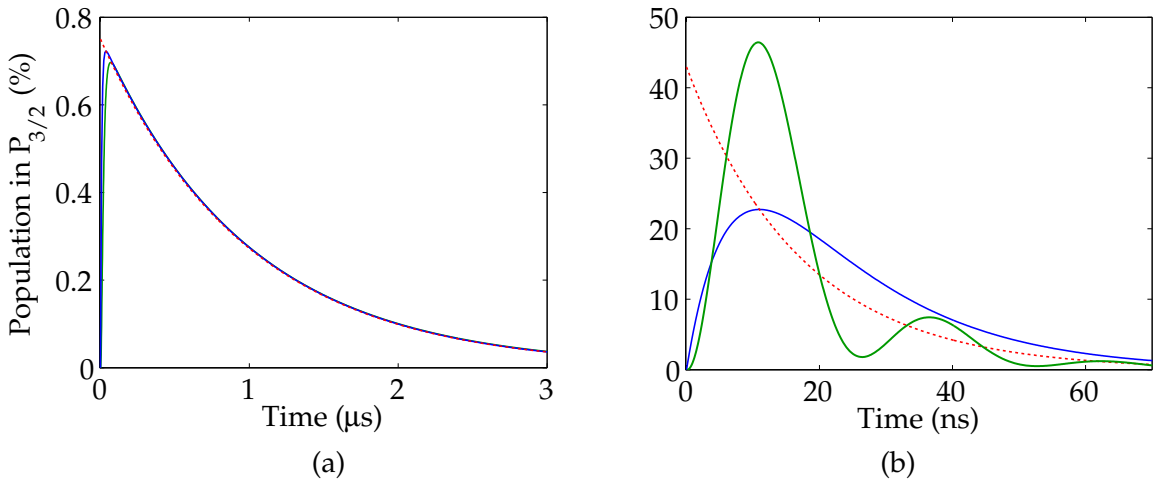

Figure 2.4.: Temporal evolution of the population in $P_{3/2}$ simulated by the solution of the Bloch equations (solid green line), the rate equation model (solid blue line) and the simple exponential decay (dashed red line): (a) for a weak 854 nm laser excitation with a Rabi frequency $\Omega_{854} = 2\pi \cdot 2\,\mathrm{MHz}$. The Bloch equations are well approximated by the rate equation model and the exponential decay function. (b) for strong 854 nm laser excitation with a Rabi frequency $\Omega_{854} = 2\pi \cdot 40\,\mathrm{MHz}$. Here coherent dynamics become visible in the Bloch equation solution (solid green line) while for the strong excitation regime the other models can not simulate the proper dynamics anymore.

excitation regime given by a Rabi frequency of $\Omega_{854} = 2\pi \cdot 40\,\mathrm{MHz}$. In this regime only the Bloch equations including atomic coherences describe the full dynamics correctly. The deviation of the rate equation model and the exponential approximation from the correct dynamics become obvious, since the conditions for this models ($\Omega_{854} \ll \Gamma_{P_{3/2}}$, $\frac{\rho_{PP}(t)}{\rho_{DD}(t)} \ll 1$) are not valid anymore. Furthermore the rate-equation model does not treat atomic coherences. However, since the Rabi frequency is higher than Γ the transition is saturated and we start to observe coherent dynamics, i.e. damped Rabi oscillations between $D_{5/2}$ and $P_{3/2}$ with a period of 25 ns which are properly described only by the Bloch equation solution where coherent coupling terms are included.

2.5.2. Rate of single 393 nm Raman-scattered photons

Finally the time dependent rate at which 393 nm photons are scattered is written as

$$R_{393}(t) = A_{393}\,\rho_{PP}(t). \tag{2.49}$$

The generation of single photons is typically performed in a pulsed sequence mode which runs with a repetition rate ν_{rep} for a certain acquisition time t_{acq}. The average number of scattered photons during t_{acq} with the excitation period of T is derived by

$$\langle n_{393}\rangle(T) = \nu_{\mathrm{rep}}\, t_{\mathrm{acq}} \int_{t'}^{t'+T} R_{393}(t)\,\mathrm{d}t \tag{2.50}$$

$$= \nu_{\mathrm{rep}}\, t_{\mathrm{acq}} \int_{t'}^{t'+T} A_{393}\,\rho_{\mathrm{PP}}(t)\,\mathrm{d}t. \tag{2.51}$$

In the last equation, the time t' represents the time at which the 854 nm laser is switched on during each sequence cycle. The electronic signal which switches the laser is used for digitally gating the detector. The gate signal is fed into one channel of our time correlator PicoHarp, while the second channel of PicoHarp is connected to the photon detector. With both signals, correlation measurements are executed between the beginning of the 854 nm pulse and the detection of the photon at 393 nm, revealing the photon wave packet in a photon arrival-time histogram.

If the initial population of the $D_{5/2}$ level is completely pumped out during one excitation period of T which is much longer than the $\frac{1}{e}$ lifetime (τ_{ph}) of the photon wave packet, we generate a single photon in each experimental cycle. Integration over the whole photon wave packet, i.e. over the total temporal evolution of $\rho_{\mathrm{PP}}(t)$ means that the integral in Eq. (2.51) is close to one and we obtain the total number of emitted photons

$$n_{393,\mathrm{gen}} = \nu_{\mathrm{rep}}\, t_{\mathrm{acq}}. \tag{2.52}$$

Note that this is only valid if the state preparation efficiency of the $D_{5/2}$ state is close to one. Since we do not detect all the photons which are generally emitted isotropically into the solid angle of 4π, we have to introduce a detection efficiency factor η_{393} representing the ratio of photons that are detected with the photomultiplier to the total number of generated photons

$$\eta_{393} = \frac{n_{393,\mathrm{det}}}{n_{393,\mathrm{gen}}}. \tag{2.53}$$

2.6. Absorption and emission probabilities of dipole transitions

The calculation of all factors that contribute to the detection efficiency η presented in Eq. (2.53) firstly needs the characterization of the emission profile of the light. More importantly the dipolar emission pattern are presented in this section since they serve as a basis to understand the generation of quantum-beat-modulated single photons presented in Chapter 6.

Since the emission and absorption characteristics appear in the transition probability for the dipole transitions, we introduce the transition matrix element between two states $|\psi_a\rangle$ and $|\psi_b\rangle$ with Eq. (2.19) as

$$\langle\psi_b|\hat{H}_{\mathrm{int}}|\psi_a\rangle \propto \langle\psi_b|\hat{\vec{r}}|\psi_a\rangle \cdot \vec{e} = \vec{r}_{ba}\cdot\vec{e}. \tag{2.54}$$

So far the description of the light-matter interaction has been restricted to the situation of a three-level system with degenerate Zeeman sublevels. The total angular momentum j of the valence electron defines for each level the number of Zeeman sublevels with the quantum number $m_j = -j..j$. Now the sublevels are lifted in their degeneracy by a magnetic field B. The frequency splitting $\Delta\nu$ between Zeeman substates is determined by the Landé factors g_j, the difference in the magnetic quantum number Δm_j and the magnetic field B according to

$$\Delta\nu = \frac{\mu_\mathrm{B}}{h}\, g_j\, \Delta m_j\, B. \tag{2.55}$$

Thus the transition matrix elements have to be expressed in the basis states

$$\langle j_b, m_b | \hat{\vec{r}} \cdot \vec{e} | j_a, m_a \rangle. \tag{2.56}$$

For including the polarization and angle dependances in the probability of the transition amplitudes for the emission processes we analyze $|\vec{r}_{ba} \cdot \vec{e}|^2$ since this is related to the natural spontaneous decay rate between two manifolds a and b like

$$d\Gamma_{ba} = \frac{\alpha \omega_{ba}^3}{2\pi c^2} \cdot |\vec{r}_{ba} \cdot \vec{e}|^2 \cdot d\Omega, \tag{2.57}$$

with the fine structure constant α and the transition frequency ω_{ba} [96]. The selection rules and angular distributions of the emitted radiation are determined by the scalar product between the dipole matrix element $\vec{r}_{ba}^{\,(\mathrm{at})}$ described in the atomic coordinate system (at) and the polarization vector $\vec{e}^{\,(\mathrm{ph})}$ of the light traveling in the direction of $\vec{k}$ and which is described in the photonic coordinate system (ph). Taking this into account demands the derivation of a theoretical model showing which dipole transitions are allowed with respect to the absorbed and emitted light polarization and angular dependence of the light direction. The description follows [96].

Since the atomic system is typically described in spherical coordinates we describe the photonic polarization by the following basis vectors

$$\vec{e}_0 = \vec{e}_z, \quad \vec{e}_{+1} = -\tfrac{1}{\sqrt{2}} \left(\vec{e}_x + \mathrm{i}\vec{e}_y\right), \quad \vec{e}_{-1} = \tfrac{1}{\sqrt{2}} \left(\vec{e}_x - \mathrm{i}\vec{e}_y\right). \tag{2.58}$$

They are drawn in Fig. 2.5 (blue line and circles) describing linear light polarization in z-direction and two circular polarizations $\vec{e}_{+1}$ and $\vec{e}_{-1}$, representing right- and left circularly polarized light propagating in the z direction or in the x-y plane, respectively. Accordingly linear polarizations along x and y are described by

$$\vec{e}_x = -\tfrac{1}{\sqrt{2}} \left(\vec{e}_{+1} - \vec{e}_{-1}\right), \tag{2.59}$$

$$\vec{e}_y = \tfrac{\mathrm{i}}{\sqrt{2}} \left(\vec{e}_{+1} + \vec{e}_{-1}\right). \tag{2.60}$$

The three vectors in Eq. (2.58) are also the basis vectors for the classical description of the atomic position vector $\vec{r}$, necessary to evaluate transition matrix elements. For the latter

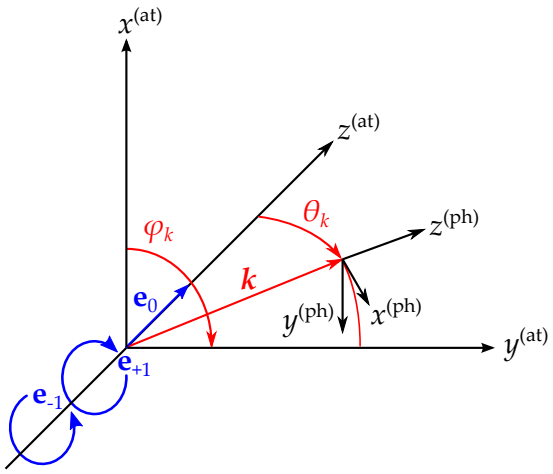

Figure 2.5.: Cartesian coordinate systems describing the atomic system ($x^{(at)}$, $y^{(at)}$, $z^{(at)}$) and the photonic system ($x^{(ph)}$, $y^{(ph)}$, $z^{(ph)}$). The $z^{(at)}$-axis coincides with the direction of the magnetic field which defines the quantization axis. The wave vector $\vec{k}$ (red) shows the propagation direction of the light. The polar coordinates φ_k and θ_k are used for coordinate transformation from the atomic into the photonic system and vice versa. The three fundamental oscillations (blue) correspond to the basis vectors $\vec{e}_{+1}$, $\vec{e}_{-1}$ and $\vec{e}_0$ which are used to describe the polarization of the light field in the photonic coordinate system and the dynamics of the atom in the atomic coordinate system.

we write the atomic position vector $\vec{r}$ in spherical coordinates and we identify the three components

$$r_0^{(at)} = z^{(at)} = r\sqrt{\tfrac{4\pi}{3}}\,Y_{1,0}(\theta,\varphi) \tag{2.61}$$

$$r_{+1}^{(at)} = -\frac{(x^{(at)} + \mathrm{i}y^{(at)})}{\sqrt{2}} = r\sqrt{\tfrac{4\pi}{3}}\,Y_{1,+1}(\theta,\varphi) \tag{2.62}$$

$$r_{-1}^{(at)} = \frac{(x^{(at)} - \mathrm{i}y^{(at)})}{\sqrt{2}} = r\sqrt{\tfrac{4\pi}{3}}\,Y_{1,-1}(\theta,\varphi), \tag{2.63}$$

with the spherical harmonics Y_{lm} with $l = 1$, $m_l = 0, +1, -1$. The general form of the atomic position vector $\vec{r}$ is summarized as

$$\vec{r}^{\,(at)} = \sqrt{\tfrac{4\pi}{3}}\,r \sum_{q=-1}^{+1} Y_{1q}(\theta,\varphi)\cdot\vec{e}_q^{\,*(at)}, \tag{2.64}$$

where $\vec{e}_q^{\,*}$ is the complex conjugate of $\vec{e}_q$ introduced in Eq. (2.58). For a transition between two energy eigenstates $|j_a\, m_a\rangle$, $|j_b\, m_b\rangle$ and light polarization $\vec{e}$, the absorption and emission

probability described in the term $\left|\vec{r}_{ba} \cdot \vec{e}^{(\mathrm{ph})}\right|^2$ is expressed as

$$\left|\vec{r}_{ba} \cdot \vec{e}^{(\mathrm{ph})}\right|^2 = \left| \sum_{q=-1}^{1} \langle m_b | r_q | m_a \rangle \cdot \vec{e}_q^{*(\mathrm{at})} \cdot \vec{e}^{(\mathrm{ph})} \right|^2 \tag{2.65}$$

$$= \left| \sqrt{\tfrac{4\pi}{3}} \sum_{q=-1}^{1} \langle \gamma_b | r | \gamma_a \rangle \, \langle j_b m_b | Y_{1q} | j_a m_a \rangle \cdot \vec{e}_q^{*(\mathrm{at})} \cdot \vec{e}^{(\mathrm{ph})} \right|^2 \tag{2.66}$$

with the radial matrix element $\langle \gamma_b | r | \gamma_a \rangle$ which can only be solved by high numerical efforts and the matrix elements $\langle j_b m_b | Y_{1q} | j_a m_a \rangle$ that are discussed in Sec. 2.6.3.

2.6.1. Polarization and angular dependence for emission process

We formulate the emission process from $|j_b, m_b\rangle \rightarrow |j_a, m_a\rangle$ with the generation of linear superpositions between Zeeman substates in $|j_a, m_a\rangle$ and obtain the final state

$$|\psi_a\rangle \propto \sum_{m_a} \langle m_a | r_q | m_b \rangle^* \cdot \vec{e}_q^{(\mathrm{at})} \cdot \vec{e}^{*(\mathrm{ph})} | j_a, m_a \rangle. \tag{2.67}$$

To see the polarization of the light which is generated by the emission process for arbitrary emission angles (φ_k, θ_k) we evaluate $\vec{e}_q^{(\mathrm{at})} \cdot \vec{e}^{*(\mathrm{ph})}$ which is possible by a rotation of the photonic reference frame into the atomic reference frame, which means we have to express $\vec{e}_q^{(\mathrm{at})}$ in terms of $\vec{e}^{(\mathrm{ph})}$ through

$$\vec{e}_{q'}^{(\mathrm{at})} = e^{\mathrm{i}q'\varphi_k} \sum_{q=-j}^{j} d^1_{qq'}(-\theta_k) \cdot \vec{e}_q^{(\mathrm{ph})}. \tag{2.68}$$

Evaluating Eq. (2.68) for $\Delta m = m_b - m_a = q' = 0, \pm 1$ results in the following polarization vectors in the photonic reference frame

$$\vec{e}_0^{(\mathrm{at})} = \tfrac{\sin\theta_k}{\sqrt{2}} \left(\vec{e}_{+1}^{(\mathrm{ph})} - \vec{e}_{-1}^{(\mathrm{ph})} \right) = \sin\theta_k \cdot \vec{e}_x^{(\mathrm{ph})} \tag{2.69}$$

$$\vec{e}_{+1}^{(\mathrm{at})} = e^{\mathrm{i}\varphi_k} \left(\cos^2\tfrac{\theta_k}{2} \, \vec{e}_{+1}^{(\mathrm{ph})} + \sin^2\tfrac{\theta_k}{2} \, \vec{e}_{-1}^{(\mathrm{ph})} \right) \tag{2.70}$$

$$\vec{e}_{-1}^{(\mathrm{at})} = e^{-\mathrm{i}\varphi_k} \left(\sin^2\tfrac{\theta_k}{2} \, \vec{e}_{+1}^{(\mathrm{ph})} + \cos^2\tfrac{\theta_k}{2} \, \vec{e}_{-1}^{(\mathrm{ph})} \right). \tag{2.71}$$

The derivation of Eq. (2.68) together with Eq. (2.69) is given in detail in App. A.1. Out of the various emission angles we restrict the analysis for the two emission angles $\theta_k = 0$ and $\theta_k = \frac{\pi}{2}$, as they correspond to the typical experimental case that the HALO collects the emitted light along ($\theta_k = 0$) and perpendicular ($\theta_k = \frac{\pi}{2}$) to the quantization axis. We clearly see that for $\theta_k = 0$, the light emitted in the direction of the magnetic field (along the $z^{(\mathrm{at})}$-axis) corresponds to pure $\sigma^+(\vec{e}_{+1})$ light, which is right circularly polarized ($|R\rangle$). Similarly, in the opposite direction with $\theta_k = \pi$, the light emitted on a $\sigma^-(\vec{e}_{-1})$ transition is left

circularly polarized ($|L\rangle$). Perpendicular to the magnetic field, with $\theta_k = \frac{\pi}{2}$, the light has a linear polarization. For the special case in the $z^{(\mathrm{at})}$-$y^{(\mathrm{at})}$ plane ($\varphi_k = \frac{\pi}{2}, \frac{3\pi}{2}$), the emitted light has pure linear polarization along the $x^{(\mathrm{ph})}$-axis in the photonic reference frame, which we define horizontally polarized ($|H\rangle$) π light. Additionally, we obtain according to Eq. (2.60) and for $\varphi_k = \frac{\pi}{2}, \frac{3\pi}{2}$, the superposition of the two circular oscillations σ^+ and σ^-, which results in vertically polarized light ($|V\rangle$), i.e. perpendicular to the $y^{(\mathrm{at})} - z^{(\mathrm{at})}$-plane.

Finally we insert Eq. (2.69) - (2.71) into Eq. (2.65) and in Eq. (2.57) to directly observe the angular distribution of the emission probability per time into the solid angle for π and σ transitions

$$d\Gamma_\pi = \frac{\alpha\omega_{ba}^3}{2\pi c^2} |\langle m_b|r_0|m_a\rangle|^2 \cdot \sin^2\theta_k \, d\Omega, \tag{2.72}$$

$$d\Gamma_\sigma = \frac{\alpha\omega_{ba}^3}{2\pi c^2} |\langle m_b|r_{\pm 1}|m_a\rangle|^2 \cdot \tfrac{1}{2}(1 + \cos^2\theta_k) \, d\Omega. \tag{2.73}$$

These two equations show that perpendicular to the magnetic field the probability to detect σ-photons is half that for π-photons, which must be taken into account for calculating emission probabilities and detection efficiencies for generated photons along the quantization axis or perpendicular to it. In Fig. 2.6 the geometry dependence of the emission intensities is plotted for π-transitions (a) with $I_\pi \propto \sin^2\theta_k$ and σ transitions (b), (c) with $I_\sigma \propto \frac{1}{2}(1 + \cos^2\theta_k)$ for $\theta_k = 0..\pi$ and for $\varphi_k = 0..2\pi$. The color code visible in the emission

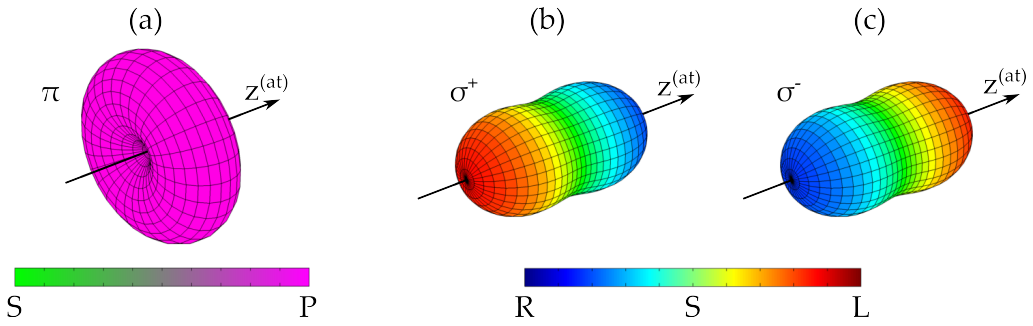

Figure 2.6.: Intensity profile of the dipolar emission pattern for π-transitions (a), σ^+-transtions (b) and σ^--transitions (c). The colorbars show the different polarizations for different emission angles. The $z^{(\mathrm{at})}$-axis coincides with the direction of the magnetic field, defining the quantization axis. The abbreviations for the polarizations are explained in the text.

pattern represents the polarization, i.e. Eq. (2.69)-(2.71) for $\theta_k = 0..\pi$. For these we introduce a new appropriate nomenclature for the polarization, namely S- and P polarization. The S polarization represents the linear polarization between $|R\rangle$ and $|L\rangle$ in Fig. 2.6(b) and (c) and is defined to be perpendicular to the plane spanned by the wavevector $\vec{k}$ and $z^{(\mathrm{at})}$ when light is emitted for $\theta_k = \frac{\pi}{2}$ and φ_k is arbitrary. For the case of a π-transition, the

light has P-polarization which is parallel to the $\vec{k} - z^{(\mathrm{at})}$-plane. As we will see in Sec. 6.2.1 and Sec. 6.2.2, the different emission pattern become crucial when explaining the different types of quantum-beat-modulated arrival-time distributions of single photons, which are emitted by the ion.

2.6.2. Polarization and angular dependence for absorption process

Analogously to the emission process described above, the absorption process for the transition from $|j, m_a\rangle$ to $|j, m_b\rangle$ is formulated as

$$|\psi_b\rangle \propto \sum_{m_b} \langle m_b | r_q | m_a \rangle \cdot \vec{e}_q^{\,*(\mathrm{at})} \cdot \vec{e}^{\,(\mathrm{ph})} | j_b\, m_b \rangle. \tag{2.74}$$

For this case, the transformation has to be performed from the atomic reference frame into the reference frame of the photon

$$\vec{e}_{q'}^{\,(\mathrm{ph})} = \sum_{q=-j}^{j} e^{-\mathrm{i}q\varphi_k} d^1_{qq'}(\theta_k) \cdot \vec{e}_q^{\,(\mathrm{at})}, \tag{2.75}$$

and the photonic polarization states are expressed by evaluating Eq. (2.75) for the possible transitions as

$$\vec{e}_{+1}^{\,(\mathrm{ph})} = e^{\mathrm{i}\varphi_k} \sin^2\tfrac{\theta_k}{2}\, \vec{e}_{-1}^{\,(\mathrm{at})} + \tfrac{\sin\theta_k}{\sqrt{2}}\, \vec{e}_0^{\,(\mathrm{at})} + e^{-\mathrm{i}\varphi_k} \cos^2\tfrac{\theta_k}{2}\, \vec{e}_{+1}^{\,(\mathrm{at})} \tag{2.76}$$

$$\vec{e}_{-1}^{\,(\mathrm{ph})} = e^{\mathrm{i}\varphi_k} \cos^2\tfrac{\theta_k}{2}\, \vec{e}_{-1}^{\,(\mathrm{at})} - \tfrac{\sin\theta_k}{\sqrt{2}}\, \vec{e}_0^{\,(\mathrm{at})} + e^{-\mathrm{i}\varphi_k} \sin^2\tfrac{\theta_k}{2}\, \vec{e}_{+1}^{\,(\mathrm{at})} \tag{2.77}$$

$$\vec{e}_x^{\,(\mathrm{ph})} = e^{\mathrm{i}\varphi_k} \tfrac{\cos\theta_k}{\sqrt{2}}\, \vec{e}_{-1}^{\,(\mathrm{at})} - \sin\theta_k\, \vec{e}_0^{\,(\mathrm{at})} - e^{-\mathrm{i}\varphi_k} \tfrac{\cos\theta_k}{\sqrt{2}}\, \vec{e}_{+1}^{\,(\mathrm{at})} \tag{2.78}$$

$$\vec{e}_y^{\,(\mathrm{ph})} = \tfrac{\mathrm{i}}{\sqrt{2}} \left(e^{\mathrm{i}\varphi_k}\, \vec{e}_{-1}^{\,(\mathrm{at})} + e^{-\mathrm{i}\varphi_k}\, \vec{e}_{+1}^{\,(\mathrm{at})} \right) \tag{2.79}$$

Depending of the angle of incidence θ_k, the equations above show which kind of transitions are excited for different incoming polarizations. As an example, for an excitation on quantization axis (along $z^{(\mathrm{at})}$) with $\theta_k = 0$, pure σ^+ transitions ($\vec{e}_{+1}^{\,(\mathrm{at})}$) are excited by $|R\rangle$ light ($\vec{e}_{+1}^{\,(\mathrm{ph})}$) and pure σ^- transitions with $|L\rangle$. An excitation with horizontal polarization $|H\rangle$ for $\varphi_k = \frac{\pi}{2}$ ($\vec{e}_x^{\,(\mathrm{ph})}$) results in a coherent excitation of σ^+ and σ^- transitions according to

$$\vec{e}_x^{\,(\mathrm{ph})} = \tfrac{i}{\sqrt{2}} (\vec{e}_{-1}^{\,(\mathrm{at})} + \vec{e}_{+1}^{\,(\mathrm{at})}) = \vec{e}_y^{\,(\mathrm{at})}. \tag{2.80}$$

2.6.3. Clebsch-Gordan coefficients

Finally we come back to the remaining part in Eq. (2.66), namely the matrix elements of the spherical harmonics in the LS-coupling regime $\langle j_b m_b | Y_{1q} | j_a m_a \rangle$. With the Wigner-Eckart theorem they are decomposed into

$$\langle j_b m_b | Y_{1q} | j_a m_a \rangle = \langle j_a\, 1; m_a, q | j_b, m_b \rangle \langle \gamma_b j_b || Y_1 || \gamma_a j_a \rangle \tag{2.81}$$

with the reduced matrix element $\langle \gamma_b j_b || Y_1 || \gamma_a j_a \rangle$ which is independent of the geometry. The second term is the Clebsch-Gordan coefficient[4] which can be expressed in terms of the the Wigner 3j-symbol [97]

$$C_{m_a,q,m_b} = C^{j_a,1,j_b}_{m_a,q,m_b} := \langle j_a\, 1; m_a, q | j_b, m_b \rangle = (-1)^{j_a - 1 + m_b} \sqrt{2j_b + 1} \begin{pmatrix} j_a & 1 & j_b \\ m_a & q & -m_b \end{pmatrix}. \quad (2.82)$$

With this formula the Clebsch-Gordan coefficients for the transitions between Zeeman substates from $|D_{5/2}, m_j\rangle$ to $|P_{3/2}, m_j\rangle$ and from $|P_{3/2}, m_j\rangle$ to $|S_{1/2}, m_j\rangle$ are calculated and the squared values are shown in Fig. 2.7. The Clebsch-Gordan coefficients will become important, especially for single-photon interference experiments as presented in Chapter 6.

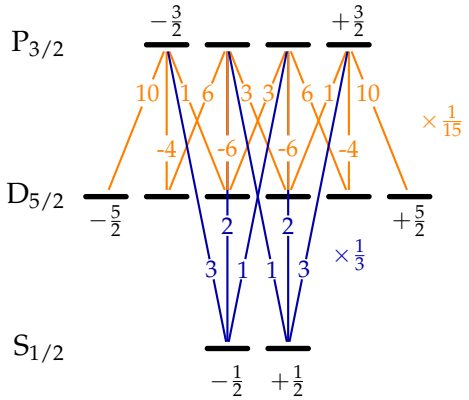

Figure 2.7.: Squared Clebsch-Gordan coefficients for the $D_{5/2}$ to $P_{3/2}$ transition and for the $P_{3/2}$ to $S_{1/2}$ transition. The negative sign indicates the sign of the Clebsch-Gordan coefficient, e.g. for $|P_{3/2}, -1/2\rangle \rightarrow |D_{5/2}, -1/2\rangle$ we get $-\sqrt{6/15}$.

Summary

In this chapter, I presented the basic theory of light-matter interaction. Starting from a semiclassical approach of laser-ion interaction, the dynamics for a three-level system interacting with one laser was described with three different models to obtain the temporal evolution of the population in the $P_{3/2}$ level, representing the temporal shape of the photonic wave packet at 393 nm. For low laser excitation below the saturation intensity, the three models agreed in the temporal shape by which the most simple exponential decay function is used in the next chapters to obtain the $\frac{1}{e}$ lifetime of the photons. For strong laser excitations coherent dynamics play a more and more dominant role, such that only

[4] Note that different notations for the Clebsch-Gordans coefficients can be found in literature like $C_{m_a,q,m_b} = C^{j_a,1,j_b}_{m_a,q,m_b} = \langle j_a\, m_a; 1, q | j_a, 1, j_b, m_b \rangle$.

the Bloch equations can still describe the dynamics properly. Finally the emission and absorption probabilities of dipole transitions were presented. The angle- and polarization dependance of the emission and absorption processes were analyzed which together with the Clebsch-Gordan coefficients become important in Chapter 6, when selected transitions between Zeeman sublevels are excited.

3. Controlled generation of single photons at 393 nm and 854 nm

Single photons are the unique resource to transport quantum information in a quantum network between distant nodes like single ions in separate traps. They allow for entanglement between the nodes through different strategies. One approach is the use of a parametric down-conversion process as a source of entangled photon pairs. The photon pairs are split up and individually sent to two distant single ions, where they are absorbed, thus transferring the entanglement to the ions [98]. An alternative way consists in the creation of atom-photon entanglement [99, 52] to directly transfer the quantum state to another node by mapping the photonic quantum state onto the atom which entangles the two nodes [37]. Besides there is the way for entanglement of two nodes, e.g. two distant atoms that have not interacted directly. If the atoms emit photons such that atom-photon entanglement at each atom is created, one can transfer the atom-photon entanglement through a projective measurement of the photons, i.e. after overlapping their emitted photons on a beam splitter [41] to atom-atom entanglement. This general scheme is known as entanglement swapping [100, 43].

All these schemes have a probabilistic nature. If a herald for the successful creation of entanglement is incorporated, it offers deterministic quantum information processing after its detection [101]. Furthermore the schemes require a high success probability given by a high rate of generated photons that ideally should be in pure quantum state, i.e. the photons must have a single polarization and be in a single spatial mode. More importantly, the spectral and temporal character of the photons should ideally show a minimal time-bandwidth product, which we call Fourier limited photons.

In the context of fiber-based quantum networks, the latter is an essential feature for multiplexing, known from classical optical fiber communication systems. Multiplexing allows for transmission of more than one optical signal through the same fiber. In order to reach a maximum number of different transmission channels within the available transmission bandwidth while keeping a high transmission rate, the photons should be Fourier limited.

The following section 3.1 treats the controlled generation of single 393 nm photons in a spontaneous Raman process, triggered by the absorption of 854 nm laser photons. It is shown that the temporal shape of the photonic wave packet is controlled by the 854 nm laser intensity. The true single photon character is proven by the presentation of the second-order correlation function. The change of the depopulation rate of the $D_{5/2}$ level for different 854 nm polarizations shows the controlled preparation of a single Zeeman substate in the $D_{5/2}$ level. With this preparation it is possible to generate 393 nm photons

in a pure polarization and frequency state and with an almost Fourier-limited time bandwidth product which makes them suitable as carriers of quantum information in transfer schemes.

In section 3.2, the controlled generation of 854 nm photons which is important for proof-of-principle experiments towards (hybrid) quantum networks is presented. In contrast to the 393 nm photons, the generation of 854 nm photons is executed in a three-photon resonance condition whose investigation is assisted by numerical simulations. It will be shown that these photons are far away from being Fourier limited due to the three-photon excitation and the branching ratio of the $P_{3/2}$ level. However, we couple them into a single-mode fiber with a rate sufficient for photonic interaction measurements between two single ions, presented in Chapter 4.

3.1. Single 393 nm photons as heralds for quantum memories

One of the goals of our work towards the realization of a quantum network lies in the entanglement transfer of the polarization of photon pairs from a SPDC source to two distant single ions as originally proposed by [98] and adapted to our experimental situation by [102]. The photon pair source used in our experiment generates polarization entangled photon pairs which are resonant with the 854 nm transition at the ion. In our experimental protocol, we want to use the 393 nm photons as a herald for the successful state transfer from the 854 nm photons into the ground state of the ion, leading to a high fidelity for the mapping process even if the absorption probability of the 854 nm photons is low. In order to reach this, we first have to show the full control of the atom-photon interface, i.e. the control over the absorption of 854 nm photons and the emission of 393 nm photons. Concerning the emission, we have to generate 393 nm photons in a spontaneous Raman process which are ideally in a clean frequency and polarization state. Characterizing 393 nm photons in a pure polarization state can be viewed as an essential prerequisite for Chapter 6, when superpositions of pure polarization states of 393 nm photons are used to perform single-photon interference experiments.

3.1.1. Experimental setup

The experimental setup for the generation of single 393 nm photons and the corresponding level scheme with all relevant transitions are shown in Fig. 3.1(a) and (b), respectively. The ion is addressed by the 397 nm and 866 nm laser for Doppler cooling. The population is optically pumped to the $D_{5/2}$ manifold together with the 850 nm laser on the $D_{3/2}$ to $P_{3/2}$ transition. For the generation of 393 nm photons we can either use the 854 nm pump beam at 45° with respect to the HALO axis or the 854 nm beam which is sent in through HALO 1 along the quantization axis, i.e. in the direction of the magnetic field B. Its polarization is rotated from right-circularly polarized $|R\rangle$ to left circularly polarized $|L\rangle$ light with the quarter-wave plate (QWP 854 nm). The laser beams are focused with plano-convex

lenses to focal-spot diameters of 120 µm (397 nm), 250 µm (866 nm) and 125 µm (850 nm and 854 nm pump). The 854 nm beam is focused by the HALO to a focal-spot diameter of ~ 2.5 µm.

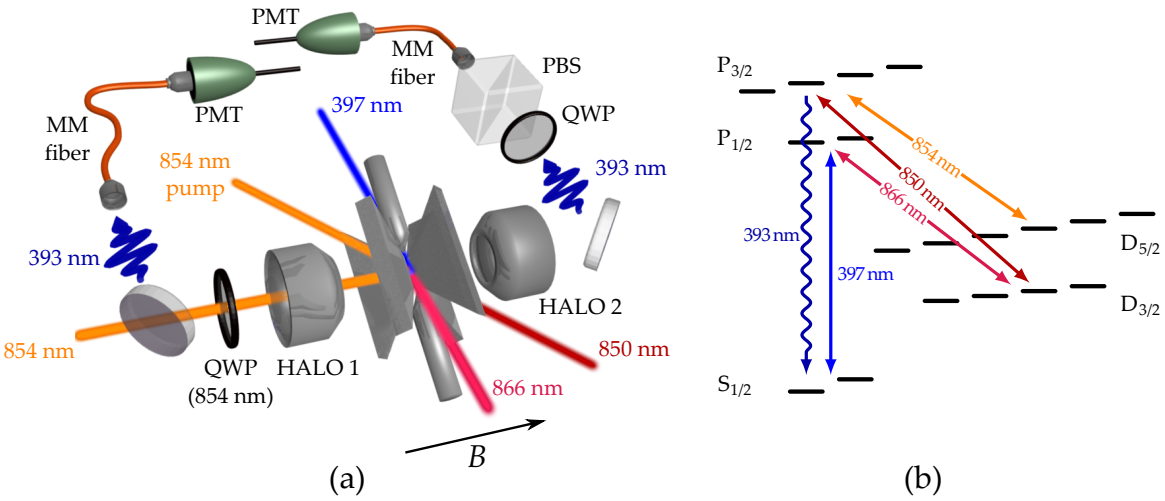

Figure 3.1.: (a) Experimental setup for generating 393 nm photons. PMT stands for photomultiplier tube, QWP for quarter-wave plate and PBS for polarizing beam splitter. (b) Level scheme with the transitions adressed by laser light (double arrows) for 393 nm photon generation (wavy arrow). For further details see text.

The generated 393 nm photons are collected parallel to the magnetic field from HALO 1 and HALO 2, coupled to multi-mode fibers (MM fiber) and sent to photomultiplier tubes (PMT). The position of HALO 1 with respect to the ion is optimized to have the focus at 854 nm wavelength at the position of the ion. The collection of 397 nm fluorescence photons from the $P_{1/2}$ to $S_{1/2}$ transition with HALO 1 is maintained by an array of lenses which are built up behind HALO 1 and the dichroic mirror which is used to transmit the 854 nm light while reflecting 397 nm and 393 nm light. A detailed description of this experimental setup is found in [27].

Since we aim to collect 393 nm photons with highest efficiency we have to built up a stack of lenses ($f = -100$ mm, $f = 200$ mm) behind HALO 1 that compensate for the effective focal length difference between 397 nm and 393 nm and which optimizes the coupling of the 393 nm photons to the multi-mode fiber. The stack is built on a magnetic flip mount, enabling easy switching between efficient collection of 393 nm or 397 nm photons. The position of HALO 2 is optimized to collect 397 nm photons, which necessitate again the setup of a compensation-lens stack ($f = -75$ mm, $f = 100$ mm) for the coupling of the 393 nm photons to the multi-mode fiber. For polarization sensitive measurements, the 393 nm photons collected by HALO 2 can optionally be projected to a linear polarization by inserting a quarter-wave plate (QWP) followed by a polarizing beam splitter (PBS).

3.1.2. 393 nm photons in a mixed quantum state

Experimental sequence

The experimental sequence is illustrated in Fig. 3.2 and begins with Doppler cooling lasting typically between $t_{\text{cool.}} = 0.6 - 1\,\mu\text{s}$ with the 397 nm and 866 nm laser. During the "cooling" period the 854 nm pump beam transfers any remaining population out of the $D_{5/2}$ level which is left from the previous sequence cycle. The cooling period is followed by a "state preparation" period within which the population is pumped to the $D_{5/2}$ level with an 850 nm laser through a three-photon excitation explained in detail in Sec. 3.2.2. Through a coupling of three lasers with different polarizations we expect the population to be distributed in the six $D_{5/2}$ Zeeman substates. In order to achieve a high-rate single-photon source, we optimize the overall sequence length by searching for an optimum state preparation time. We find a value of 2.25 µs with the consequence that we pump only 75 % of the total population to the $D_{5/2}$ level. Between state preparation and "photon generation" there is a fixed waiting period of $t_{\text{wait}} = 1\,\mu\text{s}$, to ensure that all acousto-optic modulators (AOMs) are completely switched off before the 854 nm AOM pulse for photon generation starts. During the photon generation, the PMT is gated, i.e. we detect the single photon events only during this time. The 854 nm pump laser has a polarization which excites a combination of π and $\sigma^{\pm}$ transitions between the $D_{5/2}$ to $P_{3/2}$ levels. This leads to a multitude of $P_{3/2}$ to $S_{1/2}$ transitions (cf. Fig. 2.7) and thus to photons in a mixed quantum state regarding polarization and frequency.

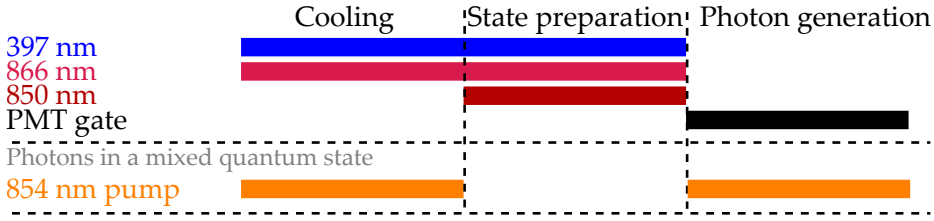

Figure 3.2.: Experimental sequence for generating 393 nm photons in a mixed quantum state with the 854 nm pump beam.

Single-photon arrival-time distributions

The 393 nm photons are collected with both HALOs and detected with the two PMTs gated during the photon-generation period. The PMT signals are fed into the counting module PicoHarp together with the sequence trigger pulses which correspond to the onset of the 854 nm laser for photon generation. The time tagged photon clicks and trigger pulses from the pulse sequencer HYDRA are finally evaluated for their time correlation. Its intuitive meaning is that of Fig. 3.3(a) which shows such a correlation measurement in an

arrival-time histogram[1] of generated 393 nm photons for different 854 nm laser powers. The events are sorted in time bins of 10 ns. The temporal length τ_{ph} defined as the $\frac{1}{e}$ arrival time in the photonic wave packet is obtained from the exponential fit. It is controlled by the power of the 854 nm laser beam and ranges from $\tau_{ph} = 0.325(3)$ µs for $P_{854} = 7$ µW up to $\tau_{ph} = 2.23(1)$ µs for $P_{854} = 0.875$ µW of power. The period lengths of the photon generation is adapted to the laser power and varies between $4 - 14$ µs such that the $D_{5/2}$ population is completely pumped out. Consequently we work with different repetition rates for the different photon lengths, ranging from $\nu_{rep} = 56\,\text{kHz} - 127\,\text{kHz}$. With the fastest repetition rate of 230 kHz for $t_{\text{state prep.}} = 1.95$ µs, $t_{\text{cool.}} = 600$ ns, $t_{\text{wait}} = 1$ µs and $t_{\text{phot. gen.}} = 800$ ns, we achieve a rate of multi-mode fiber coupled photons of $7.4(3) \cdot 10^3\,\text{s}^{-1}$. Fig. 3.3 (b) shows the

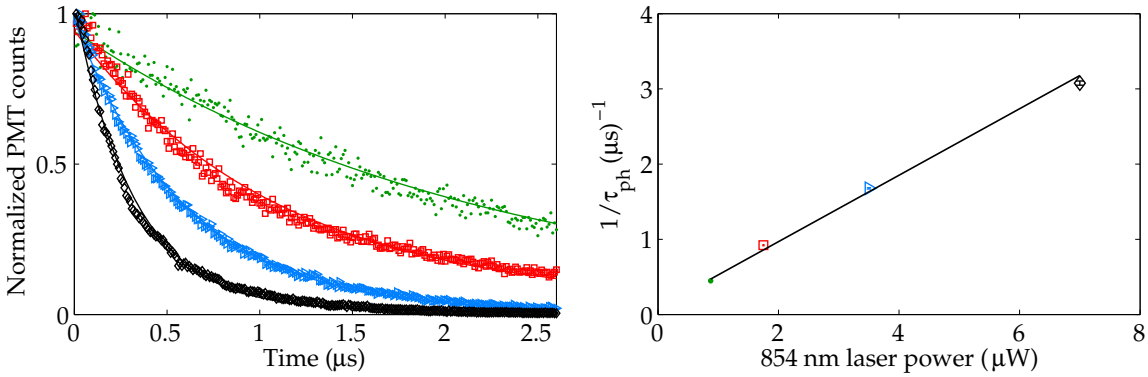

Figure 3.3.: (a) Arrival-time distribution of 393 nm photons for different values of 854 nm laser power. The arrival times τ_{ph} determined by an exponential fit (solid lines) to the data are $\tau_{ph} = \{0.325(3), 0.596(3), 1.08(1), 2.23(1)\}$ µs, from the shortest (black diamonds) to the longest (green dots) wave packet. The measurement time for each wave packet is 5 min with a bin size of 10 ns. The repetition rates, from short to long photons are $\nu_{rep} = \{127, 113, 92, 56\}$ kHz. (b) The inverse photon duration clearly shows the linear dependance with the 854 nm laser power.

dependance of the 393 nm photon rate, $R_{D\to S} = \frac{1}{\tau_{ph}}$, on the 854 nm laser power which is linearly proportional to the intensity. This result was also found for the generation of 397 nm Raman photons by weak excitation at 866 nm shown in [63]. According to Eq. (2.44), we expect that the rate $R_{D\to S}$ increases linearly with higher 854 nm power, i.e. Rabi frequencies if $\Omega_{854} \ll \Gamma_{P_{3/2}}$.

There are two possibilities to check that this condition is fulfilled. We can either use Eq. (2.40) and determine the Rabi frequency at the ion for different 854 nm intensities that we calculate from different 854 nm laser powers focused to a focal-spot size of 125 µm.

[1]The derivation for estimating the probability for single photon clicks in a certain time bin is given in App. A.2.

Besides we can calculate the Rabi frequency from the rate $R_{D\to S}$ with the measured values shown in Fig. 3.3(b) for a certain detuning Δ. With the latter method we see for a laser power of 7 µW that the Rabi frequency (for $\Delta = 0$) is $\Omega_{854} = 2\pi \cdot 3.55\,\mathrm{MHz}$ such that the condition $\Omega_{854} \ll \Gamma_{P_{3/2}}$ is fulfilled. Calculating the Rabi frequency with the laser power and expected focus at the ion results in $\Omega_{854} = 2\pi \cdot 18.9\,\mathrm{MHz}$ such that only $\Omega_{854} < \Gamma_{P_{3/2}}$ is fulfilled.

The difference between the two values are explained by the following: at a later stage in the experiment it became apparent, that the alignment of the fiber couplers and the mirrors for guiding the light to the ion can change over days due to a certain settling of the mechanical components in combination with temperature fluctuations so that the intensity at the ion is drastically reduced and thereby the values for the Rabi frequencies. By performing 854 nm spectroscopy presented in Sec. 5.3 we obtain precise values for the true Rabi frequency at the ion. These measurements revealed that the difference of the true Rabi frequency to the expected one from intensity calculations can easily differ by more than a factor of two due to misalignment. A minor contribution to the discrepancy comes from the 854 nm frequency detuning from the atomic resonance. It is determined in continuous mode with the 397 nm, 850 nm and a weak 854 nm laser, through changing the 854 nm detuning as long as the value for the highest combined 397 nm and 393 nm fluorescence rate is found. This condition is not necessarily identical to the real detuning of the 854 nm laser frequency from the atomic transition frequency due to two-photon resonance conditions between the 850 nm and 854 nm laser.

For higher 854 nm laser intensities ($\Omega > \Gamma$), the population in $P_{3/2}$ level increases and goes for the case of saturated occupation to the limit of 50 % which leads to the highest possible rate of $R_{D\to S} = 0.5 \cdot A_{393} = 67.5\,\mu\mathrm{s}^{-1}$ according to Eq. (2.43). The photonic wave packet then has a minimum duration of

$$\tau_{\mathrm{ph,min}} = \frac{1}{R_{D\to S}} = 14.8\,\mathrm{ns}. \tag{3.1}$$

This regime can be viewed as a transient between the weak excitation regime ($\Omega \ll \Gamma$) explained in Sec. 2.5.1 and the strong excitation regime such that $\Omega \gg \Gamma$, in which we see a Rabi-oscillation structure in the generated photon wave packet, shown in Sec. 3.1.3.

Analysis of antibunching

To proof that the 393 nm photons have a true single-photon character without multi-photon contributions we additionally perform a second-order correlation ($g^{(2)}$) function measurement known from Hanburry Brown and Twiss [103]. In a typical setup, the photons are sent to a non-polarizing beam splitter which splits with equal probability the photons to two different outputs. At each output one detector measures the incoming photons. The photon clicks from both detectors are used to create a histogram of coincidences as a function of the time delay between consecutive clicks at the detectors, known as second-order correlation function.

In contrast to the setup described above, we use the ion as a beam splitter where photons are generated and split in two directions by the collection from two sides with the HALOs. For the photon generation, we use the experimental sequence shown in Fig. 3.2. With an 854 nm power of 6 µW that we send through the HALO we generate short 393 nm photons with a $\frac{1}{e}$ arrival time of 14.8(7) ns. The photons are detected with two PMTs within a gate time of 800 ns and their arrival times are correlated, shown in Fig. 3.4(a). With a repetition rate of 206 kHz we see clear coincidences for time delays which correspond to the sequence period. The cleanness of the single-photon source is characterized by the number of coinci-

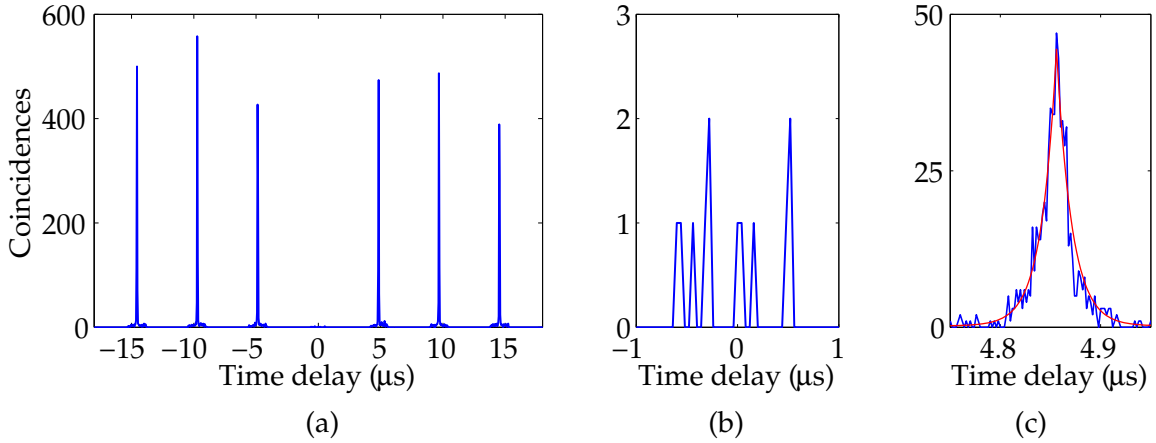

Figure 3.4.: Second-order correlation function of detected 393 nm photons collected with both HALOs for a total acquisition time of 6 min and a repetition rate of 206 kHz. (a) Coincidences are observable in the peaks as the inverse of the repetition rate. (b) Magnification of the central peak at zero time delay. (c) Magnification of the first peak at 4.856 µs together with a double-sided exponential fit (red line). The bin size is 40 ns for (a) and (b), and 2 ns for (c).

dences for zero time delay which are shown in Fig. 3.4(b) and which ideally should be zero. From the experimental sequence in Fig. 3.2, the probability that more than one photon is generated during one experimental cycle seems to be excluded, since after the detection of a 393 nm photon in the photon generation phase, the ion is projected to the $S_{1/2}$ ground state. The only way the ion could be re-excited in the photon generation phase is due to a leakage of light through the AOMs, which are not completely switched off. As it is seen in Fig. 3.4(b) we have 12 coincidences in the central peak, which we compare to the number of coincidences in the one of the side peaks for calculating the two-photon to single photon generation probability. By summing over all events in the first peak at $t_0 = 4.856\,\mu s$ (see Fig. 3.4(c)) we obtain 785 coincidences within 6 min of acquisition. Together with the dark count rates for the two detectors ($13\,s^{-1}$ and $18\,s^{-1}$) we calculate the two-photon to single photon generation probability as 0.33(15) %. This number indicates that we generate anti-bunched single photons while multi-photon processes are suppressed. This allows us to

calculate detection efficiencies of the photons from the ion to the PMT by treating the ion as a single photon source, i.e. in every sequence cycle, one photon is emitted. In Fig. 3.2(c) we show a magnification of the first peak at $t_0 = 4.856\,\mu s$ to analyze the temporal shape of the peak. Since the second order correlation function is an intensity autocorrelation function, we expect to see the autocorrelation between two exponential functions with the same decay constant τ, which gives a two sided exponential function as $e^{-|\frac{t-t_0}{\tau}|}$. We fit the function (red line) to the data and obtain the exponential decay time of $\tau = 15.2(6)$ ns. This number is in agreement to the arrival time of 14.8(7) ns that we determined from the arrival-time histogram measured before the correlation-function measurement. For the high 854 nm power of 6 µW that we use for the generation of photons in both experiments we expect from calculations of the intensity at the ion to see Rabi oscillations in the temporal shape of the photon wave packet (since $\Omega_{854} \gg \Gamma$). Therefore we analyze the temporal shapes in the arrival-time histogram and in the second-order correlation measurement again for a higher temporal resolution, i.e. we choose a time binning of 0.4 ns which should be sufficient to resolve any coherent dynamics. However, any oscillations are hardly visible in the photon wave packet which means that the intensity is not that high as we expect it. Indeed we discovered later that due to daily work and operations around the ion trap table, the very sensitive coupling of the light field through the HALO to the ion is easily distorted. We reasoned that a day-to-day realignment of the mirror before the HALO became necessary for best coupling.

3.1.3. 393 nm photons in a pure quantum state

For the generated photons presented so far the ion was prepared in the $D_{5/2}$ level only through optical pumping by the 850 nm laser, resulting in a statistical mixture of the Zeeman substates in the $D_{5/2}$ level. During the photon generation period, the 854 nm pump beam excited this population to $P_{3/2}$ in a multitude of possible absorption channels, and the population decayed in different emission channels to the $S_{1/2}$ level. This leads to photons in a mixed polarization and frequency state. We avoid the mixed states by optically pumping the population into one of the outermost Zeeman substates in the $D_{5/2}$ level with the 854 nm pump beam from 45° relative to the quantization axis. Now the polarization of this beam is adjusted by inserting a PBS with a half-wave plate (HWP) and quarter-wave plate (QWP) to excite a superposition of σ^+ and π transitions but no σ^- transition. This combination transfers the population to $|D_{5/2}, m_j = +\frac{5}{2}\rangle$. By the rotation of the 854 nm pump-laser wave plates, we are also able to adjust the polarization to σ^- and π which allows us to pump the population to $|D_{5/2}, m_j = -\frac{5}{2}\rangle$.

We find out the proper polarizations in cw excitation condition, i.e. with the 397 nm, 866 nm, 850 nm and 854 nm pump laser switched on, by observing the steady-state fluorescence trace at 397 nm. We change the polarization of the 854 nm pump laser by a rotation of the HWP and QWP until we find two sharp minimum in the 397 nm fluorescence, namely at QWP $= 155.5°$ and QWP $= 245.5°$ for the same HWP angle. In both cases we either

pump to $|D_{5/2}, m_j = +\frac{5}{2}\rangle$ or to $|D_{5/2}, m_j = -\frac{5}{2}\rangle$. The clear assignment of the wave-plate angles to a specific Zeeman substate was done at a later time for the same experimental configuration with the help of the 729 nm laser, enabling the readout of the Zeeman substates. After this measurement we assign QWP $= 155.5°$ to a pumping in $|D_{5/2}, m_j = -\frac{5}{2}\rangle$ and QWP $= 245.5°$ to a pumping in $|D_{5/2}, m_j = +\frac{5}{2}\rangle$.

Experimental sequence

According to the sequence in Fig. 3.5 we see that the 397 nm, 866 nm and 850 nm lasers are used in the sequence in the same way as for photons in a mixed state. In contrast to the procedure so far, we pump with the 854 nm pump beam during the state preparation the population to $|D_{5/2}, m_j = \pm\frac{5}{2}\rangle$ with a state preparation efficiency close to one by extending the state preparation time to 100 µs. For photon generation we now use the 854 nm beam as the trigger.

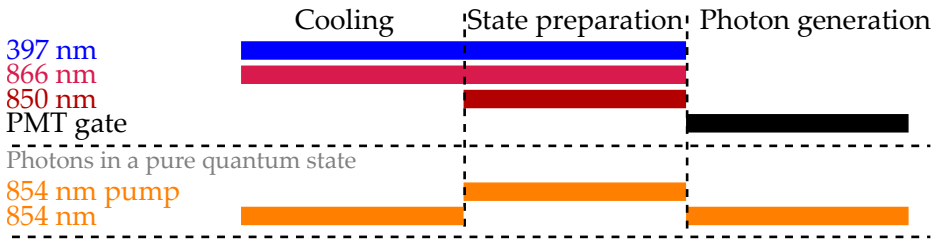

Figure 3.5.: Experimental sequence for generating 393 nm photons in a pure quantum state. The 854 nm pump beam now prepares the state $|D_{5/2}, m_j = \pm\frac{5}{2}\rangle$ while the 854 nm beam is used for photon generation (cf. Fig. 3.1(a)).

With the QWP (854 nm) the polarization of the 854 nm beam is varied between $|R\rangle$ and $|L\rangle$ (and polarizations in between). Thus it is possible to generate photons by an excitation from $|D_{5/2}, m_j = +\frac{5}{2}\rangle$ via $|P_{3/2}, m_j = +\frac{3}{2}\rangle$ to the $|S_{1/2}, m_j = +\frac{1}{2}\rangle$ ground state. The only possible 393 nm decay channel leads to a generation of $|\sigma^+\rangle$ photons which are in a pure quantum state with respect to polarization and frequency. Alternatively, we generate pure $|\sigma^-\rangle$ photons via $|P_{3/2}, m_j = -\frac{3}{2}\rangle$ to $|S_{1/2}, m_j = -\frac{1}{2}\rangle$. Note that due to the branching fraction from $P_{3/2}$, the probability that the ion decays from $P_{3/2}$ back to $D_{5/2}$ is 5.87 %. Through the decay to another Zeeman substate in $D_{5/2}$ the ion can be subsequently re-excited by the 854 nm laser leading to other polarization and frequency components in the emitted photon. This is, however, only the case for excitation with laser light. Since the long-term objective is the entanglement transfer of heralded 854 nm photons from the SPDC source [46], this effect vanishes through the absorption of single photons, where re-excitation is not possible since no second photon is available.

393 nm photons in a pure polarization state

Fig. 3.6(a) displays the depopulation rate $\frac{1}{\tau_{\mathrm{ph}}}$ as the inverse of the arrival time τ_{ph} which is plotted for different QWP (854 nm) angles. For each polarization we take an arrival-time histogram of the scattered 393 nm photons and determine the $\frac{1}{e}$ arrival time. Before photon generation, we choose the settings of the 854 nm pump beam such that we pump the population to $|\mathrm{D}_{5/2}, m_j = -\frac{5}{2}\rangle$.

The clean preparation of this single Zeeman substate is shown by changing the polarization of the 854 nm beam with the rotation of the QWP (854 nm). Since the 854 nm laser is sent in on quantization axis, we depopulate $|\mathrm{D}_{5/2}, m_j = -\frac{5}{2}\rangle$ with right-circularly polarized light $|R\rangle$ (corresponding to a $|\sigma^+\rangle$ transition) at a QWP (854 nm) angle of 45°. In contrast, for the angle at 135°, the left circularly polarized light $|L\rangle$ (corresponding to a $|\sigma^-\rangle$ transition) can not be absorbed anymore. The sinusoidal fit to the data yields a visibility close to unity and confirms that the population is pumped into the outermost Zeeman substate $|\mathrm{D}_{5/2}, m_j = -\frac{5}{2}\rangle$. In Fig. 3.6(b) the polarization of the emitted 393 nm photons is verified

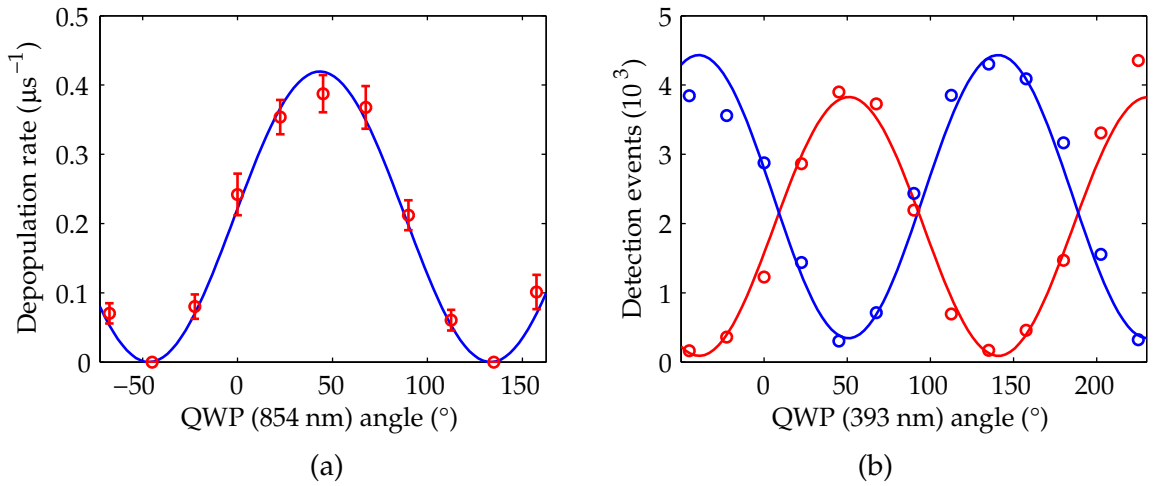

Figure 3.6.: (a) Depopulation rate $R_{\mathrm{D}\to\mathrm{S}} = \frac{1}{\tau_{\mathrm{ph}}}$ of the population in $\mathrm{D}_{5/2}$ showing a sinusoidal behavior under variation of the angle of QWP (854 nm). (b) Number of detection events within the emitted 393 nm photonic wave packets for a measurement time of 1 min with a repetition rate of 9.75 kHz. For two different initial Zeeman substates $|\mathrm{D}_{5/2}, m_j = -\frac{5}{2}\rangle$ (red data) and $|\mathrm{D}_{5/2}, m_j = +\frac{5}{2}\rangle$ (blue data) the QWP (393 nm) angle is changed. The error bars are smaller than the size of the symbols.

by measuring the number of photon detection events within the photonic wave packet for different QWP (393 nm) angles in combination with a PBS (see Fig. 3.1) that both are placed behind HALO 2. For the first set of measured arrival-time distributions (red data in Fig. 3.6(b)) we pump into $|\mathrm{D}_{5/2}, m_j = -\frac{5}{2}\rangle$ and set the QWP (854 nm) angle to 45°. Thus we generate $|L\rangle$ ($|\sigma^-\rangle$) 393 nm photons which are transformed to a linear polarization with the

QWP (393 nm). Depending on the angle of the QWP (393 nm) the photons are transmitted or reflected by the PBS. Analogously, we perform the measurement with optical pumping to $|D_{5/2}, m_j = +\frac{5}{2}\rangle$. With the QWP (854 nm) angle at 135° we now generate 393 nm $|R\rangle$ ($|\sigma^+\rangle$) photons which are transformed to a linear polarization as shown with the blue data. From the fit, we infer a visibility of 95(8) % (red curve) and 85(10) % (blue curve), respectively. The reduced visibility in both cases is mainly attributed to the QWP (393 nm) which is designed for 397 nm. This also explains the deviations of the blue data points from the fitted curve. A minor contribution to the reduction in visibility might be the introduced ellipticity through the mirror behind HALO 2, which would affect a reduction in visibility, too. Nevertheless, the high values for the visibility confirm the high degree of circular polarization of the emitted photons.

393 nm photon with Rabi oscillations

Finally we want to see Rabi oscillations in the arrival-time distribution of the emitted photons. Since we need a high 854 nm intensity at the ion we first realigned the position of HALO 1 with respect to the ion. In order to achieve the highest absorption strength on the $D_{5/2}$ to $P_{3/2}$ transition it is favorable to prepare the ion in one of the outermost Zeeman substates $|D_{5/2}, m_j = \pm\frac{5}{2}\rangle$. From there the 854 nm transition offers the highest Clebsch-Gordan coefficients (see Fig. 2.7). We decide to prepare $|D_{5/2}, m_j = -\frac{5}{2}\rangle$ by setting the waveplate accordingly and set the QWP (854 nm) to 45° to absorb $|\sigma^+\rangle$ photons. For the 393 nm photon generation we use the sequence from Fig. 3.5 with a repetition rate of 9.75 kHz. For a total measurement time of 320 s and for a 854 nm laser power of 3.1 µW sent through the HALO, we record the arrival-time histogram which is presented in Fig. 3.7. The envelope

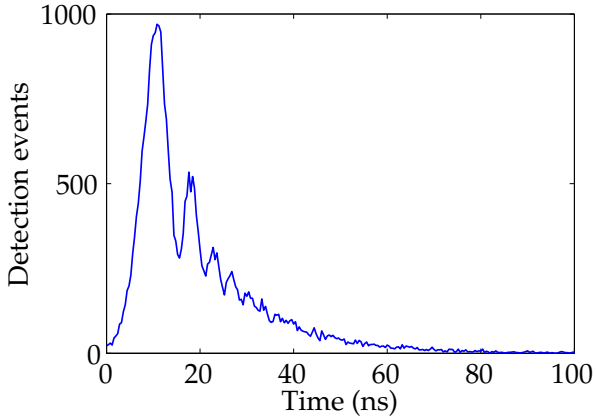

Figure 3.7.: Arrival time distribution of a 393 nm photon for strong 854 nm laser excitation $\Omega_{854} \gg \Gamma_{P_{3/2}}$ where Rabi oscillations becomes visible. The total measurement time is 320 s with a repetition rate of 9.75 kHz. The bin size is 0.4 ns.

of the photon has a $\frac{1}{e}$ decay time of $\sim$ 14 ns and is modulated with Rabi oscillations with a

period of ~ 5 ns. The visibility of the modulation is low and the modulation period is not constant over the wave packet. Simulations with the Bloch equation program confirm the low visibility if the population is not completely pumped to the outermost Zeeman sublevel such that population is also in $|D_{5/2}, m_j = -\frac{3}{2}\rangle$. Perfect optical pumping has a sharp condition, i.e. finding the proper polarization with the waveplate rotation is extremely sensitive to any changes of the rotation mount ($< 0.5°$). When rotating the mount to the proper angle which was necessary before the measurement, there was probably a slight deviation from the angle left that caused the optimum polarization to change such that perfect pumping to the outermost Zeeman substate alone is not possible anymore. Once the population is distributed over more than one Zeeman substate it is transferred via different channels to $S_{1/2}$. These channels have different oscillator strength which means that the Rabi frequencies are different. Together with a non perfect σ^+ polarized 854 nm photon which is absorbed we obtain a mixture of Rabi frequencies explaining the modulation whose frequency is not constant over the wave packet.

Single-photon detection efficiencies

The evaluation of detection efficiencies is done by summing over all detection events within the measured wave packet and divide the number by the total amount of repetitions for a certain acquisition time, as given in Eq. (2.52). The detection efficiencies of 393 nm photons in a mixed polarization state are 5.03(3) ‰ for HALO 1 and 7.90(4) ‰ for HALO 2. Together with the PMT detection efficiency of 28 % and the HALO collection efficiency of 4.17 % we calculate the corresponding multi-mode coupling efficiency of 43 % and 67 %, respectively.

For comparing to the overall detection efficiency between photons in a mixed and pure quantum state we collect photons from both HALOs to the same time. For the mixed quantum state the measurement yields a detection efficiency of $\eta = 1.241(6)$ %. This situation changes if we pump the population into one of the two outermost Zeeman substates. Then we generate photons in a nearly pure quantum state which are σ polarized. The detection efficiency we calculate from both HALOs is enhanced to $\eta_\sigma = 1.71(3)$ %. The ratio between these two values is

$$\left(\frac{\eta}{\eta_\sigma}\right)_{\text{exp}} = 0.72(1). \tag{3.2}$$

It is explained by calculating the amount of light which is collected by the two HALOs (see Fig. 3.1(a)) along the quantization axis, presented in the following. The emission probability of σ and π light from Eq. (2.72) and (2.73) is

$$\mathrm{d}P_\pi \propto \sin^2(\theta_k)\,\mathrm{d}\Omega \tag{3.3}$$

$$\mathrm{d}P_\sigma \propto \tfrac{1}{2}(1 + \cos^2(\theta_k))\,\mathrm{d}\Omega \tag{3.4}$$

with the solid angle $\mathrm{d}\Omega$ which is covered by each HALO. As the focus of HALO 2 is aligned to the ion for an efficient collection of 397 nm photons, the light cone of the HALO is well

determined with a half opening angle of $\theta = 23.6^\circ$ corresponding to a total collection efficiency of 4.17 % and is fully described by

$$\Omega = \int_0^{2\pi} \int_0^{23.6^\circ} \sin\theta_k \, \mathrm{d}\theta_k \, \mathrm{d}\phi_k. \tag{3.5}$$

Integrating over the opening angle leads to

$$P_\pi \propto \int_0^{2\pi} \int_0^{23.6^\circ} \sin^2(\theta_k) \sin(\theta_k) \, \mathrm{d}\theta_k \, \mathrm{d}\phi_k = \tfrac{8\pi}{3} \cdot 0.51\,\%, \tag{3.6}$$

$$P_\sigma \propto \int_0^{2\pi} \int_0^{23.6^\circ} \tfrac{1}{2}(1 + \cos^2(\theta_k)) \sin(\theta_k) \, \mathrm{d}\theta_k \, \mathrm{d}\phi_k = \tfrac{8\pi}{3} \cdot 6\,\% \tag{3.7}$$

which shows that HALO 2 collects 0.51 % of the π light which is emitted predominantly perpendicular to the quantization axis. The amount of σ light is 6 %.

The focus of HALO 1 is aligned for a wavelength of 854 nm which means that the back focal length, given as the distance from the closest lens to the ion is $f_{\mathrm{bf},854} \sim 15$ mm (as it is given for 866 nm in [27]). Due to normal dispersion the focus for 393 nm lies now between the HALO and the position of the ion, i.e. at the back focal length for 397 nm of $f_{\mathrm{bf},393} \sim 13.7$ mm. With the diameter d of the light at the closest lens, we can formulate the opening angle θ for 393 nm

$$\sin\theta_{393} = \frac{d/2}{f_{\mathrm{bf},393}} \tag{3.8}$$

which should be 23.6°. If we assume that d is the same when collecting 393 nm light for a position of HALO 1 with $f_{\mathrm{bf},854}$ we can calculate the new opening angle as

$$\sin\theta'_{393} = \frac{f_{\mathrm{bf},393}}{f_{\mathrm{bf},854}} \sin\theta_{393} \tag{3.9}$$

resulting in a slightly smaller value of $\theta'_{393} = 21.3^\circ$. We can repeat the calculations from Eq. (3.6) and Eq. (3.7) and obtain the new collection efficiencies[2] of $P_\pi = \frac{8\pi}{3} \cdot 0.34\,\%$ and $P_\sigma = \frac{8\pi}{3} \cdot 4.95\,\%$. Assuming an equal population distribution in all Zeeman substates in $D_{5/2}$ and through 854 nm excitation the equal distribution in $P_{3/2}$, the probability to scatter σ photons (i.e. on $\Delta m \neq 0$ transitions) is $\frac{2}{3}$ whereas the probability for π photons (i.e. on $\Delta m = 0$ transitions) is $\frac{1}{3}$ (see Fig. 2.7). Thus the theoretical value for the ratio between the mixture and the clean polarization for a collection with both HALOs is

$$\left(\frac{\eta}{\eta_\sigma}\right)_{\mathrm{theo}} = \frac{10.95\,\% \cdot \frac{2}{3} + 0.84\,\% \cdot \frac{1}{3}}{10.95\,\%} = 0.693. \tag{3.10}$$

This value is very close to the measured ratio in Eq. (3.2). We see that the detection efficiency is higher for photons with pure σ polarization instead of a mixture of σ and π photons. The remaining deviation is explained by the fact that the population in $D_{5/2}$ is not

[2] Note that these calculations are done for the collection of π and σ light which is coupled into a multi-mode fiber. For single-mode fiber coupling, π photons are not coupled if they are collected along the quantization axis. This effect is discussed in more detail in Sec. 3.2.3

equally distributed between the six Zeeman substates. With the 18-level Bloch-equation program we see that the population distribution in $D_{5/2}$ is not equal if we use typical values of polarization and detunings of the involved lasers, i.e. 397 nm, 866 nm and 850 nm. Due to the enhanced detection efficiency with two HALOs of $\eta_\sigma = 1.71(3)\,\%$ and a repetition rate of 9.36 kHz, we have a rate of multi-mode fiber coupled photons of 571(23) s^{-1} which is more than with ion-based cavity experiments, e.g. 95 s^{-1} in [51].

3.1.4. Frequency spectrum of 393 nm photons

Protocols for converting quantum information from an atomic state into a photonic state and vice versa need the states of the photons to be pure, i.e. the photons should ideally carry single polarizations and frequencies. For the description of the frequency spectrum of single photons one has to keep in mind that the temporal shape of the photon is described as a wave packet through repeated measurements which has a temporal width determined by the $\frac{1}{e}$ arrival time. If the photon is fully coherent according to its temporal and spectral properties, than the envelope function of the wave packet is said to be Fourier-limited. The latter means that the spectral shape and width of the photonic wave packet is the Fourier transform of the temporal shape. The universal time-bandwidth product known from signal theory is expressed by the following inequality [104]

$$\Delta t \cdot \Delta\omega \geq \tfrac{1}{2}. \tag{3.11}$$

The minimum value of 0.5 is only reached if the envelope function has a Gaussian pulse shape and the product is calculated by the temporal and spectral standard deviations Δt and $\Delta\omega$.

For single photons the derivation of the (Fourier-limited) time-bandwidth product is more challenging, since the full description of single photons needs the quantization of the electromagnetic field represented by quantum states of light known as the number (or Fock) states $|n\rangle$ [105]. In this representation the expectation value of the electric field gives $\langle n|\hat{E}|n\rangle = 0$ which can not be explained classically. It means that any phase in the electric field amplitude is undefined, whereas phase changes within single-photon wave packets can have observable effects [106]. However, the expectation value of $\langle n|\hat{E}^2|n\rangle \neq 0$ shows that the electric field intensity is defined, corresponding to the measured quantity in the experiment.

In contrast to the quantized description of the photon we can assign the temporal intensity distribution $I(t) \propto |E(t)|^2$, i.e. the single-photon wave packet, to the temporal probability distribution $p(t)$ of the photon that we measure as the photon arrival-time distribution. The probability distribution is normalized as $\int_{-\infty}^{\infty} p(t)dt = 1$ and follows as the intensity distribution an exponential decay

$$p(t) = \tfrac{1}{\tau} e^{-\frac{t}{\tau}} \cdot \Theta(t). \tag{3.12}$$

It allows us to formulate the electric field as the square root of $p(t)$ (in corresponding units) as

$$E(t) = \frac{1}{\sqrt{\tau}} e^{-\frac{t}{2\tau}} \cdot \Theta(t) \cdot e^{i\phi(t)}, \tag{3.13}$$

where $\Theta(t)$ is the Heaviside function and $\phi(t) = \phi_0 + \omega_0 t$ is the phase of the electric field with the carrier frequency ω_0, assuming that nonlinear phase changes are not present. We note that τ is the $\frac{1}{e}$ decay time of the intensity wave packet for a photon which is Fourier-limited. The frequency spectrum is given by the Fourier-transform of $E(t)$ as

$$\mathcal{FT}(E(t)) = \int_{-\infty}^{\infty} e^{-i\omega t} E(t) dt \tag{3.14}$$

which is separated by the inverse of the convolution theorem to

$$= e^{i\phi_0} \left(\int_{-\infty}^{\infty} \frac{1}{\sqrt{\tau}} e^{-i\omega t} e^{-\frac{t}{2\tau}} \cdot \Theta(t) dt * \int_{-\infty}^{\infty} e^{-i\omega t} e^{i\omega_0 t} dt \right) \tag{3.15}$$

$$= e^{i\phi_0} \left(\frac{1}{2\tau} \frac{2\tau}{2i\omega\tau + 1} * 2\pi\, \delta(\omega - \omega_0) \right). \tag{3.16}$$

After the convolution we obtain

$$E(\omega) = e^{i\phi_0} 4\pi \sqrt{\tau} \frac{1}{2i(\omega - \omega_0)\tau + 1}. \tag{3.17}$$

From Eq. (3.17) we see that the assumption of a linear phase variation $\phi(t)$ in the temporal domain only leads to a shift of the carrier frequency but not to any spectral broadening in the electric field amplitude. The spectral intensity distribution $I(\omega) \propto |E(\omega)|^2$ is assigned to the spectral probability distribution $p(\omega)$ and with the normalization $\int_{-\infty}^{\infty} p(\omega) d\omega = 1$ we obtain

$$p(\omega) = \frac{2\tau}{\pi} \cdot \frac{1}{4(\omega - \omega_0)^2 \tau^2 + 1} \tag{3.18}$$

which has a Lorentzian shape. From the arrival-time distributions we determine the $\frac{1}{e}$ decay times which gives $\Delta t_{1/e} = \tau$ for the Fourier limited case. The spectral component of interest is the full width at half maximum of the Lorentzian which is $\Delta\omega_{\mathrm{FWHM}} = \frac{1}{\tau}$. Thus the Fourier-limit condition for our pulse shapes, i.e. the minimal product between the decay time of the photonic wave packet $\Delta t_{1/e} = \tau$ and the full width at half maximum of the Lorentzian shaped frequency spectrum $\Delta\omega_{\mathrm{FWHM}} = \gamma_{\mathrm{ph}}$ reads

$$\tau \cdot \gamma_{\mathrm{ph}} = 1. \tag{3.19}$$

Next, we have to analyze how the branching ratio in $P_{3/2}$ affects this time-bandwidth product.

Time-bandwidth product of single 393 nm photons

The decoherence process during scattering is the decay back into various $D_{5/2}$ Zeeman substates from which partial quantum information on the atom-photon system is lost. The generation of 393 nm photons, i.e. the decay from $P_{3/2}$ to $S_{1/2}$ is accompanied by the decay from $P_{3/2}$ to $D_{3/2}$ which we neglect since the branching fraction is only $6.6 \cdot 10^{-3}$. The total amount of incoherence is then given by the probability for a parasitic decay from $P_{3/2}$ back to $D_{5/2}$ upon a decay from $P_{3/2}$ to $S_{1/2}$, i.e. by the mean number of scattered 854 nm photons $\bar{n}_{854}$ for an excitation attempt, which is given by the ratio of the Einstein coefficients

$$\bar{n}_{854} = \frac{A_{854}}{A_{393}} = 0.0628. \tag{3.20}$$

As explained in detail in the Ph.D. thesis of C. Kurz [107] the amount of incoherence of 6.28 % limits the time-bandwidth product to

$$\tau_{\mathrm{ph}} \cdot \gamma_{\mathrm{ph}} = 1.0628, \tag{3.21}$$

where $\tau_{\mathrm{ph}} = \tau(\bar{n}_{854} + 1)$. It is important to note, that τ_{ph} is the $\frac{1}{e}$ decay time which we have determined from the wave packets shown in Fig. 3.3. We see that the small amount of incoherence introduces a temporal retardation in the 393 nm photon emission probability due to unwanted (parasitic) photon emissions at 854 nm. Equation (3.21) shows that the generated 393 nm photons are close to the Fourier limit given in Eq. (3.19). Furthermore it highlights that we are able to fully taylor the spectral and temporal shape as well as the frequency of the photons by the detuning and Rabi frequency of the 854 nm laser. Taking Eq. (3.21) we calculate the spectral width of the emitted photons presented in Fig. 3.3 as

$$\Delta\nu_{\mathrm{ph}} = \frac{1.0628}{2\pi\,\tau_{\mathrm{ph}}} = \{520...76\}\,\mathrm{kHz} \text{ for } \tau_{\mathrm{ph}} = \{0.33...2.23\}\mu\mathrm{s}. \tag{3.22}$$

From Eq. (3.22) we see that the spectral widths of the photons are small compared to the atomic transition linewidth. This imposes a high resolution, i.e. a narrow linewidth of less than 1 MHz to the analysis cavity. Alternatively, the temporal width of the photons is further reduced through stronger 854 nm laser excitation leading to photons with a broader linewidth.

An important notice to mention is that these values are the spectral widths of the individual photons which are scattered via a single Zeeman substate in $P_{3/2}$ to a single Zeeman substate in $S_{1/2}$. In order to get the full spectrum, one would have to take the various frequency components into account, corresponding to all involved Zeeman transitions from $P_{3/2}$ to $S_{1/2}$.

3.2. Single 854 nm photons for quantum networks

In the context of the realization of a quantum network between distant single ions or as a prerequisite, the photonic interaction between them, the absorption process has to be investigated with single 854 nm photons that are generated by a single trapped ion. Beside the interconnection of two distant single ions, a future goal is the networking of different quantum systems, e.g. the connections of ions with solid-state based systems. Therefore the different transition frequencies have to be bridged by quantum frequency conversion [108] which was already shown by the conversion from visible photons from quantum dots to the low-loss telecom wavelength for long distance networks. Due to ongoing work for a quantum frequency conversion at 854 nm [109], the opportunity arises to generate single 854 nm photons with the ion, that are converted to the telecom wavelength opening the way for long range interactions in hybrid quantum systems.

For both experimental scenarios we first have to show the controlled emission of single 854 nm photons from a single ion. Thereto we explain in the following the generation of 854 nm photons in a three-photon resonance excitation which leads to a higher transfer rate of the population from the $S_{1/2}$ to the $D_{5/2}$ level compared to the optical pumping case. We show that we control the temporal shape of the photons by the power of the 850 nm laser. In the last part of the chapter we discuss the influence of the $P_{1/2}$ and $P_{3/2}$ branching fractions to the time-bandwidth product of the 854 nm photons which are far away from being at the Fourier limit.

3.2.1. Experimental sequence

The experimental setup, shown in Fig. 3.8(a), is similar to the case for 393 nm photons, except that now 854 nm photons are efficiently collected by HALO 1 which is optimized for this wavelength, and coupled into a 2 m long single-mode fiber (SM fiber) which is connected with an avalanche photodiode (APD). Figure 3.8(b) shows the relevant transitions in the level scheme and the laser excitation scheme is illustrated in Fig. 3.8(c). For triggered generation of single 854 nm photons, the sequence starts with Doppler cooling for 1 µs using laser light at 397 and 866 nm. Subsequently, a third laser at 850 nm wavelength couples the $D_{3/2}$ to the $P_{3/2}$ level, thereby optically pumping the ion to the $D_{5/2}$ level and triggering the emission of a single 854 nm photon. Depending on the temporal length of the photon, the photon-generation period varies between 5 µs and 30 µs. In order to reach generation periods as short as 5 µs we have to optimize the excitation process from $S_{1/2}$ to $P_{3/2}$ which is explained in the following section. The beginning of the 850 nm laser pulse is used as a time stamp for the photon generation. After 1 µs of relaxation phase (not shown in Fig. 3.8 (c)), an 854 nm laser repumps the ion to the $S_{1/2}$ level within 1 µs and concludes the sequence. For continuous generation of 854 nm photons, all four lasers are constantly switched on.

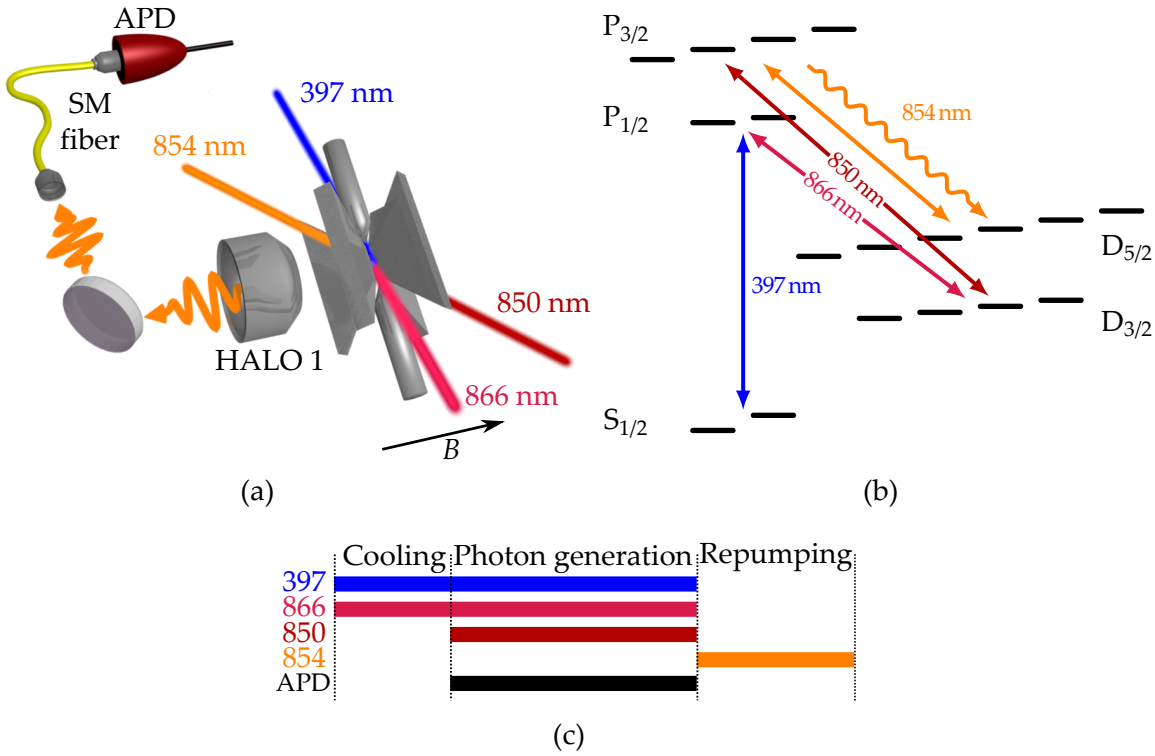

Figure 3.8.: (a) Experimental configuration, (b) relevant transitions in the level scheme and (c) experimental sequence for the generation of 854 nm photons which are collected by HALO 1 and sent to an avalanche photodiode (APD) via a single-mode fiber (SM fiber). See text for details.

3.2.2. Three-photon resonance excitation

The photon-generation part in the sequence (Fig. 3.8(c)) demands an optimization of the three-photon excitation process because of the unfavorable branching ratio of the $P_{1/2}$ level, which has to be taken into account together with the branching ratio of the $P_{3/2}$ level. Both contribute to an incoherent broadening, i.e. stochastical fluctuations in the probability distribution of the emitted 854 nm photon that prolongate the temporal width of the wave packet. This makes it important to optimize the photon generation period to reduce the overall sequence length that leads to a high-rate single-photon source at 854 nm. The way to improve the excitation probability from $S_{1/2}$ to $P_{3/2}$ is to reduce the population in $P_{1/2}$, i.e. the number of scattered 397 nm photons and enhance the population in $P_{3/2}$. This has the effect that the scattering rate of 393 nm photons increases and similarly the number of 854 nm photons. Ideally, the fastest way to pump into the $D_{5/2}$ state would be with a 393 nm laser whose setup is currently integrated in the experiment. The laser is replaced in this thesis by the combination of the 397 nm, 866 nm and 850 nm lasers, which have to

couple coherently.

Optical pumping excitation

We analyze the influence of the $P_{1/2}$ level for the excitation from $S_{1/2}$ to $P_{3/2}$ by comparing the photon scattering rates R_{397} and R_{393} for pure optical pumping. This means that the 866 nm laser is switched off during the excitation from $S_{1/2}$ to $P_{3/2}$. Here we treat the cw-excitation condition, i.e. the 854 nm laser is used to prevent optical pumping to $D_{5/2}$. With the following rate equations, similar to Sec. 2.5.1 with the Einstein coefficients A and the pumping rates r we formulate the equations as

$$\dot{\rho}_{D_{3/2}} = -r_{850}\,\rho_{D_{3/2}} + A_{866}\,\rho_{P_{1/2}} + A_{850}\,\rho_{P_{3/2}} + r_{850}\,\rho_{P_{3/2}} \tag{3.23}$$

$$\dot{\rho}_{P_{3/2}} = r_{850}\,(\rho_{D_{3/2}} - \rho_{P_{3/2}}) + r_{854}\,(\rho_{D_{5/2}} - \rho_{P_{3/2}}) - (A_{393} + A_{850} + A_{854})\,\rho_{P_{3/2}} \tag{3.24}$$

$$\dot{\rho}_{D_{5/2}} = -r_{854}\,\rho_{D_{5/2}} + A_{P_{3/2}-D_{5/2}}\,\rho_{P_{3/2}} + r_{854}\,\rho_{P_{3/2}}. \tag{3.25}$$

For continuous excitation the steady state situation demands $\dot{\rho} = 0$ for all levels. From this we can solve Eq. (3.23) and Eq. (3.25) and derive

$$r_{850} = \frac{A_{866}\,\rho_{P_{1/2}} + A_{850}\,\rho_{P_{3/2}}}{\rho_{D_{3/2}}}, \tag{3.26}$$

$$r_{854} = \frac{A_{854}\,\rho_{P_{3/2}}}{\rho_{D_{5/2}}}, \tag{3.27}$$

which, inserted into Eq. (3.24), yield

$$R_{393} = A_{393}\,\rho_{P_{3/2}} = A_{866}\,\rho_{P_{1/2}}. \tag{3.28}$$

Together with the rate for 397 nm photons $R_{397} = A_{397}\,\rho_{P_{1/2}}$ we finally arrive at the ratio between the two scattering rates for optical pumping of

$$\frac{R_{393}}{R_{397}} = \frac{A_{866}}{A_{397}} = \frac{6.435\,\%}{93.565\,\%} = 0.0688, \tag{3.29}$$

which is close to the branching ratio from $P_{1/2}$ to $D_{3/2}$.

Resonant excitation

In order to improve the ratio given in Eq. (3.29) the three lasers have to couple coherently in such a way that the population in the intermediate levels, i.e. in $P_{1/2}$ and $D_{3/2}$ is decreased. In the following we explain by means of a simple three-level system the principle of such resonant excitations before we use typical experimental parameters to display the dynamics in the ion with the Bloch equations. Finally we present the method how to find the best laser parameters in the experiment.

In the simple picture, we consider a three-level system between $S_{1/2}$, $P_{1/2}$ and $D_{3/2}$ as shown in Fig. 3.9(a). If the detuning of the 397 nm laser[3] is equal to the detuning of the 866 nm laser, i.e. if $\Delta_{397} = \Delta_{866}$, the system decouples from the $P_{1/2}$ level while a coherent superposition state between $S_{1/2}$ and $D_{3/2}$ is generated [75]. The meaning of the decoupling becomes clear in Fig. 3.9(b). For a red detuning of the 397 nm laser of $\Delta_{397} = -5$ MHz we see that the 397 nm fluorescence signal drops at $\Delta_{866} = -5$ MHz, i.e. the $P_{1/2}$ population is decreased. Depending on the phase coherence of the two lasers, the population in $P_{1/2}$ tends to zero for equal detunings such that the coherent superposition state is called a dark state and the resonance dip is called dark resonance. If we choose both detunings to use the dark resonance in the three-photon excitation we reduce the temporal length of the pumping process to the $D_{5/2}$ level once we use the 850 nm laser. A shorter pumping time to $D_{5/2}$ means that the temporal length of the 854 nm photon wave packet is reduced with the consequence that we can increase the repetition rate of the photon generation sequence. Ideally the 850 nm laser couples to the 397 nm and 866 nm laser such that the population

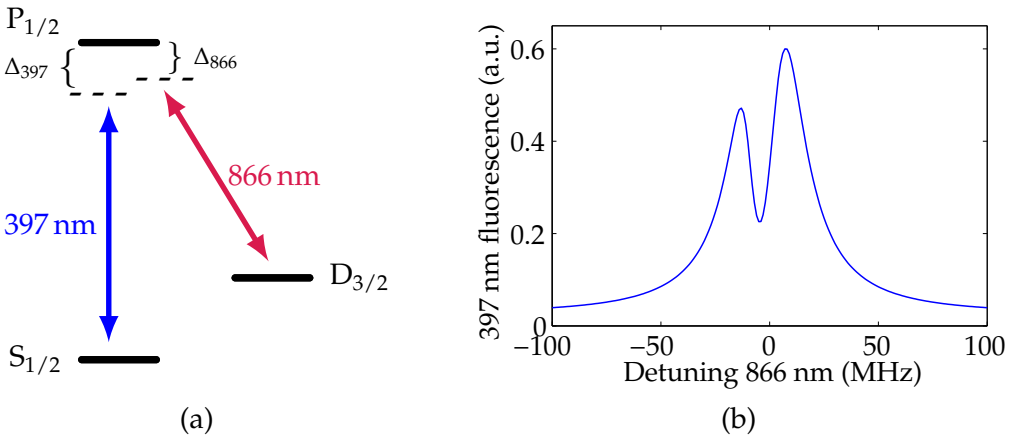

Figure 3.9.: (a) Three-level system with two red-detuned lasers at 397 nm and 866 nm wavelength. (b) Simulated 397 nm fluorescence spectrum for different 866 nm detunings. For equal detunings $\Delta_{397} = \Delta_{866} = -5$ MHz a dip in the fluorescence signal appears which is termed dark resonance.

which is coherently distributed between $S_{1/2}$ and $D_{3/2}$ is transferred coherently to $P_{3/2}$. From there the ion scatters 393 nm photons while the scattering of 397 nm photons is ideally still suppressed. With the resonance condition the population is transferred faster to $P_{3/2}$ from which it decays to the $D_{5/2}$ level, enabling short 854 nm photons. Due to the magnetic field which lifts the degeneracy of the Zeeman sublevels, there are 12 different states and their individual coupling. Depending on the polarization, different Zeeman states couple depending on the allowed transition such that we expect to see a manifold of

[3] The detuning $\Delta_{397} = \omega_{397} - \omega_{SP}$ is given by the difference of the laser frequency ω_{397} and the atomic transition frequency ω_{SP} from $S_{1/2}$ to $P_{1/2}$.

dark resonances in the spectrum. Accordingly we expect to have more than one resonance that we can use to excite quickly to the $P_{3/2}$ level.

In order to analyze to resonance condition in more detail we use in the following the 18-level Bloch equations to show the population dynamics for the three-photon case when using experimental parameters. For this triggered photon generation this means that we initialize the population in the $S_{1/2}$ level before we switch on simultaneously the 397 nm, 866 nm and 850 nm laser until the population is completely pumped into the $D_{5/2}$ level. In the experiment we find a high population in $P_{3/2}$ through high scattering rates at 393 nm by changing iteratively the detunings and intensities of the three lasers, explained in detail below. With the iterative process we end with the high power values (397 nm: 330 µW, 866 nm: 3 mW, 850 nm: 316 µW) that we measured before the vacuum chamber and which are focused to different spot-size diameters. For the simulation we assume the following detunings, including a common laser detuning of $\Delta_{397} = \Delta_{866} = -5$ MHz and the 850 nm laser on resonance $\Delta_{850} = 0$ MHz. We show in Fig. 3.10(a) the temporal evolution of the population for all five levels which are given as the sum over their individual Zeeman substates.

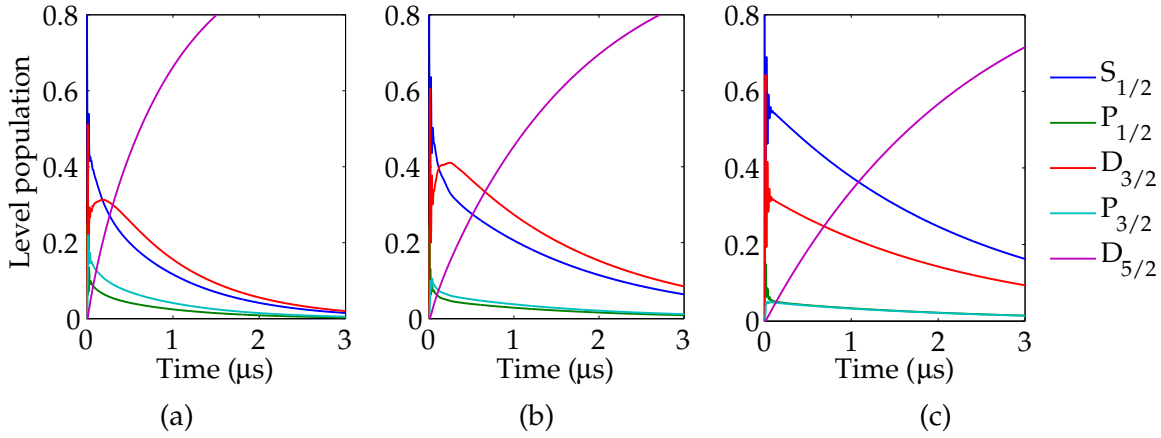

Figure 3.10.: Temporal evolution of the population in five levels (see legend) with the initial population in $S_{1/2}$ and laser excitation with the 397 nm, 866 nm and 850 nm laser. (a) for the experimental parameters, (b) for a lower 850 nm power, (c) for a different 850 nm polarization. The initial population of $S_{1/2}$ (see blue line) actually starts from 1 which is completely transferred to $D_{5/2}$ (see purple line). For a better overview the population is plotted only to 0.8.

Since the 397 nm and 866 nm laser power is high, we observe fast dynamics in $S_{1/2}$ (blue line) and $D_{3/2}$ (red line) after the onset of the laser fields. These are Rabi oscillations that quickly relax into a steady-state from which the population decays without modulation into the $D_{5/2}$ level (purple line). For these conditions we see that the population in $P_{3/2}$ (light-blue line) is higher than the one in $P_{1/2}$ (green line). With these conditions we are

able to generate the fastest 854 nm photons, i.e. the population transfer to the $D_{5/2}$ level is completed within 5 µs. In Fig. 3.10(b) we observe the dynamics for a lower 850 nm laser power ($\sim$ 110 µW). The decrease of the population ratio between $P_{3/2}$ and $P_{1/2}$ is reflected in a lower rate with which population is pumped to $D_{5/2}$ and thus the temporal shape of the 854 nm photon is extended. To see the influence of different polarizations we display in Fig. 3.10(c) the population dynamics for the same parameters as used in (a) except that the 850 nm polarization is changed from horizontal to vertical. The change causes a different coupling of the 850 nm laser to the dark resonances between $S_{1/2}$ and $D_{3/2}$ resulting in a lower population transfer out of $S_{1/2}$ and thus a slower excitation into $P_{3/2}$ and $D_{5/2}$, respectively.

We now analyze the dependance of the ratio between the average number of scattered 393 nm photons (N_{393}) to the average number of 397 nm photons (N_{397}) as a function of the 866 nm detuning. Therefore we take the values for the simulation in Fig. 3.10(a) and calculate the average number of scattered photons by integrating the population in $P_{3/2}$ and $P_{1/2}$ for a total decay time T of the population to the $D_{5/2}$ level as

$$N_{393} = \int_0^T A_{393}\, \rho_{P_{3/2}}(t)\, \mathrm{d}t, \tag{3.30}$$

$$N_{397} = \int_0^T A_{397}\, \rho_{P_{1/2}}(t)\, \mathrm{d}t. \tag{3.31}$$

Fig. 3.11 shows the ratio between the two values for different 866 nm detunings. With the parameters from Fig. 3.10(a), i.e. a 397 nm detuning of -5 MHz and 850 nm power of 316 µW (blue line) we find the maximum ratio for a 866 nm detuning of -7 MHz. For these conditions we see that the ratio between the number of scattered photons is increased to $\sim$ 1.8, compared to the value for pure optical pumping in Eq. (3.29). According to the polarization of the 397 nm and 866 nm laser we expect 4 dark resonances to appear in the maximum of Fig. 3.11 but due to the high laser intensities ($\Omega > \Gamma$) of the 397 nm and 866 nm lasers, the transition is power broadened and the 4 dark resonances appear as one resonance. Furthermore the high intensity of the 850 nm laser also contributes to the power broadening and the shift of the maximum value to -7 MHz. This influence of the 850 nm laser becomes clear, if we repeat the simulation for a lower 850 nm power of 28 µW (red line). We see that the power broadening is strongly reduced and the maximum ratio is at -5 MHz as it should be the case for a dark resonance from $S_{1/2}$ to $D_{3/2}$ as shown in Fig. 3.9 for the three-level system.

In the experiment, the increase of the scattering ratio between 393 nm and 397 nm photons is determined with the following method. In cw-excitation conditions we want to measure the scattering rates R_{393} and R_{397} for the ideal parameters. The separation of both wavelengths with the HALOs demands a precise knowledge of all detection efficiencies which is explained in the following. We take single-photon arrival-time distributions from which we can determine the single-photon detection efficiencies. For HALO 2 we insert the compensation lens to increase 393 nm coupling to the fiber and determine two detection efficiencies. With a single photon sequence for 393 nm we obtain $\eta_{393,\mathrm{w}} = 4.31(3)\,‰$. We

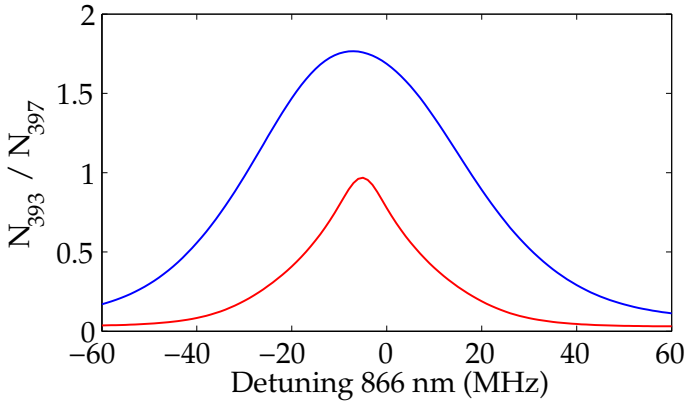

Figure 3.11.: Ratio between the number of 393 nm and 397 nm photons, which are scattered during excitation as presented in Fig. 3.10(a) for different 866 nm detunings. The 397 nm detuning is -5 MHz. The 850 nm power is 316 µW (blue) and 28 µW (red).

change to a 397 nm photon sequence [63] and obtain $\eta_{397,\mathrm{w}} = 0.30(1)\,‰$. The same procedure is repeated for the HALO 1 side but without compensation lens for good 397 nm coupling. We obtain the detection efficiencies $\eta_{393,\mathrm{wo}} = 0.63(1)\,‰$ and $\eta_{397,\mathrm{wo}} = 7.40(4)\,‰$. In cw-excitation conditions we record the PMT count rates C_w and C_wo, i.e. with and without compensation lens, respectively, with both HALOs. From the measurement we formulate the following system of linear equations

$$C_\mathrm{w} = \eta_{393,\mathrm{w}} R_{393} + \eta_{397,\mathrm{w}} R_{397}, \tag{3.32}$$

$$C_\mathrm{wo} = \eta_{393,\mathrm{wo}} R_{393} + \eta_{397,\mathrm{wo}} R_{397}, \tag{3.33}$$

which is solved for the two scattering rates

$$R_{393} = \frac{\eta_{397,\mathrm{wo}} C_\mathrm{w} - \eta_{397,\mathrm{w}} C_\mathrm{wo}}{\eta_{393,\mathrm{w}}\,\eta_{397,\mathrm{wo}} - \eta_{397,\mathrm{w}}\,\eta_{393,\mathrm{wo}}}, \tag{3.34}$$

$$R_{397} = \frac{\eta_{393,\mathrm{w}} C_\mathrm{wo} - \eta_{393,\mathrm{wo}} C_\mathrm{w}}{\eta_{393,\mathrm{w}}\,\eta_{397,\mathrm{wo}} - \eta_{397,\mathrm{w}}\,\eta_{393,\mathrm{wo}}}. \tag{3.35}$$

We implement Eqs. (3.34) and (3.35) in a LabView program to monitor online the improvement of the ratio between the two scattering rates by optimizing the laser parameters, i.e. detuning and intensity of the 397 nm, 866 nm and 850 nm laser.

With the optimized laser parameters that we found in the experiment and that were used in the simulation in Fig. 3.10(a) and the blue curve in Fig. 3.11 we measure on HALO 1 side the count rate $C_\mathrm{wo} = 98.5(3) \cdot 10^3\,\mathrm{s}^{-1}$ and on HALO 2 side $C_\mathrm{w} = 80.2(3) \cdot 10^3\,\mathrm{s}^{-1}$. This leads to the scattering rates $R_{393} = 17.78(14) \cdot 10^6\,\mathrm{s}^{-1}$ and $R_{397} = 11.79(8) \cdot 10^6\,\mathrm{s}^{-1}$ and finally to the ratio

$$\frac{R_{393}}{R_{397}} = 1.51(2). \tag{3.36}$$

Compared to optical pumping (see Eq. (3.29)) we enhance the pumping process from $S_{1/2}$ to $P_{3/2}$ by a factor of 22 despite the manifold of Zeeman transitions that complicate the situation. The value in Eq. (3.36) found for cw-excitation condition is close to the maximum value of 1.8 in Fig. 3.11 (blue line) for the triggered photon generation. The difference can be explained by a coupling of the 854 nm laser in cw condition to the three-photon resonance, which slightly decreases the population in $P_{3/2}$ and thus the number of scattered 393 nm photons. The quality of the coherent excitation is also a function of the phase coherence between the three lasers. Since the lasers are individually frequency locked to their corresponding transfer cavities, the ratio given in Eq. (3.36) might be already limited through the corresponding laser linewidths. A higher ratio would be feasible if, as explained in Sec. 7.3, the lasers would be phase-locked to a common reference, e.g. the frequency comb.

With such optimized parameters we reach in cw condition detected photon rates of 854 nm photons up to $4500(67)\,\mathrm{s}^{-1}$. With the quantum efficiency of the APD of $\eta_{\mathrm{APD}} = 24(5)\,\%$, this corresponds to a single-mode fiber coupled rate of $19(4)\cdot 10^3\,\mathrm{s}^{-1}$.

3.2.3. Single-photon arrival-time distributions

In order to characterize the 854 nm single-photon source from the ion, we excite the ion with the optimized parameters described above, but without the 854 nm beam during the photon generation, to generate triggered single photons in sequence mode, shown in Fig. 3.8(c). The photons are collected in a single-mode fiber, their arrival times are recorded and correlated with respect to the onset of the 850 nm laser pulse that triggers the emission.

Fig. 3.12(a) displays the arrival-time distributions, i.e. the shapes of the respective single-photon wave packets, for power values of the 850 nm laser ranging from 20 µW up to 316 µW. The variation of the 850 nm laser power allows us to control the wave packet duration τ_{ph} between 0.834(2) and 5.89(6) µs. For the shortest measured photons of $\tau_{\mathrm{ph}} = 545$ ns we could reduce the photon generation period to 5 µs which results in the highest repetition rate of 125 kHz and thus in the highest photon generation rate into a single spatial (fiber) mode of $R_{854,\mathrm{triggered}} = 3.0(6)\cdot 10^3\,\mathrm{s}^{-1}$.

Fig. 3.12(b) shows the inverse of the photon durations as a function of the 850 nm laser power together with a numerical solution of the 18-level Bloch equations, which includes the experimental laser parameters. With the Bloch equations, the sequence from Fig. 3.8(c) is simulated and the $\frac{1}{e}$ decay time of the population in $P_{3/2}$ during the photon-generation period is calculated. The inverse of this decay time is plotted for the experimental parameters used for Fig. 3.10(a). With a slight variation of the fit parameters (397 nm power and the 850 nm polarization) we find the simulation in good agreement with the inverse of the measured photon lengths. From the solid line we see a close to linear behavior for low 850 nm laser power, similar to the weak excitation regime in the case of 393 nm photons (see Fig. 3.3(b)), which runs asymptotically to a maximum value of $1.41\cdot 10^6\,\mathrm{s}^{-1}$ for a laser power of 600 µW. Due to a saturation of the 850 nm transition, we expect the maximum rate of 854 nm photons in that regime which is explained in Sec. 3.2.4.

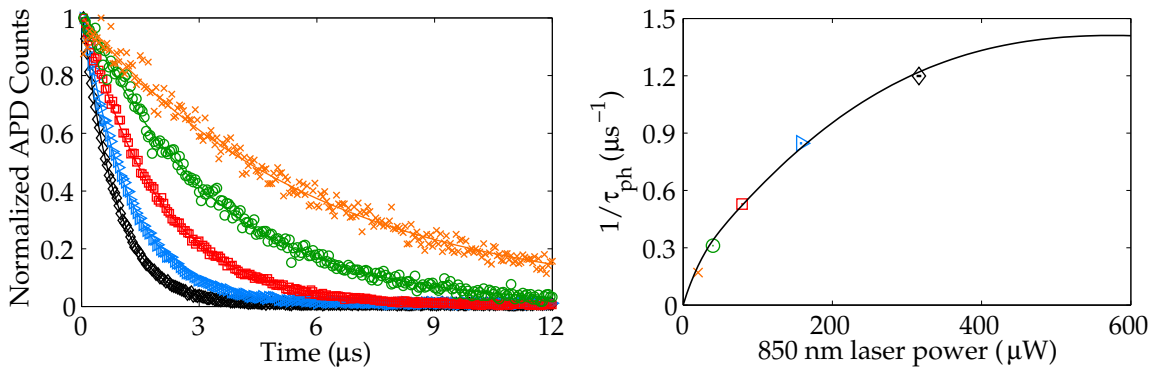

Figure 3.12.: (a) Arrival-time distribution of 854 nm photons for different powers of the 850 nm laser. The arrival time τ_{ph} is determined by an exponential fit to the data (solid lines) as $\tau_{ph} = \{0.834(2), 1.181(4), 1.891(7), 3.22(2), 5.89(6)\}$ µs, from the shortest (black diamonds) to the longest (orange crosses) wave packet. Each curve corresponds to 15 min of data acquisition at a repetition rate of 55.5 kHz (first three curves) or 30 kHz (last two curves). (b) Inverse wave packet duration $\frac{1}{\tau_{ph}}$ as a function of the 850 nm laser power. The solid line is calculated by numerically solving the optical Bloch equations using experimental parameters. The fit parameters are the 397 nm power and the 850 nm polarization.

Single-photon detection efficiencies

In cw excitation, the measured rate of 393 nm photons of $R_{393} = 17.78(14) \cdot 10^6\,\mathrm{s}^{-1}$ determines the rate of scattered 854 nm photons by the relation

$$R_{854} = \frac{A_{854}}{A_{393}} R_{393} = \frac{5.87\,\%}{93.47\,\%} R_{393} = 1.12(1) \cdot 10^6\,\mathrm{s}^{-1}. \tag{3.37}$$

The measured countrate of 854 nm photons with the APD of $4100(64)\,\mathrm{s}^{-1}$ corresponds to a detection efficiency of

$$\eta_{854,\mathrm{cw}} = 3.66(7)\ ‰. \tag{3.38}$$

For triggered photon excitation, we determine the detection efficiencies similarly as for 393 nm photons (see Sec. 3.1.2). For the same experimental parameters as for the continuous excitation, we find a detection efficiency of

$$\eta_{854,\mathrm{triggered}} = 5.03(1)\ ‰. \tag{3.39}$$

The discrepancy between the two detection efficiencies is explained by the fact that the 854 nm laser with a power of 46 µW, is switched on for the cw excitation. For this 854 nm power we expect the Rabi frequency of the 854 nm transition to be in a regime where stimulated emission is not completely negligible. This leads to a preferred emission of photons

into the direction of the laser. Thus, the detection efficiency value decreases for cw excitation since the laser is sent in from 45° with respect to the HALO axis, while the photons are collected on HALO axis. We also expect a minor contribution to the difference by the 854 nm laser that changes with its polarization and detuning the population in $P_{3/2}$ such that in steady state the probability to scatter π photons is slightly increased for the cw excitation condition.

Characterizing the quality of a single ion as a single-photon source with the detection efficiency of the photons always has the disadvantage that it includes the quantum efficiency η_{qe} of the detectors, that are quite different depending on the measured wavelength. A better value to mention when comparing experimental protocols for ion-based quantum networks is the collection efficiency η_{coll} and (single-mode) fiber-coupling efficiency η_{fc} [110, 46]. The relation between all values is

$$\eta_{854,\mathrm{triggered}} = \eta_{\mathrm{coll}} \cdot \eta_{\mathrm{fc}} \cdot \eta_{\mathrm{qe}}. \tag{3.40}$$

With the quantum efficiency of the APD of $\eta_{\mathrm{qe}} = 24(5)\,\%$, we obtain a mode-matching efficiency of single photons into a single-mode fiber of

$$\eta_{\mathrm{SM}} = \frac{\eta_{854,\mathrm{triggered}}}{\eta_{\mathrm{qe}}} = \eta_{\mathrm{coll}} \cdot \eta_{\mathrm{fc}} = 2.1(4)\,\%. \tag{3.41}$$

Considering the case that during excitation to $P_{3/2}$ the population is equally distributed, the collection efficiencies for σ- and π photons are weighted by their decay distribution and the amount of the dipole emission pattern covered by the HALO to

$$\eta_{\mathrm{coll}} = 6\,\% \cdot \tfrac{2}{3} + 0.51\,\% \cdot \tfrac{1}{3}. \tag{3.42}$$

Since we use a single-mode fiber, the small amount of π photons that are collected by the HALO and focused to the single-mode fiber interfere destructively at the single-mode fiber. This is explained if the coupling efficiency, i.e. the overlap integral of the emitted field mode for π light with the Gaussian fiber mode, is calculated. For a collection of π light with the HALO along the quantization axis, one finds that the overlap integral is zero [111]. This is why the mode-matching efficiency (Eq. (3.41)) has to be multiplied with $\frac{3}{2}$ for the collection of σ-photons to

$$\eta^{\sigma}_{\mathrm{SM}} = 6\,\% \cdot \eta_{\mathrm{fc}} = 3.2(6)\,\%. \tag{3.43}$$

This finally leads to a single-mode fiber coupling efficiency of single σ photons of $\eta_{\mathrm{fc}} = 53(1)\,\%$.

3.2.4. Frequency spectrum of 854 nm photons

As described in Sec. 3.1.4, the 393 nm photons have a close to Fourier-limit time-bandwidth product which is in contrast to the photons at 854 nm wavelength. Here the 854 nm photons suffer, in their temporal and spectral properties, from the preferred decay of the $P_{3/2}$

to $S_{1/2}$ level before the decay from $P_{3/2}$ to $D_{5/2}$ takes place and an 854 nm photon is generated. This causes a significant incoherent contribution to the time-bandwidth product which shall be discussed in detail in the following.

Incoherent broadening through branching ratio of $P_{3/2}$

Due to the branching fractions of the $P_{3/2}$ level and the resonant three-photon excitation, the situation to describe the spectral width of the 854 nm photons is a more complex one than in the case of 393 nm photons. Ideally, the lasers included in the three-photon excitation process mimic a direct excitation with an 393 nm laser. Once the population is in the $P_{3/2}$ state, there is the probability of 0.66 % for a decay back to the $D_{3/2}$ state at 850 nm. In following this decay is neglected. The main incoherent broadening mechanism when calculating the spectral properties of the 854 nm photons comes from the decay from $P_{3/2}$ back to the $S_{1/2}$ ground state. Analogous to the calculation of the spectral properties of 393 nm photons in Sec. 3.1.4, we start with the mean number of scattered 393 nm photons per excitation cycle

$$\bar{n}_{393} = \frac{A_{393}}{A_{854}} = 15.92. \tag{3.44}$$

The time-bandwidth product, which is ideally $\tau \cdot \gamma_{\mathrm{ph}} = 1$ is far away from this value with

$$\tau_{\mathrm{ph}} \cdot \gamma_{\mathrm{ph}} = 16.92. \tag{3.45}$$

In the limit of a strong three-photon resonance excitation from $S_{1/2}$ to $P_{3/2}$ the population occupation in $P_{3/2}$ tends to 50 % as a transient regime between weak excitation and the strong excitation including Rabi oscillations. Thus, we formulate the maximum rate

$$R_{\mathrm{S}\to\mathrm{D}} = 0.5 \cdot A_{854} = 4.24\,\mu\mathrm{s}^{-1}, \tag{3.46}$$

and the minimum temporal width of the wave packet in analogy to Eq. (3.1) by

$$\tau_{\mathrm{ph,min}} = \frac{16.92}{0.5 \cdot (\Gamma_{\mathrm{P}_{3/2}} - A_{850})} = \frac{1}{R_{\mathrm{S}\to\mathrm{D}}} = 235.8\,\mathrm{ns}. \tag{3.47}$$

The spectral width of the emitted photons presented in Fig. 3.12 is then calculated with Eq. (3.45) as

$$\Delta\nu_{\mathrm{ph}} = \frac{\gamma_{\mathrm{ph}}}{2\pi} = \frac{16.92}{2\pi\,\tau_{\mathrm{ph}}} = \{3.23...0.46\}\,\mathrm{MHz} \text{ for } \tau_{\mathrm{ph}} = \{0.83...5.89\}\mu\mathrm{s}. \tag{3.48}$$

Incoherent broadening through branching ratio of $P_{1/2}$

The description of the frequency spectrum so far incorporates only the incoherent broadening mechanism by the unfavorable branching fraction from $P_{3/2}$ which would be valid if we excited with a 393 nm laser or a perfect three-photon resonance excitation. Since

the three-photon resonance condition is not perfect, i.e. the non-perfect phase coherence between the lasers and the power broadening cause some remaining population of the $P_{1/2}$ level, an additional broadening mechanism has to be taken into account related to the branching fraction of $P_{1/2}$. For the photons shown in Fig. 3.12(a) we want to know the incoherent broadening. Thus we use the fitted experimental parameters from Fig. 3.12(b) to simulate again the ratio between the scattering rates R_{393} and R_{397} as it was done in Fig. 3.11. We find a 866 nm detuning corresponding to a maximum scattering ratio between the scattering rates R_{397} and R_{393} and thus the incoherent broadening factor[4] of

$$\zeta = \frac{R_{397} + R_{393}}{R_{393}} = 1.54. \tag{3.49}$$

The total spectral width of the photonic wave packet is now given by the total amount of spectral broadening due to various decay processes under optimized excitation as

$$\tau_{\mathrm{ph}} \cdot \gamma_{\mathrm{ph}} = 16.92 \cdot 1.54. \tag{3.50}$$

From this equation we evaluate the minimum temporal width for a strong excitation, i.e. for a 850 nm laser power of 600 µW where the inverse of the temporal length in Fig. 3.12(b) saturates. From numerical simulations as Fig. 3.10(a) we read out the maximum population in $P_{3/2}$ for a power of 600 µW to $\sim$ 25 %. With this we formulate the minimum temporal width as

$$\tau_{\mathrm{ph}} = \frac{16.92 \cdot 1.54}{0.25 \cdot (\Gamma_{\mathrm{P}_{3/2}} - A_{850})} = 726\,\mathrm{ns}. \tag{3.51}$$

This lead to the highest rate for a triggered excitation of

$$R_{\mathrm{S}\to\mathrm{D}} = \frac{1}{\tau_{\mathrm{ph}}} = 1.38\,\mu\mathrm{s}^{-1}. \tag{3.52}$$

Comparing this number to the Bloch-equation calculation in Fig. 3.12(b) we see that for higher 850 nm laser powers the inverse of the photon duration asymptotically converges to a value of 1.41 $\mu\mathrm{s}^{-1}$, which is close to the value of Eq. (3.52).

For the measured photon duration $\tau_{\mathrm{ph}} = 834$ ns the spectral broadening then corresponds to a final spectral width of

$$\Delta\nu_{\mathrm{ph}} = \frac{16.92 \cdot 1.54}{2\pi \cdot 834\,\mathrm{ns}} = 4.97\,\mathrm{MHz}. \tag{3.53}$$

If the population is distributed in $P_{3/2}$, the photons are emitted with various frequency components due to the splitting of the $P_{3/2}$ and $D_{5/2}$ Zeeman manifolds. Furthermore, each decay channel is accompanied with three possible transitions (σ^+, σ^- and π) leading to a photonic state which leaves the ion in a mixed state. The different frequency- and polarization components within the photonic wave packet will be discussed in more detail in Sec. 4.2.2, when absorption probabilities of single photons by a single ion are investigated.

[4] If we assume the case for pure optical pumping from $S_{1/2}$ to $P_{3/2}$ without the 866 nm laser, the broadening factor would change to $\zeta = 1 + \frac{R_{397}}{R_{393}} = 15.5$, using Eq. (3.29).

Summary

In this chapter I presented the use of a single trapped ion as a source for single photons at two different wavelengths.

First the generation of single 393 nm photons in a mixed quantum state yielded $7.4(3) \cdot 10^3\,\mathrm{s}^{-1}$ multi-mode fiber-coupled photons with a maximum sequence repetition rate of 230 kHz. The arrival-time distributions manifested the control of the temporal shape of the photons ranging from 325(3) ns to 2.23(1) µs for low 854 nm laser powers between 7 and 0.875 µW. In the low power regime, the expected linear behavior of the scattering rate as a function of the 854 nm power was shown. The single photon character was emphasized by the $g^{(2)}$-function measurement highlighting the antibunching by the low probability for multi-photon emission at zero time delay. With the preparation of the outermost Zeeman substates in $D_{5/2}$ and excitation with circular polarization it became possible to generate photons in a pure quantum state regarding polarization and frequency. The pure photons were generated with a rate up to 9.36 kHz, resulting in $571(23)\,\mathrm{s}^{-1}$ multi-mode fiber coupled photons in a pure quantum state. Their spectro-temporal analysis showed that the time-bandwidth product is close to the Fourier limit, which means that the photons are fully coherent according to their temporal width of the wave packet. The properties make these photons suitable as carriers of quantum information for quantum networking protocols.

The second part of the chapter showed the generation of single 854 nm photons. With a sequence repetition rate of 125 kHz we reached $3.0(6) \cdot 10^3\,\mathrm{s}^{-1}$ single-mode fiber-coupled photons, sufficient to perform photonic interaction measurements between single ions in separate traps as it will be presented in the next chapter. With the variation of the 850 nm laser powers we controlled the temporal shape of the 854 nm photon wave packets from 0.834(2) to 5.89 µs for 850 nm laser power ranging from 316 to 20 µW. The rate with which population is transferred from $S_{1/2}$ to $D_{5/2}$ was simulated for different 850 nm laser powers by the Bloch equation program and fitted to the data. The shortest photons were achieved for a fast excitation from $S_{1/2}$ to $D_{5/2}$ by employing a three-photon resonance condition. We found a resonance condition that increased the ratio between the 393 nm and 397 nm scattering rates by a factor of 22 compared to the optical pumping case. In contrast to the 393 nm photons we saw that the 854 nm photons have a incoherently broadened spectrum which leads to a time-bandwidth product which is far away from being Fourier-limited.

4. Photonic interactions between distant single ions

Quantum networks form the basis for the realizations of integrated quantum computing and quantum communication scenarios in the novel and fascinating field of quantum information processing. The elementary network incorporates nodes where quantum information is stored and processed and photonic quantum channels to transfer quantum information [36].

Single ions are ideal candidates as nodes in quantum networks since they are highly controllable in their internal and motional degrees of freedom and highly isolated from environmental disturbances. The coherent communication between distant single ions requires the controlled emission of photons at one ion, which are transmitted ideally in a pure state to the second ion, stored in a separate trap, where the photonic quantum information is stored and further processed. A major prerequisite for coherent exchange of quantum information between distant single ions is the control of the emission and absorption of single photons by the ion, i.e. the control of the bi-directional atom-photon interface which is studied extensively in our group. The controlled emission of single photons by a single ion at different wavelengths has already been presented in Chapter 3 of this thesis. Concerning experiments investigating the absorption process of single photons by a single atomic ion in free space, our group still presents state of the art results [112], i.e. heralded single photons from a spontaneous parametric down-conversion (SPDC) source at 854 nm which are absorbed by a single ion [64]. In another absorption experiment, the ion has also been used to verify the entanglement of the SPDC photons [82].

In the following sections we present the first experiments in our group that combine our knowledge from controlled emission of single photons from a single ion and absorption experiments from heralded SPDC photons. This will take the experimental status to a higher level towards the establishment of a real quantum network with distant nodes. So far, single ions in two distant traps were used to emit photons that entangle the ions by projective measurements [44]. Alternatively, entanglement between two distant ions would be achieved by directly transferring quantum information between the ions by the emission of photons at one ion and the subsequent absorption at the distant ion, which has not been established yet with single ions. Here we perform an elementary step towards this through the direct photonic interaction between two distant single ions.

Sec. 4.1 shows the first interaction experiment in our group, the direct free-space continuous photon transmission at 393 nm wavelength between two distant single ions. In Sec. 4.2 the 854 nm transition is used to generate photons which are coupled to a single-

mode fiber, acting as transmission channel between the two distant ions. We present the interaction between the two ions in cw and triggered photon transmission mode. The absorption probabilities of ion-generated photons and photons from a highly attenuated laser are compared and analyzed with respect to their spectral distribution and polarization degree of freedom. For triggered interaction measurements we correlate the emission trigger from the *sender* ion with the first 397 nm scattered photon at the *receiver* ion and observe clear coincidences between these two events. The chapter closes with a summary and discussion about general limitations of absorption probabilities from single photons by a single ion for free space coupling the light to the ion with the HALO, as used in our experimental setup.

4.1. Free-space interaction at 393 nm wavelength

After we achieved the controlled generation of single 393 nm photons by a single ion presented in Sec. 3.1 it became obvious to use these photons for the first proof-of-principle photonic interaction measurements that had ever been done in our group. Concerning our experimental goals, 393 nm photons are preferentially used as heralds for a successful quantum-state transfer of 854 nm photons. As shown in Sec. 3.1, we can generate the 393 nm photons in a pure quantum state, allowing the photons to carry quantum information, e.g. encoded in the polarization degree of freedom. One scenario to transfer this quantum information to a distant ion would be the mapping of the photonic quantum information into the distant ion's metastable $D_{5/2}$ level by the absorption of the 393 nm photon and subsequent emission of a 854 nm photon. A simple example in the following shows that this protocol becomes inefficient considering the 393 nm absorption process.

As already pointed out in Sec. 3.1.3, we can generate pure σ^- polarized photons at 393 nm by spontaneous Raman scattering from $|D_{5/2}, m_j = -\frac{5}{2}\rangle$ via $|P_{3/2}, m_j = -\frac{3}{2}\rangle$ to $|S_{1/2}, m_j = -\frac{1}{2}\rangle$ at one ion. If we could prepare a second, separately trapped ion in $|S_{1/2}, m_j = -\frac{1}{2}\rangle$, then the process is not reversible. This means that after the absorption of the σ^- photon via $|P_{3/2}, m_j = -\frac{3}{2}\rangle$ there is a multitude of possible transitions from $|P_{3/2}, m_j = -\frac{3}{2}\rangle$ to $|D_{5/2}, m_j = -\frac{5}{2}\rangle$, $|D_{5/2}, m_j = -\frac{3}{2}\rangle$ and $|D_{5/2}, m_j = -\frac{1}{2}\rangle$, leaving the ion in a mixed atomic state. For superpositions of photon polarizations such as $\frac{1}{\sqrt{2}}(\sigma^- + \sigma^+)$, the mixing of atomic states in $D_{5/2}$ becomes even more complicated, making any mapping process of quantum information between two distant $^{40}Ca^+$ ions very inefficient and not promising for future applications without higher experimental efforts. One way out would be a heralding photon (heralding the absorption) at 854 nm with a certain polarization whose detection projects the ion to a specific Zeeman substate in $D_{5/2}$ which can be readout by the 729 nm laser.

As a proof-of principle experiment for future applications, we applied our knowledge from the controlled generation of 393 nm photons explained in Sec. 3.1 to perform photonic interaction measurement with our double-trap setup.

4.1.1. Experimental setup

The experimental setup comprises our two ion traps separated by a distance of ~ 1 m and shown in Fig. 4.1(a). In the sender trap we generate 393 nm photons in cw mode with the lasers shown in Fig. 4.1(c). The photons are in a mixed state, similar to the generation

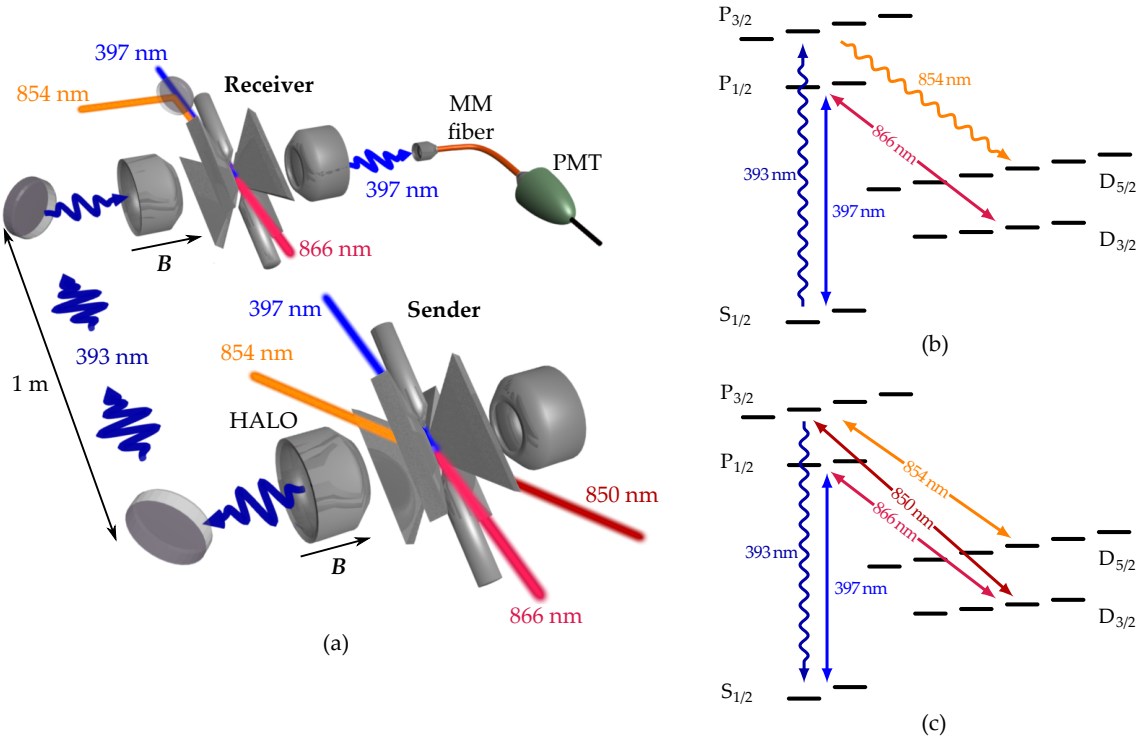

Figure 4.1.: (a) Experimental setup for 393 nm interaction between two single ions separately trapped at one meter distance. The photons are sent free-space from the sender ion to the receiver ion where quantum jumps in the 397 nm fluorescence signal herald the successful absorption of a 393 nm photon. Level scheme and relevant transitions for the (b) receiver ion and for the (c) sender ion. For details see text.

presented in Sec. 3.1.2. In the receiver trap we also load a single ion which is continuously Doppler cooled. The scattered fluorescence photons at 397 nm are collected with one HALO and are guided with a multi-mode (MM) fiber to a photomultiplier tube (PMT) where they are detected. Any successful absorption of a 393 nm photon followed by the decay to $D_{5/2}$ is heralded by a quantum jump from a *bright* to a *dark* state, i.e. by the suppression of the 397 nm fluorescence to the background level (see Fig. 4.1(b)). In the receiver trap, the telescope in front of the HALO and the HALO itself are aligned from previous measurements for an efficient atom-photon coupling at 397 nm wavelength. We use the alignment as is and establish the alignment of the optical path between the two traps by sending a weak 397 nm laser beam from the PMT side through the receiver trap along the

HALO axis. Behind the HALO and telescope on the other side of the receiver ion trap, we use mirrors to redirect the light and overlap it with the optical path for efficient 397 nm coupling at the sender ion trap.

4.1.2. Heralding absorption events: The quantum-jump scheme

Experimental protocols in quantum networks need high success probabilities for faithful quantum-information transfer between distant nodes, given by an efficient collection efficiency of photons at one ion and a high absorption probability at a distant ion. We now present a first estimate about the expected success probability, based on preceding measurements.

In Chapter 3 we have seen that typical cw emission rates of 393 nm photons are on the order of $\sim 10^6\,\mathrm{s}^{-1}$, from which $\sim 1\,\%$ are collected by one HALO. These photons are sent to a second, distant ion, where they are absorbed. From resonant single-photon absorption measurements from a spontaneous parametric down-conversion source at 854 nm, a typical absorption probability conditioned that the ion has decayed via the 393 nm transition to the $S_{1/2}$ ground state after absorption is on the order of $\sim 10^{-4}$. The probability for this event is given by the product of the branching fractions of the $P_{3/2}$ level which are proportional to the corresponding oscillator strengths [27]. If we consider the inverse case, i.e. the absorption of 393 nm photons and the subsequent decay to $D_{5/2}$, then the product of the two branching fractions is identical. Assuming the same value for the condition that the ion has decayed to the $D_{5/2}$ after a 393 nm absorption, we can combine the numbers and obtain an absorption rate of 393 nm photons of $\sim 1\,\mathrm{s}^{-1}$. In the level scheme in Fig. 4.1(b), we see that a 393 nm photon absorption can be detected by the subsequent emission of a 854 nm photon, which would be called a herald for the photon absorption. If we attempted to detect these 854 nm photons with an avalanche photodiode, the detected absorption rate would be reduced to $\sim 5 \cdot 10^{-3}\,\mathrm{s}^{-1}$ according to the typical detection efficiency of 854 nm photons. Since the APD has a typical dark count rate of $10\,\mathrm{s}^{-1}$ it would take days of acquisition time to obtain enough statistics for a decent signal-to-noise ratio.

Here we present an alternative method to detect the absorption event of 393 nm photons which in the original scheme is called the *shelved optical electron amplifier* [113]. The scheme does not rely on the low detection probability of the 854 nm herald but detects the absorption event with high efficiency by monitoring atomic states through quantum jumps. The way how quantum jumps are observed is shown in Fig. 4.2. For that the fluorescence light at 397 nm wavelength is continuously recorded during Doppler cooling. Once an absorption takes place, the ion can randomly decay to the metastable $D_{5/2}$ level which causes a quantum jump from bright to dark. We call this quantum jump a *herald* for the absorption event. The $D_{5/2}$ level has a mean lifetime of 1.168 s [81] during which no 397 nm photons are scattered (Fig. 4.2 (b)). From the $D_{5/2}$ level, the ion spontaneously decays back to the $S_{1/2}$ level and enters the fluorescence cycle again. This is seen by a quantum jump from dark to bright (Fig. 4.2 (c)). Thereafter the ion is sensitive again for absorption of sender photons. By the use of the 397 nm fluorescence light, we have a signal with a high ratio

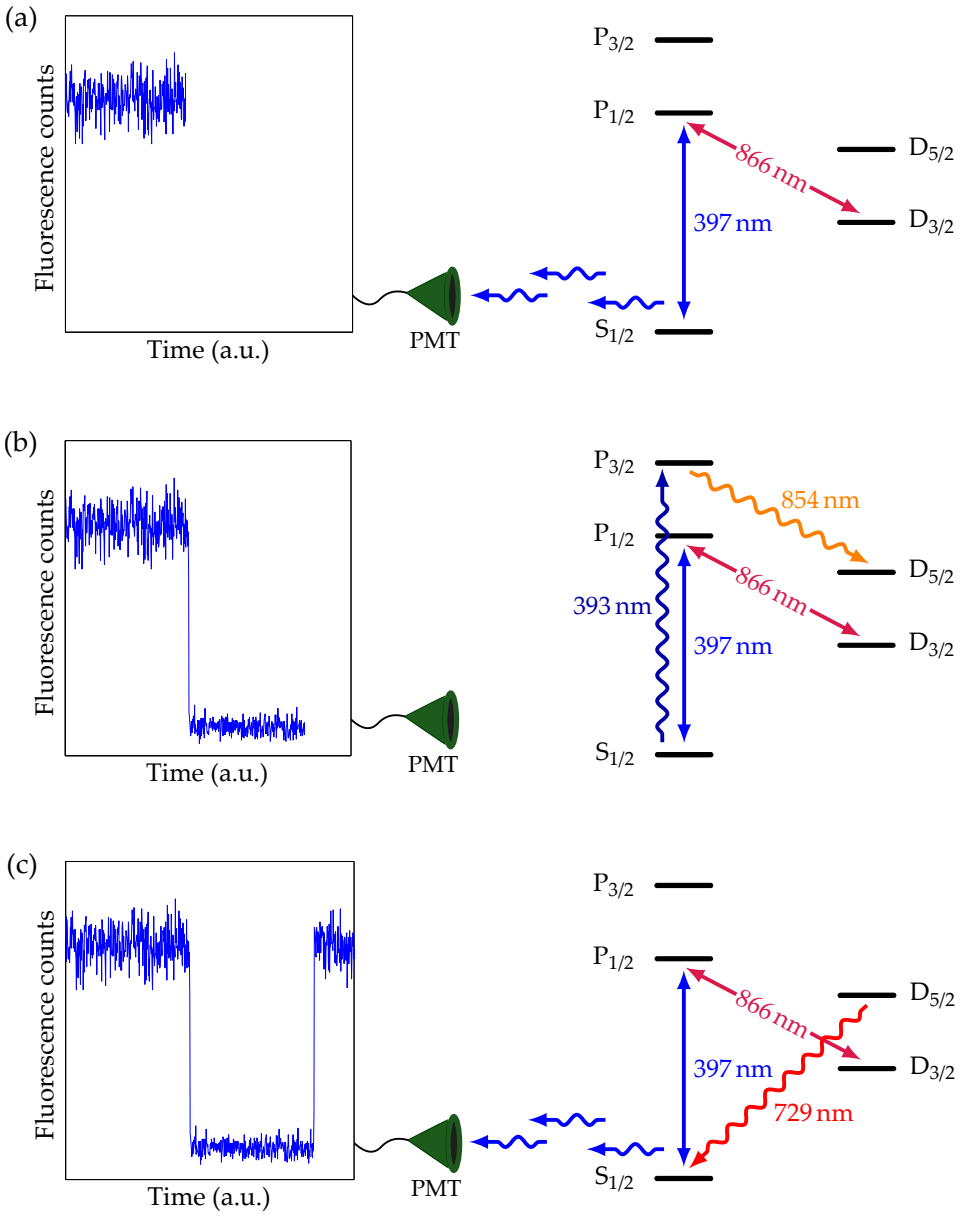

Figure 4.2.: Quantum-jump scheme for heralding the absorption in the receiver trap consisting of three steps: (a) During Doppler cooling the receiver ion, 397 nm fluorescence photons are scattered continuously which are detected by the PMT yielding the fluorescence trace shown on the left hand side. (b) Once a 393 nm photon is absorbed, a quantum jump from the $S_{1/2}$ to the $D_{5/2}$ level causes a cease in the fluorescence from bright to dark. (c) By the spontaneous decay from $D_{5/2}$ to $S_{1/2}$ via the 729 nm transition we get an onset in the fluorescence trace again, making the ion sensitive again for photon absorption.

between the bright and the dark state that is used to detect the absorption event with almost 100 % efficiency. In particular, since there are no other sources of 393 nm light during the measurements, we only see quantum jump events by successful absorption of 393 nm photons from the sender. Quantum jumps induced by collisions with background gas are conceivable but have a very low probability.

4.1.3. Continuous-wave (cw) photon transmission

For the continuous generation of 393 nm photons we have the 397, 866, 850 and 854 nm lasers at the sender trap constantly switched on (see Fig. 4.1 (c)). The photons are collected by the HALO, optimized for 854 nm wavelength, followed by the compensation telescope for 393 nm and are guided with mirrors to the telescope and HALO at the receiver trap, both aligned for 397 nm. There photon absorption is signaled with the quantum-jump scheme. With the PMT we record a fluorescence trace for which a typical example is seen in Fig. 4.3. We show a recorded fluorescence trace for a time of 60 s in time bins of 1 ms. Within this time we record 31 quantum jumps from bright to dark which correspond to successful 393 nm photon absorption events. In principle one could also trigger a quantum jump from bright to dark with a three-photon excitation by the absorption of 850 nm photons that are scattered at the sender ion. Since the HALO at the sender trap is aligned for collecting 854 nm light and the compensation telescope is built up for a highly efficient collection of blue light (393 nm and 397 nm), the probability to transmit 850 nm photons to the receiver ion is low and can be neglected compared to 393 nm photons. In the time trace we see that

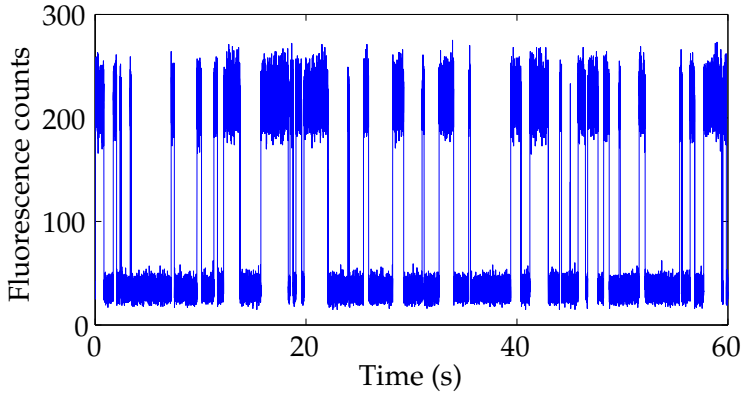

Figure 4.3.: 397 nm fluorescence time trace from the receiver ion for a time of 60 s and 1 ms time bin. The trace contains 31 quantum jumps from bright to dark, heralding the absorption of 393 nm photons.

the bright-state count rate has an average value of $219(15) \cdot 10^3 \frac{\text{counts}}{\text{s}}$, whereas the dark-state count rate is $34(6) \cdot 10^3 \frac{\text{counts}}{\text{s}}$. The 397 nm and 393 nm photons that are generated and collected at the sender trap contribute to the high amount of background light leading to

the high level of dark-state count rate. Although we collect the 393 nm most efficiently from the sender by inserting the compensation lens we still get 397 nm photons which are sent together with 393 nm photons to the receiver. There the position of the HALO is optimized for 397 nm coupling and both wavelengths are sent through the trap, collected by the second HALO in the receiver and detected by the PMT.

From a fluorescence trace like the one in Fig. 4.3 we obtain the dark period lengths by using the following method: First the time axis is divided in time bins of size δt. The bins contain the counted number of photon clicks therein. In Fig. 4.4 the number of photon clicks in a time bin of 1 ms from the fluorescence trace in Fig. 4.3 is put into a histogram. The

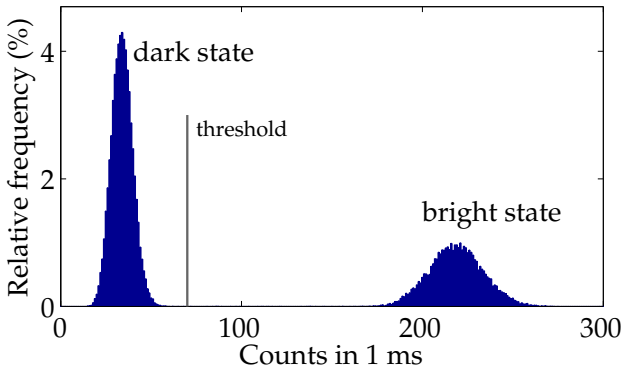

Figure 4.4.: Histogram of detected fluorescence counts for a binning of 1 ms. The two observed distributions allow one to define a threshold that lies in between the two distributions of bright and dark state for searching quantum-jump events in fluorescence time traces.

two photon-number distributions are used to obtain a threshold number of counts which is set between the two distributions for discriminating between dark and bright state. Taking the point which has the minimum counts between the two distributions serves for a proper threshold value. This threshold value is used in a Matlab program for comparing the number of photon counts in a time bin with the threshold, determining in this way the onset and cease of the fluorescence and thus the time the ion spent in the dark state.

For a total acquisition time of 4 min, we present 73 absorption events heralded by quantum jumps and sorted according to their dark period lengths in the histogram of Fig. 4.5. Note that the data is taken from different measurement days and thus shows a lower absorption rate than the trace in Fig. 4.3 due to a different degree of optical-path alignment between the two traps. However, in the histogram we analyze the length of dark periods which does not suffer from different rates. The only possibility to enter the fluorescence cycle after a quantum jump to the metastable $D_{5/2}$ level is the spontaneous decay via the 729 nm transition. This has the advantage of a background-free signal, as long as there are no other processes, like background light from a 393 nm source, inducing quantum jumps. The mean lifetime of the $D_{5/2}$ level has a value of 1168(9) ms [80]. We calculate the mean

dark period duration and the standard error of the mean to $\tau = 1106(106)$ ms that is for the low number of events in agreement to the literature value within the error margins.

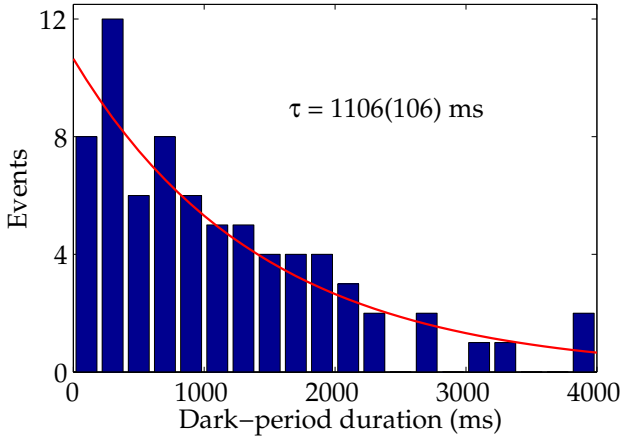

Figure 4.5.: Histogram of dark-period durations of the fluorescence in the receiver trap. The mean dark period τ is calculated for a bin size of 1 ms from a fluorescence time trace of 4 min including 73 detected quantum jumps events from bright to dark. The bin size of the histogram is 200 ms. The red curve is an exponential fit to the data, serving as a guide to the eye.

To calculate the absorption probability, we first determine the rate of absorbed photons from the measurement presented in Fig. 4.3. In an acquisition time of 59.996(1) s, we see 31 quantum jumps. In the total time of 38.455(62) s the ion spends in the dark state, it is not sensitive to further absorption events. The time the ion is sensitive for absorption is thus 21.541(63) s. This number is in agreement with the total bright-period duration which is derived by summing over all bright-state events in Fig. 4.4. The rate of absorption with a subsequent decay to $D_{5/2}$ is then given by

$$R = \frac{31}{21.541(63)\,\mathrm{s}} = 1.439(4)\,\mathrm{s}^{-1}. \tag{4.1}$$

The branching fractions of the $P_{3/2}$ level show that the ion decays only in 5.87 % of the cases to the $D_{5/2}$ level, which means that the real absorption rate of 393 nm photons, including the absorption events where the ion decays to the $S_{1/2}$ or $D_{3/2}$ level is

$$R_{\mathrm{abs}} = \frac{1}{0.0587} \cdot R = 24.52(7)\,\mathrm{s}^{-1}. \tag{4.2}$$

Here the branching fractions of the $P_{3/2}$ level which are proportional to the corresponding oscillator strength [27], show a very general aspect of the efficiency with which 393 nm photon absorption events can be successfully detected. Although the oscillator strength on the absorption transition from $S_{1/2}$ to $P_{3/2}$ is high with 93.47 % $\cdot\, \Gamma_{P_{3/2}}$, it decays only

with a weak strength of $5.87\,\% \cdot \Gamma_{P_{3/2}}$ to $D_{5/2}$, making an absorption detectable by a quantum jump. This means that the product of these two describes the absorption efficiency concerning the oscillator strength and would take the highest value if both had a value of $50\,\% \cdot \Gamma_{P_{3/2}}$.

4.1.4. Absorption probability

For determining the absorption probability of 393 nm photons, we first calculate the collection efficiency of 393 nm photons at the sender trap. We take the collection efficiency of 393 nm photons from HALO 1 calculated in Sec. 3.1.3 as

$$\eta_{\text{coll}} = 3.4\,\%. \tag{4.3}$$

We have not directly measured the emission rate of 393 nm photons for the laser parameters used in the measurement presented in Fig. 4.3, but we estimate from numerical simulations a scattering rate of 393 nm photons of $\sim 2 \cdot 10^6\,\text{s}^{-1}$ which leads to a rate of collected photons of $R_{\text{coll}} = 6.8 \cdot 10^4\,\text{s}^{-1}$. These photons are sent to the receiver and are absorbed with a probability of

$$p_{\text{abs}} = \frac{R_{\text{abs}}}{R_{\text{coll}}} = 3.6 \cdot 10^{-4}. \tag{4.4}$$

The value for the absorption probability can be viewed as a upper limit, since the assumption that all the collected photons from the sender ion are coupled to the receiver ion is rather optimistic. Additionally we also calculate the probability to see an absorption event, i.e. the absorption probability given that the ion is in $D_{5/2}$ after an absorption. Thereto we take the absorption rate from Eq. (4.1) and obtain the absorption probability conditioned on the observation of a quantum jump as

$$p_{\text{abs, jump}} = 2.1 \cdot 10^{-5}. \tag{4.5}$$

The low absorption probabilities are mainly limited by the spatial overlap between the incoming photonic wave packet with the atomic wave packet. This is attributed to the alignment, i.e. the telescope and HALO which is aligned for 397 nm wavelength. We further have to point out that the value of the absorption probability is composed of many physical quantities and the interplay of all of them is a complex task, which is nowadays under current investigation in state-of-the art experiments. After the presentation of the 854 nm interaction in Sec. 4.2, we will come back to the discussion about absorption probabilities in a much more detailed manner.

4.2. Single-mode interaction at 854 nm wavelength

After the experimental interlude of the 393 nm interaction measurement, we proceed with our transition of choice at 854 nm, which has been extensively studied with absorption experiments of heralded single photons from the SPDC source [82, 114, 64]. The main advantage using this transition for absorbing single photons is found in the possibility to transfer entanglement in polarization of 854 nm photons to the ion's internal ground state [46]. Figure 4.6 shows the double-trap setup consisting of the two traps separated by $\sim$ 1 m distance. Each of the two traps is coupled with a 2 m single-mode (SM) fiber, whereby both fibers are connected with a single-mode (SM) fiber coupler. The latter is

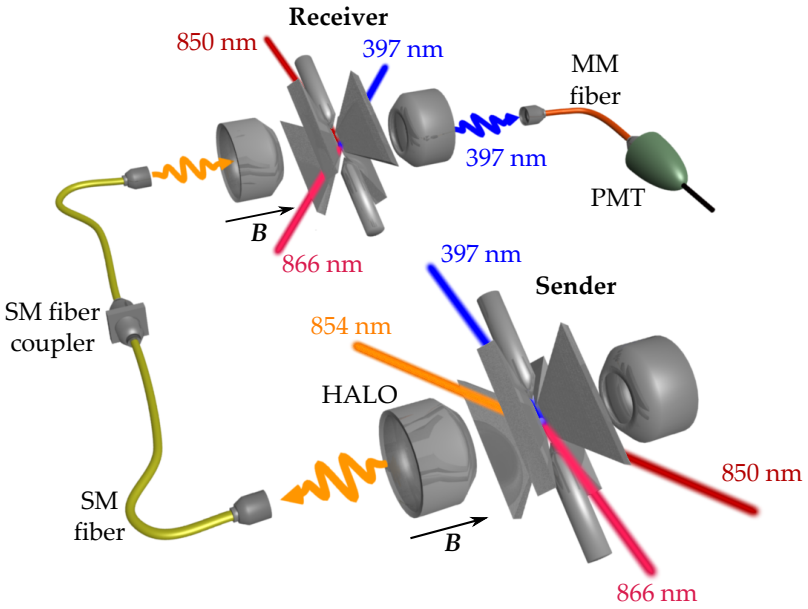

Figure 4.6.: Experimental setup for 854 nm photonic interaction between two distant ion traps, each confining a single $^{40}Ca^{+}$. In the sender trap, single 854 nm photons are generated in continuous and triggered mode and coupled to a single-mode (SM) fiber which is connected by a SM fiber coupler to a second SM fiber. In the receiver ion, various laser beams guarantee the successful detection of an absorption event by collecting the scattered 397 nm light which is coupled to a multi-mode (MM) fiber connected to a photomultiplier tube (PMT). In both traps the direction of the magnetic field B is oriented along the HALO axis.

also used to separately connect each of the two traps with a highly attenuated, single-mode fiber coupled laser at 854 nm wavelength as a weak source of 854 nm photons. The laser photons serve as a source of narrow-bandwidth photons. If they are absorbed from the receiver ion we can compare the absorption probability to the value if the ion absorbs

single photons from the ion with respect to their spectral linewidths. Alternatively, we connect an avalanche photodiode with the single-mode fiber which is connected to the sender ion to record an arrival-time distribution of single 854 nm photons. For photonic-interaction measurements between the two traps, the photons are generated in the sender trap, coupled with the HALO along the quantization axis into the single-mode fiber and sent to the receiver ion trap. There the photons are coupled to the ion with the HALO which is now optimized in alignment to efficiently focus 854 nm photons onto the ion. The orientation of the magnetic field is similar to the sender ion trap chosen along the HALO axis. At the receiver ion trap, absorption events are signaled with the quantum jump from *dark to bright* by monitoring the 397 nm fluorescence light with the PMT.

4.2.1. Continuous generation of 854 nm photons

We perform a first interaction measurement by continuously generating 854 nm photons at the sender ion by having all four lasers (namely 397, 866, 850 and 854 nm) constantly switched on. The laser parameters are optimized in such a way that we generate the highest possible number of 854 nm photons measured with an APD which is directly connected to the single-mode fiber from the sender trap. We measure a background-corrected count rate of $3100(56)\,\mathrm{s}^{-1}$, corresponding to a single-mode fiber coupled rate of $1.29(27)\cdot 10^4\,\mathrm{s}^{-1}$, taking into account the APD detection efficiency of $24(5)$ %. For interaction measurements we connect both traps with a fiber coupler with a transmission efficiency of $\eta_{\mathrm{fc}} = 94.5(3)$ %, giving finally a single-mode coupled photon rate of

$$R_{\mathrm{fc,\,ph}} = 1.22(26)\cdot 10^4\,\mathrm{s}^{-1}, \tag{4.6}$$

which is transmitted to the receiver ion where quantum jumps are monitored.

At the receiver ion we observe quantum jumps as explained in Fig. 4.7. While the receiver ion is Doppler cooled with the 397 nm and 866 nm laser, a highly attenuated 850 nm laser serves for random quantum jumps from $D_{3/2}$ to $D_{5/2}$ causing the fluorescence to cease. We adjusted the power such that on average the ion spends half of the time in the $D_{5/2}$ level where it stays dark. In contrast to the quantum jump scheme for 393 nm interaction, the quantum jump from dark to bright occurs in two different ways. Besides the absorption of an 854 nm photon the ion can spontaneously decay from the $D_{5/2}$ to the $S_{1/2}$ level. Both processes take the population back to the fluorescence cycle and result in an onset of the fluorescence. The quantum jump event from dark to bright is called a herald for the photon absorption, since beside the spontaneous decay contribution, it tells us that there was a successful absorption event.

Sender ion off

First we calibrate the receiver ion for sender-photon absorption events by transmitting no photons to the receiver by switching off the 850 nm laser in the sender ion. With the

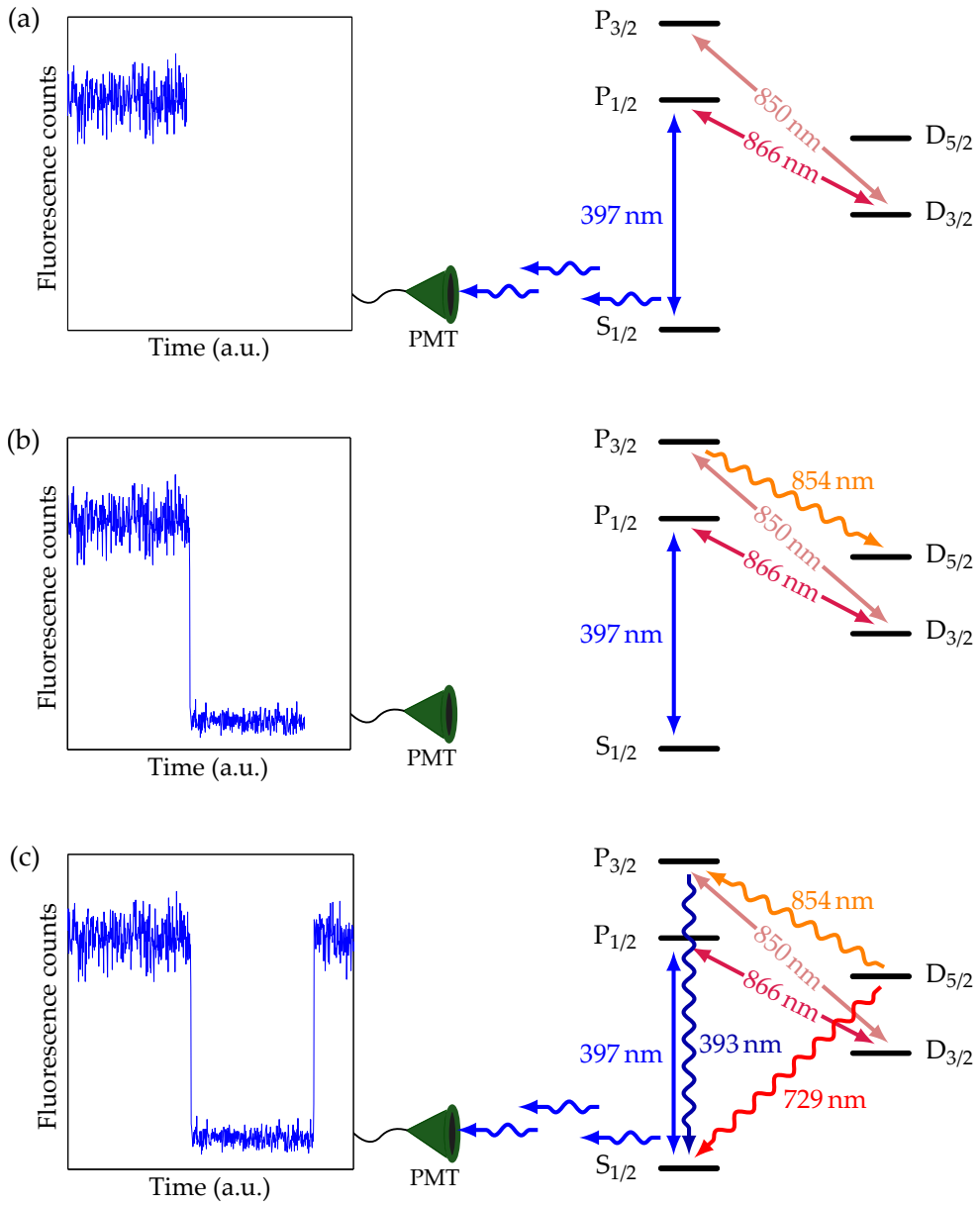

Figure 4.7.: Level-scheme and detected time trace of 397 nm fluorescence counts for illustrating the observation of quantum jumps at the receiver ion. (a) During Doppler cooling with the 397 and 866 nm laser, the ion fluoresces continuously before (b) a highly attenuated 850 nm laser randomly causes a population transfer to the metastable $D_{5/2}$ state by a quantum jump from bright to dark. (c) The ion remains dark until an 854 nm photon absorption from the sender ion takes place. This process competes with the spontaneous decay of the $D_{5/2}$ via the 729 nm transition. Both events result in an onset of the fluorescence which is analyzed and used as a time stamp for correlation measurements.

laser configuration in the receiver ion, dark-to-bright quantum jumps signal the spontaneous decay of the $D_{5/2}$ level. In Fig. 4.8(a) we extract the lifetime of the $D_{5/2}$ level from a total fluorescence measurement time of 20 min by determining the mean dark period length $\tau_{\text{off}} = 1022(33)$ ms, as explained in Sec. 4.1.3. This corresponds to a decay rate of

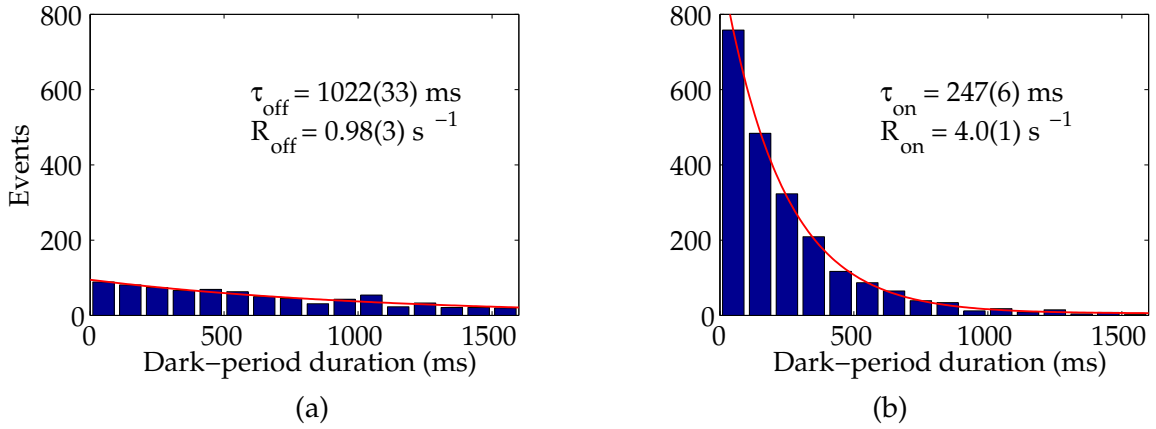

Figure 4.8.: Histograms of dark-period lengths in the receiver ion after a quantum jump to $D_{5/2}$. (a) Without photons from the sender ion we get 979 quantum jumps for a total measurement time of 20 min. (b) With photons from the sender ion, the number of quantum jumps is increased to 2186 within 15 min. For both histograms we display the mean dark period length $\tau_{\text{on, off}}$ and the corresponding decay rates $R_{\text{on, off}} = 1/\tau_{\text{on, off}}$.

$R_{\text{off}} = 0.98(3)\,\text{s}^{-1}$ when the sender ion is switched off. Comparing the value of τ_{off} to the literature value of 1168(9) ms [80] reveals that we have sources of disturbance that reduce the lifetime. We attribute these to stray light of the nearby 854 nm laser setup causing 854 nm photons to enter the receiver ion trap.

Sender ion on

With the 850 nm laser switched on at the sender ion, the effective lifetime of the $D_{5/2}$ state is significantly reduced to $\tau_{\text{on}} = 247(6)$ ms for a total measurement time of 15 min as depicted in Fig. 4.8(b). From the increased quantum jump rate of $R_{\text{on}} = 4.0(1)\,\text{s}^{-1}$ we calculate the absorption rate of 854 nm photons at the receiver as $R_{\text{on}} - R_{\text{off}} = 3.0(1)\,\text{s}^{-1}$, conditioned on the subsequent decay from $P_{3/2}$ to $S_{1/2}$ or to $D_{3/2}$. Taking into account the probability of 5.87 % that the ion decays back to $D_{5/2}$ which is not detected by a quantum jump yields a total absorption rate of

$$R_{\text{abs}} = \frac{1}{0.9413}\,(R_{\text{on}} - R_{\text{off}}) = 3.2(1)\,\text{s}^{-1}. \tag{4.7}$$

With the fiber-coupled rate R_{fc} of transmitted photons, this gives a single-photon absorption probability per photon of

$$p_{\mathrm{abs,\,ph}} = \frac{R_{\mathrm{abs}}}{R_{\mathrm{fc}}} = 2.6(5) \cdot 10^{-4}. \tag{4.8}$$

Here we see that this number coincides well with absorption probabilities measured with 854 nm photons from an SPDC source [114]. In the case of SPDC photons, they are spectrally and temporally tailored to the atomic decay rate of the $P_{3/2}$ level. Here the temporal and spectral properties of the photons from the sender ion are quite different. In order to analyze the dependance of the absorption probability from the spectral behavior of the photons we replace the single-photon source of the ion by a highly attenuated 854 nm laser, that serves as a narrowband photon source. After this measurement we can compare the absorption probability of the laser photons to the absorption probability of single photons generated in triggered sequence mode.

4.2.2. Comparison to absorption of 854 nm laser photons

For replacing the single-photon source from the sender ion by an easy to tune and high brightness source of photons we use the 854 nm laser in a highly attenuated fashion. Of course, one has to keep in mind that the photon statistics of both sources differ significantly. As it was shown for 393 nm photons, we expect to see in the $g^{(2)}$ correlation function of the 854 nm photons a clear antibunching[1], which is not the case for laser photons. However, since the ion is capable to only absorb one single photon at a certain time, we still can use this source for single-photon absorption probability measurements.

First we use the three lasers at the receiver ion trap shown in Fig. 4.6 together with the 854 nm laser sent through the HALO to find proper detuning for the 854 nm laser to resonantly excite the $D_{5/2}$ to $P_{3/2}$ transition. For that we use a 397 nm laser together with a weak 850 nm laser to avoid any level shifts of the $P_{3/2}$ level. The weak 854 nm laser is then frequency-scanned over the transition while from the detected fluorescence at 397 nm the resonance frequency is determined. Then the laser is attenuated which is achieved by a cascade of neutral density filters that are placed in the laser beam. The single-mode fiber coupled laser is connected the APD and adjusted to a rate of $3955(63)\,\mathrm{s}^{-1}$ background corrected photons. With this rate we connect the single-mode coupled laser via the fiber-coupler to the single-mode fiber of the receiver ion trap, with a single-mode fiber coupled rate of

$$R_{\mathrm{fc,\,laser}} = 1.56(33) \cdot 10^4\,\mathrm{s}^{-1}. \tag{4.9}$$

[1] With only one HALO aligned for efficient collection of 854 nm photons in the sender trap we had to use a fiber beam splitter connected to the single mode fiber to perform a second-order correlation measurement. The beam splitter introduced high photon losses with the consequence that the measurement time had to be increased. This caused the problem that true two-photon events could not be distinguished anymore from two-photon events by detector dark counts. This made us unable to characterize the 854 nm photons concerning their statistics.

which is comparable to the rate of continuously generated photons from the sender ion that we used before. Similar to the cw interaction of single photons from the sender, we first suppress the photon generation by blocking the laser and determine the decay rate of the $D_{5/2}$ level at the receiver ion to $R_{\text{on}} = 0.85(2)\,\text{s}^{-1}$ from the mean dark period length (Fig. 4.9(a)), this time in agreement with the literature value $0.856\,\text{s}^{-1}$ [80]. For the case that laser photons are absorbed, shown in Fig. 4.9(b), the rate is increased to $R_{\text{off}} = 7.4(1)\,\text{s}^{-1}$ which results in a absorption rate of

$$R_{\text{abs, laser}} = \frac{1}{0.9413}\left(R_{\text{on}} - R_{\text{off}}\right) = 7.0(1)\,\text{s}^{-1}. \tag{4.10}$$

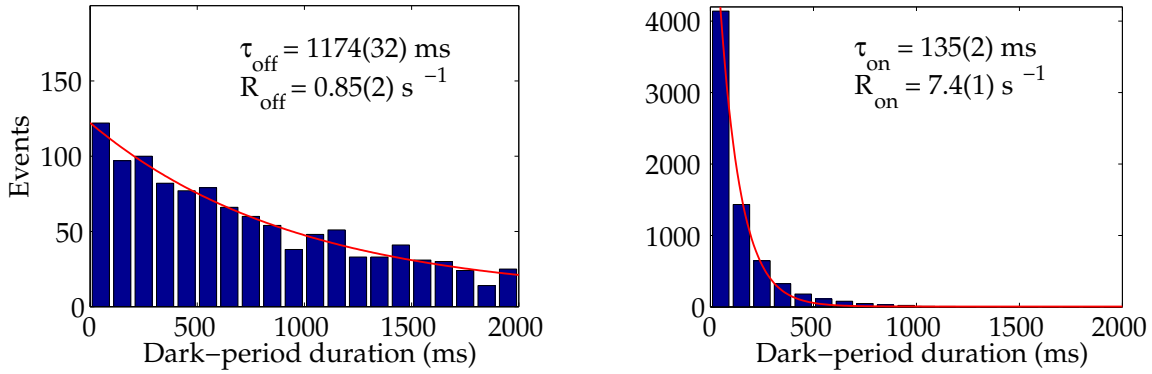

Figure 4.9.: Histograms of dark-period lengths in the receiver ion after a quantum jump to $D_{5/2}$. (a) Without laser photons, 1365 events in 30 min acquisition time contribute to the distribution. (b) With laser photons, the number of quantum-jump events is increased to 7042 in 30 min.

Taking into account the fiber-coupler efficiency leads to an absorption probability of

$$p_{\text{abs, laser}} = 4.5(1.0) \cdot 10^{-4}. \tag{4.11}$$

The ratio between the two absorption probabilities is

$$\frac{p_{\text{abs, laser}}}{p_{\text{abs, ph}}} = 1.7(5). \tag{4.12}$$

Eq. (4.11) clearly shows that within the error margins, the absorption rate is increased if we send narrow-bandwidth laser photons to the receiver ion instead of photons from the sender ion. It depends on spectro-temporal, spatial and polarization degrees of freedom of the incoming photons. The properties are discussed in Sec. 4.3 when we compare the absorption probability from laser photons with the absorption probability with triggered photons from the ion.

4.2.3. Triggered single-photon transmission

Beside the continuous interaction, we transmit single photons that we generate in sequence mode, as presented in Sec. 3.2.3. The photons have an arrival time of 1.1 µs and are generated with a repetition rate of 31.25 kHz. In order to show the successful absorption at the receiver ion, the emission trigger, i.e. the electronic pulse which is sent to the 850 nm AOM leading to the onset of the 854 nm Raman scattered photon, is used in one channel of PicoHarp. In the second channel we record the 397 nm fluorescence from the receiver ion and extract the first 397 nm fluorescence photon after a quantum jump by the following procedure, which is performed by in a C program and discussed in detail in [115].

To obtain the first scattered 397 nm photon, the trace is filtered by a moving average, i.e. the number of clicks are counted for a given time bin and then averaged over a certain number of bins. The averaged filter is then scanned over the fluorescence trace, while comparing the number of fluorescence counts with a threshold. This method yields the coarse times for quantum jumps, i.e. the resolution is determined by the bin size, which is typically 1 ms. Therefore the program continues with the analysis of the clicks around the coarse absorption time to find the time t_m of the first 397 nm photon after the onset of fluorescence. By comparing the time intervals $\Delta t_m = t_m - t_{m-1}$ between two pairs of three subsequent photon clicks, the intervals are compared to a threshold delay τ_{th} such that a quantum jump from dark to bright fulfills the condition $\Delta t_{m+1} < \tau_{\text{th}}$ and $\Delta t_m > \tau_{\text{th}}$.

The evaluation of the interaction between photon-emission trigger at the sender ion and the first fluorescence photon at the receiver ion is shown by a histogram in Fig. 4.10. It contains the time delays of the first 397 nm photons with respect to the emission trigger, starting at zero time delay for a total measurement time of 65 min. Within one sequence repetition time of 32 µs (blue bars), we see coincidences between trigger and absorption events that are clearly visible as a peak on top of uncorrelated background events. In order to explain the shape of the correlation function we describe each part of the rising and falling slope step by step before we finally present the analytical expression for the expected theory, drawn as the red solid curve in Fig. 4.10. First we describe the probability distribution of generated single photons as

$$p(t)_{\text{ph}} = \frac{1}{\tau_{\text{ph}}} e^{-\frac{t}{\tau_{\text{ph}}}} \Theta(t), \tag{4.13}$$

with $\tau_{\text{ph}} = 1.1\,\mu\text{s}$ and the Heaviside function $\Theta(t)$. Next, the probability distribution of 397 nm fluorescence photons has to be analytically expressed. If we consider that the time of detected fluorescence events follows a Poisson distribution, we conclude for scattering rates much lower than the atomic decay rate that subsequent photon detections are independent from each other which results in a probability distribution of

$$p(t)_{\text{fl}} = \frac{1}{\tau_{\text{fl}}} e^{-\frac{t}{\tau_{\text{fl}}}} \tag{4.14}$$

where $\tau_{\text{fl}} = \frac{1}{R_{\text{fl}}}$ is the inverse of the 397 nm scattering rate at the receiver ion. The scattering rate is important, since it determines the temporal resolution for detecting the first 397 nm

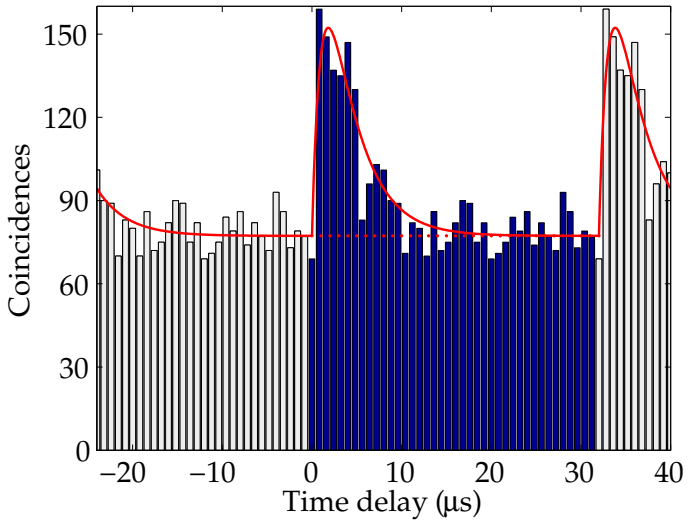

Figure 4.10.: Temporal correlation function between single-photon emission triggers at the sender ion and dark-to-bright quantum jumps at the receiver ion. For a measurement time of 65 min and a repetition rate of 31.25 kHz, the data is displayed with a bin size of 800 ns. The blue data shows the histogram for time delays up to one sequence period. The red line shows the theoretical model that fits the data very well, the red dots indicate the background level.

fluorescence photon and thus the precision for the absorption event. From this point of view, we have to set the scattering rate to the highest possible level, which is $R_{\mathrm{fl}} = 3 \cdot 10^5\,\mathrm{s}^{-1}$, corresponding to a time constant of $\tau_{\mathrm{fl}} = 3.3\,\mu\mathrm{s}$ as the average time between two subsequent fluorescence clicks. The correlation measurement between the emission trigger of single photons and the first 397 nm fluorescence photon is given by a convolution

$$(p_{\mathrm{ph}} * p_{\mathrm{fl}})(t) = \int_{-\infty}^{\infty} p_{\mathrm{ph}}(\tau)\, p_{\mathrm{fl}}(t-\tau)\, d\tau, \tag{4.15}$$

with τ marking the point in time when a photon is emitted by the sender ion. As both functions are defined in the range from $\tau \in [0;\infty[$, Eq. (4.15) can be reformulated and finally leads to the solution

$$(p_{\mathrm{ph}} * p_{\mathrm{fl}})(t) = \int_{0}^{t} p_{\mathrm{ph}}(\tau)\, p_{\mathrm{fl}}(t-\tau)\, d\tau, \tag{4.16}$$

$$= \frac{\left(e^{\frac{t}{\tau_{\mathrm{ph}}}} - e^{\frac{t}{\tau_{\mathrm{fl}}}}\right) e^{-\frac{t(\tau_{\mathrm{fl}}+\tau_{\mathrm{ph}})}{\tau_{\mathrm{fl}}\,\tau_{\mathrm{ph}}}}}{\tau_{\mathrm{fl}} - \tau_{\mathrm{ph}}} \tag{4.17}$$

$$= \frac{1}{\tau_{\mathrm{fl}} - \tau_{\mathrm{ph}}} \left(e^{-\frac{t}{\tau_{\mathrm{fl}}}} - e^{-\frac{t}{\tau_{\mathrm{ph}}}}\right). \tag{4.18}$$

Note that the condition $\tau_{\mathrm{fl}} \neq \tau_{\mathrm{ph}}$ has to be fulfilled. For the case that $\tau_{\mathrm{fl}} = \tau_{\mathrm{ph}}$, the integral in Eq. (4.15) has to be evaluated, yielding a different result. The convolution given in Eq. (4.18) incorporates the emission process by the single-photon probability distribution and the detection of the first 397 nm photon by the fluorescence probability distribution. For the experimental parameters of τ_{ph} and τ_{fl} determined in independent measurements, the convolution is plotted as the red curve in Fig. 4.10. With the expected parameters, we see that the theory fits nicely to the data. Following from zero time delay, the time from 0.8 to 1.6 µs shows a steep rise, represented by the theory, as the onset with the length of the photon. The rise is followed by an exponential decay containing the probability distribution of the fluorescence photons with the $\frac{1}{e}$ time of $\tau_{\mathrm{fl}} = 3.3\,\mu\mathrm{s}$. The background level of 77 events per 0.8 µs bin, indicated as the dotted line in Fig. 4.10, contains the uncorrelated pairs of emission trigger with spontaneous decay events via the 729 nm transition.

With the data presented in Fig. 4.10 we calculate the absorption probability of sender photons by the receiver ion in triggered mode as well as the overall success probability for successful photonic transmission between distant single ions. Concerning the first, we subtract the background level in every time bin in the blue-shaded area in Fig. 4.10 and sum over the remaining events in order to obtain all events above the background level, representing real absorption events. Integrating them yields $n_{\mathrm{abs}} = 589(81)$ absorption events. Assuming that every 850 nm trigger generates a single 854 nm photon, we generate in the total measurement time of 65 min with a repetition rate of 31.25 kHz a maximum number of photons of $n_{\mathrm{ph}} = 1.219 \cdot 10^8$. Taking the mode-matching efficiency of single photons into the single-mode fiber from Eq. (3.41) of $\eta_{\mathrm{SM}} = 2.1(4)\,\%$ we calculate the number of photons in the single-mode fiber $n_{\mathrm{ph,SM}} = 2.6(5) \cdot 10^6$ which leads with the fiber coupling efficiency to the absorption probability of

$$p_{\mathrm{abs,\,trig}} = 2.4(5) \cdot 10^{-4}. \tag{4.19}$$

Within the error margins, we see that this value is in agreement with the absorption probability for continuous photon transmission. The overall success probability, i.e. the probability for a successful photon absorption at the receiver, given that a photon generation is triggered at the sender is calculated by

$$p_{\mathrm{success}} = \frac{n_{\mathrm{abs}}}{n_{\mathrm{ph}}} = 4.8(7) \cdot 10^{-6}. \tag{4.20}$$

To our knowledge, this value can be seen so far as unparalleled in the ion trapper community, since our experiment for direct photonic interaction between distant single ion is seen as unique. Related work with photonic interaction measurements between distant network nodes has been so far established with spectroscopy measurements on a single molecule with cw scattered photons from a distant single molecule [116] and with single atoms in optical cavities [37]. In the latter scheme the light-matter interaction at each node is strongly enhanced by the use of optical cavities. With a photon generation efficiency of

3 % into the cavity[2] at the sender atom, a mode matching efficiency of an intracavity photon to a single mode fiber (fiber coupling efficiency) of 90 %, the transmission of the optical fiber of 40 % and the storage efficiency at the receiver atom of 20 %, the overall success probability for a quantum state transfer is $2 \cdot 10^{-3}$.

4.3. Comparison between absorption probabilities

From Eq. (4.19) we see that the absorption probability for triggered photons from the ion is reduced compared to the case for laser photons as given in Eq. (4.11). From both values we obtain a ratio of

$$\frac{p_{\text{abs, laser}}}{p_{\text{abs, trig}}} = 1.9(6). \tag{4.21}$$

As both photon sources are coupled into the same single-mode fiber pointing towards the receiver ion trap we can expect their spatial mode profile out of the fiber to be identical. The remaining different spectral properties and the different polarizations between the photons shall be analyzed now.

For the triggered 854 nm interaction measurements, we generated photons with an arrival time of 1.1 µs. They correspond to a three-photon resonance where laser detunings and intensities were optimized in cw excitation to the highest ratio between 393 nm and 397 nm photons. Here we obtain $R_{393} = 14 \cdot 10^6\,\text{s}^{-1}$ and $R_{397} = 23 \cdot 10^6\,\text{s}^{-1}$ leading to an incoherent broadening factor of 2.64 according to Eq. (3.49). From Eq. (3.50) we can calculate the incoherently broadened full-width at half-maximum of the Lorentzian-shaped frequency spectrum of 854 nm photons from the ion as

$$\Delta\nu_{\text{ph}} = \frac{16.92 \cdot 2.64}{2\pi \cdot 1.1\,\mu\text{s}} = 6.5\,\text{MHz}. \tag{4.22}$$

Note that this width only describes the full width at half maximum of photons from a single transition from $|\text{P}_{3/2}, m_j\rangle$ to $|\text{D}_{5/2}, m_j\rangle$ out of the multitude of possible transitions, i.e. single-mode fiber coupled photons, shown in Fig. 4.11, that are weighted with the Clebsch-Gordan coefficients (see Fig. 2.7) and the populations.

For the description we take an equally distributed population in the $\text{P}_{3/2}$ level which leads to two quartets of σ transitions, namely σ^+ and σ^-. Note that the possible π transitions are collected along the quantization axis with a very low efficiency and do not enter the single-mode fiber, since the mode overlap of the emission profile of π light with the fiber mode vanishes if we collect this light along the quantization axis [52]. The remaining possible σ photons that are transmitted by the SM fiber are shown in Fig. 4.11 and they are cast in the following into an analytical form to see the difference in absorption probabilities caused by different spectral shapes between photons from the ion and from the laser. We

[2]This value was deliberately set for this experiment. Typical generation efficiencies reach values up to 56 % [117].

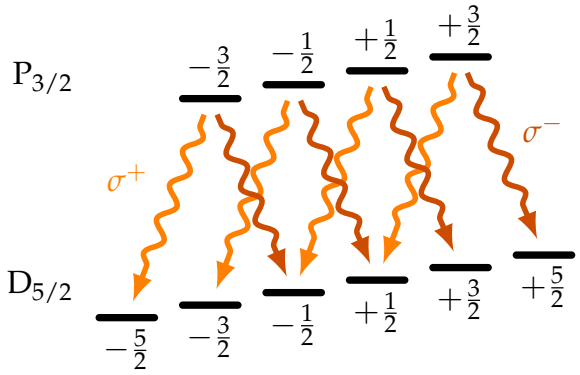

Figure 4.11.: Relevant 854 nm decay channels for an equally distributed population in $P_{3/2}$, observed along the quantization axis and coupled into a single-mode fiber. The two quartets of σ^+ and σ^- contribute to the total spectral shape of the emitted photons.

first describe all possible transitions in the σ^- and σ^+ quartet for $i,k = \{0,1,2,3\}$

$$\sigma^- : \nu_i = \nu_{\mathrm{LC}} + \left(g_j^{\mathrm{P}} \cdot m^{\mathrm{P}}_{i-\frac{3}{2}} - g_j^{\mathrm{D}} \cdot m^{\mathrm{D}}_{i-\frac{1}{2}}\right) \frac{\mu_{\mathrm{B}}}{h} \cdot B, \tag{4.23}$$

$$\sigma^+ : \nu_k = \nu_{\mathrm{LC}} + \left(g_j^{\mathrm{P}} \cdot m^{\mathrm{P}}_{k-\frac{3}{2}} - g_j^{\mathrm{D}} \cdot m^{\mathrm{D}}_{k-\frac{5}{2}}\right) \frac{\mu_{\mathrm{B}}}{h} \cdot B \tag{4.24}$$

Here ν_{LC} describes the line-center frequency, i.e. the resonance transition frequency one would determine from 854 nm spectroscopy, which we now can take to be zero without loss of generality. For the Raman-scattered photon generated in triggered mode on one of the 8 transitions we assume a spectral probability distribution described by a Lorentzian lineshape as shown in Sec. 3.1.4 and given by

$$s(\nu)_{\mathrm{ph}} = \frac{1}{2\pi} \frac{\Delta\nu_{\mathrm{ph}}}{(\nu - \nu_{i,k})^2 + (\frac{\Delta\nu_{\mathrm{ph}}}{2})^2}. \tag{4.25}$$

Every transition between individual Zeeman substates has to be weighted by the corresponding Clebsch-Gordan coefficient $C_{m_{\mathrm{D}},m_{854},m_{\mathrm{P}}}$ (see Fig. 2.7) so that the total emission profile of one polarization is given by the sum of the weighted transitions as

$$s(\nu)^{\sigma^-}_{\mathrm{ph}} = \sum_{i=0}^{3} C_{m^{\mathrm{D}}_{i-\frac{1}{2}},m_{854},m^{\mathrm{P}}_{i-\frac{3}{2}}} \cdot \frac{1}{2\pi} \frac{\Delta\nu_{\mathrm{ph}}}{(\nu - \nu_i)^2 + (\frac{\Delta\nu_{\mathrm{ph}}}{2})^2} \tag{4.26}$$

and accordingly for σ^+

$$s(\nu)^{\sigma^+}_{\mathrm{ph}} = \sum_{k=0}^{3} C_{m^{\mathrm{D}}_{k-\frac{5}{2}},m_{854},m^{\mathrm{P}}_{k-\frac{3}{2}}} \cdot \frac{1}{2\pi} \frac{\Delta\nu_{\mathrm{ph}}}{(\nu - \nu_k)^2 + (\frac{\Delta\nu_{\mathrm{ph}}}{2})^2}. \tag{4.27}$$

The total emission spectrum is normalized via

$$s(\nu)_{\mathrm{ph,\,tot}} = \frac{s(\nu)^{\sigma^+}_{\mathrm{ph}} + s(\nu)^{\sigma^-}_{\mathrm{ph}}}{\int_{-\infty}^{\infty} \left(s(\nu)^{\sigma^+}_{\mathrm{ph}} + s(\nu)^{\sigma^-}_{\mathrm{ph}} \right) d\nu}, \tag{4.28}$$

such that

$$\int_{-\infty}^{\infty} s(\nu)_{\mathrm{ph,\,tot}}\, d\nu = 1. \tag{4.29}$$

The spectrum is depicted in Fig. 4.12. Due to the magnetic field of 2.3 G we see a double-peak shaped frequency spectrum (gray line). Each peak corresponds to a branch of 4 transitions that belongs to one polarization. While each photon has a spectral width of 6.5 MHz,

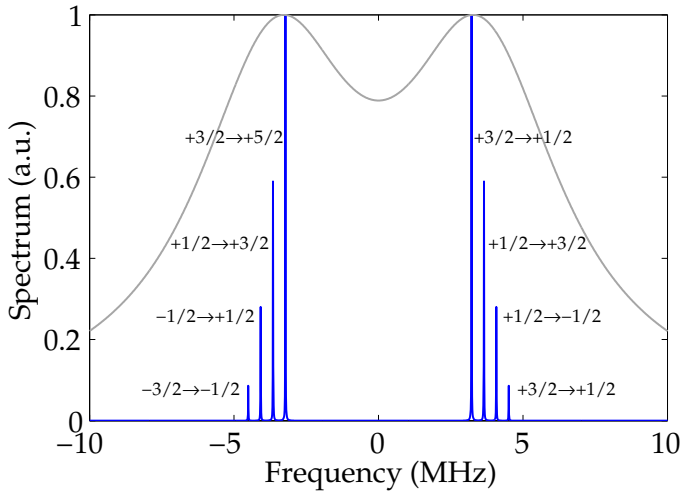

Figure 4.12.: Photonic spectrum from eight σ transitions between Zeeman substates $m_j^{\mathrm{P}} \rightarrow m_j^{\mathrm{D}}$ for a spectral photon linewidth of 10 kHz (blue line) and 6.5 MHz (light gray line) for a magnetic field of 2.3 G.

the total spectrum is broadened by the various frequency components from all 8 transitions. All 8 transitions are resolved if the individual photon linewidth is chosen as 10 kHz. Together with the assignment of the transitions they are also displayed (blue line). There the different oscillator strengths due to different Clebsch-Gordan coefficients become visible. The spectrum for photons with a linewidth of 6.5 MHz is also shown in Fig. 4.13 as the blue line for comparison with the atomic line shape at the receiver ion and the line shape of the laser. Note that there the normalization to unity serves for a better overview and comparison to the other spectra.

Similar to the emission spectrum we describe the atomic absorption spectrum at the receiver ion. The two quartets of possible σ absorption channels as given in Eq. (4.23) and Eq. (4.24) contribute now to the linewidth of one transition from $D_{5/2}$ to $P_{3/2}$ which is the

linewidth of the excited $P_{3/2}$ level of $\Delta\nu_{at} = 22.992\,\text{MHz}$ and the spectrum reads

$$s(\nu)_{at} = \frac{1}{2\pi}\frac{\Delta\nu_{at}}{(\nu-\nu_{i,k})^2 + (\frac{\Delta\nu_{at}}{2})^2}. \tag{4.30}$$

The individual absorption branches for the two different polarizations can be also written in a similar way as in Eq. (4.26) and Eq. (4.27) such that the total absorption spectrum of the receiver ion is

$$s(\nu)_{at,tot} = \frac{s(\nu)^{\sigma^+}_{at} + s(\nu)^{\sigma^-}_{at}}{\int_{-\infty}^{\infty}\left(s(\nu)^{\sigma^+}_{at} + s(\nu)^{\sigma^-}_{at}\right)d\nu}, \tag{4.31}$$

which is shown as the black line in Fig. 4.13. For a magnetic field of 2.2 G we obtain a transition linewidth which is slightly broadened. Finally, the laser spectrum is also given

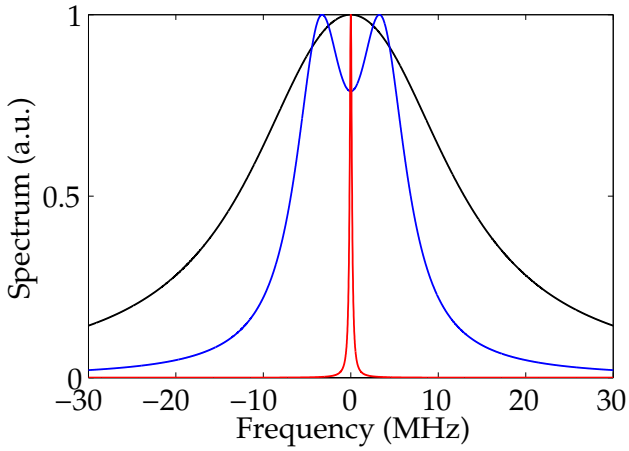

Figure 4.13.: Emission spectrum of single photons from the sender ion for a magnetic field of 2.3 G (blue line) and spectral shape of the 854 nm laser (red line). Black line: Absorption profile of the receiver ion for a magnetic field of 2.2 G. For the sake of clarity, all spectra are normalized to unity.

by a Lorentzian function (red line in Fig. 4.13), now with a typical spectral linewidth of $\Delta\nu_{Laser} = 300\,\text{kHz}$. Since we set the laser to the resonance frequency in the experiment we obtain

$$s(\nu)_{Laser} = \frac{1}{2\pi}\frac{\Delta\nu_{Laser}}{\nu^2 + (\frac{\Delta\nu_{Laser}}{2})^2}, \tag{4.32}$$

which is normalized by $\int_{-\infty}^{\infty} s(\nu)_{Laser}\,d\nu = 1$.

In order to compare the two absorption probabilities we first derive the spectral overlap between the full photonic spectrum and the atomic absorption spectrum. By numerical simulations with the optical Bloch equations, we see with the given experimental laser parameters, particularly the laser polarizations, an almost equal population distribution in the $P_{3/2}$ level of the sender ion as well as in the $D_{5/2}$ level of the receiver ion. Thus

the assumption for an equal population distribution is satisfied and we write the spectral overlap as,

$$\chi_{\mathrm{ph}} = \int_{-\infty}^{\infty} s(\nu)_{\mathrm{ph,\,tot}} \cdot s(\nu)_{\mathrm{at,\,tot}}\, d\nu. \tag{4.33}$$

We compare this result to the overlap between the laser spectrum and the absorption spectrum

$$\chi_{\mathrm{Laser}} = \int_{-\infty}^{\infty} s(\nu)_{\mathrm{Laser}} \cdot s(\nu)_{\mathrm{at,tot}}\, d\nu. \tag{4.34}$$

From both values we calculate the ratio of

$$\frac{\chi_{\mathrm{Laser}}}{\chi_{\mathrm{ph}}} = 1.2. \tag{4.35}$$

We find that this value is close to the measurement ratio of 1.9(6) for the given error margins. The theoretical value shows that the spectral properties of the photons do not have a huge influence on the absolute value of the absorption probabilities as long as the spectrum remains narrower than the atomic line. One parameter which is not precisely known is the polarization of the sender photons. Even though we know their emission spectrum, if we assume an equal probability distribution, the polarization experiences changes by the optical elements in the optical path to the single-mode fiber and to the receiver ion. We analyzed this situation and found that the absorption probability of the photons is reduced if the σ polarizations are completely swapped and thus the ratio in Eq. (4.35) is increased to 1.3. Further deviations might occur by a non-equilibrium in the populations at the sender and at the receiver ion. The complex interplay of laser parameters like intensity, detuning and polarization of the lasers involved in the excitation for photon generation in the sender ion and in the preparation of the $D_{5/2}$ level in the receiver ion makes it hard to simulate the real distribution. This could only be achieved by individual laser spectroscopy, in order to determine the real intensities, detunings and polarizations at the position of the ion.

4.3.1. Discussion of absorption probabilities

The absorption probability of single photons by a single ion in free space is a quantity which is composed of many photonic as well as atomic properties. Ongoing research demonstrates the importance of this topic concerning the free space spatial mode matching of the incoming light with the single quantum emitter [53, 112, 118] and leads to novel trap designs for enhanced optical access [119]. Alternatively, strong coupling between light and matter is achieved by placing an atom inside a high-finesse resonator, known as the field of cavity quantum electrodynamics [120, 121, 122].

Concerning the coupling between ions and photons, enhancement of the coupling can be reached by the improved spatial overlap [112]. More precisely, in the ideal case the photons which are sent to the ion should mimic a dipole wave [123] similar to the dipole emission profile. From this mode one expects the highest electric field in the focus at the ion. So far, there are designs of a mode converter, i.e. a deep parabolic mirror where a

plane electromagnetic field is transformed into an inward-moving dipole wave. With the mirror, single-photon absorption efficiencies close to 100 % are intended [124]. This means that in free space, a high coupling between photons and ion can only be achieved if the full solid angle weighted with the angular emission pattern for π and σ light is covered by the incident photon wave packet. For example, for perfectly exciting π transition, one would have to mimic the dipolar emission pattern which is shown in Fig. 2.6(a) with the incoming photonic wave packet, including the proper polarization at any spatial point.

In our case we know that the NA of the HALO limits the maximum solid angle which is occupied by the incoming photon along the quantization axis. Thus the maximum absorption probability given by the spatial overlap between the incoming photon and the dipole emission pattern is HALO limited by

$$p^{\sigma}_{\text{abs, max}} = 6\,\% \tag{4.36}$$

$$p^{\pi}_{\text{abs, max}} = 0.51\,\% \tag{4.37}$$

if the HALO axis is parallel to the magnetic field direction. Taking account of the oscillator strength and the highest squared Clebsch-Gordan coefficients for a σ transition ($\frac{10}{15}$) and π transition ($\frac{6}{15}$), the maximum absorption probabilities have to be weighted by the branching fractions and we obtain

$$p^{\sigma}_{\text{abs, max, 854}} = 6\,\% \cdot 5.87\,\% \cdot \tfrac{10}{15} = 23.5 \cdot 10^{-4}. \tag{4.38}$$

$$p^{\pi}_{\text{abs, max, 854}} = 0.51\,\% \cdot 5.87\,\% \cdot \tfrac{6}{15} = 1.2 \cdot 10^{-4}. \tag{4.39}$$

4.3.2. Uncertainties in 854 nm absorption probability

Comparing the number of Eq. (4.38) to the measured absorption probability in Eq. (4.19) for sending triggered photons from the sender ion we see that the expected value is still higher by one order of magnitude. If we incorporate the mode-matching efficiency of single photons from the sender into the single-mode fiber, the maximum success rate is given by

$$p^{\sigma}_{\text{success, max, 854}} = 6\,\% \cdot 5.87\,\% \cdot 2.1\,\% \cdot \tfrac{10}{15} = 4.9 \cdot 10^{-5}. \tag{4.40}$$

Possible uncertainties responsible that we do not reach these values are manifold and hard to determine. This starts with a population distribution which is not precisely known in the sender and receiver ion. This causes different weights of CGCs on the possible decay channels at the sender and absorption channels at the receiver. Next, the amount of polarization change through the optical elements in the optical path is not known. Furthermore, the incoupling of the photons into the single-mode fiber changes the spatial profile of the photons out of the HALO to the mode of the single-mode fiber. This might be a minor effect but is not the situation of the ideal case, which would be the face-to-face situation of the two HALOs. Then the light emitted by the sender ion could directly be absorbed at the receiver, i.e. the spatial profile and the polarization would not be changed.

Summary

In the present chapter we showed direct photonic interaction between two distant single ions at two different wavelengths. For continuous photon generation at 393 nm, they were coupled via free-space transmission from the sender ion to the receiver ion, where absorption was heralded by a quantum jump from bright to dark. From a histogram of dark-period lengths we determined the decay rate of the $D_{5/2}$ level which is in agreement within the error margins by the reference value. With a measured absorption rate of $24.52(7)\,s^{-1}$, we estimated the maximum absorption probability per photon to be $3.6 \cdot 10^{-4}$.

In the second part of the chapter we showed a state-of-the-art experiment for heralded individual photon absorption by a single ion. In continuous mode, up to $1.2 \cdot 10^4\,s^{-1}$ photons are coupled into a single-mode fiber and are transmitted between the ions, leading to a reduction to 24 % of the $D_{5/2}$ lifetime and a single-photon absorption probability of $2.6(5) \cdot 10^{-4}$. We compared the absorption probability of triggered single photons from the ion with narrowband laser photons. The measured ratio between laser photons and photons from the ion of 1.9(6) is within the error margins close to the expected value from the theoretical model. Finally, we showed in triggered photon-transmission mode the correlation function between the emission trigger of single photons, i.e. the onset of the 850 nm laser, and the photon absorption, heralded with close to 100 % efficiency by a quantum jump at the receiver ion. Within a time resolution of 3 µs, which is set by the detection rate of fluorescence photons, the correlation function reveals coincidences of both processes. Here we reach an absorption probability of $2.4(5) \cdot 10^{-4}$ and an overall success probability of $4.8(7) \cdot 10^{-6}$.

In both experimental configurations we showed proof-of-principle experiments for photonic interaction measurements between two distant single ions that can be viewed as an interim stage towards the realization of quantum networking experiments between distant single ions.

5. Experimental tools for atomic state preparation

The experiments presented so far in this thesis were executed without regard to the coherent manipulation of the internal state of the ion both prior and after the spontaneous Raman-scattering process. However, for establishing a real quantum network and using the ion as a real quantum processor therein, it becomes indispensable to include the controlled coherent manipulations on the qubit transition of the ion.

In $^{40}Ca^{+}$, the transition of choice for coherent manipulations is the optical qubit transition from $S_{1/2}$ to $D_{5/2}$ at 729 nm wavelength. For coherent manipulations on the $S_{1/2}$ to $D_{5/2}$ quadrupole transition, J. Huwer set up and characterized within his Ph.D. thesis [82] a narrow-bandwidth laser at 729 nm, which serves as the workhorse for many tasks in ion-trapping experiments, including quantum-logic operations with one [125] or multiple ions [21], state discrimination by electron shelving [126], sideband cooling to the motional ground state [126] and preparation of coherent superpositions between Zeeman substates in the $D_{5/2}$ level. The controlled addressing of this transition is essential for the creation of coherent superposition states in $D_{5/2}$ necessary to investigate the coherence of 393 nm Raman-scattering process. This can be seen as a prerequisite for the quantum state transfer from 854 nm photons into the electronic ground state of the ion.

This chapter introduces the tools which are necessary to coherently manipulate the electronic state of the ion. First the subsequent parts of the experimental sequence are introduced step-by-step. Then three experimental applications of the sequence are presented, namely the 729 nm carrier spectroscopy, the 729 nm pulse length scan and the 854 nm spectroscopy.

5.1. Experimental setup and sequence

In Fig. 5.1 the experimental setup for coherent manipulations is shown. The 729 nm laser is sent into the trap at 45° with respect to the direction of the magnetic field, the latter being oriented perpendicularly to the HALO axis. With a polarizing beam splitter (PBS) and a half-wave plate (HWP) the polarization of the 729 nm laser is set to excite allowed quadrupole transitions from $S_{1/2}$ to $D_{5/2}$. For optical pumping of the population to a Zeeman substate in $S_{1/2}$ we use the 397 nm pump laser which is sent antiparallel to the quantization axis, i.e. to the direction of the magnetic field and which is adjusted to circular polarization with a combination of a PBS, HWP and QWP. The 397 nm and 866 nm laser

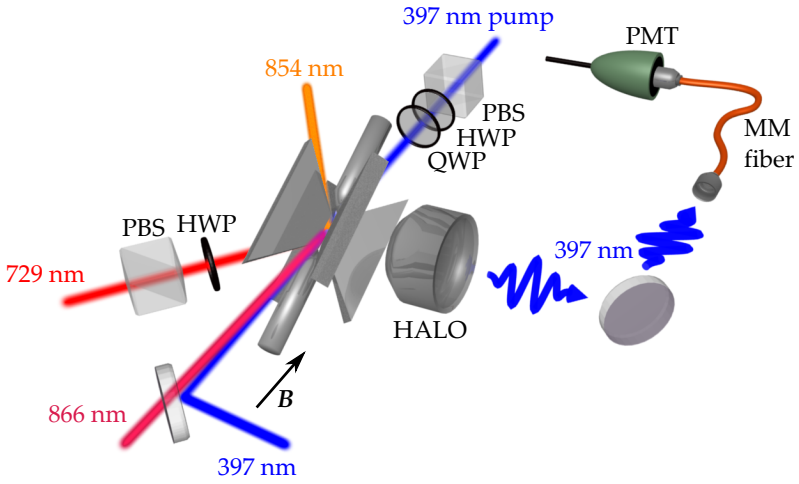

Figure 5.1.: Experimental setup for coherent manipulations on the $S_{1/2}$ to $D_{5/2}$ transition with the 729 nm laser at 45° with respect to the magnetic field B, pointing now perpendicularly to the HALO axis at which fluorescence light is collected and sent to a PMT. Optical pumping is facilitated by the 397 nm pump laser whose polarization is adjusted by a combination of a polarizing beam splitter (PBS), a quarter-wave (QWP) and half-wave plate (HWP).

are used for Doppler cooling and the 854 nm laser for repumping the residual population from the $D_{5/2}$ level after the coherent excitation with the 729 nm laser. The scattered fluorescence photons at 397 nm are collected with one HALO, coupled to a multi-mode fiber and detected with a PMT.

In the following we explain a typical laser sequence shown in Fig. 5.2 that is used to perform coherent manipulations on the 729 nm transition. The sequence starts with Doppler cooling followed by a optical-pumping period. In the third part, coherent manipulations on the 729 nm transition are executed. Finally, with the state detection period we discriminate with the 397 nm fluorescence, if the ion is in the $S_{1/2}$ or in the $D_{5/2}$ level. The sequence parts are now individually discussed in detail.

Doppler cooling

With the Doppler cooling technique we want to reduce the motion of the ion to achieve a low mean motional quantum number of the ion, as discussed in Sec. 2.2. Furthermore, efficient Doppler cooling provides a low damping in Rabi oscillations on the $S_{1/2}$ to $D_{5/2}$ transition and thus making a high population transfer from the $S_{1/2}$ to the $D_{5/2}$ level feasible [82]. It turns out, that the quality of Doppler cooling is very sensitive to the 397 nm and 866 nm laser parameters as the detunings and intensities. Once we have found the

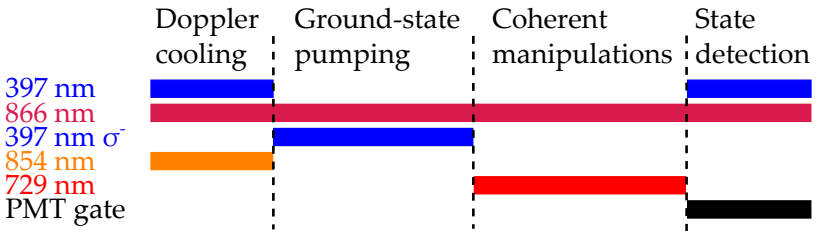

Figure 5.2.: Sequence for excitations on the $S_{1/2}$ to $D_{5/2}$ transition with coherent manipulations (variable durations), initialized by Doppler cooling (100 µs) and subsequent optical pumping (5 µs). The sequence ends with a state-detection phase (100 µs), incorporating fluorescence-sensitive state discrimination between the $S_{1/2}$ and $D_{5/2}$ level. For details see text.

best laser parameters for good Doppler cooling it becomes indispensable to have the same laser parameters every day. However, on this timescale the transfer cavities used for the laser stabilization scheme (cf. Sec. 1.2.2) experience barometric changes that cause a slight variation in the laser frequency once they are locked to the cavities. In order to compensate for these changes, we have to perform 866 nm spectroscopy every day to calibrate the 397 nm and 866 nm laser parameters for further measurements. With our pulse sequencer we apply a frequency sweep to the 866 nm AOM. For each frequency point we integrate the steady-state scattered fluorescence light at 397 nm for 100 ms integration time and obtain a fluorescence spectrum like the one in Fig. 5.3. The magnetic field lifts the degeneracy of

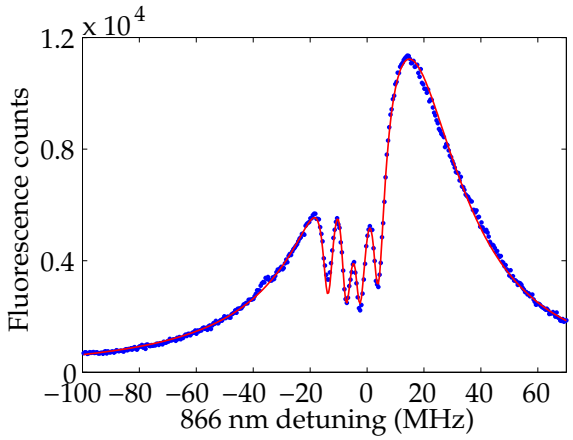

Figure 5.3.: 397 nm fluorescence spectrum for different 866 nm detuning; the red line is fitted to the data by numerically solving the Bloch equations. Around zero detuning, 4 dark resonances become clearly visible. From the fit we obtain a Rabi frequency for the 397 nm laser of $\Omega_{397} = 2\pi \cdot 6\,\mathrm{MHz}$ and a detuning from resonance by -14.4 MHz. The 866 nm laser has a Rabi frequency of $\Omega_{866} = 2\pi \cdot 13.4\,\mathrm{MHz}$.

the Zeeman substates. The 397 nm (vertically polarized) and the 866 nm laser (horizontally polarized) are both sent parallel to the quantization axis to the ion. As already pointed out in Sec. 3.2.2 we find for equal detunings of the 866 nm and 397 nm laser a decoupling from the $P_{1/2}$ state which leads with the laser polarizations and the Zeeman splitting to the appearance of 4 dark resonances. We see that the population in the $P_{1/2}$ level is reduced in the dark resonances by an amount which depends on the relative phase coherence between the two lasers. From fitting the Bloch equation model to the data we obtain the proper detunings for both lasers that leads to the lowest mean motional quantum number of the ion. With the best laser parameters, the ion is Doppler cooled in the sequence for a period of 100 µs, which is found as a trade-off between a proper cooling time and a high sequence repetition rate.

Ground-state pumping

In the second part of the sequence we optically pump the population to one of the two Zeeman substates in the $S_{1/2}$ level before we perform coherent manipulations on the $S_{1/2}$ to $D_{5/2}$ transition. In Fig. 5.4 the level scheme for ground-state pumping is depicted with all relevant transitions. With the circularly polarized 397 nm laser which is sent to the ion

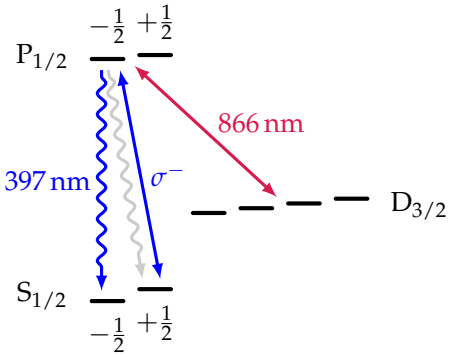

Figure 5.4.: Optical pumping of the population to the state $|S_{1/2}, -\frac{1}{2}\rangle$ with a σ^--polarized laser at 397 nm. The 866 nm laser counteracts the decay to the $D_{3/2}$ level.

anti-parallel to the magnetic field, we excite σ^- transitions from $|S_{1/2}, +\frac{1}{2}\rangle$ to $|P_{1/2}, -\frac{1}{2}\rangle$ from where it decays with a fraction of $\frac{1}{3}$, given by the Clebsch-Gordan coefficient, to the $|S_{1/2}, -\frac{1}{2}\rangle$ state. The 866 nm laser repumps the population from the $D_{3/2}$ level. With this configuration the 397 nm pump laser optically pumps the population to the $|S_{1/2}, -\frac{1}{2}\rangle$ state within 5 µs. We determine the pumping efficiency within this time to 99.88(1) % [107], limited by the non-perfect σ^- polarization of the 397 nm pump laser.

The successful pumping of the population into one substate allows us to completely transfer the population into one of the $D_{5/2}$ Zeeman substates with a resonant 729 nm laser pulse. Alternatively, the population is coherently distributed from $|S_{1/2}, +\frac{1}{2}\rangle$ or $|S_{1/2}, -\frac{1}{2}\rangle$

to different $D_{5/2}$ substates with controlled, subsequent 729 nm laser pulses for generating coherent superposition states in $D_{5/2}$ [82].

Coherent manipulations on the 729 nm transition

In the third part of the sequence, different 729 nm pulse sequences are executed, depending on the type of experiment, which results in a different duration for this sequence part. This contains sweeps of the laser frequency or laser pulse lengths as it is explained in Sec. 5.2. The adjustment of the 729 nm polarization allows us to excite the quadupole transition according to the selection rules $|\Delta m| = 0, 1, 2$. More precisely, with φ as the angle between the wavevector $\vec{k}$ and the magnetic field $\vec{B}$, and γ as the angle between the linear laser polarization and the direction of $\vec{B}$, the excitation of all transitions shown in Fig. 5.5 is enabled for the case that $\varphi = \gamma = 45°$ [82].

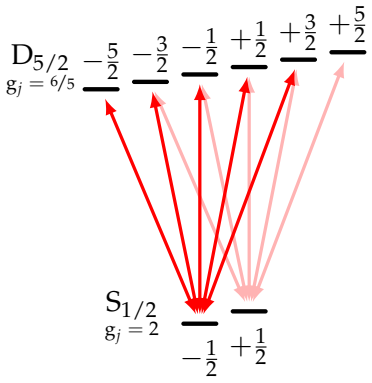

Figure 5.5.: The allowed quadrupole transitions between the Zeeman substates with selection rules $|\Delta m| = 0, 1, 2$ of the $S_{1/2}$ and $D_{5/2}$ level including the magnetic quantum numbers and the Landé factors g_j as the measure for the level splitting from the external magnetic field.

State-selective fluorescence detection

In the last part of the sequence, the 397 nm laser is switched on again with a laser frequency and power that is adjusted for a higher fluorescence rate as for the case of Doppler cooling and a counter in HYDRA records the photon clicks from the PMT for a 100 µs time gate for a decision if the ion is in the $S_{1/2}$ or $D_{5/2}$ state. If the rate of scattered fluorescence photons is high, then the detection projects the ion onto the $S_{1/2}$ level. If the ion is in the $D_{5/2}$ level, it remains dark and no photons (except detector dark counts and laser stray light) are detected. Thus the ion is projected onto the $D_{5/2}$ level. For a typical measurement, e.g. 729 nm spectroscopy, the total measurement range is divided into N measurement points. For each

measurement point, the sequence is repeated many times in order to obtain statistics to derive the $D_{5/2}$ state occupation in the following way: for each sequence cycle, the number of 397 nm fluorescence counts is integrated for a fixed time and compared to a threshold which is used to distinguish between the bright and dark level [126]. The threshold number of fluorescence counts is determined as the value for which the error probability for a wrong decision, i.e. the ion is identified to be in $S_{1/2}$ while it was in $D_{5/2}$ and vice versa, is minimized. For this criterion, we find the optimum integration time together with the requirement to have it short for fast sequence repetition rates to be 100 µs. If the ion is in the $S_{1/2}$ level, the typical fluorescence rate is $\sim 1.5 \cdot 10^5\,\mathrm{s}^{-1}$ while it is $100\,\mathrm{s}^{-1}$ for the case that the ion is in the $D_{5/2}$ level. For such scattering rates a histogram of the number of counts in 100 µs for a total number of repetitions of $2 \cdot 10^5$ is shown in Fig. 5.6. The optimum threshold for separating the two states is found to be 2, with an error probability of $1.3 \cdot 10^{-5}$ [82].

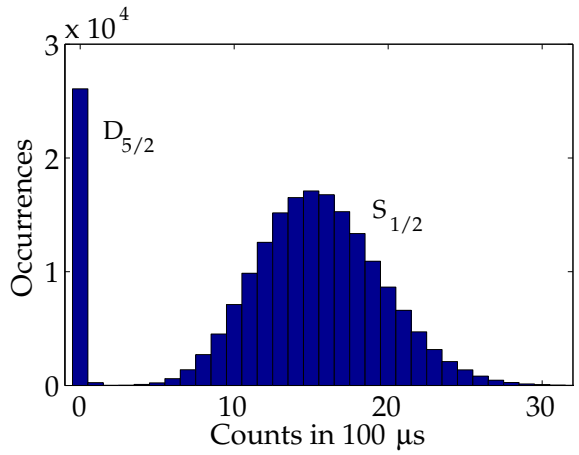

Figure 5.6.: Histogram for state discrimination between $D_{5/2}$ and $S_{1/2}$ for a state detection time of 100 µs. The 397 nm and 866 nm laser parameters are chosen such that the continuous scattering rate of fluorescence photons for $S_{1/2}$ is $1.55 \cdot 10^5\mathrm{s}^{-1}$ whereas the rate for $D_{5/2}$ is 100 s^{-1}. The optimum threshold for a distinction between the two states with the smallest error probability is at 2.

So far, we only know how to distinguish between the $S_{1/2}$ and $D_{5/2}$ level. In order determine the amount of population which is transferred from $S_{1/2}$ to $D_{5/2}$ during the coherent-manipulation phase, we use a Bayesian-inference approach, which is derived in [107] and summarized in App. A.2.

5.2. Carrier spectroscopy and pulse-length scan

After the introduction of a typical sequence we now present two examples for coherent operations during the coherent manipulation period.

Carrier spectroscopy

For resonant excitation of qubit transitions we have to know precisely the transition frequencies that are highly sensitive to magnetic field fluctuations. We see long-term drifts of the magnetic field as well as minor drifts of the high-finesse cavity to which the 729 nm laser is stabilized. Thus we perform spectroscopy on a daily basis between different Zeeman transitions from $S_{1/2}$ to $D_{5/2}$ to obtain the precise value of the transition frequency. We choose carrier transitions, i.e. those which do not change the motional state of the ion. After the ion is optically pumped to the $|S_{1/2}, -\frac{1}{2}\rangle$ state, the selection rules for the quadrupole transition $|\Delta m| = 0, 1, 2$ allow us to excite the ion on 5 different transitions as shown in Fig. 5.5. Fig. 5.7(a) depicts such a spectroscopy measurement on the carrier transition from $|S_{1/2}, -\frac{1}{2}\rangle$ to $|D_{5/2}, -\frac{5}{2}\rangle$. For a fixed pulse length of 200 µs and laser power in the range of 1 µW, the laser frequency is detuned by an AOM which is driven by the pulse sequencer HYDRA. The pulse width is chosen to be 200 µs, leading to a Fourier width of 800 Hz. This is still smaller then the incoherently broadened linewidth of the transition which we obtain from the fit (red line) of 2.69(5) kHz. The broadening is mainly given due to magnetic field fluctuations. With the resonance frequency that we obtain from the fit we perform a pulse-length scan which is discussed below.

Pulse-length scan

In order to coherently transfer the population with so called Rabi pulses from $S_{1/2}$ to $D_{5/2}$ we execute pulse-length scans to infer the duration t for different pulse areas, e.g. a π pulse, which is defined with the Rabi frequency Ω_R by the relation $\Omega_R \cdot t = \pi$. After we obtained the resonance frequency from spectroscopy, we set the AOM to the corresponding value and perform a pulse-length scan. The pulse-length scan is performed for the electron-shelving technique, i.e. through the transfer of the population of one $S_{1/2}$ Zeeman sublevel to one $D_{5/2}$ sublevel. There it is not sensitive anymore to the onset of the 397 nm cooling laser which discriminates between $S_{1/2}$ and $D_{5/2}$. Fig. 5.7(b) displays a pulse length scan on the $|S_{1/2}, -\frac{1}{2}\rangle$ to $|D_{5/2}, -\frac{5}{2}\rangle$ transition. The pulse length is varied from 0 to 10 µs in steps of 50 ns. For every time step the sequence is repeated 500 times to obtain statistics for calculating the $|D_{5/2}, -\frac{5}{2}\rangle$ occupation. The pulse-length scan is executed for an optical power of 63 mW. We see damped Rabi oscillations, where the damping originates from the thermal distribution of the ion's motion that leads to a thermal distribution of different Rabi frequencies [127]. Good Doppler cooling conditions are required in order to minimize this effect. For longer pulse-length scans, additional damping occurs due to magnetic field fluctuations that enters with the coherence time of $T_2^* = 340(3)$ µs, measured in a Ramsey

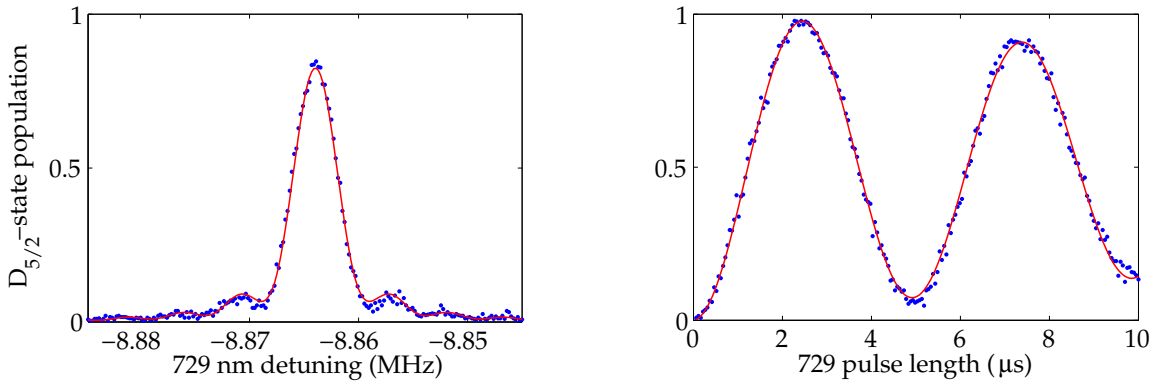

Figure 5.7.: (a) Pulsed spectroscopy on the $|S_{1/2}, -\frac{1}{2}\rangle$ to $|D_{5/2}, -\frac{5}{2}\rangle$ carrier transition for an optical power in the range of 1μW and a pulse length of 200 μs. For every frequency step of 200 Hz, the sequence is repeated 500 times. The fit (solid line) yields the resonance frequency to be at $-8.863\,95(2)$ MHz and a Rabi frequency of 2.63(3) kHz. (b) 729 nm pulse-length scan on the $|S_{1/2}, -\frac{1}{2}\rangle$ to $|D_{5/2}, -\frac{5}{2}\rangle$ transition for 63 mW optical power. The fit yields a Rabi frequency of 202.7(2) kHz and a duration for a π pulse of $t_\pi = 2.447(2)$ μs.

experiment for the $|S_{1/2}, -\frac{1}{2}\rangle$ to $|D_{5/2}, -\frac{5}{2}\rangle$ transition. The fit in Fig. 5.7(b) yields a maximum population in $|D_{5/2}, -\frac{5}{2}\rangle$ of 97.8(6) %. From the high value we see that we transfer almost all population with a π pulse from $|S_{1/2}, -\frac{1}{2}\rangle$ to $|D_{5/2}, -\frac{5}{2}\rangle$[1]. Now we are also able to generate coherent superposition states in $D_{5/2}$. For example, given that the population is initialized by optical pumping in $|S_{1/2}, -\frac{1}{2}\rangle$, a $\frac{\pi}{2}$ Rabi pulse on the $|S_{1/2}, -\frac{1}{2}\rangle$ to $|D_{5/2}, -\frac{5}{2}\rangle$ transition transfers 50 % of the population to $|D_{5/2}, -\frac{5}{2}\rangle$. A subsequent π pulse transfers the remaining population in $|S_{1/2}, -\frac{1}{2}\rangle$ to $|D_{5/2}, +\frac{3}{2}\rangle$, which generates the coherent superposition state of $\frac{1}{\sqrt{2}}\left(|D_{5/2}, -\frac{5}{2}\rangle + |D_{5/2}, +\frac{3}{2}\rangle\right)$. These states play an important role in single-photon interference experiments and are explained in more detail in Chapter 6.

5.3. Spectroscopy at 854 nm

After we prepare single Zeeman substates or even coherent superposition states in the $D_{5/2}$ level, the controlled transfer of this population within a Raman process to the $S_{1/2}$ ground state needs a precise knowledge of the 854 nm resonance frequency and the 854 nm Rabi frequency. Thereto we incorporate a sequence for 854 nm spectroscopy.

We perform 854 nm spectroscopy in a pulsed sequence according to the scheme shown in Fig. 5.2, but with an additional 854 nm pulse between the coherent-manipulation and the state-detection phase. In the coherent-manipulation phase, we perform a π pulse on

[1]Similar high values are also obtained if we perform π pulses to other $D_{5/2}$ Zeeman sublevels.

the $|S_{1/2}, -\frac{1}{2}\rangle$ to $|D_{5/2}, -\frac{5}{2}\rangle$ transition. From the $|D_{5/2}, -\frac{5}{2}\rangle$ state the 854 nm laser typically transfers the population via the $P_{3/2}$ level to the $S_{1/2}$ level within 3 µs, and we measure the remaining population $\rho_D(\Delta_{854})$ in $D_{5/2}$ as a function of the 854 nm detuning Δ_{854} by fluorescence-sensitive state detection. This is depicted in Fig. 5.8(a). We see that around zero detuning the 854 nm laser transfers most of the population to the $S_{1/2}$ level. We use the following relation

$$\rho_D(\Delta_{854}) = \rho_D(0) \cdot e^{-R_{D\to S}(\Delta_{854})T} \tag{5.1}$$

with the pulse duration T to solve this equation for the detuning-dependent repumping rate $R_{D\to S}(\Delta_{854})$ which is plotted Fig. 5.8(b). By fitting the relation in Eq. (2.43) to the data, the rate allows us to obtain directly the Rabi frequency Ω_{854} and the resonance frequency from the fit.

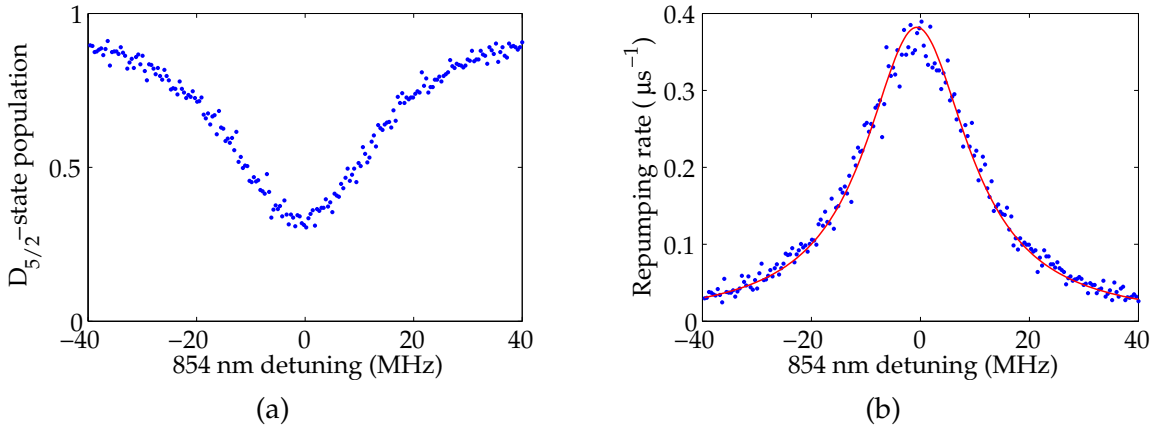

Figure 5.8.: 854 nm spectroscopy on the $|D_{5/2}, -\frac{5}{2}\rangle$ to $|P_{3/2}, -\frac{3}{2}\rangle$ transition for 1 µW of optical power. (a) The remaining $|D_{5/2}, -\frac{5}{2}\rangle$-state population as a function of the 854 nm detuning for a 854 nm pulse duration of 3 µs. (b) Repumping rate $R_{D\to S}$ as a function of the 854 nm detuning. The fit (red solid line) yields the resonance frequency at $-0.67(9)$ MHz and a Rabi frequency $\Omega_{854} = 1.222(4)$ MHz.

Summary

In this chapter I presented the experimental tools for atomic state preparation in the $S_{1/2}$ and the $D_{5/2}$ level. With the 866 nm spectroscopy we obtained laser parameters for efficient Doppler cooling. In order to coherently distribute the population from the $S_{1/2}$ level to the Zeeman substates in the $D_{5/2}$ level we first initialized all the population in $|S_{1/2}, -\frac{1}{2}\rangle$ by ground-state pumping with an efficiency of 99.88(1) %. Together with the state-selective fluorescence detection we showed a 729 nm carrier spectroscopy and a 729 nm pulse-length scan. The latter yielded after a π pulse a population in $|D_{5/2}, -\frac{5}{2}\rangle$ of 97.8(6) %. Finally we

showed the 854 nm spectroscopy to obtain precise values for the 854 nm detuning and Rabi frequencies.

With all these techniques at hand we are able to prepare specific Zeeman substates and coherent superposition states in $D_{5/2}$. With the precise knowledge of the 854 nm detuning and Rabi frequency we can analyze how the coherent superposition states in the $D_{5/2}$ level are transferred into the 393 nm Raman scattering process which is the content of Chapter 6.

6. Quantum interference for quantum networking experiments

After we introduced the tools enabling coherent manipulations on the qubit transition and having the spectroscopy techniques at hand, we are now able to study a new type of spontaneous Raman scattering process, which includes quantum interference phenomena. The latter goes back to the early description of quantum mechanics, where the appearance of quantum beats caused by interference of emission paths from excited atoms was already predicted [128]. In current quantum-network experiments with single atoms as nodes and single photons transferring information between them [36, 31], quantum interference is an essential feature which allows for entangling the nodes [44, 40, 43] and employing coherent phenomena at atom-photon interfaces to faithfully convert quantum information between photonic communication channels and atomic quantum processors [37]. As our group investigated such an interface concerning the controlled absorption of photons by a single ion and the emission of photons from a single ion, we proceed with the investigation of the quantum-coherent character of the absorption and emission of single photons through the interference between indistinguishable quantum channels in a single atom. The major part of the following chapter is also found again in our publication [129].

Experimental evidence of quantum beats was first observed for pulsed optical excitation of atoms with two excited states decaying to the same ground state [130], and later for continuous excitation with a coherent superposition state in a calcium cascade [131] and in cavity-mediated systems with coherent ground states [132]. For a single trapped ion, transient effects of the internal dynamics showed oscillations in scattered photons through interference in absorption [133].

In the following chapter we describe the controlled generation of quantum beats in a spontaneous Raman-scattering process of single 393 nm photons by the absorption of 854 nm laser photons in two distinct excitation schemes, called Λ and V. For both schemes we utilize the control of the qubit transition at 729 nm to generate a coherent superposition state of two Zeeman substates in the metastable $D_{5/2}$ manifold. After a theoretical introduction in Sec. 6.2 we present arrival-time distributions of detected 393 nm photons in Sec. 6.3, which reveal quantum beats that are controlled through changes of the phase in the atomic superposition and the polarization of the photonic input state. We further analyze the phase-dependent photon scattering probability in Sec. 6.4 and finally reveal the two distinct physical origins of the quantum beats in Sec. 6.5, namely, quantum interference of two 854 nm absorption amplitudes and two 393 nm emission amplitudes, respectively. The two absorption-emission pathways resemble a which-way experiment where

indistinguishability is maintained by a quantum eraser [134].

6.1. Experimental setup and sequence

The experimental setup is illustrated in Fig. 6.1 and shows all lasers involved in the sequence except the two cooling lasers at 397 nm and 866 nm which are omitted for the sake of clarity.

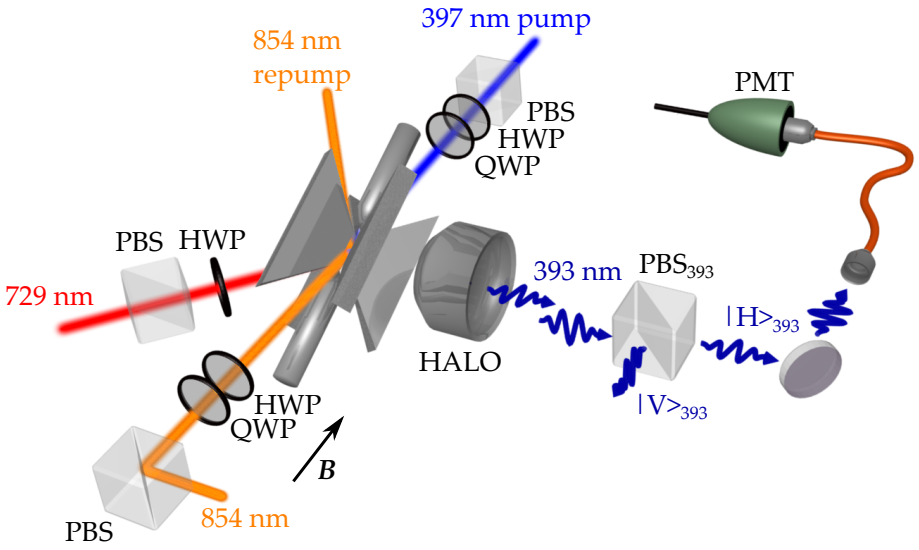

Figure 6.1.: Schematic of the experimental setup: of the various laser beams, we emphasize the 854 nm laser which is sent to the ion parallel to the magnetic field and whose polarization is adjusted by a combination of a polarizing beam splitter (PBS), quarter-wave plate (QWP) and half-wave plate (HWP). The detection of Raman scattered 393 nm photons is performed perpendicular to the quantization axis. With the PBS_{393} the polarization is projected onto a linear basis, i.e. we only transmit horizontally polarized photons $|H\rangle_{393}$, while the vertically polarized ones $|V\rangle_{393}$ are reflected to the side. With a rotation of the PBS_{393} by 90° we swap the transmitted photons to $|V\rangle_{393}$ and the reflected to $|H\rangle_{393}$, respectively. In this configuration the $|H\rangle_{393}$ photons are reflected upwards. The transmitted photons are coupled to a multi-mode fiber and detected with a photomultiplier tube (PMT).

The sequence is shown in Fig. 6.2. It starts with 25 µs of Doppler cooling of the ion on the $S_{1/2}$-$P_{1/2}$ transition, facilitated by a 397 nm laser and an 866 nm laser, repumping the population from the metastable $D_{3/2}$ level. The 854 nm repump laser from 45° with respect to the quantization axis takes any remaining population in $D_{5/2}$ from the preceding cycle into the cooling cycle. Subsequently, a right-handed circularly polarized 397 nm pump beam which is sent to the ion anti-parallel to the magnetic-field direction serves for optically

pumping the ion to the $|S_{1/2}, -\frac{1}{2}\rangle$ state within 5 µs. With two pulses from the 729 nm laser entering under 45° we create a coherent superposition state in $D_{5/2}$ which is excited to the $P_{3/2}$ level by the absorption of an 854 nm laser photon. The 854 nm laser is sent along the quantization axis with controlled polarization, set by a combination of a PBS, QWP and HWP. The Raman-scattered 393 nm photons are collected by the HALO perpendicularly to the quantization axis and are filtered by their polarization degree of freedom through a projection onto a linear polarization basis. Fig. 6.1 shows the transmission for horizontally polarized photons $|H\rangle_{393}$. By a rotation of the PBS by 90°, we can swap to vertically polarized photons $|V\rangle_{393}$ in transmission. In both cases, the photons are multi-mode fiber coupled and detected by a PMT within the photon-generation period. Alternatively we open the PMT gate after the photon-generation period, i.e. we collect 397 nm fluorescence photons during state detection for $D_{5/2}$ population-analysis experiments.

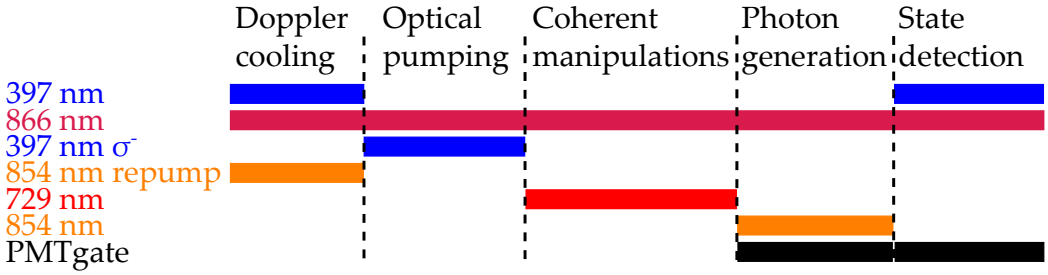

Figure 6.2.: Experimental sequence composed of Doppler cooling for 25 µs followed by optical pumping to $|S_{1/2}, -\frac{1}{2}\rangle$ for 5 µs. Subsequently, a sequence of two 729 nm pulses creates a coherent superposition state in $D_{5/2}$. Depending on the experiment we open the PMT gate for detecting 393 nm photons in the photon-generation period or analyze the remaining population in $D_{5/2}$ after photon absorption in the state-detection period.

6.2. Theoretical analysis

Before we show experimental results, we first introduce a compact theoretical description of the population transfer from $D_{5/2}$ to $S_{1/2}$, which emphasizes the coherent evolution of the internal states for the two different level configurations. Fig. 6.3 shows the Λ- and V-type level configuration with the relevant transitions and the squared Clebsch-Gordan coefficients (CGCs). After the preparation of the $|S_{1/2}, -\frac{1}{2}\rangle$ state, two 729 nm laser pulses initialize a coherent superposition state for both schemes,

$$|\psi_D(t)\rangle = \sqrt{\rho_1}\,|D_{5/2}, m_D\rangle + e^{i\Phi_D(t)}\sqrt{\rho_2}\,|D_{5/2}, m_{D'}\rangle\ , \tag{6.1}$$

with populations ρ_1 and ρ_2 adjusted by two consecutive resonant pulses from $|S_{1/2}, -\frac{1}{2}\rangle$. With the superposition state, the ion starts to precess in the magnetic field with the Larmor frequency. The phase $\Phi_D(t) = \Phi_D(0) + \omega_L t$ is composed of a starting phase $\Phi_D(0)$ which

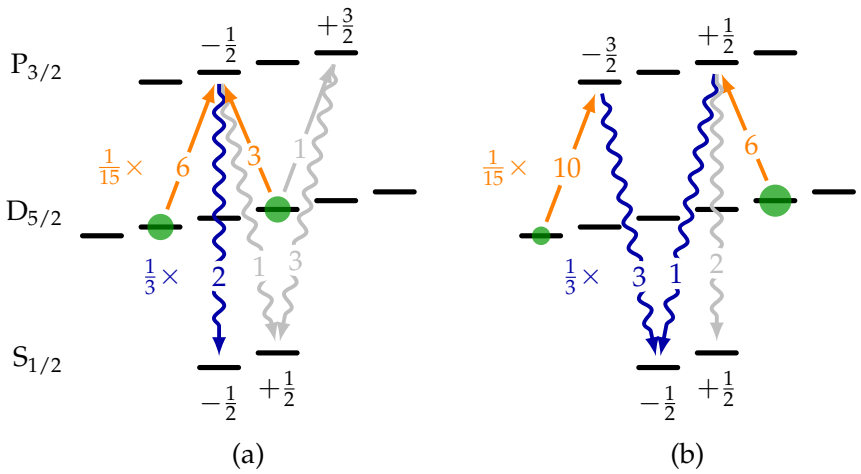

Figure 6.3.: (a) The Λ-shaped system consisting of $|D_{5/2}, -\frac{3}{2}\rangle$, $|D_{5/2}, +\frac{1}{2}\rangle$ and $|P_{3/2}, -\frac{1}{2}\rangle$, including the relevant transitions with their squared Clebsch-Gordan coefficients. (b) The V-shaped three-level system consisting of $|P_{3/2}, -\frac{3}{2}\rangle$, $|P_{3/2}, +\frac{1}{2}\rangle$ and $|S_{1/2}, -\frac{1}{2}\rangle$, including the relevant transitions with their squared Clebsch-Gordan coefficients. Orange arrows: absorption of 854 nm photons (σ^+ and σ^-). Blue wavy arrows: emission of 393 nm photons. Gray: parasitic absorption (854 nm) and emission channels (393 nm).

is set by our sequence controller HYDRA as the relative phase between the two 729 nm pulses and a part oscillating at the Larmor frequency

$$\nu_L = \frac{\mu_B}{h} \cdot \Delta m_j \cdot g_j \cdot B, \tag{6.2}$$

including the magnetic field B, the Landé factor $g_j = 6/5$ and the Bohr magneton μ_B. The polarization state of the laser photons at 854 nm is defined as a superposition of two orthogonal states, namely right ($|R\rangle$) and left ($|L\rangle$) circularly polarized light

$$|\psi_{854}\rangle = \cos\tfrac{\vartheta}{2}\,|R\rangle + \sin\tfrac{\vartheta}{2} e^{i\Phi_{854}}\,|L\rangle\,. \tag{6.3}$$

Any linear photonic polarization state, such as horizontal $|H\rangle$, vertical $|V\rangle$, diagonal $|D\rangle$, and antidiagonal $|A\rangle$ is adjusted by rotating the two wave plates (see Fig. 6.1) in the optical path of the 854 nm laser to change Φ_{854}, while ϑ is fixed to $\frac{\pi}{2}$. With the propagation direction of the incoming laser photons parallel to the applied magnetic field, the photon polarization translates into the reference frame of the atom according to

$$|\psi_{854}\rangle = \cos\tfrac{\vartheta}{2}\,|+1\rangle + \sin\tfrac{\vartheta}{2} e^{i\Phi_{854}}\,|-1\rangle\,, \tag{6.4}$$

whereby $|m_{854}\rangle = |\pm 1\rangle$ stands for the photon polarizations that effect $\Delta m = \pm 1$ (i.e. $\sigma^{\pm}$) transitions, respectively, between the Zeeman sublevels of $D_{5/2}$ and $P_{3/2}$. The coupled quantum system is represented by a joint state between photon and atom,

$$|\psi(t)\rangle = |\psi_D(t)\rangle \otimes |\psi_{854}\rangle\,. \tag{6.5}$$

We use our well-established formalism from [102] and describe the absorption process by the following absorption operator

$$\hat{A} = \sum_{m_\mathrm{D}, m_\mathrm{P}} C_{m_\mathrm{D}, m_{854}, m_\mathrm{P}} \, \tilde{c}_{m_\mathrm{D}, m_\mathrm{P}}(\Delta) \, |m_\mathrm{P}\rangle \, \langle m_\mathrm{D}| \, \langle m_{854}| \tag{6.6}$$

where $m_{854} = 0, \pm 1$, and $C_{m_\mathrm{D}, m_{854}, m_\mathrm{P}}$ are the Clebsch-Gordan coefficients (CGCs)[1]. The proper description of the absorption process requires taking into account the detuning-dependent atomic response

$$\tilde{c}_{m_\mathrm{D}, m_\mathrm{P}}(\Delta) = |\tilde{c}(\Delta)| e^{i\phi(\Delta)} \tag{6.7}$$

which has a complex Lorentzian lineshape with linewidth $\Gamma_{\mathrm{P}_{3/2}}$ and contains the atomic phase response $\phi(\Delta)$ for different detunings Δ of the absorbed laser photons. Since the absorption takes place on two absorption channels we expect the phase difference between the two atomic phase responses to appear in the Raman scattering process as a function of the detuning, which is currently under investigation. Here the 854 nm detuning is fixed which results in a constant phase offset. We combine these coefficients according to

$$C_{m_\mathrm{D}, m_{854}, m_\mathrm{P}} \, \tilde{c}_{m_\mathrm{D}, m_\mathrm{P}}(\Delta) = c_{m_\mathrm{D}, m_\mathrm{P}}(\Delta) \tag{6.8}$$

using $m_\mathrm{P} = m_\mathrm{D} + m_{854}$. $\Delta = \omega_\mathrm{l} - \omega_0$ is the detuning between the laser frequency ω_l and the $\mathrm{D}_{5/2}$ to $\mathrm{P}_{3/2}$ line center ω_0, which is the frequency of the $\mathrm{D}_{5/2}$ to $\mathrm{P}_{3/2}$ transition for zero magnetic field. The frequency of the line center is determined by 854 nm spectroscopy on one of the two transitions. The detuning is then used to compensate for the different CGCs in the two absorption channels (see Fig. 6.3), which is explained in detail in App. A.3.

After the absorption, the ion decays in a spontaneous (Raman) emission process to the $\mathrm{S}_{1/2}$ ground state, described by the emission operator

$$\hat{E} = \sum_{m_\mathrm{S}, m_\mathrm{P}} C_{m_\mathrm{P}, m_{393}, m_\mathrm{S}} \, |m_{393}\rangle \, |m_\mathrm{S}\rangle \, \langle m_\mathrm{P}| \,, \tag{6.9}$$

with $m_{393} = 0, \pm 1$, corresponding to the transitions $\Delta m = \pi, \sigma^\pm$. Applying the absorption and emission operator to the joint state of Eq. (6.5) gives $\hat{E}\hat{A} \, |\psi(t)\rangle$, a new joint state of the atom in $\mathrm{S}_{1/2}$ and a single photon in the 393 nm mode. Since we collect only photons with a certain polarization from transitions which ends in $\left|\mathrm{S}_{1/2}, -\frac{1}{2}\right\rangle$ the detection of the 393 nm photon projects the joint state onto $\left|\mathrm{S}_{1/2}, -\frac{1}{2}\right\rangle$. In the following the theoretical description is treated in more detail for both schemes.

6.2.1. Quantum interference in absorption: the Λ system

For the Λ-shaped level configuration, the ion is initially prepared in the state $\left|\mathrm{S}_{1/2}, -\frac{1}{2}\right\rangle$. The first resonant $\frac{\pi}{2}$ pulse at 729 nm transfers 50 % of the population to $\left|\mathrm{D}_{5/2}, +\frac{1}{2}\right\rangle$ while

[1] The definition that we use for the CGCs is related to "standard" notations through $C_{m_\mathrm{D}, m_{854}, m_\mathrm{P}} = C^{5/2,1,3/2}_{m_\mathrm{D}, m_{854}, m_\mathrm{P}} = \langle 5/2, m_\mathrm{D}; 1, m_{854} | 5/2, 1, 3/2, m_\mathrm{P}\rangle$, and likewise for $C_{m_\mathrm{P}, m_{393}, m_\mathrm{S}}$

the remaining population is transferred to $\left|\mathrm{D}_{5/2}, -\frac{3}{2}\right\rangle$ with a π pulse, which results in the coherent superposition state

$$|\psi_{\mathrm{D}}(t)\rangle = \sqrt{\tfrac{1}{2}}\left(\left|\mathrm{D}_{5/2}, -\tfrac{3}{2}\right\rangle + e^{i\Phi_{\mathrm{D}}(t)}\left|\mathrm{D}_{5/2}, +\tfrac{1}{2}\right\rangle\right). \tag{6.10}$$

Applying the absorption operator to the joint state gives

$$\begin{aligned}\hat{A}\,|\psi(t)\rangle = &\sqrt{\tfrac{1}{2}}\cos\tfrac{\vartheta}{2}\; c_{-3/2,-1/2}(\Delta)\left|\mathrm{P}_{3/2}, -\tfrac{1}{2}\right\rangle \\ &+ \sqrt{\tfrac{1}{2}}\sin\tfrac{\vartheta}{2}\; c_{+1/2,-1/2}(\Delta)\; e^{i\Phi_{\mathrm{D}}(t)}e^{i\Phi_{854}}\left|\mathrm{P}_{3/2}, -\tfrac{1}{2}\right\rangle \\ &+ \sqrt{\tfrac{1}{2}}\cos\tfrac{\vartheta}{2}\; c_{+1/2,+3/2}(\Delta)\; e^{i\Phi_{\mathrm{D}}(t)}\left|\mathrm{P}_{3/2}, +\tfrac{3}{2}\right\rangle.\end{aligned} \tag{6.11}$$

Highest visibility of the quantum beats is expected when the interfering transitions have equal weights. The amplitudes of the two absorbing paths are determined by the detuning Δ, which is adjusted in order to compensate for the two different CGCs, i.e. such that $|c_{-3/2,-1/2}(\Delta)| = |c_{+1/2,-1/2}(\Delta)| = c$. For a linear photonic polarization state ($\vartheta = \frac{\pi}{2}$) it follows

$$\begin{aligned}\hat{A}\,|\psi(t)\rangle = &\tfrac{1}{2}c\left(1 + e^{i\Phi_{\mathrm{D}}(t)}e^{i\Phi_{854}}\right)\left|\mathrm{P}_{3/2}, -\tfrac{1}{2}\right\rangle \\ &+ c'\tfrac{1}{2}e^{i\Phi_{\mathrm{D}}(t)}\left|\mathrm{P}_{3/2}, +\tfrac{3}{2}\right\rangle.\end{aligned} \tag{6.12}$$

with $c' = c_{+1/2,+3/2}(\Delta)$. Here the term $\left(1 + e^{i\Phi_{\mathrm{D}}(t)}e^{i\Phi_{854}}\right)$ already shows the temporal interference of the two absorption paths in the amplitude of $\left|\mathrm{P}_{3/2}, -\frac{1}{2}\right\rangle$ which oscillates with the Larmor frequency. The transfer of this oscillation to the emitted 393 nm photons is obtained by applying the emission operator $\hat{E}$,

$$\begin{aligned}\hat{E}\hat{A}\,|\psi(t)\rangle = &\sqrt{\tfrac{1}{6}}c\left(1 + e^{i\Phi_{\mathrm{D}}(t)}e^{i\Phi_{854}}\right)|0\rangle\left|\mathrm{S}_{1/2}, -\tfrac{1}{2}\right\rangle \\ &+ \sqrt{\tfrac{1}{12}}c\left(1 + e^{i\Phi_{\mathrm{D}}(t)}e^{i\Phi_{854}}\right)|-1\rangle\left|\mathrm{S}_{1/2}, +\tfrac{1}{2}\right\rangle \\ &+ \sqrt{\tfrac{1}{8}}c'e^{i\Phi_{\mathrm{D}}(t)}\,|+1\rangle\left|\mathrm{S}_{1/2}, +\tfrac{1}{2}\right\rangle.\end{aligned} \tag{6.13}$$

As it is known from many quantum-interference experiments, the which-way information of the interfering paths is strongly connected with the amount of quantum interference one observes. The interference completely vanishes, if one knows which path the quantum particle takes while it is fully available, if there is no which-way information [135]. For the interference experiment with single 393 nm photons this means that keeping indistinguishability between the two interfering scattering channels is crucial to maintain the interference in the 393 nm scattered photon. As it is seen from (Fig. 6.3(a)), the indistinguishability is guaranteed if the two absorption paths share the same emission channel, which means that out of the three different decay channels, a selection of $\Delta m = 0$, i.e. of π-photons will keep the quantum-interference character. A π-photon detected perpendicularly to the magnetic field transforms to an $|\mathrm{H}\rangle$-polarized photon in the photonic reference

frame. The detection of these photons leads a projection $\hat{\pi} := |0\rangle\langle 0|$ of the joint state of Eq. (6.13) onto $\left|S_{1/2}, -\frac{1}{2}\right\rangle$. The intensity of the emitted light is derived as

$$I \propto \tfrac{1}{3}c^2(1 + \cos(\Phi_D(t) + \Phi_{854})) \tag{6.14}$$

and shows the capability to be controlled by changing the photonic input phase Φ_{854} or the atomic superposition phase $\Phi_D(t)$ through the offset phase $\Phi_D(0)$. We note again that interference happens in the absorption process, since two pathways lead to the same excited intermediate state before the emission process takes place.

Influence of interference on the Raman scattered photons

From the angular distribution of the emission probability per time for π transitions, as given in Eq. (2.72), we can formulate the time-dependent intensity distribution of π photons at 393 nm, emitted on the transition from $\left|P_{3/2}, -\frac{1}{2}\right\rangle$ to $\left|S_{1/2}, -\frac{1}{2}\right\rangle$. As this is a $\Delta m = q = 0$ transition, we describe the intensity using the spherical harmonic $Y_{1q}(\theta, \varphi)$ as

$$I \propto |Y_{10}(\theta, \varphi)|^2 \sin^2\theta\,(1 + \cos(\Phi_D(t) + \Phi_{854})) \tag{6.15}$$

Fig. 6.4 illustrates the emission for five different times t within one oscillation period with the Larmor frequency ω_L, corresponding to five phase angles. Depending on the phase angle we see the repetitive appearance and disappearance of the π photon emission pattern, reflecting the constructive and destructive interference that occurs in the two 854 nm absorption channels. The figure also shows the direction of the magnetic field B (black arrow) and the solid angle covered by the HALO.

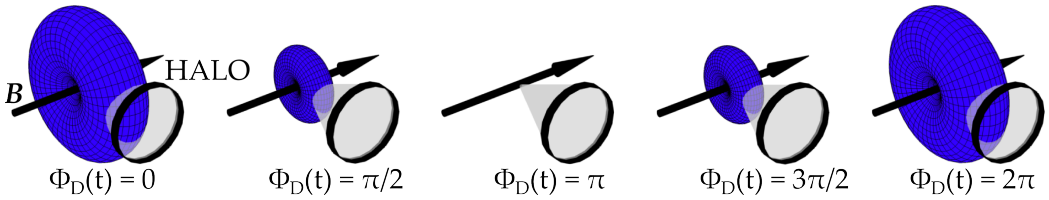

Figure 6.4.: Simulated intensity distribution of the dipolar emission pattern for the π transition from $\left|P_{3/2}, -\frac{1}{2}\right\rangle$ to $\left|S_{1/2}, -\frac{1}{2}\right\rangle$ which is modulated with the Larmor frequency of the superposition state in $D_{5/2}$. With the time-dependent phase $\Phi_D(t) = \omega_L t$ the emission profile is shown for five times t corresponding to five different phase angles. It shows that the emission of 393 nm photons pulsates perpendicularly to the magnetic-field direction B (black arrow) into the solid angle (gray cone) covered by the HALO.

6.2.2. Quantum interference in emission: the V system

The V-type configuration and the corresponding excitation scheme for the generation of 393 nm photons is shown in Fig. 6.3(b). In contrast to the Λ-type configuration there are

two emission channels (see blue wavy arrows in Fig. 6.3(b)) with different CGCs that are involved in the interference process. To achieve a high visibility in the interference fringes the two absorption and emission amplitudes should be equal. The different CGCs in the absorption channels are compensated by the 854 nm detuning, similar to the Λ scheme.

The unequal CGCs of the two 393 nm decay channels are compensated for by an unequal initial population distribution in $D_{5/2}$ as explained in the following. For this we consider first the two decay channels from $\left|P_{3/2}, +\frac{1}{2}\right\rangle$. From the ratio of the two CGCs we see that the probability to decay from $\left|P_{3/2}, +\frac{1}{2}\right\rangle$ to $\left|S_{1/2}, -\frac{1}{2}\right\rangle$ is only one third to the probability to decay to $\left|S_{1/2}, +\frac{1}{2}\right\rangle$. This means that if we transfer 75 % of the total population to $\left|P_{3/2}, +\frac{1}{2}\right\rangle$ only 25 % decays via one of the interfering emission channels. As the population in $\left|P_{3/2}, -\frac{3}{2}\right\rangle$ totally decays to $\left|S_{1/2}, -\frac{1}{2}\right\rangle$ we have to transfer the same population value of 25 % to $\left|P_{3/2}, -\frac{3}{2}\right\rangle$ to reach the same emission amplitudes for both decay channels, i.e. $\left|P_{3/2}, -\frac{3}{2}\right\rangle$ to $\left|S_{1/2}, -\frac{1}{2}\right\rangle$ and $\left|P_{3/2}, +\frac{1}{2}\right\rangle$ to $\left|S_{1/2}, -\frac{1}{2}\right\rangle$ and thus the highest visibility.

Starting in the eigenstate $\left|S_{1/2}, -\frac{1}{2}\right\rangle$, the first resonant 729 nm pulse transfers 75 % of the population to $\left|D_{5/2}, +\frac{3}{2}\right\rangle$. The remaining population is subsequently transferred to $\left|D_{5/2}, -\frac{5}{2}\right\rangle$ with a π-pulse, resulting in the coherent superposition state

$$|\psi_D(t)\rangle = \sqrt{\tfrac{1}{4}}\left|D_{5/2}, -\tfrac{5}{2}\right\rangle + e^{i\Phi_D(t)}\sqrt{\tfrac{3}{4}}\left|D_{5/2}, +\tfrac{3}{2}\right\rangle. \tag{6.16}$$

Applying the absorption operator (Eq. (6.6)) to the joint state gives

$$\begin{aligned}\hat{A}\,|\psi(t)\rangle = &\sqrt{\tfrac{1}{4}}\cos\tfrac{\vartheta}{2}\; c_{-5/2,-3/2}(\Delta)\left|P_{3/2}, -\tfrac{3}{2}\right\rangle \\ &+ \sqrt{\tfrac{3}{4}}\sin\tfrac{\vartheta}{2}\; c_{+3/2,+1/2}(\Delta)\; e^{i\Phi_D(t)}e^{i\Phi_{854}}\left|P_{3/2}, +\tfrac{1}{2}\right\rangle.\end{aligned} \tag{6.17}$$

The two different CGCs on the 854 nm absorption channels are again compensated for by two different 854 nm repumping rates, set by adjusting the detuning Δ such that we write $|c_{-5/2,-3/2}(\Delta)| = |c_{+3/2,+1/2}(\Delta)| = c$. For a linear 854 nm polarization with phase Φ_{854}, we find

$$\hat{A}\,|\psi(t)\rangle = \sqrt{\tfrac{1}{8}}c\left|P_{3/2}, -\tfrac{3}{2}\right\rangle + \sqrt{\tfrac{3}{8}}c\; e^{i\Phi_D(t)}e^{i\Phi_{854}}\left|P_{3/2}, +\tfrac{1}{2}\right\rangle. \tag{6.18}$$

Applying the emission operator (6.9) results in

$$\begin{aligned}\hat{E}\hat{A}\,|\psi(t)\rangle = &\left(|-1\rangle + e^{i\Phi_D(t)}e^{i\Phi_{854}}\,|+1\rangle\right)\sqrt{\tfrac{1}{8}}c\left|S_{1/2}, -\tfrac{1}{2}\right\rangle \\ &+ \tfrac{1}{2}c\; e^{i\Phi_D(t)}e^{i\Phi_{854}}\,|0\rangle\left|S_{1/2}, +\tfrac{1}{2}\right\rangle.\end{aligned} \tag{6.19}$$

The first term in this state shows the oscillating phase between two atomic ($\sigma^{\pm}$) transitions leading to interference of two emission channels when they are projected onto the same axis to keep the indistinguishability in the polarization degree of freedom. The measurement of the photonic superposition $|V\rangle = \sqrt{\frac{1}{2}}\left(|\sigma^+\rangle - |\sigma^-\rangle\right)$ projects the joint state of Eq. (6.19) onto $\left|S_{1/2}, -\frac{1}{2}\right\rangle$ which results in the intensity

$$I \propto \tfrac{1}{8}c^2(1 - \cos\left(\Phi_D(t) + \Phi_{854}\right)), \tag{6.20}$$

showing again oscillations at the Larmor frequency. The second term in (6.19) describes the emission of parasitic π-photons which transforms in the photonic reference frame to $|\mathrm{H}\rangle$. They are suppressed by rotating the PBS by 90° with respect to the Λ-case.

Influence of interference on the Raman scattered photons

In contrast to the Λ scheme, the two absorption channels are followed by two emission channels from $\left|\mathrm{P}_{3/2}, +\frac{1}{2}\right\rangle$ and $\left|\mathrm{P}_{3/2}, -\frac{3}{2}\right\rangle$ to the common ground state $\left|\mathrm{S}_{1/2}, -\frac{1}{2}\right\rangle$, corresponding to a $\Delta m = q = +1$ and $\Delta m = q = -1$ transition. Thus the interference occurs in the emission process, i.e. we formulate the intensity of the emission pattern by the superposition of two spherical harmonics $Y_{1q}(\theta, \varphi)$ as

$$I \propto \left| Y_{1\,+1}(\theta, \varphi) + e^{i(\Phi_{\mathrm{D}}(t)+\Phi_{854})} Y_{1\,-1}(\theta, \varphi) \right|^2 \frac{1}{2}(1 + \cos^2\theta) \tag{6.21}$$

For the simulation shown in Fig. 6.5, we set the photonic phase Φ_{854} and atomic phase $\Phi_{\mathrm{D}}(0)$ to zero and present the dipolar emission pattern for five different phase angles, i.e. five different times t. Within one Larmor period we now see a rotation of the dipolar emission pattern about the quantization axis due to a superposition of σ^- and σ^+, which leads to a temporal modulation of the detected photons in the direction perpendicular to that axis.

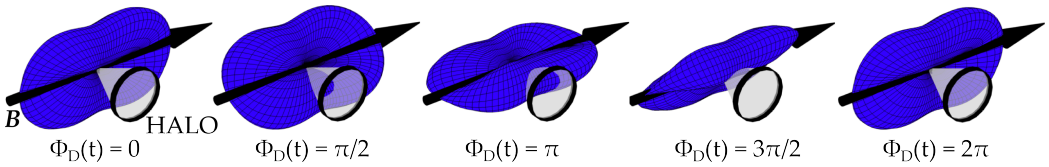

Figure 6.5.: Intensity profile of the 393 nm dipolar emission pattern of the superposition of σ^+ and σ^- Raman-scattered photons, whose frequency difference leads to a rotation about the quantization axis given by the magnetic-field direction B (black arrow). The collection of the photons with the HALO perpendicularly to the magnetic field transforms in the photonic reference frame to $|\mathrm{V}\rangle$ polarization, making both emission channels indistinguishable.

6.3. Quantum beats in arrival-time distributions

After the theoretical introduction we present the experimental results in the following sections. An inherent experimental requirement for quantum interference between two scattering paths is to keep indistinguishability in all degrees of freedom of the involved quantum channels. In the Λ- and V-type level configuration, the two absorption channels exhibit a frequency difference originating from the differential Zeeman shift of the two

$D_{5/2}$ sublevels, up to ∼20 MHz for typical magnetic fields of ∼3 G. The PMT time resolution of 300 ps sets a much lower frequency resolution and thus erases the information of this frequency splitting [136]. The indistinguishability concerning the polarization is attained by the detection perpendicular to the magnetic field of only $|H\rangle$-polarized or only $|V\rangle$-polarized 393 nm photons (i.e. polarization parallel or orthogonal to the quantization axis, respectively).

In the following we present the results for the Λ scheme. For this we first perform 729 nm spectroscopy on the $|S_{1/2}, -\frac{1}{2}\rangle$ to $|D_{5/2}, -\frac{3}{2}\rangle$ transition and on the $|S_{1/2}, -\frac{1}{2}\rangle$ to $|D_{5/2}, +\frac{1}{2}\rangle$ yielding a frequency difference between the two transition frequencies of 9.4 MHz which leads to a Larmor period of 106.4 ns. With the Larmor frequency we determine the magnetic field at the position of the ion to 2.8 G. The superposition state as given in Eq. (6.10) is created by a first resonant $\frac{\pi}{2}$ pulse (1.68 µs) on the $|S_{1/2}, -\frac{1}{2}\rangle$ to $|D_{5/2}, +\frac{1}{2}\rangle$ transition followed by a resonant π pulse (2.38 µs) on the $|S_{1/2}, -\frac{1}{2}\rangle$ to $|D_{5/2}, -\frac{3}{2}\rangle$ transition. Then we calculate the ideal detuning in order to achieve equal repumping rates on both transitions as presented in App. A.3. With the 854 nm laser detuning of -15 MHz, the power of 50 µW and vertical polarization[2], we generate 393 nm photons with an arrival time distribution that is shown as the blue circles in Fig. 6.6. We see that the exponential decay

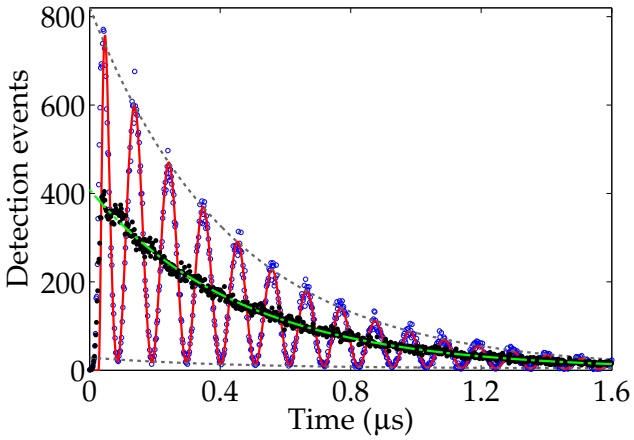

Figure 6.6.: Λ scheme: arrival-time distribution of single 393 nm photons from a coherent superposition (blue circles) and a statistical mixture (black dots) in $D_{5/2}$. Red line: fit to the data by numerically solving the 18-level Bloch equations; green dash-dotted line: exponential fit to the data for the mixture; gray dotted line: exponential fit to the envelope of the oscillation from which the visibility is determined. The bin size is 2 ns with a total measurement time of 10 min.

of the photon wave packet is modulated with a period of 106 ns, in agreement with what we found earlier by the frequency difference of the initially populated Zeeman sublevels.

[2]Note that all the following measurements in this chapter are performed with vertically polarized 854 nm light, as long as the polarization is not changed within one measurement.

The data points are fitted by numerically solving the optical Bloch equations, including all relevant sublevels and the projection of the final state according to the detection of an $|H\rangle$-polarized photon. The visibility of the oscillation, determined from the envelope of the fit (gray dotted line) at the first maximum (and the corresponding minimum), is 93.1(6) %. We attribute this value to the decoherence process from from $P_{3/2}$ back to $D_{5/2}$ which has a probability given by the branching fraction of ~ 6 %. In comparison to the quantum-beat wave packet, we also show the arrival-time distribution for the case of an initial statistical mixture in $D_{5/2}$ (black dots). The data set is generated by averaging the two individually recorded arrival-time distributions for the $\left|D_{5/2}, -\frac{3}{2}\right\rangle$ to $\left|S_{1/2}, -\frac{1}{2}\right\rangle$ and $\left|D_{5/2}, +\frac{1}{2}\right\rangle$ to $\left|S_{1/2}, -\frac{1}{2}\right\rangle$ scattering processes. From the fit of the exponential decay (green dash-dotted line) we obtain a decay time of 461(2) ns.

As the time-dependent intensities given in Eq. (6.15) and Eq. (6.20) contain two phases, namely Φ_{854} and $\Phi_D(0)$ that are adjustable experimental parameters, we want to investigate their control which is shown in the following. First we study the dependance of the the quantum beat of the 393 nm photons on the photonic phase Φ_{854}. The rotation of the wave plates allows for adjusting the polarization, i.e. the photonic phase, to the canonical basis states $|H\rangle$, $|V\rangle$, $|D\rangle$ and $|A\rangle$ (and any value in between). For clarity, Fig. 6.7(a) shows arrival-time distributions for only two polarizations, $|D\rangle$ and $|A\rangle$, out of the four measured arrival-time distributions for the different polarizations. For an 854 nm input power of 50 µW, we set the detuning to -7.9 MHz, resulting in a higher repumping rate than for the wave packet in Fig. 6.6 for the same input power. The phase difference of $\Delta\Phi_{854} = 180^\circ$ set by the wave plates is revealed in the two oscillations and determined to $178.2(1.6)^\circ$ by fitting the Bloch equations to the photons. The deviation is ascribed to the remaining uncertainty in the proper adjustment of the 854 nm polarization with the wave plates.

Besides the photonic phase, also the phase of the initial atomic superposition state $\Phi_D(0)$ enters into the quantum beats. We change the phase by setting the phase of the second 729 nm pulse from $\left|S_{1/2}, -\frac{1}{2}\right\rangle$ to $\left|D_{5/2}, -\frac{3}{2}\right\rangle$ relative to the first pulse with the pulse sequencer HYDRA. It drives the acousto-optic modulator setting the amplitude of the 729 nm laser. The change in the phase of the quantum beats induced by a change of 180° is visible in Fig. 6.7(a). From the Bloch-equation fit we extract a phase difference of $181.1(1.1)^\circ$. The small deviation between the set values and the fitted values reflects the precise control that we have over the atomic phase and thus the quantum phase in the quantum beats.

Similarly to the Λ scheme, we repeat the measurements for the V scheme. We first perform again 729 nm spectroscopy on the $\left|S_{1/2}, -\frac{1}{2}\right\rangle$ to $\left|D_{5/2}, -\frac{5}{2}\right\rangle$ transition and on the $\left|S_{1/2}, -\frac{1}{2}\right\rangle$ to $\left|D_{5/2}, +\frac{3}{2}\right\rangle$, yielding a frequency difference between the two transition frequencies of 18.73 MHz that leads to a Larmor period of 53.4 ns. With the Larmor frequency we determine the magnetic field at the position of the ion to 2.79 G. The superposition state as given in Eq. (6.16) is created by a first resonant pulse (3.73 µs) that transfers 75 % of the population from the $\left|S_{1/2}, -\frac{1}{2}\right\rangle$ to $\left|D_{5/2}, +\frac{3}{2}\right\rangle$ level, followed by a resonant π pulse (2.5 µs) on the $\left|S_{1/2}, -\frac{1}{2}\right\rangle$ to $\left|D_{5/2}, -\frac{5}{2}\right\rangle$ transition. With the 854 nm laser detuning of -6.5 MHz and

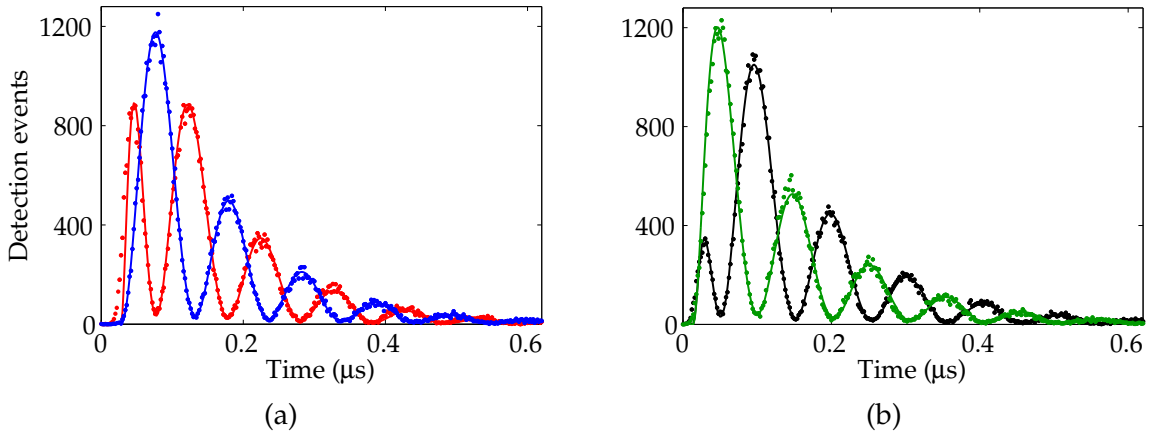

Figure 6.7.: Phase control of the quantum beats in the Λ scheme. (a) Arrival-time distributions of the 393 nm photons showing quantum beats for two different 854 nm input polarization states, $|D\rangle$ (red dots) and $|A\rangle$ (blue dots). (b) Arrival-time distributions showing quantum beats for two values, 0 (green dots) and π (black dots), of the atomic phase $\Phi_D(0)$ of the initial atomic superposition in $D_{5/2}$. In (a) and (b), the corresponding solid lines show the 18-level Bloch-equation fits to the data. The bin size is 2 ns for 6 min measurement time.

the power of 50 µW we achieve control of the phase in the 393 nm arrival-time distributions; changing the polarization of the incoming 854 nm photons and the atomic phase, set with the second 729 nm pulse, we control the quantum-beat phase as already shown for the Λ scheme.

Figure 6.8(a) shows the arrival-time distribution for two orthogonal 854 nm polarization states, $|D\rangle$ and $|A\rangle$, with a phase difference of $178.9(1.8)^\circ$ determined by Bloch equation fits to the data. In both wave packets we find the Larmor period ~ 53 ns as expected from the frequency difference of both Zeeman sublevels in $D_{5/2}$. In Fig. 6.8(b), the phase $\Phi_D(0)$ of the coherent superposition in $D_{5/2}$ is chosen to 0 and π which is recovered from the fits to $181.4(1.5)^\circ$. Similar to the Λ case, we observe only small deviations from the ideal values, highlighting our precise control of both phases.

A high oscillation visibility in the detected photons needs an optimal population distribution in the initial superposition state. For the V-type level configuration, we expect the ideal case if we choose the distribution as 25 % in $\left|D_{5/2}, -\frac{5}{2}\right\rangle$ and 75 % in $\left|D_{5/2}, +\frac{3}{2}\right\rangle$. According to the two CGCs at 393 nm, this distribution should compensate their difference. This is verified with the following procedure: From the two pulses which prepare the coherent superposition state, the duration of the first pulse from $\left|S_{1/2}, -\frac{1}{2}\right\rangle$ to $\left|D_{5/2}, +\frac{3}{2}\right\rangle$ is varied to adjust the amount of transferred population. The subsequent π pulse to $\left|D_{5/2}, -\frac{5}{2}\right\rangle$ transfers the remaining population. The different CGCs for the two 854 nm transitions are compensated for by the detuning of -6.5 MHz for a magnetic field of 2.79 G

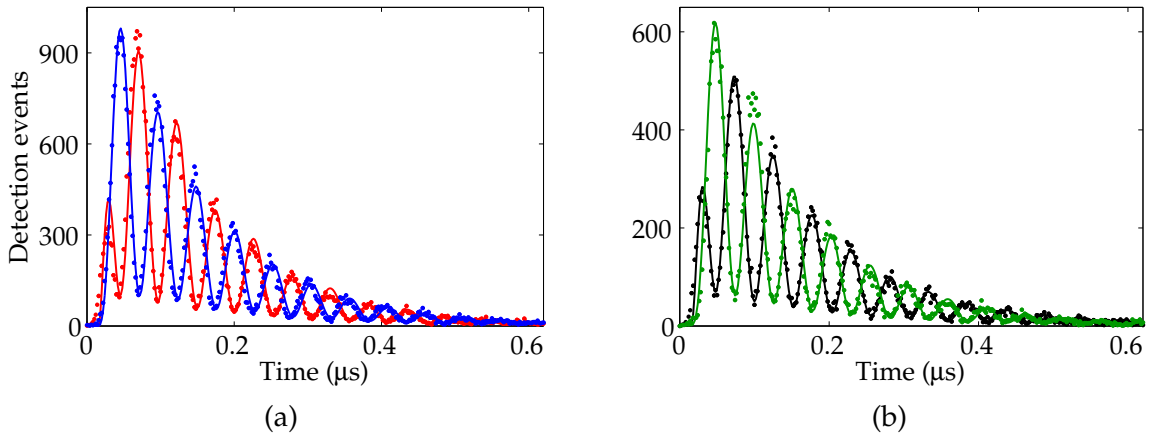

Figure 6.8.: Phase control of the quantum beats in the V scheme. (a) Arrival-time distributions of the 393 nm photons showing quantum beats for two different 854 nm input polarization states, $|\mathrm{D}\rangle$ (blue dots) and $|\mathrm{A}\rangle$ (red dots). (b) Arrival-time distributions showing quantum beats for two values, 0 (green dots) and π (black dots), of the atomic phase $\Phi_\mathrm{D}(0)$ of the initial atomic superposition in $\mathrm{D}_{5/2}$. In (a) and (b), the corresponding solid lines show the 18-level Bloch-equation fits to the data. The bin size is 2 ns for a measurement time of 10 min in (a) and 6 min in (b).

and the power of the 854 nm laser is set to 50 µW. In Fig. 6.9 the quantum-beat visibility is shown for different amounts of population in $\left|\mathrm{D}_{5/2}, +\frac{3}{2}\right\rangle$. For every population value we record the arrival-time distribution of Raman-scattered photons and determine from two exponential fits to the envelope of the observed quantum-beat modulated photons the visibility as presented in Fig. 6.6. The highest visibility value of 78.2(9) % is achieved for a population of 75 %, in agreement with the ratio of the CGCs.

Compared to the Λ scheme the visibility value of 78.2(9) % is significantly reduced which is mainly based on the distinct nature of the two interference phenomena. While in the Λ scheme the emission probability is suppressed and enhanced (see Fig. 6.4) through interference in the excitation amplitudes to the $\left|\mathrm{P}_{3/2}, +\frac{1}{2}\right\rangle$ state, the situation changes in the V scheme completely: The interference in the two emission amplitudes causes a spatial rotation of the dipolar emission pattern, which was shown in Fig. 6.5. As the HALO covers a limited solid angle, it also collects a small fraction of the dipolar emission for the case that the preferred emission direction is perpendicular to the HALO axis.

We calculate the theoretically expected visibility for the V scheme. Thereto we have to numerically evaluate Eq. (6.21) for the cases $\Phi_\mathrm{D}(t) = 0$ and $\Phi_\mathrm{D}(t) = \pi$, i.e. for a minimum and maximum emission into the solid angle of the HALO. For calculating the amount of light which is collected by the HALO perpendicular to the magnetic field we apply the coordinate transformation as given in App. A.4 to the expression in Eq. (6.21). For the two phase values we calculate a maximum HALO collection efficiency for σ photons of 6.26 %

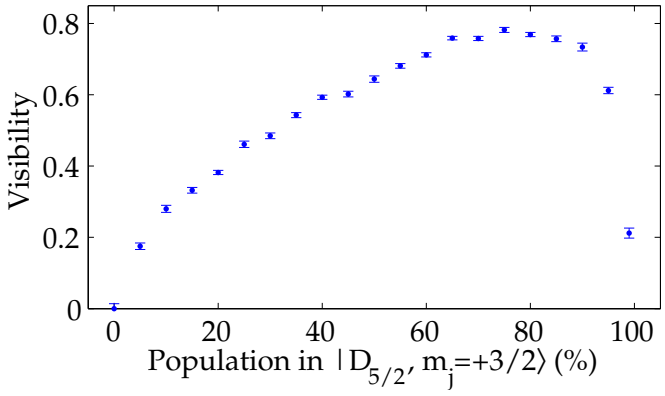

Figure 6.9.: V scheme: quantum-beat visibility as a function of the initial population in $\left|D_{5/2}, +\frac{3}{2}\right\rangle$. The values for the visibilities are determined by exponential fits of the envelopes of the measured quantum-beat photons.

(for $\Phi_D(t) = \pi$) and a minimum collection efficiency of 0.27 % (for $\Phi_D(t) = 0$). From both values we obtain a maximum visibility of 91.7 % which is limited by the solid angle of the HALO. If we include the reduction in visibility due to decoherence due to the decay from $P_{3/2}$ to $D_{5/2}$ of $\sim$ 6 % as for the Λ scheme we remain with a visibility of $\sim$ 86 %. We see that this value is still higher than the one derived from the data. This is attributed to the position of the HALO. It is not perfectly perpendicular to the magnetic field and aligned such that in the minimum intensity distribution, some light still enters into the solid angle of the HALO.

6.4. Phase-dependent photon-scattering probability

The quantum-beat wave packets presented in Fig. 6.7 and in Fig. 6.8 extend over many periods of the underlying Larmor precession. This means that the detection efficiency, i.e. the probability to detect a photon per excitation attempt is nearly independent of the two phases $\Phi_D(0)$ and Φ_{854}. Here we show that the situation changes if we generate photons with durations short compared with the Larmor period, and we determine the detection efficiency as a function of the phase $\Phi_D(0)$.

For the Λ-type level configuration we reduce the magnetic field to 0.538 G and thus increase the Larmor period to 553.4 ns. The photon-scattering probability changes with the Larmor period, which requires the photon duration as short as possible (at least shorter than the Larmor period). This leads to the highest sensitivity of the whole wave packet to enhancement and suppression due to interference. Therefore we use the highest 854 nm power available of 2.9 mW and an excitation pulse of 12.5 ns which is sent from HYDRA to the 854 nm acousto-optic modulator during the experimental sequence. Together with its limited bandwidth we reach a total photon wave-packet duration of $\sim$ 70 ns. In Fig. 6.10(a)

the time-integrated photon detection probability is shown for short excitation pulses for different values of the control phase $\Phi_D(0)$ (blue dots). With the controlled adjustment of the phase in the interference process we are able to enhance and suppress the emission probability with a visibility from the sinusoidal fit (black line) of 75.5(7) %. A faster modulation of the exciting laser would further reduce the total temporal length of the wave packet and might increase the visibility. To see the difference for a long photon that covers many quantum-beat periods, we increase the magnetic field to 2.795 G, obtain a Larmor period 106.5 ns and generate wave packets with a total length of $\sim$ 850 ns. The detection efficiencies are plotted in Fig. 6.10(a) for different phases (blue crosses) and the modulation is almost not visible.

The change in detection efficiency from $\sim$ 5.6 ‰(for long photons) to 3.45(2) ‰(for the short photon with highest detection efficiency) is explained by the following: as we only collect π photons with one HALO, we see that the detection-efficiency values for long photons are typical ones. With the 18-level Bloch equations we can simulate the population dynamics in $|P_{3/2}, -\frac{1}{2}\rangle$, including all 854 nm parameters from the experiment for the generation of long photons. Thus we obtain the time-integrated amount of population which corresponds to the detection efficiency of 5.6 ‰. If we change the 854 nm parameters to the high-power condition (for the phase of π) for short photons we see that the time-integrated amount of population in $|P_{3/2}, -\frac{1}{2}\rangle$ is reduced which means a detection efficiency of 4 ‰which is close to the measured value of 3.45(2) ‰. The reason for the reduction is due to the high 854 nm power of 2.9 mW. There the Rabi frequency is high enough to repump population from $|P_{3/2}, -\frac{1}{2}\rangle$ back to $|D_{5/2}, +\frac{1}{2}\rangle$, from where the population transfer to $|P_{3/2}, +\frac{3}{2}\rangle$ is significantly increased compared with the long photon case. This explains the lower detection efficiency for the case of short photons. The remaining deviation is attributed to the laser power used in the simulation. It can only be measured outside the trap and deviations to the real intensity at the position of the ion are easily produced with slight optical misalignment.

In analogy to the Λ scheme, we perform the same measurements for the V scheme in Fig. 6.10(b). For a reduction of the magnetic field to 0.537 G, we obtain a Larmor period of 277.4 ns. With the maximum 854 nm power available for this measurements of 500 µW, we reach a total temporal length of the wave packet of $\sim$ 120 ns. For different control phases $\Phi_D(0)$ we see again the sinusoidal behavior in the detection efficiency with a reduced visibility of 48.3(1.5) %. The reduction of this value compared to the Λ case has different reasons; as the temporal length of the photon is only about half the Larmor period, we cannot completely suppress and enhance the photon with the corresponding phase values. This would need shorter photons limited by laser power or lower magnetic fields for higher Larmor periods. For the latter it becomes hard to individually address single 729 nm carrier transitions, due to the reduced frequency splitting. A further limitation is found in the solid angle of the HALO which collects certain fraction of the emitted light even for the case that the preferred emission direction is perpendicular to the quantization axis, i.e. in the minimum of Fig. 6.10(b). We finally complete the set of measurements by generating

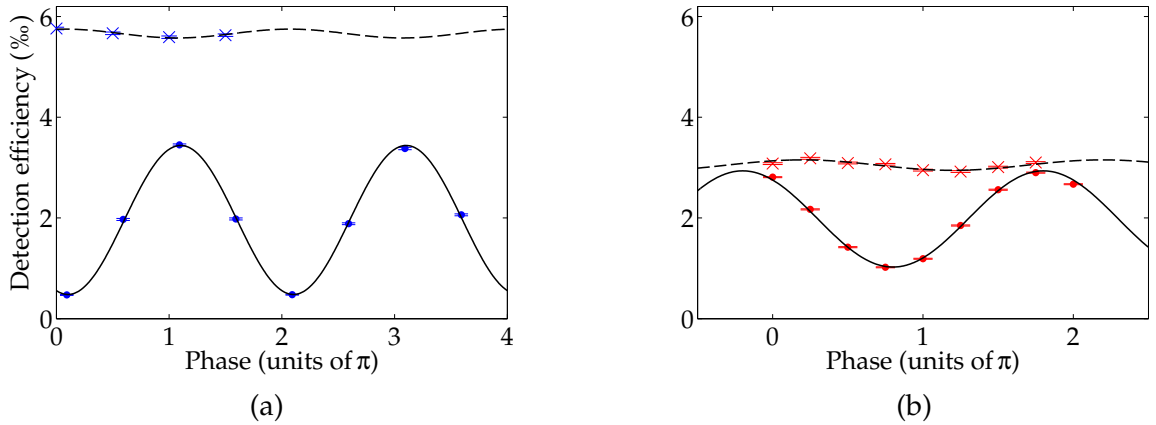

Figure 6.10.: Suppression and enhancement of the generation efficiency, i.e. the detection efficiency of 393 nm photons controlled via the atomic phase $\Phi_D(0)$. The dots and solid curves (sinusoidal fits) are for short excitation pulses (photon duration $<$ quantum-beat period), while the crosses and dashed curves are for long pulses (photon duration $>$ quantum-beat period). (a) Λ scheme: The short photon has a total temporal length of $\sim$ 70 ns while the quantum-beat period is set to 553.4 ns by a magnetic field of 0.538 G. The long photon has a total length of $\sim$ 850 ns and the quantum-beat period is set to 106.5 ns. (b) V scheme: The short photon extends over $\sim$ 120 ns at 277.4 ns beat period; for the long photon the values are $\sim$ 750 ns and 53.2 ns.

long photons for the V-type level configuration by increasing the magnetic field to 2.79 G, resulting in a Larmor period of 53.2 ns. With an 854 nm detuning of -6.5 MHz and 50 µW of power we generate photons with a total length of $\sim$ 750 ns and plot them in Fig. 6.10(b) (red crosses). Besides the insensitivity to the control phase $\Phi_D(0)$ it is conspicuous that the detection efficiency is about one half compared to the long photon for the Λ case[3]. As shown in App. A.4 the HALO collects 6 % of the total emitted π light and 3.26 % of the total σ light when the HALO axis is perpendicularly oriented to the quantization axis. The ratio between the two values of 54 % agrees well with the detection efficiencies for the two different schemes in Fig. 6.10.

6.5. Interference mechanism

In this final section we have to experimentally prove the two fundamentally different interference mechanisms for the Λ and V scheme as theoretically presented and visualized in Fig. 6.4 and Fig. 6.5. For this we analyze the remaining population in $D_{5/2}$ through

[3]This phenomenon is also visible in the total number of detection events when comparing Fig. 6.7(b) and Fig. 6.8(b) which are recorded both for a total measurement time of 6 min.

state-selective fluorescence after an excitation with 854 nm light for different 854 nm pulse lengths.

For the Λ scheme we set the magnetic field to 0.987 G and obtain a Larmor period of 301.5 ns. We set the 854 nm detuning to -15 MHz and use 50 µW optical power. The pulse length of the 854 nm excitation is varied in steps of 12.5 ns; for each pulse duration the remaining population in $D_{5/2}$ is displayed in Fig. 6.11(a). It shows that the depopulation

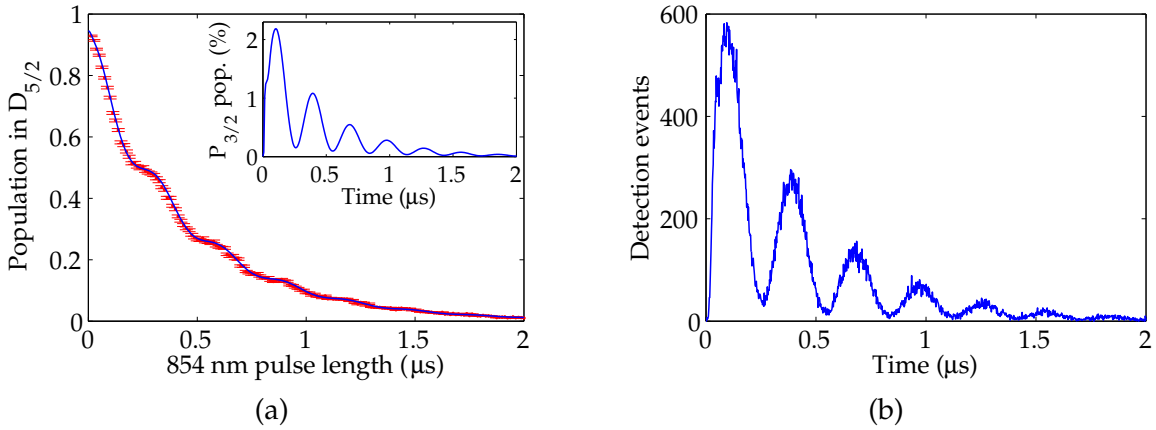

Figure 6.11.: Λ scheme: (a) Change of the $D_{5/2}$ population for different 854 nm pulse lengths. The observed stair-like behavior results from interference of two excitation amplitudes to $\left|P_{3/2}, -\frac{1}{2}\right\rangle$. The step size of the pulse length scan is 12.5 ns with 10^4 repetitions per point. The solid line is calculated with the 18-level Bloch equations including experimental parameters. Inset: Derivative of the calculated solid line showing the oscillation of the population in $P_{3/2}$, which shows the suppression and enhancement of the emission of 393 nm photons similar to the subsequent measurement, shown in (b): Arrival-time distribution of 393 nm photons showing quantum beats with the same temporal shape as calculated in the inset of (a). The bin size is 2 ns for a measurement time of 11 min.

of the $D_{5/2}$ manifold exhibits a stair-like behavior; we see a suppression and enhancement of the depopulation process from the two $D_{5/2}$ states into $\left|P_{3/2}, -\frac{1}{2}\right\rangle$ with the Larmor period due to the two interfering excitation amplitudes. The atomic dynamics are calculated with the 18-level Bloch equations (solid line) which fit very well with the experimental data. The interference process is manifested by the derivative of the calculated line which is shown in the inset of Fig. 6.11(a) and which is proportional to the population in $P_{3/2}$. We see that the Larmor-precession phase of the initial superposition state creates an oscillatory behavior in the population in $P_{3/2}$. With the subsequently recorded arrival-time distribution in Fig. 6.11(b), we confirm that the calculated population in $P_{3/2}$ is well reflected in the measured histogram.

In order to highlight the difference between the two schemes, we repeat the measure-

ment for the V scheme[4]. For the same magnetic field, we halve the Larmor period to 151.5 ns. We use an 854 nm detuning of -12.5 MHz, a power of 20 µW and perform a pulse-length scan, depicted in Fig. 6.12(a). The result exhibits a simple exponential depopulation curve of the $D_{5/2}$ level without any modulation. The Bloch-equation calculation including the experimental parameters describes the excitation from $|D_{5/2}\rangle$ to $|P_{3/2}\rangle$, and its derivative shows almost no modulation of the population in $P_{3/2}$, in contrast to the Λ case. The remaining very small modulation visible on the calculated population in $P_{3/2}$ stems from the spontaneous decay back to other $D_{5/2}$ Zeeman sublevels with 5.87 % from which the population is transferred back to common Zeeman sublevels in $P_{3/2}$ where it can interfere again. However, this effect does not significantly contribute to the clearly visible quantum beat in the measured wave packet in Fig. 6.12(b). It proves that the interference occurs in the emission process: The initial atomic phase enters into the superposition of the two emission channels with polarization σ^+ and σ^- and causes the emission pattern to spatially rotate about the quantization axis as shown in Fig. 6.5, leading to a modulation in the detection probability.

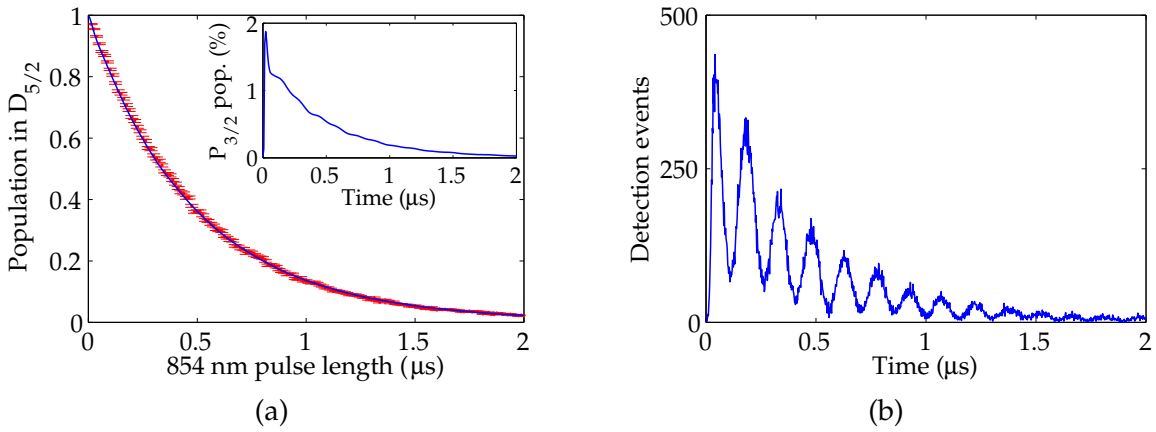

Figure 6.12.: V scheme: (a) Simple exponential decay without modulation in the depopulation of $D_{5/2}$ in the V scheme. The points are measured data; the line shows the dynamics derived from the 18-level Bloch equations. Inset: The derivative of the calculated curve shows almost no oscillations in the population of the $P_{3/2}$ level. However, we measured subsequently with the same parameters the quantum-beat modulated photon in the arrival-time distribution shown in (b). The bin size is 2 ns for a measurement time of 11 min.

The final measurement that supports the arguments given so far is provided by measuring the depletion of the $D_{5/2}$ population as a function of the control phase $\Phi_D(0)$ after a short 854 nm excitation pulse with a fixed length of 12.5 ns. We set the magnetic field

[4]For this measurement we prepared the initial atomic superposition state with equal amplitudes. However, this does not affect the conclusions.

to 0.99 G resulting in the Larmor period of 300 ns for the Λ scheme and 150 ns for the V scheme, respectively. For the Λ scheme we set the detuning and power of the 854 nm laser to -15 MHz and 660 µW, respectively. For these values we obtain the depletion of the $D_{5/2}$ level shown in Fig. 6.13 as the blue data points. From the sinusoidal fit we derive a visibility of 74.0(1.9) % which is close to the visibility value we obtained in the suppression and enhancement of the detection efficiency in Fig. 6.10(a) for the short photons. For the V scheme, we set the detuning to -6.5 MHz and used 200 µW of 854 nm power to repeat the measurement shown by the red data points. Here the $D_{5/2}$ depletion is almost insensitive to the control phase, a further evidence that the interference process takes place in the emission process.

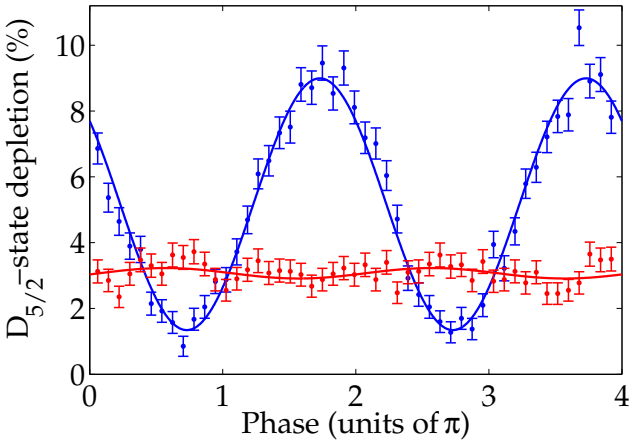

Figure 6.13.: $D_{5/2}$-state depletion for different control phases $\Phi_D(0)$ of the initial superposition after a short excitation pulse of 12.5 ns. The blue dots (solid curve) are measured (calculated) for the Λ scheme, the red dots (solid curve) for the V scheme.

Summary

We investigated experimentally quantum beats in the arrival-time distribution of single photons for two distinct experimental situations, revealing their fundamentally different physical origins by pointing out the different types of interference. For two level configurations, Λ and V, the ion is prepared in a coherent superposition state, whose phase oscillates with the Larmor frequency. Upon laser excitation on the $D_{5/2}$-to-$P_{3/2}$ transition, the ion emits a single photon on the $P_{3/2}$-to-$S_{1/2}$ transition at 393 nm wavelength. The photon shows quantum beats at the frequency of the Larmor precession, observed as oscillations in the photonic wave packet with a visibility $> 93\,\%$. This also means that we are able to map the atomic phase into the Raman-scattered photon. With the atomic and photonic phases, $\Phi_D(0)$ and Φ_{854} we have two control knobs for the quantum-beat phase by setting the initial phase of the atomic superposition and the 854 nm laser polarization.

For the Λ- and V-type level configuration, we point out the two disparate physical origins of the quantum beats. An investigation of the $D_{5/2}$-level depletion for different control-phase values $\Phi_D(0)$ revealed for the Λ scheme that the depopulation is suppressed and enhanced through two interfering absorption paths. In contrast, in the V scheme we observed an insensitivity of the depletion to the change of the atomic control phase, which manifests the fundamentally different interference process, which occurs in the two emission paths.

The presented experimental techniques cover the ability to map the atomic phase into the quantum-beat phase of the Raman-scattered photons. This is important for the application of the single-photon Raman scattering as a method for atom-to-photon quantum state conversion [137]. Besides the quantum-beat experiments serve as an essential technical ingredient for mapping arbitrary polarization states of photons into a single ion, which will be shown in Sec. 8.1.

7. Related work: experiments with a femtosecond frequency comb

This chapter comprises additional related work with an optical frequency comb that was acquired as a technical upgrade of our experimental tools for the new laboratories within the move of the experiment from ICFO to Saarbrücken. The acquirement was done with the long-term perspective to replace the laser frequency-stabilization scheme with transfer cavities to a novel scheme for which the lasers are locked to the comb. Mainly in the first half of my Ph.D. time, it was my task to develop an experimental setup around the comb to connect it with the lasers from the ion experiment, making first measurements with the comb feasible. The diploma thesis of P. Eich [138] contains the main measurement results we achieved in this time.

Precision measurements of frequencies play a fundamental role in physics and metrology. In the 70s it was already possible to have high accuracy frequency sources in the microwave regime. Hence the idea developed to transfer this stability into the optical regime with harmonic frequency chains [139, 140], where frequencies were phase coherently compared by harmonic mixing. The drawback of such chains were the complexity and the design for only measuring one particular optical standard [141]. Progress in the development of mode-locked lasers yielded spectral combs [142] with an octave spanning spectrum possible by spectral broadening through microstructured fibers [143] where the phase-coherent link between RF and optical frequencies was established. This was the essential feature to revolutionize optical frequency measurements and thus high-precision optical spectroscopy [144, 145]. Today the frequency comb technique reaches high accuracy by referencing the comb to the best worldwide cesium frequency standards. This is demonstrated in frequency metrology for high-precision frequency measurements [146, 74, 147] and direct frequency-comb spectroscopy [148, 149]. Further novel applications include experiments in the field of quantum optics [150] and the implementation of the frequency comb in quantum networks [151].

In the following chapter we treat the process of self phase modulation to observe how this process causes the spectral broadening inside the photonic crystal fiber. In Sec. 7.3 we characterize the phase-lock of the repetition rate and show the stabilization of two diode lasers to the frequency comb with 866 nm spectroscopy at the ion. After we presented the experimental tools and techniques that are needed for photon generation, we apply them here for the generation of single photons by the absorption of femtosecond pulses from the comb. We show first results concerning the comb-ion interaction in Sec. 7.4.

7.1. Theory

The generation principle of a frequency comb is based on modelocked lasers where ultrashort laser pulses are generated by many modes traveling simultaneously with a fixed phase relation inside the laser cavity. Fig. 7.1 shows pulses which are separated by their round-trip time inside the cavity $\tau = \frac{l_c}{v_g}$, where l_c is the cavity length and v_g the group velocity. Dispersion inside the cavity leads to different group and phase velocities which

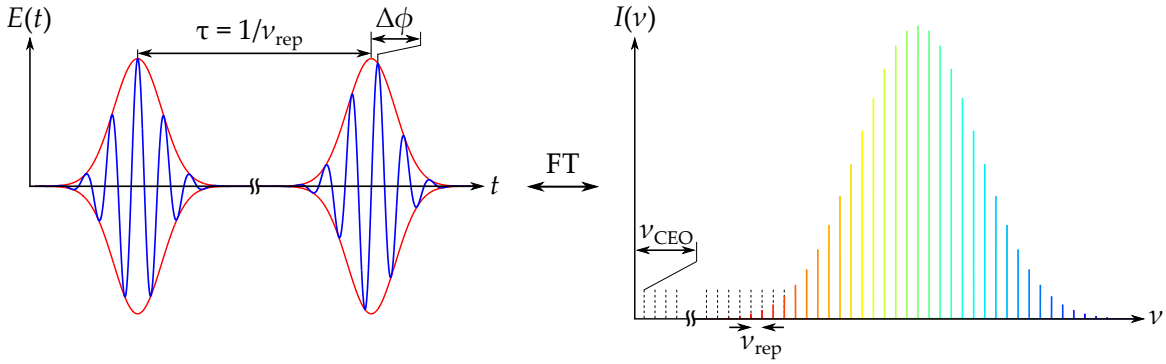

Figure 7.1.: Electric field of pulses from a modelocked laser which are separated by the cavity round-trip time τ. Dispersion inside the cavity leads to a phase $\Delta\phi$ between the carrier and the envelope. With a Fourier Transform (FT) one gets a equally spaced frequency comb where frequencies are spaced by the repetition rate ν_{rep}. The whole spectrum has an offset frequency which is the carrier-envelope frequency $\nu_{CEO} = \frac{\Delta\phi}{2\pi\tau}$.

results in a phase shift $\Delta\phi$ as [143]

$$\Delta\phi = \left(\frac{1}{v_g} - \frac{1}{v_p}\right) l_c \omega_c \mathrm{mod} 2\pi, \tag{7.1}$$

with the phase velocity $v_p = \frac{c}{n}$, the refractive index n and the carrier frequency[1] ω_c. The phase shift enters in the time domain description of the electric field of the pulse train

$$E(t) = \sum_n \hat{E}(t - n\tau) e^{i(\omega_c t - n(\omega_c \tau - \Delta\phi) + \phi_0)}, \tag{7.2}$$

with $\hat{E}(t)$ describing the envelope and ϕ_0 the overall phase offset. The Fourier transform of these pulse trains to the frequency domain leads to

$$E(\omega) = \sum_n \tilde{E}(\omega - \omega_c) e^{-in(\omega\tau - \Delta\phi)}, \tag{7.3}$$

[1] In a dispersive medium with an index of refraction n the group velocity of the pulses $v_g = \frac{c}{n + \omega \frac{dn}{d\omega}}$ contains the term $\frac{dn}{d\omega}$ that is responsible for the drift of the relative phase between carrier and envelope.

that describes an equally spaced frequency comb with a line spacing determined by the repetition frequency ν_{rep}. The frequencies in the comb spectrum appear for the condition $\omega\tau - \Delta\phi = 2m\pi$ which corresponds to

$$\nu_m = \frac{m}{\tau} + \frac{\Delta\phi}{2\pi\tau} = m \cdot \nu_{rep} + \nu_{\text{CEO}}. \tag{7.4}$$

Since ν_{rep} and ν_{CEO} are two RF frequencies they can both be measured and phase-locked to a stable reference oscillator like an atomic clock. Due to the high multiplication factor m which is of the order 10^6, the stability of the clock is transferred into the optical frequency domain.

7.2. Setup

The optical setup that was built around the frequency comb system[2] and which is described in the following is shown in Fig. 7.2. Femtosecond laser pulses at a center wavelength of 1560 nm are generated inside the resonator of the erbium fiber laser (1). Passive mode locking via nonlinear polarization rotation [152] generates a comb spectrum with a width of ∼100 nm and a frequency spacing of $\nu_{\text{rep}} = 250$ MHz. The pulses with a temporal width below 100 fs are amplified with erbium-doped fiber amplifiers (2) to send them to the non-linear interferometer (3) for the detection of ν_{CEO} and to the second harmonic generation unit (4) for frequency doubling. At the output of (4) the pulses with a temporal pulse width (FWHM) of ∼ 120 fs are spectrally centered at 795 nm with a FWHM of 16 nm and sent to the photonic crystal fiber (PCF).

7.2.1. Photonic crystal fiber

Photonic crystal fibers are fibers which show complex building structures with large refractive index contrast between the core and the surrounding medium [153]. This offers the possibility for highly nonlinear processes like supercontinuum generation, for which an overview is found in [154]. The fiber we use is a solid-core PCF. With the modification of the air hole diameters and the periodicity of the holes it is possible to change the zero dispersion wavelength (ZDW), which is in our case $\lambda_{\text{ZDW}} = 810$ nm. Sending pulses with a carrier wavelength below or above the ZDW defines the dominating nonlinear processes which happen inside the fiber. The pulses from the SHG unit have the carrier wavelength at 795 nm and a FWHM of 16 nm. This means that the pulses mainly underlie the normal dispersion regime inside the fiber and the dominating process for spectral broadening is the self phase modulation beside minor soliton dynamics [154]. A full description of all nonlinear processes that happen inside the PCF is a non-trivial task and would go beyond the scope of this thesis. Here we restrict the description of the processes inside the PCF to the main process, namely the self phase modulation[3].

[2] Menlo Systems, FC1500

[3] According to Menlo Systems this is the main broadening mechanism in the fiber.

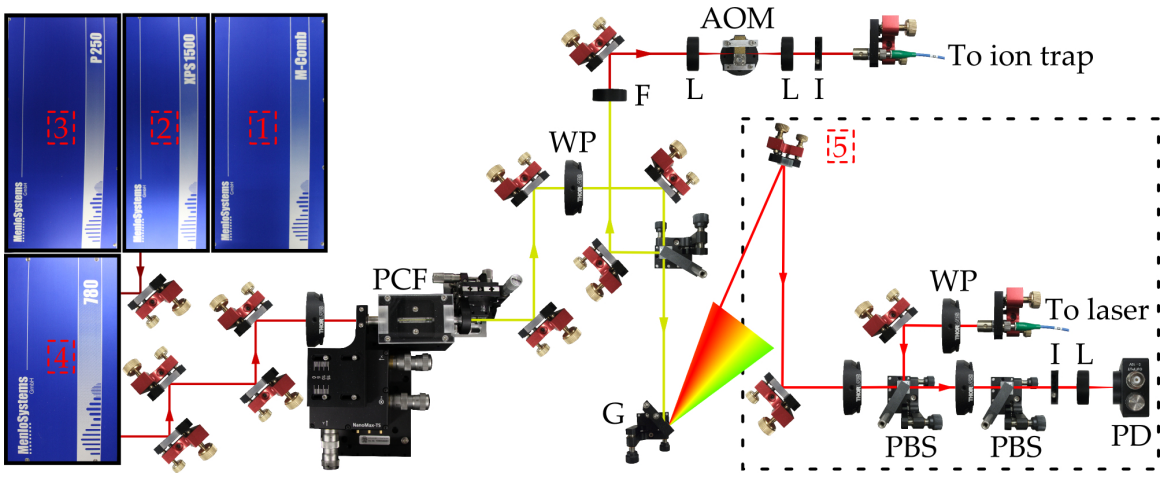

Figure 7.2.: Setup of the Menlo Systems frequency comb system (1-4) with: the photonic crystal fiber (PCF), wave plates (WP) to adjust polarizations at polarizing beam splitters (PBS), bandpass filter (F), lenses (L), irises (I), grating (G), acousto-optic modulator (AOM) and photodiode (PD). The setup allows us to send the comb light directly to the ion trap or to measure a beat signal between the comb and lasers. The beat detection unit (5) is built up five times to have simultaneously a beat signal for five different lasers (729 nm, 794 nm, 850 nm, 854 nm and 866 nm).

Self phase modulation

Here the principle of self phase modulation and the associated spectral broadening is presented in a simplified way for the fiber and pulse parameters. An extensive description of self phase modulation (SPM) is found in [155] which is adapted to the parameters of our photonic crystal fiber. One simplification is obtained by neglecting the effect of group velocity dispersion inside the fiber. The process of self phase modulation can then be described by the electric field of a Gaussian pulse

$$E(t,L) = \hat{E}(t,L)\, e^{i(\omega_c t - k L)}, \tag{7.5}$$

with the Gaussian envelope $\hat{E}(t,L)$, $k = \frac{\omega_c\, n(t)}{c}$ and ω_c as the carrier frequency (corresponding to a wavelength of 795 nm) of the incoming pulse. Since the pulse shape is not changed along the fiber length $L = 0.06$ m, the envelope remains as at the beginning of the fiber

$$\hat{E}(t,0) = E_0\, e^{-\frac{1}{2}(\frac{t}{\tau})^2}. \tag{7.6}$$

Here $\tau = 72$ fs is the Gaussian $\frac{1}{e}$ half-width corresponding to an FWHM of 120 fs of the Gaussian intensity profile. Third order susceptibility $\chi^{(3)}$ in the nonlinear response of dielectric materials for intense light pulses causes the effect of nonlinear refraction which appears in the intensity dependence of the refractive index $n(t) = n_0 + n_2 I(t)$ with n_0 as the

refractive index of the fiber and the nonlinear refractive index $n_2 = \frac{c\,A_{\text{eff}}\,\gamma}{2\pi\nu_c} = 2.44 \cdot 10^{-20}\,\frac{\text{m}^2}{\text{W}}$ where $\gamma = 87\,\frac{1}{\text{W km}}$ is the nonlinear coefficient of the fiber. The effective core area is approximated[4] by $A_{\text{eff}} = (\frac{\pi}{4})MFD^2$ with the mode field diameter $MFD = 1.68\,\mu\text{m}$. Together with the pulse peak power of $P_0 = 3.3\,\text{kW}$, the intensity is calculated to $I_0 = \frac{P_0}{A_{\text{eff}}} = 1.49 \cdot 10^{15}\,\frac{\text{W}}{\text{m}^2}$. The time-dependent variation of the nonlinear refractive index with a Gaussian intensity profile $I(t) = I_0\,e^{-(\frac{t}{\tau})^2}$, shown in Fig. 7.3(a), leads to a phase modulation of the incoming pulse. This is seen in the phase of the electric field of the pulse which is described as

$$E(t,L) = \hat{E}(t,0)\,e^{i(\omega_c t - \frac{\omega_c L}{c}(n_0 + n_2 I(t)))}. \tag{7.7}$$

It propagates in a medium with nonlinear refractive index n_2 with the Gaussian envelope $\hat{E}(t,0)$ for the fiber length L. From the phase term in Eq. (7.7) one derives the instantaneous frequency as

$$\nu(t) = \frac{\mathrm{d}\phi}{\mathrm{d}t} = \nu_c - \frac{\nu_c L}{c} n_2 \frac{\partial I(t)}{\partial t}, \tag{7.8}$$

and the frequency variation

$$\Delta\nu(t) = \nu(t) - \nu_c = \frac{2\nu_c L}{c\tau^2} I_0\,n_2\,t\,e^{-(\frac{t}{\tau})^2}, \tag{7.9}$$

which is plotted in Fig. 7.3(b) for the experimental parameters. From the plot we see that

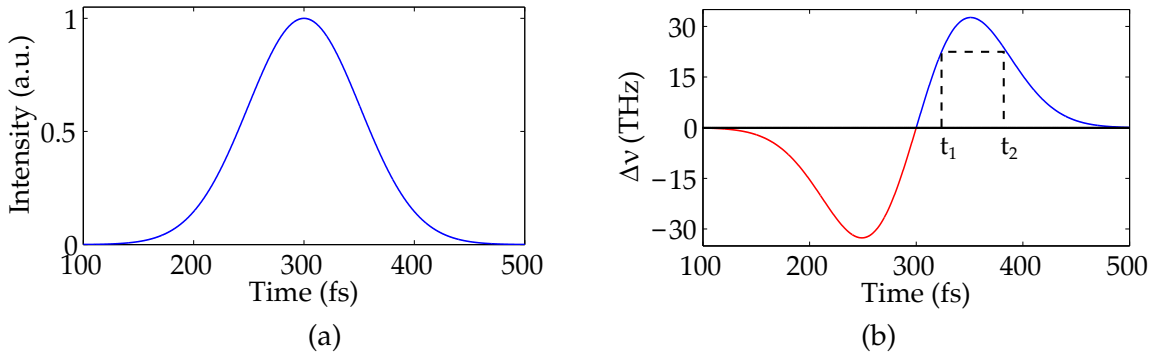

Figure 7.3.: (a) Gaussian intensity profile with a FWHM of 120 fs and its time derivative (b) which causes new frequency components $\Delta\nu$ over the temporal profile. The carrier frequency is blue shifted at the trailing part of the pulse and red shifted at the beginning of the pulse. Each frequency is generated at two different times. Depending on the time delay $t_1 - t_2$ there is constructive or destructive interference giving the spectrum its characteristic shape.

the same generated frequency value is generated at two different times t_1, t_2 which leads to

[4] Further fiber parameters like the pitch and air hole diameter, which we don't know, would be needed to calculate a correction factor for A_{eff} precisely.

destructive interference ($t_1 - t_2 = \frac{n\,\pi}{\omega}$, for odd n) or constructive interference ($t_1 - t_2 = \frac{2n\,\pi}{\omega}$, if n is a integer). This results in the characteristic modulation of the spectrum when taking the Fourier transform of Eq. (7.7). The equation is shown in Fig. 7.4(a) to see the effect of self phase modulation in the time domain. The temporal effect of self phase modulation is a pulse chirp due to a nonlinear change in the phase of the pulse. In order to present the spectral broadening one has to take the Fourier transform of Eq. (7.7)

$$\tilde{E}(\omega, L) = \mathcal{FT}\left\{E(t, L)\right\}. \tag{7.10}$$

The frequency power spectrum is defined as $S(\omega) = |\tilde{E}(\omega, L)|^2$ and is used to show the wavelength spectrum $S(\lambda) = |\frac{\mathrm{d}\nu}{\mathrm{d}\lambda}|S(\nu)$ in Fig. 7.4(b) for our pulse and fiber parameters. As shown in Fig. 7.4(b) one frequency value is generated at two different times inside the pulse, leading to destructive or constructive interference between them which yields the characteristic modulation inside the spectrum. We see that the spectrum at -20 dB ranges

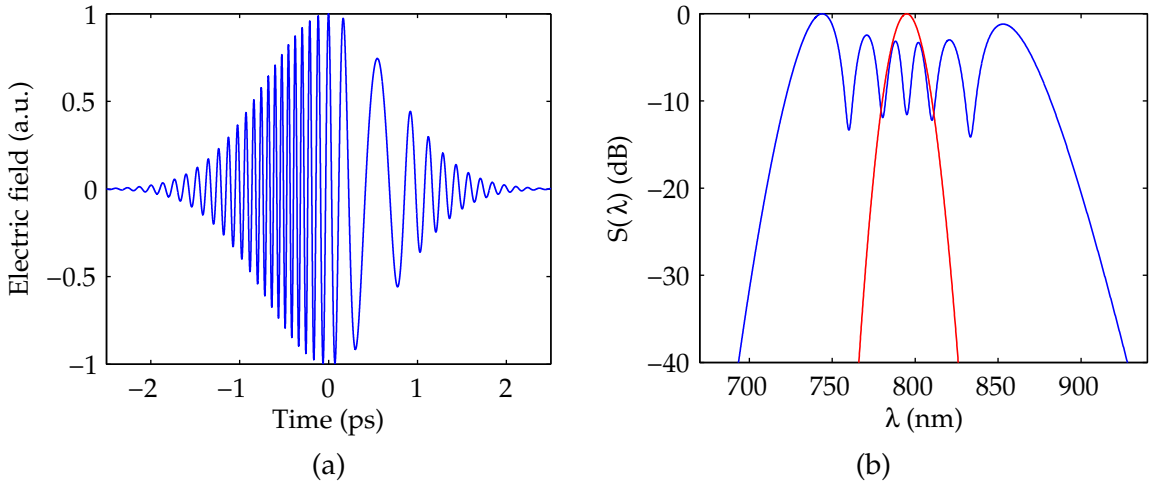

Figure 7.4.: (a) Effect of self phase modulation in the time domain for arbitrary pulse and fiber parameters. (b) Broadened wavelength spectrum (*blue*) by self phase modulation inside the PCF for an incoming spectrum (*red*) of a Gaussian pulse for the experimental pulse and fiber parameters.

from $\sim 720 - 900$ nm. This width is lower than the output spectrum of the fiber at -20 dB which is specified by MenloSystems from 550 nm to 1000 nm for the same input power.

The reason is that the SPM transfer of spectral content into the anomalous dispersion regime ($> \lambda_{\mathrm{ZDW}}$) is neglected. In this regime soliton dynamics appear which are responsible for further spectral broadening [154]. Also processes between soliton and nonsoliton field components contribute to the complexity of processes inside the fiber. Tiny fluctuations in pulse parameters like the pulse power, the initial pulse chirp and the temporal width are also highly sensitive for the shape of the spectrum.

7.2.2. Beat detection unit

After the light has been spectrally broadened by the PCF, it is separated by a PBS to send it either directly to the ion for single-photon generation (see Sec. 7.4) or to a holographic grating[5] to spatially disperse the individual modes. An grating illumination of 4 mm sets the resolution limit to 192 modes for 866 nm up to 228 modes for 729 nm. In order to get a beat signal between the laser and the closest comb mode out of the comb spectrum, pick-up mirrors send a small part of the spectrum to the beat detection units (see (5) in Fig. 7.2) which are built up for each laser wavelength (including 729 nm, 794 nm, 850 nm, 854 nm and 866 nm). There both beams are spatially overlapped and projected to the same polarization axis with wave plates and polarizing beam splitters to reach the highest possible signal-to-background ratio in the beat signal. Both beams are spatially filtered with an iris to get rid of remaining comb modes which contribute to noise. One finds an optimum for the highest signal-to-background ratio at the photodiode by iris diameters of $\sim$ 1 mm. Together with the dispersion of the grating there are still $\sim$ 340 modes for 866 nm and $\sim$ 560 modes for 729 nm behind the iris which contribute to noise. Reducing the iris diameter further to reach the resolution limits cuts already the intensity profile of both beams. This results in a lower signal-to-background ratio for the measured beat signal. The latter is filtered to a frequency range between 40 and 100 MHz. It is detected with a photodiode[6] and sent through an amplifier[7] with 28 dB gain. Behind the irises, the typical power of the comb spectrum ($\sim$10 µW) and the laser ($\sim$500 µW) gives a signal to noise ratio up to 35 dB which is necessary for a proper laser stabilization. However due to power fluctuations of the comb light caused by drifts of the outgoing polarization at the PCF it is quite hard to keep this value for each individual laser beat over the day. One solution would be to replace the PCF by a new generation which is not showing the effect of polarization drifts anymore or to further amplify the light at 1550 nm with an additional erbium-doped fiber amplifier.

7.3. Phase-locking scheme

Our main application of the frequency comb aims for the phase stabilization of the lasers for the ion experiment. Using the Pound-Drever-Hall method to lock the lasers to the transfer cavities yields a frequency stabilization but the relative phase between the lasers is still fluctuating. In order to excite transitions in the ion which need a relative phase stability between the lasers, like high-contrast dark resonances [75] in 866 nm spectroscopy, one has to change the scheme to a phase-lock of each laser to the corresponding comb modes. From each beat measurement one extracts the phase fluctuations of the laser relative to the comb mode which allows the stabilization of each laser to the comb mode enabling relative phase

[5] Thorlabs, GH13-18V
[6] Thorlabs, DET 10A
[7] Mini Circuits, ZFL-500LN+

stabilities between lasers. For this we ideally have to phase-lock both ν_{rep} and ν_{CEO} to the rubidium clock[8] as the absolute phase reference.

7.3.1. Repetition-rate lock

According to Eq. (7.4) it is important to have a highly-stable repetition rate since the multiplication factor m reaching 10^6 drastically scales up the noise from the RF into the optical frequency domain. Instead of using the fundamental repetition rate at 250 MHz for the stabilization we use the 6th harmonic at 1.5 GHz since the response to phase fluctuations is faster. For comparing the stability before and after the stabilization we first record the free-running repetition rate signal at 1.5 GHz. For recording frequencies we use a frequency counter[9] that is referenced to the 10 MHz clock signal from the Rb clock. The dead-time free counter is capable of measuring frequencies between 5 MHz and 50 MHz. Thereto we mix down the 6th harmonic of ν_{rep} at 1500 MHz with a signal from a VCO[10] at 1530 MHz which is phase locked to the clock. We record over a time of 4 hours the mixed-down signal at 30 MHz, i.e. at 29.990050 MHz and show the deviations from this value in Fig. 7.5. Beside a few short-term fluctuations that we see as frequency jumps, the drift is dominated by long-term temperature fluctuations and spans a range over $\sim$ 100 Hz. Since the VCO signal for mixing is phase-locked to the clock we assign the measured frequency drift as a drift at 1.5 GHz of the repetition rate. As the multiplication factor between 1.5 GHz and the optical frequency spectrum is $\sim 2.5 \cdot 10^5$ we obtain an optical frequency drift of $\sim$ 25 MHz which makes the need for a stabilization of the repetition rate obvious.

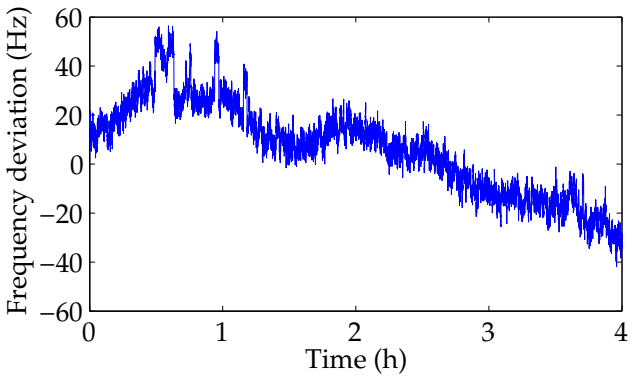

Figure 7.5.: Frequency deviation of the free-running repetition rate at 29.990050 MHz recorded over 4 hours with a frequency counter at a sampling rate of $1\,s^{-1}$. For details see text.

[8] Stanford Research Systems, FS725. It has a relative Allan deviation for 1 s averaging time of $\sigma_{1s} < 2 \cdot 10^{-11}$ at 10 MHz and a yearly aging in accuracy of $< 5 \cdot 10^{-10}$

[9] Menlo Systems, FXM

[10] Analog Devices, AD9858PCB

For locking the repetition rate to the Rb clock we mix down again the repetition rate signal at 1.5 GHz with the phase-locked VCO signal at 1530 MHz to 30 MHz. The 30 MHz signal is split into two signals. One is measured with the frequency counter and the second one is mixed down to DC with a phase-locked DDS signal at 30 MHz resulting in an error signal that depends on the phase deviation of ν_{rep} to the clock signal. The error signal is then feed through a self built PI controller to close the feedback loop by sending the output signal of the PI to the cavity piezo of the erbium fiber laser. The piezo of the laser cavity adjusts the pulse round-trip time by the cavity length and finally the repetition rate (see Eq. (7.4)). For the locked repetition rate at 1.5 GHz, Fig. 7.6(a) shows the frequency deviation from 30 MHz (i.e. from 29.992999975 MHz) which is recorded over 4 hours with the clock-referenced frequency counter. The dead-time-free sampling rate is $1\,\mathrm{s}^{-1}$. Here we see deviations of ± 30 mHz at the 1.5 GHz repetition rate signal. The deviations are three orders of magnitude lower than for the free-running case in Fig. 7.5, highlighting the performance of the repetition rate lock.

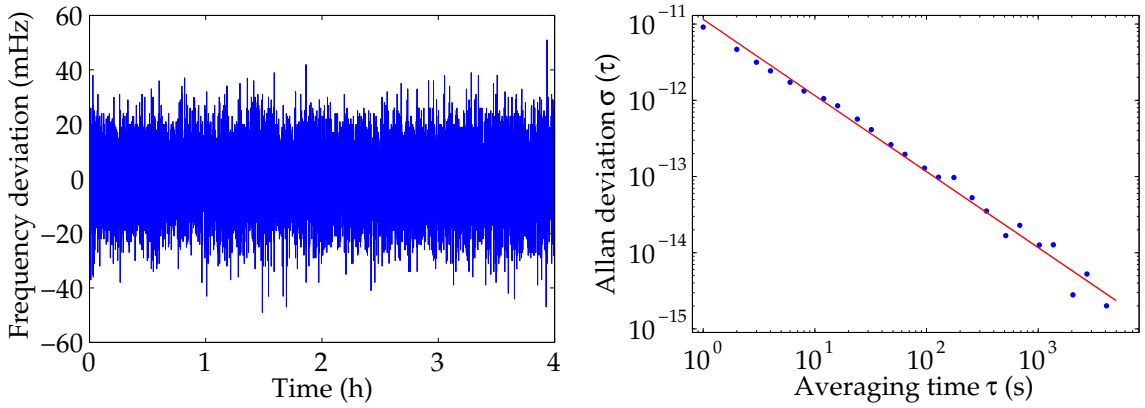

Figure 7.6.: (a) Frequency deviation from the mixed down repetition rate at 30 MHz over 4 hours of acquisition. The sampling rate is $1\mathrm{s}^{-1}$. (b) Allan deviation of the data from (a); the fit (red line) shows a slope of $\frac{1}{\tau}$, expected for a phase lock of the repetition rate to the atomic clock.

To analyze the stability of the repetition rate, the Allan deviation $\sigma(\tau)$ [156] is calculated from the data and shown in Fig. 7.6(b). For an averaging time of $\tau = 1\,\mathrm{s}$ the value of $\sigma_{1\mathrm{s}} = 9.14(7) \cdot 10^{-12}$ results in an absolute error at 1.5 GHz of $\sigma_{1\mathrm{s}} = 13.7(1)$ mHz. Taking this value into the optical frequency domain (e.g. for 729 nm), one has to multiply the Allan deviation by $m = 274293$ which ends up in a total frequency deviation of $\sigma_{1\mathrm{s}} = 3.76(3)$ kHz. From a fit to the data (red line) one can see that the stability averages down as $1/\tau^{0.99(2)}$. This limits the remaining noise sources to white phase noise or flicker phase noise which both have a slope of $\frac{1}{\tau}$, confirming the phase lock. The two noise types are related

to the noise in the electronics and can be reduced by selected components.

7.3.2. Lock of 794 nm and 866 nm laser to the comb

From the beat detection unit of the 794 nm and 866 nm laser, the beat signal of each laser is amplified, filtered and mixed down to a DC signal with a RF-frequency signal from a DDS[11] that has the same frequency as the beat note. The DC signal, i.e. the error signal is sent to the PID controller to generate a feedback signal which is sent to the current modulation input of the diode lasers for regulating phase deviations of the laser. Once the two feedback loops are closed we have individually phase locked the 794 nm and 866 nm laser to the comb.

In order to characterize the phase-coherence between two lasers we perform 866 nm spectroscopy at the ion which is sensitive to the relative phase between the two lasers used for the spectroscopy, i.e. the 397 nm (794 nm) laser and the 866 nm laser [75]. First we perform the spectroscopy with the two lasers locked to their transfer cavities. The result is shown in Fig. 7.7(a). From the depth of the four dark resonances we obtain from a fit of the 8-level Bloch equation the laser linewidth for the lasers at 794 nm and 866 nm of 118 kHz. Next, we perform the measurement with both lasers locked to the comb in-

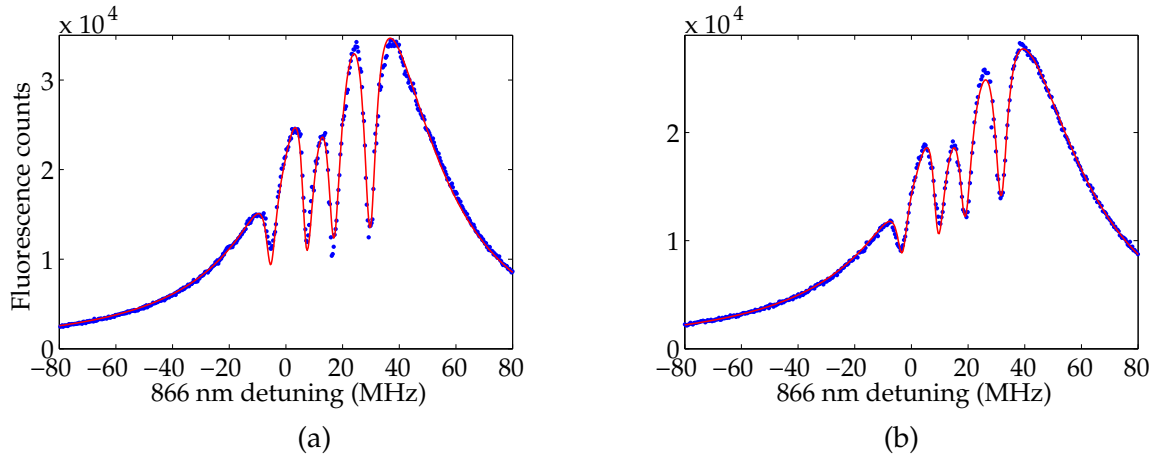

Figure 7.7.: 397 nm fluorescence spectrum for different 866 nm detuning with (a) both lasers locked to the transfer cavities and (b) both lasers are locked to the frequency comb. The total span of the 866 nm detuning is divided in 0.4 MHz steps. For each frequency step the fluorescence is integrated for 200 ms.

cluding a phase-locked repetition rate. In Fig. 7.7(b) we see that the depth of the four dark resonances is decreased compared to the cavity-locked case in Fig. 7.7(a). From the fit we obtain the linewidth of both lasers of 175 kHz. This value is slightly higher than for

[11] Analog Devices, AD9858PCB

the same measurement but with the lasers locked to the transfer cavities. The reason for a higher linewidth for both lasers stabilized to the comb is the CEO frequency that was not locked to the atomic clock since the linewidth of the CEO has been excessively high (~ 4 MHz). The broadening against typical values for the CEO linewidth of 300 kHz made the lock almost not possible. Later the problem could be backtracked to a damaged piezo mirror inside the fiber-laser resonator. The losses of light at the mirror result in an increase of quantum noise which is caused by spontaneous emission inside the laser resonator [157]. Together with the amplification in the Er-doped fiber the spontaneous emitted light is amplified resulting in a significant increase of the optical phase noise for the CEO frequency. This also results in phase fluctuations of the individual comb modes which were not well correlated. We manifested this by the measurement of different linewidths in the beat signals with different lasers. Since the phases of the lasers stabilized to the comb are locked to the phases of the corresponding comb modes, also the phases of the lasers relative to each other were not well correlated. Thus the measurements have to be repeated with the new piezo mirror inside the fiber laser resonator. With the new mirror, a CEO linewidth of 400 kHz could already be measured. Now a phase lock of the CEO to the atomic clock should be straight forward which enhances the performance of the laser lock to the comb. In this case a significant improvement of the spectroscopy result is expected.

Alternative stabilization scheme

For high phase coherence between the lasers from short integration times for fast laser sequences as well as long integration times of hours one has to circumvent the problem of an unstable frequency comb. This can be avoided by an alternative locking technique [158] where the comb is not used as the reference but as a transfer oscillator. In this scheme the frequency fluctuations of ν_{rep} and ν_{CEO} do not enter the measurement but cancel out. The beat signals of two lasers with their individual comb mode are mixed in such a way, that the final beat signal serves as an error signal that depends only on the phase difference of the two lasers. Once we use the 729 nm laser stabilized to the high-finesse cavity as the reference, it can be used to stabilize the phase of all other lasers to the phase of this laser. Together with fast PID regulators this would mean that in principle all other lasers could be reduced in their spectral linewidth and long term fluctuations to the one performed by the 729 nm laser. This would yield a high laser-to-laser phase coherence which would allow one to study coherent phenomena at the ion with higher precision.

7.4. 393 nm photon generation with frequency-comb light

Besides using the frequency comb for phase-locking the diode lasers used in the ion experiment, we directly excite the ion with the light from the comb. One future application could be direct frequency-comb spectroscopy [159] or the investigation of resonant multi-photon excitations at the ion. Comb-ion interaction measurements may exploit the phase

coherence between successive ultrashort pulses which allow one to study fast dynamics if the temporal length of the pulses τ is much shorter than the atomic lifetime of the excited state. Here we show a first step toward investigations of fast dynamics in the ion by the generation of 393 nm photons through absorption of 854 nm photons out of the comb spectrum.

Experimental setup and sequence

The experimental setup in the comb laboratory is shown in Fig. 7.2. The spectrum from the photonic-crystal fiber (PCF) spans from $\sim$ 550 nm to $\sim$ 1000 nm. We cut out the spectral part of interest by sending the light through a bandpass filter[12] which has a center wavelength of 850 nm with a FWHM of 10 nm. This corresponds to a frequency FWHM of 4.15 THz, translating to 16600 comb modes. The vertically polarized light is sent through an acousto-optic modulator (AOM) for frequency tuning and coupled to a 16 m long single-mode fiber, connecting the comb laboratory with the ion laboratory. The experimental

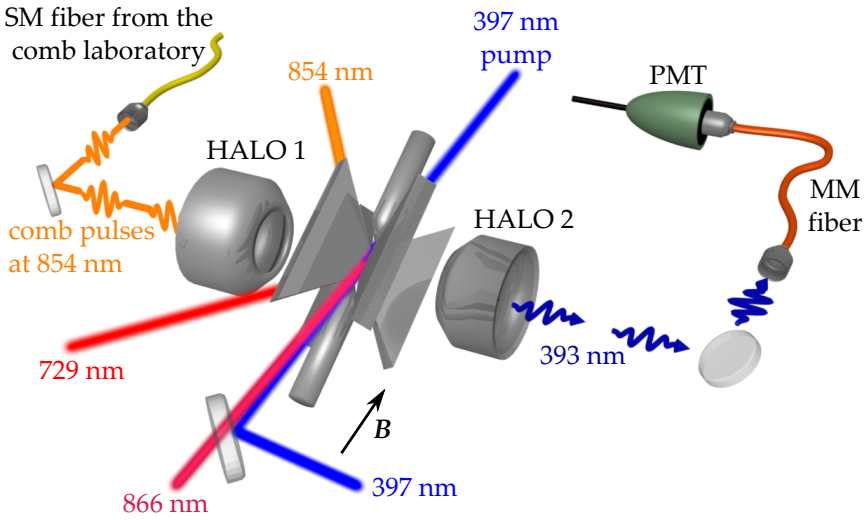

Figure 7.8.: Experimental setup in the ion laboratory for the generation of 393 nm photons by absorption of 854 nm frequency-comb photons that are transmitted by a single-mode fiber from the comb laboratory. The details are given in the text.

setup in the ion laboratory is depicted in Fig. 7.8. The frequency comb pulses are focused onto the ion through HALO 1 perpendicularly to the quantization axis (the magnetic-field direction). With HALO 2 we collect the generated 393 nm photons which are coupled to a multi-mode fiber (MM fiber) and detected by a photomultiplier (PMT). The 397 nm and 866 nm laser are used for Doppler cooling while the 397 nm pump beam optically pumps the population to one Zeeman substate in $S_{1/2}$. The 729 nm laser is sent to the ion from 45°

[12] Thorlabs FL05850

with respect to the HALO axis for coherent manipulations on the quadrupole transition between $S_{1/2}$ and $D_{5/2}$. The 854 nm beam repumps the remaining population in $D_{5/2}$ after photon generation.

The sequence as displayed in Fig. 7.9 is initialized by Doppler cooling with the 397 nm and 866 nm laser for 100 µs while the 854 nm laser transfers any remaining population in $D_{5/2}$ into the cooling cycle. It is followed by an optical pumping period where the 397 nm pump laser is switched on for 5 µs to prepare all the population in $\left|S_{1/2}, -\frac{1}{2}\right\rangle$. Then we transfer the population with a 729 nm π-pulse in 3.33 µs to $\left|D_{5/2}, +\frac{1}{2}\right\rangle$. In the fourth part of the sequence we detect the comb pulses within a period of 12.5 ns which is explained in detail below. Subsequently, frequency comb photons from the filtered 854 nm part of the comb spectrum are absorbed and generate 393 nm photons within a photon generation period of 2 µs during which the photomultiplier is gated on.

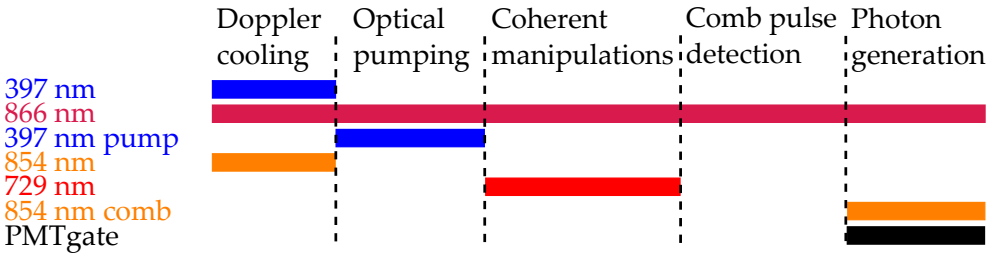

Figure 7.9.: Sequence for the generation of 393 nm photons by the absorption of 854 nm frequency comb photons. For details see text.

Frequency-comb pulse detection

In order to see the comb pulses separated in time by 4 ns in the temporal shape of the generated 393 nm photon we need a reference signal from the frequency comb which is used as sequence trigger for a correlation measurement with the arrival-time of the generated photons. For this we use the "RF Out" output signal from the frequency-comb laser head that delivers sharp output pulses separated by 4 ns which are measured by a fast photodiode inside the resonator. In the frequency domain this signal corresponds to the repetition rate (250 MHz) and its higher harmonics. For detecting one pulse that arrives in the comb pulse detection period of the sequence, we amplify the signal[13] as shown in Fig. 7.10 and gate it inside the gate box with the HYDRA gate signal of 12.5 ns. After attenuation we send the signal to the first channel of PicoHarp, a time-correlated counter where the signal is time-tagged. For the second channel we gate the PMT signal for 2 µs and send the attenutated signal to PicoHarp. With both signals we are able to correlate the comb pulses, serving as a trigger for photon generation, with the generated 393 nm photon for every sequence cycle.

[13] Mini Circuits ZHL-1-2W

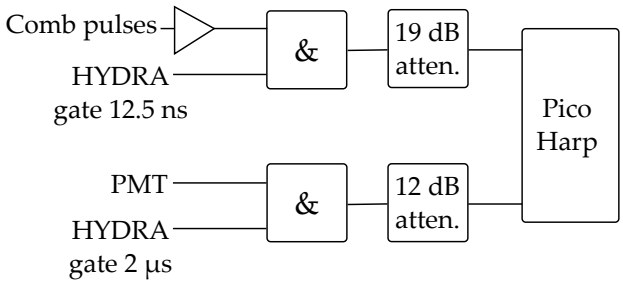

Figure 7.10.: Signal processing for correlation measurements between the frequency-comb pulses and the detected 393 nm photons within one sequence cycle.

393 nm arrival-time histogram

Acquiring statistics to obtain a decent 393 nm photon wave packet in the arrival-time distribution requires a measurement time of (at least) several minutes. Within this time, the comb modes in the optical frequency domain should ideally be frequency stabilized, for which the repetition rate and the CEO frequency both have to be phase locked to a common reference. We phase lock the repetition rate to the Rb-clock reference oscillator such that an optical comb mode at 854 nm is as close as possible to the resonant atomic transition frequency from $D_{5/2}$ to $P_{3/2}$, while the unstabilized CEO frequency is set to DC. Remaining frequency deviations from the closest comb mode to the atomic resonance are compensated by the AOM detuning. After the stabilization of the repetition rate, we set the output power of the comb light measured in front of the HALO to 340 µW and adjust the AOM frequency to a value which yields the highest rate of 393 nm photons that are generated in cw excitation condition. Thereto we measure the scattered 397 nm photons, i.e. with the 397 nm, 866 nm, 729 nm and 854 nm comb switched on. After the optimization we switch to the sequence mode for photon generation.

In Fig. 7.11 we show the arrival-time distribution of Raman-scattered 393 nm photons, generated by the absorption of 854 nm comb photons. We identify the measured photon wave packet with fast temporal dynamics (blue line), i.e. excitations which are separated by 4 ns. Beside the fast dynamics we see a slowly-varying envelope which is represented by the population in the $P_{3/2}$ level (red line) from a simulation.

First we describe the envelope shape by considering the atomic absorption spectrum that has a width of $\Gamma_{P_{3/2}} = 2\pi \cdot 22.99\,\mathrm{MHz}$. Within this bandwidth the ion filters one comb mode (which is ideally on resonance) out of the comb spectrum. This mode mainly contributes to the absorption process and defines the overall slowly-varying temporal shape which we show in the following: we obtain the shape of the envelope by simulating the population in $P_{3/2}$ with the 18-level Bloch equations (see red curve in Fig. 7.11). For the simulation we use a single-mode 854 nm laser. With a measured average power of the comb spectrum of 340 µW, we calculate the power in the closest comb mode to be 1.84 nW. This corresponds to a Rabi frequency of 32.2 MHz. From the simulation of the population

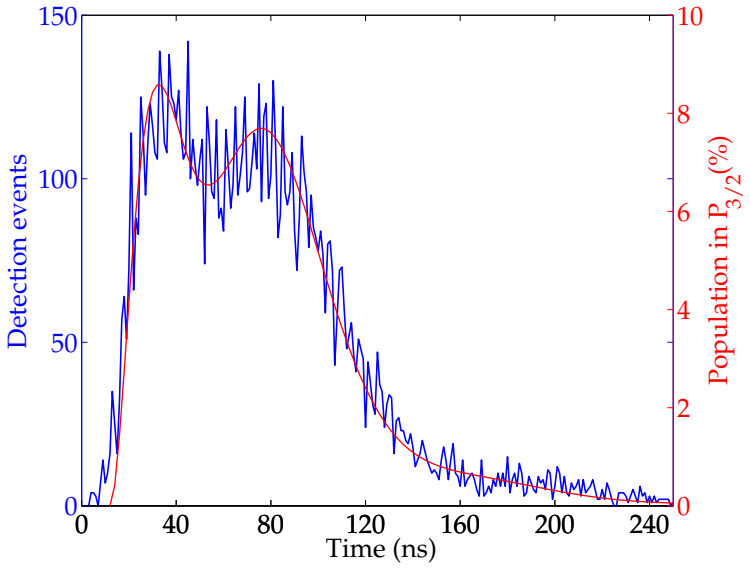

Figure 7.11.: Arrival-time distribution of 393 nm photons (blue line) generated by the absorption of 854 nm photons from the frequency comb. On top of the overall temporal shape of the wave packet, we see fast dynamics from the comb, i.e. short excitations which repeat every 4 ns, i.e. the inverse of the repetition rate. The bin size is 1 ns for a measurement time of 5 min. The red curve is obtained from numerical simulations with the 18-level Bloch equations representing the population in the $P_{3/2}$ level for a cw single-mode 854 nm laser excitation.

in $P_{3/2}$ (red curve), we obtain a Rabi frequency of 30 MHz for the 854 nm laser, a detuning of -4 MHz and a slight variation from vertical polarization. The deviations are attributed to power fluctuations of the comb light due to polarization drifts behind the PCF, frequency drifts due to the non-stabilized CEO frequency and polarization drifts inside the single-mode fiber connecting both laboratories. We see that the overall temporal shape of the population in $P_{3/2}$ from the simulation fits well to the overall temporal shape of the measured 393 nm photon. With the simulation, we identify a Rabi oscillation at the beginning of the overall photon shape, which is explained by the high Rabi frequency causing stimulated emission processes between $P_{3/2}$ and $D_{5/2}$. Thus the overall temporal shape is similar to an excitation with a single-mode 854 nm laser as it is the case for 393 nm Raman scattered photons presented in Sec. 3.1.2.

Besides the overall temporal shape which is simulated with a single mode 854 nm laser, we also see the temporal dynamics of the frequency comb, i.e. pulsed excitation every 4 ns. Although there is only one comb mode which is mainly contributing to the overall shape of the photon, the adjacent modes form the pulsed excitation. If only a few modes coherently contribute to the absorption process, we obtain pulses separated by 4 ns which are responsible for the fast excitation from $D_{5/2}$ to $P_{3/2}$. In the wave packet the 4 ns separation

is divided in a period of 2 ns where the ion is excited and a subsequent decay of 2 ns. The exponential decay has a time constant of $\sim$ 10 ns. We attribute this to the lifetime of the $P_{3/2}$ level ($\tau = 6.924$ ns) with which the population in $P_{3/2}$ decays. Before the population can completely decay the next 854 nm pulse add further population from $D_{5/2}$ to $P_{3/2}$. This strong, short-pulse excitation, is in contrast to the Raman-type excitation. The pulses arrive every 4 ns, which is too fast in order to observe a full atomic decay of $P_{3/2}$ level in the arrival-time distribution after each pulse. One solution would be a pulse picker that could increase the temporal distance of the pulses from 4 ns to 8 ns or more.

Simulation of the dynamics for pulsed 854 nm excitation

We also simulate the pulsed dynamics in the population of the $P_{3/2}$ level with the Bloch equation program. The laser pulses from the comb are simulated by a single-mode 854 nm laser which is periodically switched on and off. The periods for on and off are divided in time steps and for each time step the population in $P_{3/2}$ is calculated. The evolution of the population in $P_{3/2}$ is shown in Fig. 7.12(a) for a 854 nm pulse length of 2 ns. Similar to the

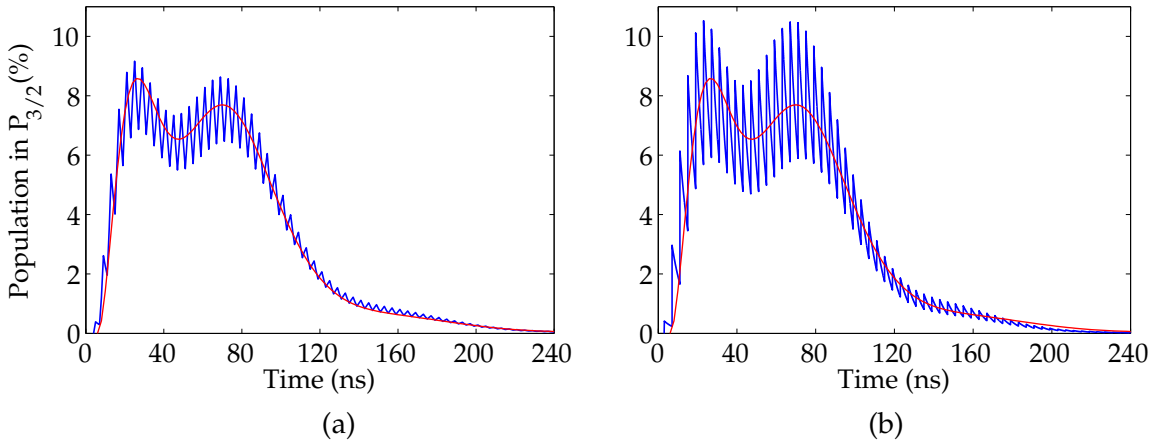

Figure 7.12.: Temporal evolution of the population in the $P_{3/2}$ level for a simulated pulsed 854 nm laser excitation (blue line) and the single-mode 854 nm laser excitation (red line) from Fig. 7.11. (a) The pulse length is 2 ns and the 854 nm pulse power is 5.8 nW. (b) With the pulse length of 20 ps we use a power of 58 µW to obtain the same overall temporal shape. The time step size is 1 ns (a) and 10 ps (b).

measurement, we initialize the total population in $\left|D_{5/2}, +\frac{1}{2}\right\rangle$. With a time step size of 1 ns where the population in $P_{3/2}$ is calculated, the 854 nm laser is switched on for 2 ns leading to a fast and strong excitation. After the excitation the laser is switched off for 2 ns where the population decays. In order to fit the simulated dynamics to the measured photon in Fig. 7.11, we change the 854 nm laser power to 5.8 nW and the detuning to -6 MHz. With these parameters we obtain the dynamics which fit well to the temporal dynamics of the

measured photon. To compare the simulated dynamics to the measured one, we also show again the simulation from Fig. 7.11 for cw excitation (red line). The simulations fits best to the measured photon for a pulse length of 2 ns and a power of 5.8 nW. We compare the dynamics to the case that the 854 nm pulse length is divided by a factor of 10^2 to 20 ps (with a time step size of 10 ps) in Fig. 7.12(b). In order to obtain the same overall temporal shape (as given by the red line for cw excitation) we have to make sure that the power P_{854} is increased by 10^4 to 58 µW. This is explained by the fact that the pulse area has to be constant, i.e. the Rabi frequency $\Omega_{854} \propto \sqrt{P_{854}}$ and the pulse width τ_{854} has to fulfill the relation

$$\Omega_{854} \cdot \tau_{854} \propto \sqrt{P_{854}} \cdot \tau_{854} = \text{const.} \tag{7.11}$$

to obtain the same overall temporal shape. We further see in Fig. 7.12(b) that for a shorter pulse the population transfer per pulse is increased and the pulsed structure becomes more pronounced. Here the number of comb modes that contribute to the excitation is increased. Although the modes are multiple integers of 250 MHz away from the resonant mode they still contribute to the excitation.

From the maximum and minimum population of the excitation in Fig. 7.12 that leads to the highest population in $P_{3/2}$ (at ∼25 ns) we define a visibility value for the pulsed excitation as a measure for the excitation probability per pulse. In Fig. 7.13 we show the visibility for different comb pulse lengths. Starting from a pulse width of 2 ns we see that

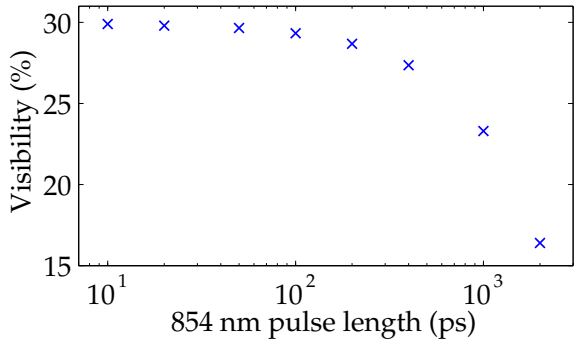

Figure 7.13.: Visibility of pulsed excitations in the arrival time of single photons for different 854 nm frequency-comb pulse lengths.

the visibility increases for shorter pulses for the same pulse area. If we reduce the pulse width to 20 ps, we see that the excitation probability per pulse does not further change. There the modes are too far away from the absorption profile of the ion such that they are suppressed and do not contribute anymore to the excitation.

Summary

In this chapter I presented first experiments with the frequency comb. Thereto we phase-locked the repetition rate to the atomic clock and obtain a Allan deviation of $\sigma_{1s} = 9.14(7) \cdot$

10^{-12} resulting in a optical frequency deviation at 729 nm of 3.76(3) kHz. With the locked repetition rate we locked two diode lasers to the comb and performed 866 nm spectroscopy. The higher laser linewidth compared to the case when both lasers are locked to their transfer cavities could be explained by an excess phase noise due to a damaged piezo mirror inside the laser resonator.

Besides we showed the generation of 393 nm photons by the excitation with 854 nm laser pulses from the frequency comb. By correlating the comb pulses with the single-photon clicks from the PMT we obtained an arrival-time distribution in which the temporal shape of the photon showed pulsed dynamics from the comb (i.e. pulses that are separated by 4 ns) on top of an overall slowly-varying envelope. With the 18-level Bloch equation program we observed the same slowly-varying envelope by a single-mode 854 nm laser excitation. From the simulation we deduced that only one mode which was close to the resonance frequency was mainly responsible for the Raman scattering process and determined the overall shape. The comb structure in the photon was generated by adjacent comb modes which also contributed to the excitation. For a 2 ns pulse width we found the pulsed dynamics in the population of the $P_{3/2}$ level which fitted well to the temporal dynamics of the 393 nm photon. For shorter pulse widths we discovered that the pulse area had to be constant to obtain the same overall temporal shape while the excitation probability per pulse was increased. However, for $\sim$ 20 ps of pulse length, the excitation probability per pulse saturated since the outermost modes were far detuned from resonance and did not contribute to the absorption process anymore.

8. Conclusions

8.1. Continued work: experimental protocol for high-fidelity heralded photon-to-atom quantum state transfer

In Chapter 6 we showed that the coherent transfer of the atomic phase in the $D_{5/2}$ superposition state onto the scattered 393 nm photon is possible, which lets us proceed with our work toward the coherent photon-to-ion transfer of quantum information.

The following work presents an experimental protocol for such a state transfer, which is a major part of the Ph.D. thesis of C. Kurz [107] and is published in [160]. We prepare a single ion in a coherent superposition state and absorb an 854 nm laser photon. With certain probability, a single emitted photon at 393 nm is detected. Through the Raman process, we map the polarization state of the absorbed photon onto the ground state of the ion. In Chapter 3 we already motivated the use of 393 nm photons in a pure quantum state as a herald for successful photon absorption. Here, as proposed in [98, 102], we obtain with the detection of the 393 nm Raman-scattered photon a herald for the successful state transfer. This allows us to detect only successful polarization storage events, making the state-transfer fidelity independent of the transfer efficiency. The theory to describe the quantum state transfer is given in [102, 129].

Experimental sequence

The experimental sequence is shown in Fig. 8.1. The sequence starts with an optical-pumping period of 5 µs that prepares the ion in the $\left|S_{1/2}, -\frac{1}{2}\right\rangle$ state with 99.82(1) % probability by σ^--polarized light at 397 nm. Then we create a coherent superposition state in $\left|S_{1/2}, \pm\frac{1}{2}\right\rangle$ by a $\frac{\pi}{2}$ radio-frequency (RF) pulse of 2.8 µs duration from an RF coil, explained in more detail below. The following two 729 nm π pulses, each lasting for 9.6 µs, transfer the coherent superposition in $S_{1/2}$ to the new superposition in $\left|D_{5/2}, \pm\frac{3}{2}\right\rangle$. For single-photon absorption, the 854 nm laser is switched on for 3 µs with an optical power of 12 µW to drive the superposition of σ^+ and σ^- for generating 393 nm photons in a spontaneous Raman process (see Fig. 8.1(b)). Once the π photon is detected, it heralds the successful creation of a superposition of the $S_{1/2}$ Zeeman sublevels corresponding to the polarization of the absorbed 854 nm photon. Thus the state mapping is completed by the photon detection.

After the detection of the photon, we perform atomic-state analyis [161] to quantify the fidelity for the mapping protocol. If the ion is measured in the $\left|S_{1/2}, \pm\frac{1}{2}\right\rangle$ basis, the

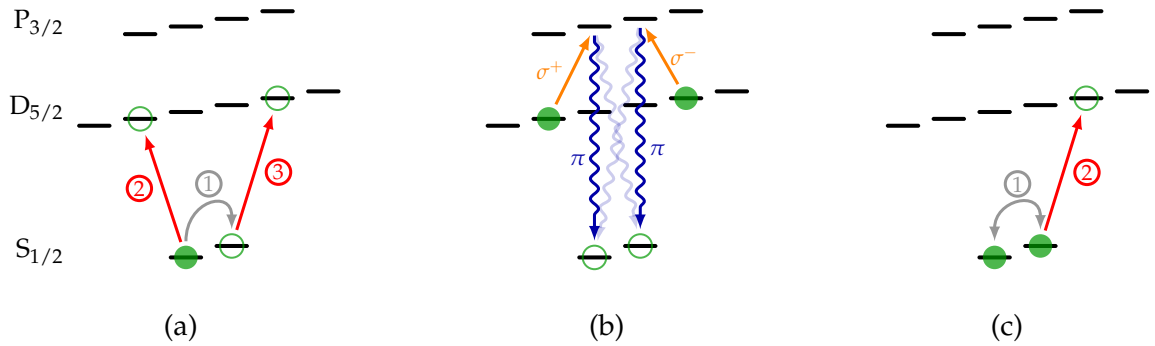

Figure 8.1.: Experimental sequence: (a) After the ion is initialized in $|S_{1/2}, -\frac{1}{2}\rangle$, a $\frac{\pi}{2}$ RF-pulse creates a coherent superposition state in $S_{1/2}$ (gray arrow). Two resonant 729 nm pulses (red arrows) transfer the superposition to $D_{5/2}$. (b) With the absorption of 854 nm laser photons along the quantization axis, the emission of 393 nm photons is triggered, at which π photons are filtered and detected. (c) Electron shelving (red arrow) followed by atomic-fluorescence detection are used to distinguish the $S_{1/2}$ Zeeman sublevels. Depending on the measurement basis, we apply another RF pulse before (gray arrow).

$|S_{1/2}, +\frac{1}{2}\rangle$ state is transferred to the $D_{5/2}$ manifold (see Fig. 8.1(c)), before switching on the cooling lasers. A projection of the ion onto the $S_{1/2}$ state is given by the detection of the 393 nm photon. The distinction of the two $S_{1/2}$ Zeeman substates is then signaled by the onset of fluorescence (ion in $|S_{1/2}, -\frac{1}{2}\rangle$) or no fluorescence (ion in $|S_{1/2}, +\frac{1}{2}\rangle$). To project the ion onto a superposition basis, we apply a second RF pulse that acts as a basis rotation before state analysis. If the Raman photon is not detected, we apply Doppler cooling for 10 µs. The overall sequence repetition rate is 18 kHz.

Experimental setup

The experimental setup is sketched in Fig. 8.2. The novelty, compared with the setups presented so far in this thesis, is represented by the 2-loop copper-wire coil that we installed below the trap outside the vacuum vessel. Its characterization is found in [107]. The coil, as part of a series LC circuit, is driven by an RF current from our pulse sequencer, creating an oscillating magnetic field perpendicular to the quantization axis defined by the static magnetic field B. For a static magnetic-field strength of 2.8 G, we are able to excite the $|S_{1/2}, -\frac{1}{2}\rangle$ to $|S_{1/2}, +\frac{1}{2}\rangle$ transition at a frequency of 7.8 MHz at Rabi frequencies up to ~ 100 kHz.

The 854 nm laser with its variable polarization is sent in along the quantization axis, while the scattered 393 nm photons are collected perpendicularly to it by one HALO. In the photonic reference frame, the emitted $|\pi\rangle$ photons correspond to $|H\rangle$-polarized photons that are filtered by the PBS_{393} such that they are transmitted via the multi-mode fiber to

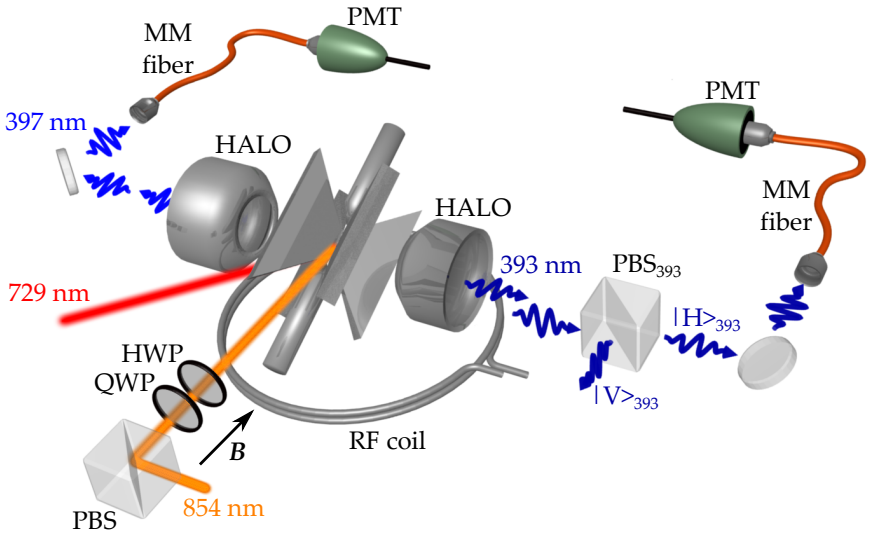

Figure 8.2.: Experimental setup for photon-polarization storage: HALO, high-NA laser objective; PMT, photomultiplier tube; MM fiber, multi-mode fiber; PBS, polarizing beam splitter; HWP, half-wave plate; QWP, quarter-wave plate; RF coil, radio-frequency coil; For further details, see text.

the PMT while parasitic σ photons are reflected as $|V\rangle$-polarized photons. The 397 nm fluorescence photons are collected by the second HALO, coupled into the multi-mode fiber and are detected by another PMT.

Experimental results

For the first measurement we set the 854 nm polarization to right-handed circular which leads to an excitation from $|D_{5/2}, -\frac{3}{2}\rangle$ to $|S_{1/2}, -\frac{1}{2}\rangle$ by the emission of a 393 nm π photon. After the detection, the atomic-state analysis is executed in the $|S_{1/2}, \pm\frac{1}{2}\rangle$ basis and the arrival times are sorted according to the measurement outcome. Fig. 8.3(a) shows that the emission of photons conditioned on the projection onto the $|S_{1/2}, -\frac{1}{2}\rangle$ state is suppressed.

For a linear 854 nm input polarization, the detection of a π photon heralds the projection of the ion onto the superposition of $|S_{1/2}, -\frac{1}{2}\rangle$ and $|S_{1/2}, +\frac{1}{2}\rangle$ that corresponds to the 854 nm light polarization. Analysis in the superposition basis is enabled by a second $\frac{\pi}{2}$ RF pulse before state analysis. Fig. 8.3(b) shows the arrival-time distributions sorted for a projection onto state $|S_{1/2}, -\frac{1}{2}\rangle$ and $|S_{1/2}, +\frac{1}{2}\rangle$, respectively, after the basis rotation. Here we find oscillations in the photonic wave packet. Due to our previous measurements investigating the quantum beats in the wave packet (presented in Chapter 6), we can quickly identify the oscillations; in this case, they result from the difference between the Larmor frequency of the initial superposition of $|D_{5/2}, \pm\frac{3}{2}\rangle$ and the final superposition of $|S_{1/2}, \pm\frac{1}{2}\rangle$. The oscillation period is calculated for a magnetic field $B = 2.8\,\mathrm{G}$ with the corresponding

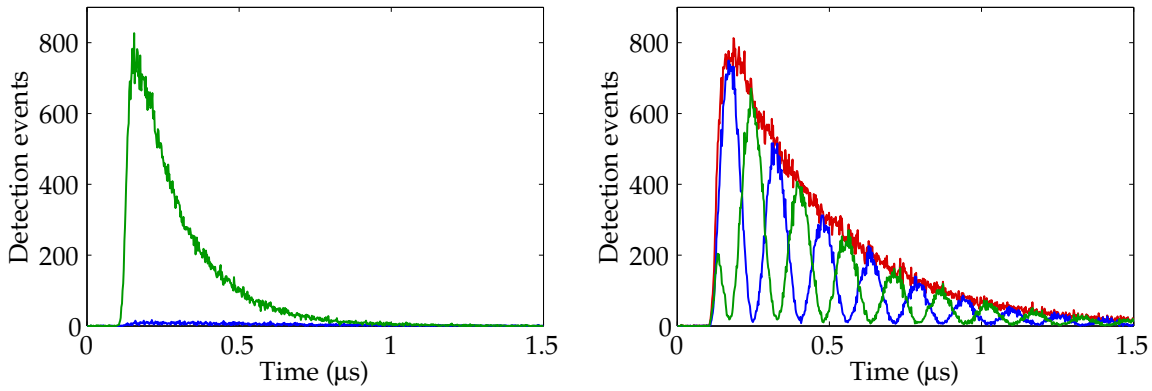

Figure 8.3.: Arrival-time distributions of 393 nm photons: (a) conditioned on the projection onto $|S_{1/2}, +\frac{1}{2}\rangle$ (blue) and $|S_{1/2}, -\frac{1}{2}\rangle$ (green) for right handed circularly polarized 854 nm light. (b) conditioned on the projection onto the superposition basis for linearly polarized 854 nm light. The red curve shows the unconditional case , i.e. the sum of the two histograms. For each graph, the bin size is 2 ns and the overall measuring time is 20 min.

Landé factors as $T = \frac{h}{1.6\mu_B B} = 160\,\text{ns}$.

In order to characterize the quality of the mapping protocol, we analyze phase and contrast of the oscillations in the 393 nm wave packets. The phase which is accumulated in the $|D_{5/2}, \pm\frac{3}{2}\rangle$ superposition is given by the time until the 393 nm photon is detected. Thus each detection time t is assigned to a phase value $\varphi = 2\pi\frac{t}{T}$. As we expect the same final atomic states of the detection time t for integer multiples of the Larmor period T, we use the reduced phase $\phi = \varphi \bmod 2\pi$. For various input polarizations we show in Fig. 8.4 the probability of projecting the ion onto the $|S_{1/2}, +\frac{1}{2}\rangle$ state after the $\frac{\pi}{2}$ RF pulse, which is derived from arrival-time histograms, as a function of the reduced phase.

The expected sinusoidal behavior as well as the relative phase shift between the polarizations V, D, H and A appear very well in the data. From the sinusoidal fit, we obtain the corresponding fidelity values for V, D, H and A and together with the fidelities for circular polarization, we obtain an average fidelity of 96.9(1) %. We also perform quantum process tomography [162], a tool for quantifying the transfer fidelity of the mapping process and derive a process fidelity of 95.0(2) %.

Summary

We demonstrated a protocol for heralded high-fidelity mapping of a photonic polarization state onto the $S_{1/2}$ Zeeman qubit of the ion. The successful storage process of the 854 nm input polarization state is heralded by the detection of the 393 nm scattered π photon. The values of the process fidelity of 95.0(2) % and the average fidelity of 96.9(1) % both cor-

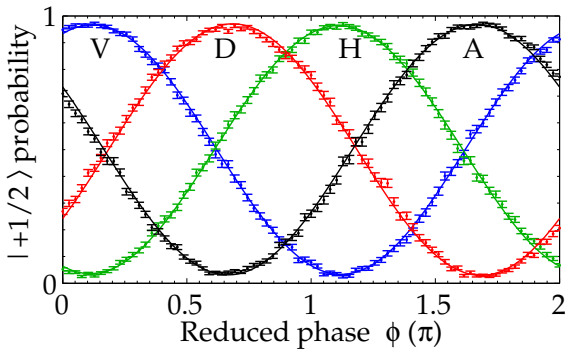

Figure 8.4.: Atomic-state analysis with the probability that the ion is in the state $\left|S_{1/2}, +\frac{1}{2}\right\rangle$ after the $\frac{\pi}{2}$ RF pulse as a function of the reduced phase ϕ for four different 854 nm input polarizations.

roborate the quality of our experimental control and performance. In a next step, we will repeat the experiment with the absorption of true single photons, generated by the improved spontaneous parametric down-conversion source. This will pave the way toward the entanglement transfer from the entangled photon-pair source to two distant ions, a milestone experiment in quantum networking.

8.2. Summary

The work presented in this thesis comprises the investigation of fundamental light-matter interactions at the quantum interfaces of two distant quantum network nodes involving single trapped $^{40}Ca^{+}$ ions. The control of emission processes at the quantum interface of one ion was shown by the controlled generation of single photons. This opens up the way to investigating single-photon absorption experiments and, at the same time, demonstrating proof-of-principle experiments with direct photonic interactions between two distant single ions. The progress toward the distribution of quantum information in the elementary network nodes was pushed with quantum-interference experiments. As a quantum-optical phenomenon, they highlighted the coherent character of the single-photon scattering processes at the interface.

A highly controlled quantum-interface for quantum networking requires the controlled emission of single photons. To this end we introduced the generation of single 393 nm photons in a spontaneous Raman process by the absorption of 854 nm laser photons. Varying the laser intensities allowed us to control the temporal shape of the photonic wave packets between 325(3) ns and 2.23(1) µs. The single-photon character was shown in the second-order correlation function of the arrival times of the emitted photons, yielding a two photon probability of 0.33(15) %. By optical pumping to the outermost Zeeman substates in the $D_{5/2}$ manifold, we generated photons in a pure quantum state in terms of polarization and

frequency. A theoretical analysis of the frequency spectrum emphasized the pure quantum state of the photons whose time-bandwidth product is minimal, i.e. the photons fulfill the Fourier-limitation criterion. Thus, they are excellent candidates for carriers of quantum information in entanglement-transfer schemes. Besides we also generated 393 nm photons by the absorption of 854 nm laser pulses from the frequency comb. The pulses separated by 4 ns were found again in the arrival-time distribution of the scattered 393 nm photons. The temporal shape of the 393 nm photon wave packet was confirmed by a simulation with the 18-level Bloch equations. Analyzing the inverse process led to the generation of near-infrared 854 nm photons. Here the excitation on a single dipole transition was replaced by a coherent three-photon process. Its coherence was manifested by the suppression of photon scattering from the intermediate states by a factor of 22. The resonance condition of the excitation led to a high rate of single-mode fiber-coupled photons up to $3.0(6) \cdot 10^3\,\mathrm{s}^{-1}$, with a mode-matching efficiency into the single-mode fiber of 3.2(6) %. We tailored the temporal shape of the wave packets between 834(2) ns and 5.89(6) µs.

We used the emitted photons to perform direct photonic interaction measurements between two $^{40}Ca^+$ ions in two distant traps at the two wavelengths. At 393 nm, the photons were transmitted through free-space between the distant traps. In continuous generation mode at the sender, photon absorption was heralded at the receiver ion by quantum jumps from bright to dark. From the recorded quantum-jump trace, we obtained an absorption rate of $24.52(7)\,\mathrm{s}^{-1}$ and inferred the absorption probability of $3.6 \cdot 10^{-4}$. In a similar way we performed photonic interaction measurements between the distant ions with 854 nm photons which in this case were transmitted via a single-mode fiber. In continuous transmission mode, up to $1.22(26) \cdot 10^4\,\mathrm{s}^{-1}$ photons were coupled to the single-mode fiber. With this rate we reduced the $D_{5/2}$ lifetime to 24 % and derived an absorption probability of $2.6(5) \cdot 10^{-4}$. By generating photons in a pulsed sequence, we showed the triggered photon transmission in the temporal correlation function between the emission trigger at the sender and the photon absorption at the receiver heralded by a quantum jump. With a temporal resolution of 3 µs, given by the detection rate of 397 nm fluorescence photons, we saw clear emission-absorption coincidences. The number of coincidences for the given measurement time corresponded to an absorption probability of $2.4(5) \cdot 10^{-4}$. Related to the total number of emission triggers we obtained an overall success probability of $4.8(7) \cdot 10^{-6}$. This constitutes a proof-of-principle experiment toward the direct quantum state transfer between two quantum network nodes realized in two distant-trapped single ions.

Toward the transfer of quantum information at the quantum interface of a single network node, we showed scattering of single photons by the observation of quantum interference phenomena that exhibited the coherent character of the Raman process: Quantum beats were visible in the arrival-time distribution of single photons, which we explored in two distinct level configurations, called Λ and V. Through absorption of 854 nm laser photons, we mapped the atomic phase onto the arrival-time distribution of the emitted 393 nm photons. The distribution reflected the temporal modulation of the initial atomic state at the Larmor frequency with visibilities as high as 93.1(6) %. We controlled the quantum beat

phase by setting the initial atomic phase and the polarization of the 854 nm polarization. With the atomic control phase, we had a control knob for adjusting the detection efficiency of the scattered photons for both schemes, i.e. to enhance and suppress the scattering probability. In order to reveal the physical origin behind the two schemes, we analyzed the remaining population in the $D_{5/2}$ level after an excitation with 854 nm light for different 854 nm pulse lengths. For the Λ scheme, we saw a stair-like behavior in the $D_{5/2}$ depopulation at the Larmor-period, which resulted from the interference of the two absorption paths. For the V scheme, the depopulation exhibited a pure exponential decay; we thus assigned the subsequently measured quantum beats to the two interfering emission paths resulting in an oscillating spatio-temporal emission pattern.

8.3. Outlook

Heralded single-photon to single-ion quantum state transfer

As demonstrated in the continued work we realized an experimental protocol for the heralded photon-to-atom quantum-state transfer. On a short-term perspective, the transfer scheme will be repeated after replacing the 854 nm laser by single photons from a spontaneous parametric down-conversion (SPDC) source. The rate of entangled photon pairs at 854 nm from our current pair source is not high enough to perform the measurement of photon-to-atom quantum-state transfer in a reasonable measuring time. This is why a new source, featuring an enhancement cavity, is currently under construction. With the new setup, the entanglement transfer from entangled-photon pairs to two distant ions as proposed in [46] should come into reach. Due to the lower rate of photons compared to the laser photons, it is crucial to enhance the coherence time of the ion, which allows longer waiting times in $D_{5/2}$ for photon absorption. This goal can be reached with the improved cancellation of magnetic-field fluctuations, that form the main source of decoherence. Ongoing work with passive and active magnetic-field noise compensation shows already promising results and shall be expanded in the future.

Hybrid quantum systems

Hybrid quantum systems composed of different physical platforms combine the characteristic benefits of the respective systems for building scalable quantum-communication networks. Recent proposals [163, 164] report the prospects of building hybrid quantum systems between atomic and molecular, quantum-optical and solid-state systems. Experimental realizations comprise hybrid quantum systems combining atoms with ions [165] and semiconductor quantum dots with trapped ions [166].

In our group, we realized a hybrid quantum system consisting of entangled photon pairs and a single trapped ion. We showed the heralded absorption of entangled photons from the SPDC source resonant with the $D_{5/2}$ to $P_{3/2}$ transition at 854 nm wavelength [64, 82]. Using these photons we currently perform experiments with the group of Prof. C. Becher.

With their expertise on quantum-frequency conversion, they are able to convert 854 nm photons to the telecom-wavelength at 1310 nm. The photons are sent through a 90 meter long fiber, connecting the two laboratories, into a waveguide-based frequency converter. Having the photons at 1310 nm allows low-loss long-haul fiber communication between distant network nodes. This hybrid quantum system can be expanded to a hybrid quantum network between single ions and solid-state emitters like semiconductor quantum dots [108]. This is achieved with our knowledge to generate 854 nm photons from the ion, which are frequency converted to telecom wavelength. Recent experiments show first successful results which opens new routes for connecting the two quantum systems for hybrid quantum networking.

A. Appendix

A.1. Coordinate transformation

The description of the polarization in the photonic reference frame requires the rotation of the photonic coordinate system into the atomic coordinate system. This is performed with the theory known from angular momentum transformation based on group theory [167]. Generally the rotation of a coordinate system is performed in three steps. The first rotation

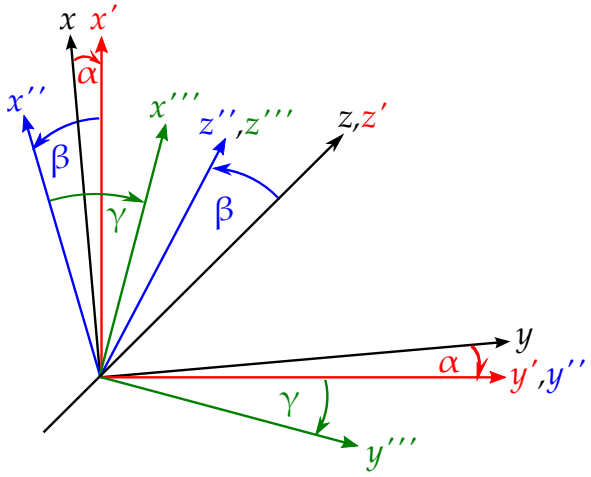

Figure A.1.: Rotation of the coordinate system in the sequence $(xy\mathbf{z}) \xrightarrow{\alpha} (x'\mathbf{y}'z') \xrightarrow{\beta} (x''y''\mathbf{z}'') \xrightarrow{\gamma} (x'''y'''z''')$. The boldface letter designates the rotation axis.

is around the z-axis by α, the second is around the new y'-axis by β and the last rotation is executed around the z''-axis by the angle γ. In terms of the angular momentum j, the rotation is written by the rotation operator

$$\hat{D}(\alpha,\beta,\gamma) = e^{-\mathrm{i}\gamma j_{z''}} e^{-\mathrm{i}\beta j_{y'}} e^{-\mathrm{i}\alpha j_z}, \tag{A.1}$$

with the matrix representation of $\hat{D}$, the Wigner D-matrix

$$D^j_{m\,m'}(\alpha,\beta,\gamma) = \langle jm|\hat{D}(\alpha,\beta,\gamma)|jm'\rangle. \tag{A.2}$$

According to [167] we can write Eq. (A.2)

$$D^j_{m\,m'}(\alpha,\beta,\gamma) = e^{-\mathrm{i}\alpha m} d^j_{m\,m'}(\beta) e^{-\mathrm{i}\gamma m'}, \tag{A.3}$$

with the reduced rotation matrix $d^j_{m\,m'}(\beta)$ which can be directly calculated. The angular momentum state $|jm'\rangle'$ in the new coordinate system can now be expressed by the state in the old coordinate system as

$$|jm'\rangle' = \sum_{m=-j}^{j} |jm\rangle\langle jm|\hat{D}(\alpha\beta\gamma)|jm'\rangle = \sum_{m=-j}^{j} |jm\rangle D^j_{m\,m'}(\alpha\beta\gamma) \tag{A.4}$$

$$= e^{-\mathrm{i}\gamma m'} \sum_{m=-j}^{j} |jm\rangle e^{-\mathrm{i}\alpha m} d^j_{m\,m'}(\beta). \tag{A.5}$$

Eq. (A.5) is applied to the situation in Sec. 2.6.1. From Fig. 2.5 we see that for $\theta_k = 0$ and $\varphi_k = 0$, the rotation around the z-axis is redundant since the two coordinate systems have the same orientation. Thus the first rotation is around the $y^{(\mathrm{ph})}$-axis with the angle $\beta = -\theta_k$. The following rotation around $z^{(\mathrm{at})}$-axis by the angle $\gamma = -\varphi_k$ completes the transformation which can now be expressed for a dipole transition ($\Delta j = 1$) with $\Delta m = q' = 0, \pm 1$ and $q = -j..j$ as

$$\vec{e}^{\,(\mathrm{at})}_{q'} = e^{\mathrm{i}\varphi_k q'} \sum_{q=-j}^{j} \vec{e}^{\,(\mathrm{ph})}_q d^1_{qq'}(-\theta_k) \tag{A.6}$$

$$= e^{\mathrm{i}\varphi_k q'} \sum_{q=-j}^{j} \vec{e}^{\,(\mathrm{ph})}_q d^1_{q'q}(\theta_k). \tag{A.7}$$

If we consider a π-transition ($\Delta m = q' = 0$) in the emission process, we express the atomic oscillation $\vec{e}^{\,(\mathrm{at})}_0$ in terms of the polarization vector in the photonic coordinate system. According to Eq. (A.7) we obtain

$$\vec{e}^{\,(\mathrm{at})}_0 = d^1_{01}(\theta_k)\vec{e}^{\,(\mathrm{ph})}_1 + d^1_{0\,-1}(\theta_k)\vec{e}^{\,(\mathrm{ph})}_{-1} + d^1_{00}(\theta_k)\vec{e}^{\,(\mathrm{ph})}_0 \tag{A.8}$$

$$= \tfrac{\sin\theta_k}{\sqrt{2}}\,\vec{e}^{\,(\mathrm{ph})}_1 - \tfrac{\sin\theta_k}{\sqrt{2}}\,\vec{e}^{\,(\mathrm{ph})}_{-1} + \cos\theta_k \vec{e}^{\,(\mathrm{ph})}_0 \tag{A.9}$$

Here we consider only the components $q = \pm 1$ that oscillate perpendicular to the $\vec{k}$-vector of the photon, since these are the physically relevant components in the scalar product of Eq. (2.66). Hence it remains

$$\vec{e}^{\,(\mathrm{at})}_0 = \tfrac{\sin\theta_k}{\sqrt{2}}\,\vec{e}^{\,(\mathrm{ph})}_1 - \tfrac{\sin\theta_k}{\sqrt{2}}\,\vec{e}^{\,(\mathrm{ph})}_{-1} = \sin\theta_k\,\vec{e}^{\,(\mathrm{ph})}_x, \tag{A.10}$$

as given in Eq. (2.69). The calculation for the circular polarization components can be done in an analogous way.

A.2. Bayes' theorem

In our experiments involing coherent manipulations with the 729 nm laser, the population of the $D_{5/2}$ state is determined by repeated excitations on the $S_{1/2}$ to $D_{5/2}$ transition followed by the state detection with the 397 nm laser.

From these measurements we are interested in an estimate for the probability p that the ion is in the state $D_{5/2}$ after the measurement is repeated n times and k successful transfer events to $D_{5/2}$ were observed. For that we use Bayes' theorem, which uses conditional probabilities.

For a given probability p, the binomial distribution

$$B(k|p) = \binom{n}{k} p^k (1-p)^{n-k} \tag{A.11}$$

describes the probability to observe k successful state transfer events. Now we can formulate the probability distribution $P(p|k)$ for the probability p given that k transfers occurred: according to Bayes' theorem

$$P(p|k) = \frac{B(k|p)P(p)}{B(k)}\,, \tag{A.12}$$

with the uniform (prior) probability distribution $P(p)$, i.e. the one before the first measurement has started. With these two equations, we can now derive the estimate for the probability p to be in $D_{5/2}$ as the expectation value with respect to P

$$\langle p \rangle = \frac{k+1}{n+2} \tag{A.13}$$

and the uncertainty of p

$$\Delta p = \sqrt{\langle p^2 \rangle - \langle p \rangle^2}\,, \tag{A.14}$$

with

$$\langle p^2 \rangle = \frac{(k+1)(k+2)}{(n+2)(n+3)}. \tag{A.15}$$

Bayes' theorem for photon-correlation measurements

Bayes' theorem is applied in this thesis for the determination of the $D_{5/2}$ population; a detailed description is found in [107]. Furthermore this approach is used for estimating the probability of detecting single photons in a certain time bin within a correlation measurement, i.e. in an arrival-time histogram. The description above can be applied in a similar way: we want an estimate for the probability p to detect a photon, for the case that the ion is excited n times and k photon counts have been detected in a certain time interval $[t; t+\tau]$ after the sequence trigger. The Bayesian ansatz allows us to obtain reasonable parameter values from fitting a theoretical model, i.e. an exponential function or the result from Bloch equations, to the detected arrival-time histograms presented in this thesis. This helps to

deal with the fact that in an arrival-time histogram, it might be the case that in several time bins, the number of photons $n_{\mathrm{ph}} = 0$ that would lead to a Poissonian-statistics error of $\sqrt{n_{\mathrm{ph}}} = 0$, whereas in a simple χ^2 fit routine, it is more difficult to deal with this case.

A.3. Ensuring equal 854 nm repumping rates

To achieve the highest visibilities of the quantum beats in the arrival-time distribution of 393 nm photons, we have to compensate for the different 854 nm Clebsch-Gordan coefficients (CGCs) by adjusting the detuning of the 854 nm laser in such a way that the repumping rates are almost equal for the transitions used in the Λ and V scheme. Before generating 393 nm photons, we first perform 854 nm spectroscopy on one of the $D_{5/2}$-to-$P_{3/2}$ transitions and determine the line-center frequency. In order to see when we achieve equal rates, we simulate the individual absorption profile of each transition which is proportional to the rate

$$R_{\mathrm{D},m_j\to\mathrm{P},m_j} = \frac{\Omega^2_{854,\mathrm{eff}}}{4\Delta^2 + \Gamma^2_{\mathrm{P}_{3/2}} + 2\Omega^2_{854,\mathrm{eff}}}\,(A_{393} + A_{850}), \tag{A.16}$$

with the detuning Δ from the line-center frequency, which is

$$\Delta = 2\pi\left(\nu - \left(g_j^{\mathrm{P}}\cdot m_j^{\mathrm{P}} - g_j^{\mathrm{D}}\cdot m_j^{\mathrm{D}}\right)\frac{\mu_{\mathrm{B}}}{h}\cdot B\right). \tag{A.17}$$

The effective Rabi frequency $\Omega_{854,\mathrm{eff}} = \frac{1}{\sqrt{2}}\cdot\Omega_{854}\cdot\mathrm{CGC}$ contains the corresponding CGCs where Ω_{854} is the pure Rabi frequency which we calculate with Eq. (2.40) and the factor of $\frac{1}{\sqrt{2}}$ due to a linear 854 nm input polarization. In Fig. A.2 the repumping rates for three different transitions are shown for the Λ scheme as a function of the 854 nm detuning.

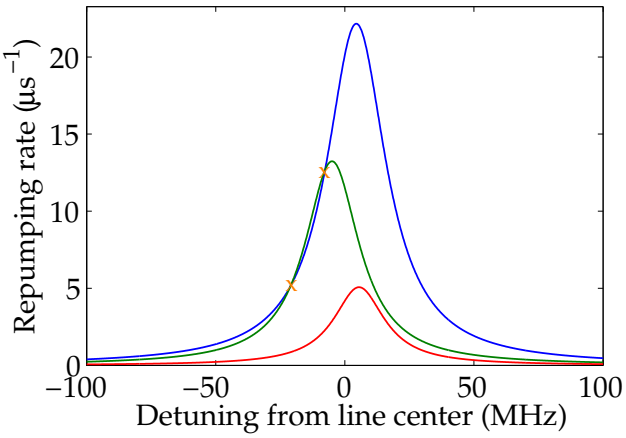

Figure A.2.: Repumping rates for the transition from $\left|D_{5/2},-\frac{3}{2}\right\rangle$ to $\left|P_{3/2},-\frac{1}{2}\right\rangle$ (blue line), $\left|D_{5/2},+\frac{1}{2}\right\rangle$ to $\left|P_{3/2},-\frac{1}{2}\right\rangle$ (green line) and the parasitic transition from $\left|D_{5/2},+\frac{1}{2}\right\rangle$ to $\left|P_{3/2},+\frac{3}{2}\right\rangle$ (red line) for an 854 nm input power of 50 μW. A detuning between −20 MHz to −8 MHz (orange crosses) leads to almost identical pumping rates for the two transitions (blue and green line).

For a magnetic field of 2.8 G and an 854 nm input power of 50 μW, the two interfering transitions (blue and green line) cross at −20 MHz and at −8 MHz (orange crosses),

leading to a frequency span of $\sim$ 12 MHz where the repumping rates are almost identical. The red line displays the repumping rate for the parasitic transition from $\left|D_{5/2}, +\frac{1}{2}\right\rangle$ to $\left|P_{3/2}, +\frac{3}{2}\right\rangle$. For a detuning of -8 MHz the rate is about $\sim$ 17 % compared with the repumping rate for the other two transitions. To compensate for this loss of population in $\left|D_{5/2}, +\frac{1}{2}\right\rangle$, we would have to choose an initial population distribution different from 50 % in each of the two $D_{5/2}$ Zeeman sublevels. Calculating the ideal ratio yields a distribution of 45 % in $\left|D_{5/2}, -\frac{3}{2}\right\rangle$ and 55 % in $\left|D_{5/2}, +\frac{1}{2}\right\rangle$ to have equal amounts of population in $\left|P_{3/2}, -\frac{1}{2}\right\rangle$. However, since we see the high oscillation visibility in the quantum-beat photons we have not included the compensation for the parasitic transition when performing the measurements presented in Chapter 6.

A.4. Collection efficiency of the HALO

In Sec. 3.1.3 we already derived the collection efficiency of the HALO for π and σ light for the case that the HALO axis coincides with the quantization axis:

$$P_\pi \propto \int_0^{2\pi} \int_0^{23.6^\circ} \sin^3\theta_k \, \mathrm{d}\theta_k \, \mathrm{d}\phi_k = \tfrac{8\pi}{3} \cdot 0.51\,\% \tag{A.18}$$

$$P_\sigma \propto \int_0^{2\pi} \int_0^{23.6^\circ} \tfrac{1}{2}(1+\cos^2\theta_k) \sin\theta_k \, \mathrm{d}\theta_k \, \mathrm{d}\phi_k = \tfrac{8\pi}{3} \cdot 6\,\% \tag{A.19}$$

Now we want to derive a general formalism that allows us to calculate the collection efficiency of π and σ light for arbitrary angles ϑ_k between the direction of the light $\vec{k}$ emitted along the HALO axis and the quantization axis, i.e. the direction of the magnetic field $\vec{B}$. This requires a coordinate transformation from θ_k and ϕ_k to a new set of angles ϑ and φ, characterizing the light cone of the HALO for every angle between HALO and magnetic-field direction. Inspired by [168], we consider in Fig. A.3 a spherical triangle (red line) as a part of the surface of a unit sphere together with the cone-like representation of the solid angle covered by the HALO (half opening angle of $\vartheta = 23.6^\circ$). In the coordinate system $\vec{x}$, $\vec{y}$, $\vec{z}$ we choose the magnetic-field direction $\vec{B}$ along the $\vec{z}$ axis.

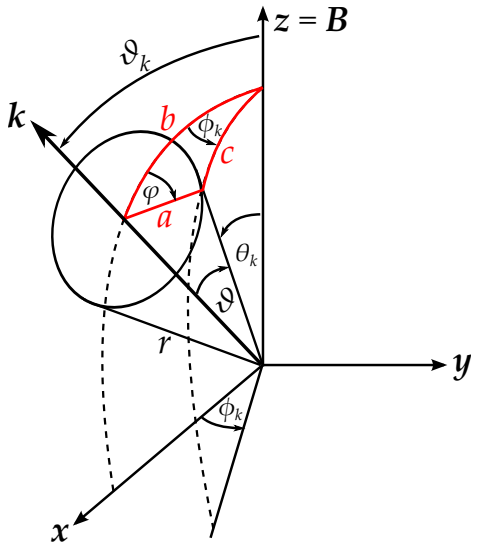

Figure A.3.: Drawing for the coordinate transformation necessary to describe the collection efficiency of the HALO for arbitrary angles between HALO axis $\vec{k}$ and quantization axis, i.e. magnetic-field direction $\vec{B}$. For details see text.

For the coordinate transformation we first consider the spherical triangle with edges a, b and c on the surface of the unit sphere. Such a triangle can be described by the spherical law of cosine

$$\cos a = \cos c \cdot \cos b + \sin c \cdot \sin b \cdot \cos\phi_k. \tag{A.20}$$

For the unit sphere ($r = 1$) the length of one edge of the triangle is the same as the oppposing angle in the middle of the sphere. Thus we can reformulate Eq. (A.20) to

$$\cos\vartheta = \cos\theta_k \cos\vartheta_k + \sin\theta_k \sin\vartheta_k \cos\phi_k. \tag{A.21}$$

For the triangle we can formulate the spherical law of cosine again in a similar way and obtain

$$\cos\theta_k = \cos\vartheta \cos\vartheta_k + \sin\vartheta \sin\vartheta_k \cos\varphi. \tag{A.22}$$

The spherical sine rule provides the relation

$$\frac{\sin\phi_k}{\sin a} = \frac{\sin\varphi}{\sin c}. \tag{A.23}$$

Applying the last equation to the unit sphere gives

$$\sin\theta_k = \frac{\sin\vartheta \sin\varphi}{\sin\phi_k}. \tag{A.24}$$

As we are interested in the collection efficiency of the HALO when collecting light perpendicularly to the magnetic field, we set $\vartheta_k = \frac{\pi}{2}$ in Eq. (A.21) and Eq. (A.22). Together with Eq. (A.24) we obtain the two following equations

$$\theta_k = \arccos(\sin\vartheta \cos\varphi) := f(\vartheta, \varphi) \tag{A.25}$$

$$\phi_k = \arctan(\tan\vartheta \sin\varphi) := g(\vartheta, \varphi). \tag{A.26}$$

In order to evaluate the integrals in Eq. (A.18) and Eq. (A.19) under coordinate transformation we first have to calculate the Jacobian determinant,

$$\begin{vmatrix} \frac{\partial f(\vartheta,\varphi)}{\partial\varphi} & \frac{\partial f(\vartheta,\varphi)}{\partial\vartheta} \\ \frac{\partial g(\vartheta,\varphi)}{\partial\varphi} & \frac{\partial g(\vartheta,\varphi)}{\partial\vartheta} \end{vmatrix} = \frac{\sin\vartheta}{\sqrt{\cos^2\vartheta\cos^2\varphi - \cos^2\varphi + 1}} := \Xi. \tag{A.27}$$

With Eq. (A.27) we calculate the collection efficiencies for π and σ light when the HALO axis is perpendicular to the direction of the magnetic field:

$$P_\pi \propto \int_0^{2\pi} \int_0^{23.6^\circ} (1 - \sin^2\vartheta \cos^2\varphi)^{3/2}\, \Xi \,\mathrm{d}\vartheta \,\mathrm{d}\varphi = \tfrac{8\pi}{3} \cdot 6.02\,\% \tag{A.28}$$

$$P_\sigma \propto \int_0^{2\pi} \int_0^{23.6^\circ} \tfrac{1}{2}(1 + \sin^2\vartheta \cos^2\varphi) \sqrt{1 - \sin^2\vartheta \cos^2\varphi}\, \Xi \,\mathrm{d}\vartheta \,\mathrm{d}\varphi = \tfrac{8\pi}{3} \cdot 3.26\,\% \tag{A.29}$$

Journal publications

The work presented in this thesis led to the following publications:

Experimental protocol for high-fidelity heralded photon-to-atom quantum state transfer
C. Kurz, M. Schug, P. Eich, J. Huwer, P. Müller, J. Eschner
Nat. Commun. **5**, 5527 (2014)

Quantum interference in the absorption and emission of single photons by a single ion
M. Schug, C. Kurz, P. Eich, J. Huwer, P. Müller, J. Eschner
Phys. Rev. A **90**, 023829 (2014)

Heralded photonic interaction between distant single ions
M. Schug, J. Huwer, C. Kurz, P. Müller, J. Eschner
Phys. Rev. Lett. **110**, 213603 (2013)

A high-rate source for single photons in a pure quantum state
C. Kurz, J. Huwer, M. Schug, P. Müller, J. Eschner
New J. Phys. **15**, 055005 (2013)

Further associated work:

Photon entanglement detection by a single atom
J. Huwer, J. Ghosh, N. Piro, M. Schug, F. Dubin, J. Eschner
New J. Phys. **15**, 025033 (2013)

Manuscripts in preparation:

Programmable ion-photon quantum interface
C. Kurz, P. Eich, M. Schug, J. Eschner

Bibliography

[1] A. M. Turing. *On Computable Numbers, with an Application to the Entscheidungsproblem*. Proc. Lond. Math. Soc. **42**, 230 (1936).

[2] G. E. Moore. *Cramming more components onto integrated circuits*. Electronics **38** (1965).

[3] S. Loth, S. Baumann, C. P. Lutz, D. M. Eigler, A. J. Heinrich. *Bistability in Atomic-Scale Antiferromagnets*. Science **335**, 196 (2012).

[4] M. A. Nielsen, I. L. Chuan. *Quantum Computation and Quantum Information*. Cambridge (2000).

[5] R. P. Feynman. *Simulating physics with computers*. Int. J. Theor. Phys. **21**, 467 (1982).

[6] R. P. Feynman. *Quantum mechanical computers*. Found. Phys. **16**, 507 (1986).

[7] D. Deutsch. *Quantum Theory, the Church-Turing Principle and the Universal Quantum Computer*. Proc. R. Soc. A: Math., Phys. Eng. Sci. **400**, 97 (1985).

[8] P. Shor. *Algorithms for quantum computation: discrete logarithms and factoring*. Proc. 35th Ann. Symp. Found. Comp. Sci. (1994).

[9] L. K. Grover. *Quantum Mechanics Helps in Searching for a Needle in a Haystack*. Phys. Rev. Lett. **79**, 325 (1997).

[10] D. Deutsch, R. Josza. *Rapid solution of problems by quantum computation*. Proc. R. Soc. Lond. A **439**, 553 (1992).

[11] E. Knill, R. Laflamme, G. J. Milburn. *A scheme for efficient quantum computation with linear optics*. Nature **409**, 46 (2001).

[12] H.-J. Briegel, T. Calarco, D. Jaksch, J. I. Cirac, P. Zoller. *Quantum computing with neutral atoms*. J. Mod. Opt. **47**, 415 (2000).

[13] D. Loss, D. P. DiVincenzo. *Quantum computation with quantum dots*. Phys. Rev. A **57**, 120 (1998).

[14] I. L. Chuang, N. Gershenfeld, M. G. Kubinec, D. W. Leung. *Bulk quantum computation with nuclear magnetic resonance: theory and experiment*. Proc. R. Soc. A: Math., Phys. Eng. Sci. **454**, 447 (1998).

[15] A. Wallraff, D. I. Schuster, A. Blais, L. Frunzio, R.-S. Huang, J. Majer, S. Kumar, S. M. Girvin, R. J. Schoelkopf. *Strong coupling of a single photon to a superconducting qubit using circuit quantum electrodynamics*. Nature **431**, 162 (2004).

[16] D. P. DiVincenzo. *The Physical Implementation of Quantum Computation*. Fortschritte der Physik **48**, 771 (2000).

[17] J. I. Cirac, P. Zoller. *Quantum Computations with Cold Trapped Ions*. Phys. Rev. Lett. **74**, 4091 (1995).

[18] F. Diedrich, J. C. Bergquist, W. M. Itano, D. J. Wineland. *Laser Cooling to the Zero-Point Energy of Motion*. Phys. Rev. Lett. **62**, 403 (1989).

[19] H. Nägerl, R. Blatt, J. Eschner, F. Schmidt-Kaler, D. Leibfried. *Coherent excitation of normal modes in a string of Ca^+ ions*. Opt. Exp. **3**, 89 (1998).

[20] D. Leibfried, B. DeMarco, V. Meyer, D. Lucas, M. Barrett, J. Britton, W. M. Itano, B. Jelenkovic, C. Langer, T. Rosenband, D. J. Wineland. *Experimental demonstration of a robust, high-fidelity geometric two ion-qubit phase gate*. Nature **422**, 412 (2003).

[21] F. Schmidt-Kaler, H. Haffner, M. Riebe, S. Gulde, G. P. T. Lancaster, T. Deuschle, C. Becher, C. F. Roos, J. Eschner, R. Blatt. *Realization of the Cirac-Zoller controlled-NOT quantum gate*. Nature **422**, 408 (2003).

[22] J. Benhelm, G. Kirchmair, C. F. Roos, R. Blatt. *Towards fault-tolerant quantum computing with trapped ions*. Nat. Phys. **4**, 463 (2008).

[23] T. Monz, P. Schindler, J. T. Barreiro, M. Chwalla, D. Nigg, W. A. Coish, M. Harlander, W. Hänsel, M. Hennrich, R. Blatt. *14-Qubit Entanglement: Creation and Coherence*. Phys. Rev. Lett. **106**, 130506 (2011).

[24] P. Schindler, D. Nigg, T. Monz, J. T. Barreiro, E. Martinez, S. X. Wang, S. Quint, M. F. Brandl, V. Nebendahl, C. F. Roos, M. Chwalla, M. Hennrich, R. Blatt. *A quantum information processor with trapped ions*. New J. Phys. **15**, 123012 (2013).

[25] R. Blatt, C. F. Roos. *Quantum simulations with trapped ions*. Nat. Phys. **8**, 277 (2012).

[26] D. Nigg, M. Müller, E. A. Martinez, P. Schindler, M. Hennrich, T. Monz, M. A. Martin-Delgado, R. Blatt. *Quantum computations on a topologically encoded qubit*. Science **345**, 302 (2014).

[27] C. Schuck. *Interfacing Single Ions and Single Photons for Quantum Networks*. Ph.D. thesis, ICFO, Barcelona (2009).

[28] S. Seidelin, J. Chiaverini, R. Reichle, J. J. Bollinger, D. Leibfried, J. Britton, J. H. Wesenberg, R. B. Blakestad, R. J. Epstein, D. B. Hume, W. M. Itano, J. D. Jost, C. Langer,

R. Ozeri, N. Shiga, D. J. Wineland. *Microfabricated Surface-Electrode Ion Trap for Scalable Quantum Information Processing*. Phys. Rev. Lett. **96**, 253003 (2006).

[29] D. Stick, W. K. Hensinger, S. Olmschenk, M. J. Madsen, K. Schwab, C. Monroe. *Ion trap in a semiconductor chip*. Nat. Phys. **2**, 36 (2006).

[30] D. Kielpinski, C. Monroe, D. J. Wineland. *Architecture for a large-scale ion-trap quantum computer*. Nature **417**, 709 (2002).

[31] H. J. Kimble. *The quantum internet*. Nature **453**, 1023 (2008).

[32] H.-J. Briegel, W. Dür, J. I. Cirac, P. Zoller. *Quantum Repeaters: The Role of Imperfect Local Operations in Quantum Communication*. Phys. Rev. Lett. **81**, 5932 (1998).

[33] C. H. Bennett, G. Brassard, C. Crépeau, R. Jozsa, A. Peres, W. K. Wootters. *Teleporting an unknown quantum state via dual classical and Einstein-Podolsky-Rosen channels*. Phys. Rev. Lett. **70**, 1895 (1993).

[34] C. H. Bennett, D. P. DiVincenzo, J. A. Smolin, W. K. Wootters. *Mixed-state entanglement and quantum error correction*. Phys. Rev. A **54**, 3824 (1996).

[35] S. Olmschenk, D. N. Matsukevich, P. Maunz, D. Hayes, L.-M. Duan, C. Monroe. *Quantum Teleportation Between Distant Matter Qubits*. Science **323**, 486 (2009).

[36] J. I. Cirac, P. Zoller, H. J. Kimble, H. Mabuchi. *Quantum State Transfer and Entanglement Distribution among Distant Nodes in a Quantum Network*. Phys. Rev. Lett. **78**, 3221 (1997).

[37] S. Ritter, C. Nölleke, C. Hahn, A. Reiserer, A. Neuzner, M. Uphoff, M. Mücke, E. Figueroa, J. Bochmann, G. Rempe. *An elementary quantum network of single atoms in optical cavities*. Nature **484**, 195 (2012).

[38] M. Schug, J. Huwer, C. Kurz, P. Müller, J. Eschner. *Heralded Photonic Interaction between Distant Single Ions*. Phys. Rev. Lett. **110**, 213603 (2013).

[39] C. Cabrillo, J. I. Cirac, P. Garcia-Fernandez, P. Zoller. *Creation of entangled states of distant atoms by interference*. Phys. Rev. A **59**, 1025 (1999).

[40] L. Slodička, G. Hétet, N. Röck, P. Schindler, M. Hennrich, R. Blatt. *Atom-Atom Entanglement by Single-Photon Detection*. Phys. Rev. Lett. **110**, 083603 (2013).

[41] C. Simon, W. T. M. Irvine. *Robust Long-Distance Entanglement and a Loophole-Free Bell Test with Ions and Photons*. Phys. Rev. Lett. **91**, 110405 (2003).

[42] S. Ates, S. M. Ulrich, S. Reitzenstein, A. Löffler, A. Forchel, P. Michler. *Post-Selected Indistinguishable Photons from the Resonance Fluorescence of a Single Quantum Dot in a Microcavity*. Phys. Rev. Lett. **103**, 167402 (2009).

[43] J. Hofmann, M. Krug, N. Ortegel, L. Gérard, M. Weber, W. Rosenfeld, H. Weinfurter. *Heralded Entanglement Between Widely Separated Atoms*. Science **337**, 72 (2012).

[44] D. L. Moehring, P. Maunz, S. Olmschenk, K. C. Younge, D. N. Matsukevich, L.-M. Duan, C. Monroe. *Entanglement of single-atom quantum bits at a distance*. Nature **449**, 68 (2007).

[45] H. Bernien, B. Hensen, W. Pfaff, G. Koolstra, M. S. Blok, L. Robledo, T. H. Taminiau, M. Markham, D. J. Twitchen, L. Childress, R. Hanson. *Heralded entanglement between solid-state qubits separated by three metres*. Nature **497**, 86 (2013).

[46] N. Sangouard, J.-D. Bancal, P. Müller, J. Ghosh, J. Eschner. *Heralded mapping of photonic entanglement into single atoms in free space: proposal for a loophole-free Bell test*. New J. Phys. **15**, 085004 (2013).

[47] P. Maunz, D. L. Moehring, S. Olmschenk, K. C. Younge, D. N. Matsukevich, C. Monroe. *Quantum interference of photon pairs from two remote trapped atomic ions*. Nat. Phys. **3**, 538 (2007).

[48] Z. Ficek, S. Swain. *Quantum Interference and Coherence*. Springer (2005).

[49] A. D. Boozer, A. Boca, R. Miller, T. E. Northup, H. J. Kimble. *Reversible State Transfer between Light and a Single Trapped Atom*. Phys. Rev. Lett. **98**, 193601 (2007).

[50] T. Wilk, S. C. Webster, A. Kuhn, G. Rempe. *Single-Atom Single-Photon Quantum Interface*. Science **317**, 488 (2007).

[51] A. Stute, B. Casabone, P. Schindler, T. Monz, P. O. Schmidt, B. Brandstätter, T. E. Northup, R. Blatt. *Tunable ion-photon entanglement in an optical cavity*. Nature **485**, 482 (2012).

[52] J. Volz, M. Weber, D. Schlenk, W. Rosenfeld, J. Vrana, K. Saucke, C. Kurtsiefer, H. Weinfurter. *Observation of Entanglement of a Single Photon with a Trapped Atom*. Phys. Rev. Lett. **96**, 030404 (2006).

[53] M. K. Tey, Z. Chen, S. A. Aljunid, B. Chng, F. Huber, G. Maslennikov, C. Kurtsiefer. *Strong interaction between light and a single trapped atom without the need for a cavity*. Nat. Phys. **4**, 924 (2008).

[54] S. Gerber, D. Rotter, M. Hennrich, R. Blatt, F. Rohde, C. Schuck, M. Almendros, R. Gehr, F. Dubin, J. Eschner. *Quantum interference from remotely trapped ions*. New J. Phys. **11**, 013032 (2009).

[55] G. Vittorini, D. Hucul, I. V. Inlek, C. Crocker, C. Monroe. *Entanglement of distinguishable quantum memories*. Phys. Rev. A **90**, 040302 (2014).

[56] R. Maiwald, A. Golla, M. Fischer, M. Bader, S. Heugel, B. Chalopin, M. Sondermann, G. Leuchs. *Collecting more than half the fluorescence photons from a single ion*. Phys. Rev. A **86**, 043431 (2012).

[57] P. Grangier, B. Sanders, J. Vuckovic. *Focus on Single Photons on Demand*. New J. Phys. **6** (2004).

[58] A. Kuhn, M. Hennrich, G. Rempe. *Deterministic Single-Photon Source for Distributed Quantum Networking*. Phys. Rev. Lett. **89**, 067901 (2002).

[59] J. McKeever, A. Boca, A. D. Boozer, R. Miller, J. R. Buck, A. Kuzmich, H. J. Kimble. *Deterministic Generation of Single Photons from One Atom Trapped in a Cavity*. Science **303**, 1992 (2004).

[60] M. Keller, B. Lange, K. Hayasaka, W. Lange, H. Walther. *Continuous generation of single photons with controlled waveform in an ion-trap cavity system*. Nature **431**, 1075 (2004).

[61] H. G. Barros, A. Stute, T. E. Northup, C. Russo, P. O. Schmidt, R. Blatt. *Deterministic single-photon source from a single ion*. New J. Phys. **11**, 103004 (2009).

[62] P. Michler, A. Kiraz, C. Becher, W. V. Schoenfeld, P. M. Petroff, L. Zhang, E. Hu, A. Imamoglu. *A Quantum Dot Single-Photon Turnstile Device*. Science **290**, 2282 (2000).

[63] M. Almendros, J. Huwer, N. Piro, F. Rohde, C. Schuck, M. Hennrich, F. Dubin, J. Eschner. *Bandwidth-Tunable Single-Photon Source in an Ion-Trap Quantum Network*. Phys. Rev. Lett. **103**, 213601 (2009).

[64] N. Piro, F. Rohde, C. Schuck, M. Almendros, J. Huwer, S. Ghosh, A. Haase, M. Hennrich, F. Dubin, J. Eschner. *Heralded single-photon absorption by a single atom*. Nat. Phys. **7**, 17 (2011).

[65] J. Huwer, J. Ghosh, N. Piro, M. Schug, F. Dubin, J. Eschner. *Photon entanglement detection by a single atom*. New J. Phys. **15**, 025033 (2013).

[66] W. Paul, H. Steinwedel. *Ein neues Massenspektrometer ohne Magnetfeld*. Zeitschrift Naturforschung Teil A **8**, 448 (1953).

[67] E. Fischer. *Three-dimensional stabilization of charged particles in a quadrupole field.* Z. Phys. **156**, 1 (1959).

[68] W. Paul. *Electromagnetic traps for charged and neutral particles*. Rev. Mod. Phys. **62**, 531 (1990).

[69] W. Neuhauser, M. Hohenstatt, P. E. Toschek, H. Dehmelt. *Localized visible* Ba^+ *mono-ion oscillator*. Phys. Rev. A **22**, 1137 (1980).

[70] P. K. Ghosh. *Ion traps*. Oxford University Press (1995).

[71] D. J. Wineland, C. Monroe, W. M. Itano, D. Leibfried, B. E. King, D. M. Meekhof. *Experimental Issues in Coherent Quantum-State Manipulation of Trapped Atomic Ions*. J. Res. Natl. Inst. Stand. Technol. **103**, 259 (1998).

[72] D. Leibfried, R. Blatt, C. Monroe, D. Wineland. *Quantum dynamics of single trapped ions*. Rev. Mod. Phys. **75**, 1 (2003).

[73] C. W. Chou, D. B. Hume, J. C. J. Koelemeij, D. J. Wineland, T. Rosenband. *Frequency Comparison of Two High-Accuracy Al^+ Optical Clocks*. Phys. Rev. Lett. **104**, 070802 (2010).

[74] N. Huntemann, M. Okhapkin, B. Lipphardt, S. Weyers, C. Tamm, E. Peik. *High-Accuracy Optical Clock Based on the Octupole Transition in $^{171}Yb^+$*. Phys. Rev. Lett. **108**, 090801 (2012).

[75] F. Rohde. *Remote ion traps for quantum networking: Two-photon interference and correlations*. Ph.D. thesis, ICFO, Barcelona (2009).

[76] J. Brito. *Personal communication*. Universität des Saarlandes.

[77] M. Almendros. *Towards Long-Distance Quantum Communication*. Ph.D. thesis, ICFO, Barcelona (2010).

[78] J. Jin, D. A. Church. *Precision lifetimes for the Ca^+ $4p\,^2P$ levels: Experiment challenges theory at the* 1% *level*. Phys. Rev. Lett. **70**, 3213 (1993).

[79] R. Gerritsma, G. Kirchmair, F. Zähringer, J. Benhelm, R. Blatt, C. F. Roos. *Precision measurement of the branching fractions of the $4p\,^2P_{3/2}$ decay of Ca II*. Eur. Phys. J. D **50**, 13 (2008).

[80] A. Kreuter, C. Becher, G. P. T. Lancaster, A. B. Mundt, C. Russo, H. Häffner, C. Roos, W. Hänsel, F. Schmidt-Kaler, R. Blatt, M. S. Safronova. *Experimental and theoretical study of the $3d\,^2D$-level lifetimes of $^{40}Ca^+$*. Phys. Rev. A **71**, 032504 (2005).

[81] P. A. Barton, C. J. S. Donald, D. M. Lucas, D. A. Stevens, A. M. Steane, D. N. Stacey. *Measurement of the lifetime of the $3d\,^2D_{5/2}$ state in $^{40}Ca^+$*. Phys. Rev. A **62**, 032503 (2000).

[82] J. Huwer. *Experimental tools for quantum networking operations with single photons and single ions*. Ph.D. thesis, Universität des Saarlandes, Saarbrücken (2013).

[83] F. Rohde, M. Almendros, C. Schuck, J. Huwer, M. Hennrich, J. Eschner. *A diode laser stabilization scheme for $^{40}Ca^+$ single-ion spectroscopy*. J. Phys. B: At. Mol. Opt. Phys. **43**, 11 (2010).

[84] R. V. Pound. *Electronic frequency stabilization of microwave oscillators*. Rev. Sci. Instrum. **17**, 11 (1946).

[85] R. Drever, J. Hall, F. Kowalski, J. Hough, G. Ford, A. Munley, H. Ward. *Laser phase and frequency stabilization using an optical resonator*. Appl. Phys. B **31**, 2 (1983).

[86] M. Ramm, T. Pruttivarasin, M. Kokish, I. Talukdar, H. Häffner. *Precision Measurement Method for Branching Fractions of Excited $P_{1/2}$ States Applied to $^{40}Ca^{+}$*. Phys. Rev. Lett. **111**, 023004 (2013).

[87] W. Neuhauser, M. Hohenstatt, P. Toschek, H. Dehmelt. *Optical-Sideband Cooling of Visible Atom Cloud Confined in Parabolic Well*. Phys. Rev. Lett. **41**, 233 (1978).

[88] B. E. King, C. S. Wood, C. J. Myatt, Q. A. Turchette, D. Leibfried, W. M. Itano, C. Monroe, D. J. Wineland. *Cooling the Collective Motion of Trapped Ions to Initialize a Quantum Register*. Phys. Rev. Lett. **81**, 1525 (1998).

[89] A. Sørensen, K. Mølmer. *Quantum Computation with Ions in Thermal Motion*. Phys. Rev. Lett. **82**, 1971 (1999).

[90] S. Stenholm. *The semiclassical theory of laser cooling*. Rev. Mod. Phys. **58**, 699 (1986).

[91] H. Oberst. *Resonance fluorescence of single Barium ions*. Diploma thesis, Universität Innsbruck (1999).

[92] C. J. Foot. *Atomic Physics*. Oxford University Press (2005).

[93] P. Müller. *In preparation*. Ph.D. thesis, Universität des Saarlandes.

[94] R. Brouri, A. Beveratos, J.-P. Poizat, P. Grangier. *Single-photon generation by pulsed excitation of a single dipole*. Phys. Rev. A **62**, 063817 (2000).

[95] R. Loudon. *The Quantum Theory of Light*. Oxford Science Publications (1994).

[96] I. Hertel, C.-P. Schulz. *Atom, Moleküle und optische Physik 1*. Springer (2008).

[97] J. J. Sakurai. *Modern quantum mechanics*. Addison-Wesley (2011).

[98] S. Lloyd, M. S. Shahriar, J. H. Shapiro, P. R. Hemmer. *Long Distance, Unconditional Teleportation of Atomic States via Complete Bell State Measurements*. Phys. Rev. Lett. **87**, 167903 (2001).

[99] B. B. Blinov, D. L. Moehring, L.-M. Duan, C. Monroe. *Observation of entanglement between a single trapped atom and a single photon*. Nature **428**, 153 (2004).

[100] M. Żukowski, A. Zeilinger, M. A. Horne, A. K. Ekert. *"Event-ready-detectors" Bell experiment via entanglement swapping*. Phys. Rev. Lett. **71**, 4287 (1993).

[101] C. Kurz, J. Huwer, M. Schug, P. Müller, J. Eschner. *A high-rate source for single photons in a pure quantum state*. New J. Phys. **15**, 055005 (2013).

[102] P. Müller, J. Eschner. *Single calcium-40 ion as quantum memory for photon polarization: a case study*. Appl. Phys. B **114**, 303 (2014).

[103] R. Hanbury Brown, R. Q. Twiss. *Correlation between Photons in two Coherent Beams of Light*. Nature **177**, 27 (1956).

[104] C. Rullière. *Femtosecond Laser Pulses*. Springer (2005).

[105] M. Fox. *Quantum Optics: An Introduction*. Oxford University Press (2006).

[106] H. P. Specht, J. Bochmann, M. Mücke, B. Weber, E. Figueroa, D. L. Moehring, G. Rempe. *Phase shaping of single-photon wave packets*. Nat. Photon. **3**, 469 (2009).

[107] C. Kurz. *Quantum networking with single ions and single photons interfaced in free space*. Ph.D. thesis, Universität des Saarlandes (2015).

[108] S. Zaske, A. Lenhard, C. A. Keßler, J. Kettler, C. Hepp, C. Arend, R. Albrecht, W.-M. Schulz, M. Jetter, P. Michler, C. Becher. *Visible-to-Telecom Quantum Frequency Conversion of Light from a Single Quantum Emitter*. Phys. Rev. Lett. **109**, 147404 (2012).

[109] A. Lenhard, M. Bock, S. Kucera, J. Brito, P. Eich, P. Müller, C. Becher, J. Eschner. *Telecom-heralded single photon absorption by a single atom*. arXiv:1504.08303 (2015).

[110] L. Luo, D. Hayes, T. Manning, D. Matsukevich, P. Maunz, S. Olmschenk, J. Sterk, C. Monroe. *Protocols and techniques for a scalable atom-photon quantum network*. Fortschritte der Physik **57**, 1133 (2009).

[111] J. Volz. *Atom-Photon Entanglement*. Ph.D. thesis, Ludwig-Maximilians-Universität München (2006).

[112] G. Leuchs, M. Sondermann. *Light-matter interaction in free space*. J. Mod. Opt. **60**, 36 (2013).

[113] W. Nagourney, J. Sandberg, H. Dehmelt. *Shelved optical electron amplifier: Observation of quantum jumps*. Phys. Rev. Lett. **56**, 2797 (1986).

[114] N. Piro, A. Haase, M. W. Mitchell, J. Eschner. *An entangled photon source for resonant single-photon-single-atom interaction*. J. Phys. B **42**, 114002 (2009).

[115] N. Piro. *Controlled absorption of heralded single photons by a single atom: Towards entanglement distribution in quantum networks*. Ph.D. thesis, ICFO - The Institute of Photonic Sciences (2010).

[116] Y. L. A. Rezus, S. G. Walt, R. Lettow, A. Renn, G. Zumofen, S. Götzinger, V. Sandoghdar. *Single-Photon Spectroscopy of a Single Molecule*. Phys. Rev. Lett. **108**, 093601 (2012).

[117] M. Mücke, J. Bochmann, C. Hahn, A. Neuzner, C. Nölleke, A. Reiserer, G. Rempe, S. Ritter. *Generation of single photons from an atom-cavity system*. Phys. Rev. A **87**, 063805 (2013).

[118] D. Pinotsi, A. Imamoglu. *Single Photon Absorption by a Single Quantum Emitter*. Phys. Rev. Lett. **100**, 093603 (2008).

[119] R. Maiwald, D. Leibfried, J. Britton, J. C. Bergquist, G. Leuchs, D. J. Wineland. *Stylus ion trap for enhanced access and sensing*. Nat. Phys. **5**, 551 (2009).

[120] J. M. Raimond, M. Brune, S. Haroche. *Manipulating quantum entanglement with atoms and photons in a cavity*. Rev. Mod. Phys. **73**, 565 (2001).

[121] H. Walther, B. T. H. Varcoe, B.-G. Englert, T. Becker. *Cavity quantum electrodynamics*. Rep. Prog. Phys. **69**, 1325 (2006).

[122] G. Rempe. *Atoms in an optical cavity: Quantum electrodynamics in confined space*. Cont. Phys. **34**, 119 (1993).

[123] S. Quabis, R. Dorn, M. Eberler, O. Glöckl, G. Leuchs. *Focusing light to a tighter spot*. Opt. Commun. **179**, 1 (2000).

[124] M. Sondermann, R. Maiwald, H. Konermann, N. Lindlein, U. Peschel, G. Leuchs. *Design of a mode converter for efficient light-atom coupling in free space*. Appl. Phys. B **89**, 489 (2007).

[125] C. Monroe, D. Meekhof, B. King, W. Itano, D. Wineland. *Demonstration of a Fundamental Quantum Logic Gate*. Phys. Rev. Lett. **75**, 4714 (1995).

[126] C. Roos, T. Zeiger, H. Rohde, H. Nägerl, J. Eschner, D. Leibfried, F. Schmidt-Kaler, R. Blatt. *Quantum State Engineering on an Optical Transition and Decoherence in a Paul Trap*. Phys. Rev. Lett. **83**, 4713 (1999).

[127] C. F. Roos. *Controlling the quantum state of trapped ions*. Ph.D. thesis, Universität Innsbruck (2000).

[128] G. Breit. *Quantum Theory of Dispersion (Continued). Parts VI and VII*. Rev. Mod. Phys. **5**, 91 (1933).

[129] M. Schug, C. Kurz, P. Eich, J. Huwer, P. Müller, J. Eschner. *Quantum interference in the absorption and emission of single photons by a single ion*. Phys. Rev. A **90**, 023829 (2014).

[130] J. N. Dodd, W. J. Sandle, D. Zissermann. *Study of resonance fluorescence in cadmium: Modulation effects and lifetime measurements*. Proc. Phys. Soc. **92**, 497 (1967).

[131] A. Aspect, J. Dalibard, P. Grangier, G. Roger. *Quantum beats in continuously excited atomic cascades*. Opt. Commun. **49**, 429 (1984).

[132] D. G. Norris, L. A. Orozco, P. Barberis-Blostein, H. J. Carmichael. *Observation of Ground-State Quantum Beats in Atomic Spontaneous Emission*. Phys. Rev. Lett. **105**, 123602 (2010).

[133] M. Schubert, I. Siemers, R. Blatt, W. Neuhauser, P. E. Toschek. *Transient internal dynamics of a multilevel ion*. Phys. Rev. A **52**, 2994 (1995).

[134] M. O. Scully, K. Drühl. *Quantum eraser: A proposed photon correlation experiment concerning observation and "delayed choice" in quantum mechanics*. Phys. Rev. A **25**, 2208 (1982).

[135] D. Krause, E. Fischbach, Z. Rohrbach. *A priori which-way information in quantum interference with unstable particles*. Phys. Lett. A **378**, 2490 (2014).

[136] E. Togan, Y. Chu, A. S. Trifonov, L. Jiang, J. Maze, L. Childress, M. V. G. Dutt, A. S. Sorensen, P. R. Hemmer, A. S. Zibrov, M. D. Lukin. *Quantum entanglement between an optical photon and a solid-state spin qubit*. Nature **466**, 730 (2010).

[137] C. Kurz, P. Eich, M. Schug, J. Eschner. *Programmable ion-photon quantum interface*. In preparation .

[138] P. Eich. *Frequency and Phase Stabilization of Diode Lasers using a Femtosecond Frequency Comb*. Diploma thesis, Universität des Saarlandes, Saarbrücken (2012).

[139] K. Evenson, J. Wells, F. Petersen, B. Danielson, G. Day. *Accurate frequencies of molecular transitions used in laser stabilization: the 3.39-µm transition in CH_4 and the 9.33- and 10.18-µm transitions in CO_2*. Appl. Phys. Lett. **22**, 192 (1973).

[140] H. Schnatz, B. Lipphardt, J. Helmcke, F. Riehle, G. Zinner. *First Phase-Coherent Frequency Measurement of Visible Radiation*. Phys. Rev. Lett. **76**, 18 (1996).

[141] J. Ye, S. T. Cundiff. *Femtosecond Optical Frequency Comb: Principle, Operation, and Applications*. Springer (2005).

[142] T. Udem, J. Reichert, R. Holzwarth, T. W. Hänsch. *Absolute Optical Frequency Measurement of the Cesium D_1 Line with a Mode-Locked Laser*. Phys. Rev. Lett. **82**, 3568 (1999).

[143] S. T. Cundiff, J. Ye, J. L. Hall. *Optical frequency synthesis based on mode-locked lasers*. Rev. Sci. Instrum. **72**, 10 (2001).

[144] T. Udem, R. Holzwarth, T. W. Hänsch. *Optical frequency metrology*. Nature **416**, 233 (2002).

[145] J. Reichert, R. Holzwarth, T. Udem, T. Hänsch. *Measuring the frequency of light with mode-locked lasers*. Opt. Commun. **172**, 59 (1999).

[146] G. K. Campbell, A. D. Ludlow, S. Blatt, J. W. Thomsen, M. J. Martin, M. H. G. de Miranda, T. Zelevinsky, M. M. Boyd, J. Ye, S. A. Diddams, T. P. Heavner, T. E. Parker, S. R. Jefferts. *The absolute frequency of the ^{87}Sr optical clock transition*. Metrologia **45**, 539 (2008).

[147] A. Matveev, C. G. Parthey, K. Predehl, J. Alnis, A. Beyer, R. Holzwarth, T. Udem, T. Wilken, N. Kolachevsky, M. Abgrall, D. Rovera, C. Salomon, P. Laurent, G. Grosche, O. Terra, T. Legero, H. Schnatz, S. Weyers, B. Altschul, T. W. Hänsch. *Precision Measurement of the Hydrogen 1S-2S Frequency via a 920-km Fiber Link*. Phys. Rev. Lett. **110**, 230801 (2013).

[148] A. Cingöz, D. C. Yost, T. K. Allison, A. Ruehl, M. E. Fermann, I. Hartl, J. Ye. *Direct frequency comb spectroscopy in the extreme ultraviolet*. Nature **482**, 68 (2012).

[149] E. Peters, D. C. Yost, A. Matveev, T. W. Hänsch, T. Udem. *Frequency-comb spectroscopy of the hydrogen 1S-3S and 1S-3D transitions*. Annalen der Physik **525**, 7 (2013).

[150] D. Hayes, D. N. Matsukevich, P. Maunz, D. Hucul, Q. Quraishi, S. Olmschenk, W. Campbell, J. Mizrahi, C. Senko, C. Monroe. *Entanglement of Atomic Qubits Using an Optical Frequency Comb*. Phys. Rev. Lett. **104**, 140501 (2010).

[151] J. Roslund, R. Medeiros de Araújo, S. Jiang, C. Fabre, N. Treps. *Wavelength-multiplexed quantum networks with ultrafast frequency combs*. Nat. Phot. **8**, 109 (2014).

[152] A. Komarov, H. Leblond, F. Sanchez. *Passive harmonic mode-locking in a fiber laser with nonlinear polarization rotation*. Opt. Commun. **267**, 162 (2006).

[153] P. Russell. *Photonic Crystal Fibers*. Science **299**, 358 (2003).

[154] J. M. Dudley, G. Genty, S. Coen. *Supercontinuum generation in photonic crystal fiber*. Rev. Mod. Phys. **78**, 1135 (2006).

[155] G. P. Agrawal. *Nonlinear Fiber Optics, Third Edition*. Academic Press (2001).

[156] D. W. Allan. *Statistics of atomic frequency standards*. Proc. IEEE **54**, 221 (1966).

[157] R. Paschotta, A. Schlatter, S. Zeller, H. Telle, U. Keller. *Optical phase noise and carrier-envelope offset noise of mode-locked lasers*. Appl. Phys. B **82**, 265 (2006).

[158] J. Stenger, H. Schnatz, C. Tamm, H. R. Telle. *Ultraprecise Measurement of Optical Frequency Ratios*. Phys. Rev. Lett. **88**, 073601 (2002).

[159] M. C. Stowe, M. J. Thorpe, A. Pe'er, J. Ye, J. E. Stalnaker, V. Gerginov, S. A. Diddams. *Direct frequency comb spectroscopy*. Adv. At., Mol., Opt. Phys. **55**, 1 (2008).

[160] C. Kurz, M. Schug, P. Eich, J. Huwer, P. Müller, J. Eschner. *Experimental protocol for high-fidelity heralded photon-to-atom quantum state transfer*. Nat. Commun. **5**, 5527 (2014).

[161] H. Häffner, C. Roos, R. Blatt. *Quantum computing with trapped ions*. Phys. Rep. **469**, 155 (2008).

[162] I. L. Chuang, M. A. Nielsen. *Prescription for experimental determination of the dynamics of a quantum black box*. J. Mod. Opt. **44**, 2455 (1997).

[163] L. Tian, P. Rabl, R. Blatt, P. Zoller. *Interfacing Quantum-Optical and Solid-State Qubits*. Phys. Rev. Lett. **92**, 247902 (2004).

[164] M. Wallquist, K. Hammerer, P. Rabl, M. Lukin, P. Zoller. *Hybrid quantum devices and quantum engineering*. Phys. Scr. **2009**, 014001 (2009).

[165] C. Zipkes, L. Ratschbacher, S. Palzer, C. Sias, M. Köhl. *Hybrid quantum systems of atoms and ions*. J. Phys.: Conf. Ser. **264**, 012019 (2011).

[166] M. Meyer, H. R. Stockill, M. Steiner, C. Le Gall, C. Matthiesen, E. Clarke, A. Ludwig, J. Reichel, M. Atatüre, M. Köhl. *Direct Photonic Coupling of a Semiconductor Quantum Dot and a Trapped Ion*. Phys. Rev. Lett. **114**, 123001 (2015).

[167] D. M. Brink, G. R. Satchler. *Angular momentum*. Clarendon Press, Oxford (1962).

[168] N. A. Silant'ev. *Polarization of radiation scattered in magnetized turbulent envelopes*. A&A **449**, 597 (2006).

Danksagung

Zunächst möchte ich Jürgen Eschner danken, mir es ermöglicht zu haben, an einem spannenden und faszinierenden Experiment zu arbeiten. Das von ihm ausgehende, angenehme Arbeitsklima in der Gruppe und die vermittelte Handlungsfreiheit im wissenschaftlichen Arbeiten habe ich während der gesamten Zeit sehr geschätzt. Seine Bürotür stand für uns zu jeder Zeit offen.

Jan Huwer war mir eine große Hilfe durch seine Unterstützung bei meiner Einarbeitung in das Ionenexperiment und während des Umzugs. Die Laborarbeit mit ihm, vor allem bei endlos erscheinenden HALO-Positionsoptimierungen für maximale Zählraten, war mir stets eine große Freude. Christoph Kurz danke ich vor allem für die vielen Diskussionen über physikalische Problemstellungen, die er mit seinem Wissen vorantrieb und für die tolle, effiziente Zusammenarbeit im Labor. Ohne seine Erstellung von HYDRA-Sequenzprogrammen wären die Messungen wie die des Zustandstransfers nicht möglich gewesen. Die Wortspielereien während unseres Schreibens der Dissertationen werde ich nicht vergessen. Philipp Müller möchte ich für das von ihm entwickelte Programm der 18-Niveau-Bloch-Gleichungen danken, das ich für meine Auswertung nutzen durfte. Neben vielen Kalauern bleiben mir unsere regelmäßigen Vergleiche der Mundarten zwischen dem Nord- und Südsaarland in freudiger Erinnerung. Pascal Eich danke ich für seinen Einsatz beim Aufbau und den Messungen mit dem Frequenzkamm, auch wenn dieser wieder mal für Frustration sorgte, und für seine anschließende zielstrebige Unterstützung im Ionenlabor. *El Presidente*, José Brito, war mir über all die Jahre hinweg durch seine gute Laune ein sehr angenehmer Büronachbar. Ich danke ihm für unsere vielen, sportlichen Aktivitäten, von denen ich hier nur das Fallschirmspringen erwähnen möchte. Daneben bedanke ich mich bei der neuen Generation von Doktoranden, Stephan Kucera und Matthias Kreis. Mit der Entwicklung der neuen HYDRA und der Magnetfeldstabilisierung wird das Experiment auch in der Zukunft konkurrenzfähig sein. Ich danke Hannes Gothe für viele anregende Diskussionen, die auch über Physik hinausgingen. Besonders behalte ich seine amüsanten „Das ist so, wie wenn...“-Vergleiche in Erinnerung.

Ich danke unserer netten Sekretärin, Frau Michel, für ihre effiziente Arbeitsweise in der Bearbeitung alltäglicher Bürokratie. Auch die weiteren Arbeitsgruppen der Quantenoptik sorgten für eine angenehme Zeit, insbesondere die Gruppe um Giovanna Morigi bei unseren gemeinsamen Weihnachtsfeiern und die Gruppe um Christoph Becher. Letzteren sei an dieser Stelle auch für die jahrelange Leihgabe ihres Spektrum Analysators gedankt, der sich für viele Messungen mit dem Frequenzkamm als unentbehrlich herausstellte.

Ich danke Prof. Klaus Blaum für seine Bereitschaft zur Begutachtung der vorliegenden Dissertation.

Der größte Dank richtet sich an meine Familie für ihre Unterstützung in jeder Beziehung während der gesamten Zeit.